Novel sulfate inorganic materials with transition metals : crystal chemistry and properties

Diana Nekrasova

Ecole Doctorale "Sciences de la Matière, du Rayonnement et de l'Environnement" (EDSMRE)

Thèse

en cotutelle internationale
entre l'Université Lille et l'Université d'État de Saint-Pétersbourg (Russie)

Pour l'obtention du grade de

Docteur de L'Université de Lille

Discipline : Chimie des Matériaux
Filière : Molécules et Matière Condensée
Présentée et soutenue publiquement par

Diana Nekrasova

Le 18 Mai 2022

Novel sulfate inorganic materials with transition metals: crystal chemistry and properties

---

Cristallochimie et propriétés de nouveaux matériaux inorganiques à base de sulfate et de métaux de transition

---

Dirigée par : M[me] Marie COLMONT, Maître de conférences HDR, ENSCL, France

Dirigée par : M. Oleg SIIDRA, Professor Saint-Petresburg State University, Institute of Earth Sciences, Russia

Co-dirigée par : M. Olivier MENTRE, Professeur, UCCS, France

Membres du Jury :

Rapporteurs :

M[me] Astrid HOLZHEID, Professor, University of Kiel, Germany.

M. Olivier HERNANDEZ, Maître de conférences HDR, Université de Rennes 1, France

Examinateur :

M[me] Elena BELOGUB, Professeur, South Urals Federal Research Center of Mineralogy and Geoecology of the Urals Branch of the Russian Academy of Sciences

M. Sergey BRITVIN, Professor Saint-Petresburg State University, Institute of Earth Sciences, Russia

Novel sulfate inorganic materials with transition metals: crystal chemistry and properties

Cristallochimie et propriétés de nouveaux matériaux inorganiques à base de sulfate et de métaux de transition

Acknowledgements

First, I would like to express my sincere gratitude to my supervisors, Assoc. Prof. Marie Colmont, Prof. Dr. Oleg I. Siidra and Prof. Dr. Oliver Mentré for their support and their guidance, and above all for having instilled in me their love of research.

I am deeply grateful to members of the defense committee: Astrid Holzheid, Olivier Hernandez, Elena Belogub, Sergey Britvin and Alexey Brusnitsin for their acceptance to be in jury, and for valuable comments.

I am infinitely grateful to Evgeniy Nazarchuk, Vadim Kovrugin, Angel M. Arevalo-Lopez and Alexander Tsirlin who spend a lot of time explaining the most difficult concepts for me. I would like to express my heartfelt thanks to Anatoly Zaitsev for his help with the EDS and WDS analysis.

I am very thankful to be a part of the two labs (Saint-Petersburg state university and Lille university), for the invaluable experience of working in such a well-organized and professional teams. I am grateful to Nora Djelal, and Olga Bubnova for helping me with thermogravimetric and EDS analysis, Laurence Burylo, Florent Blanchard, Natalia Platonova and Maria Krzhizhanovskaya for XRD measurements, Frédéric Capet for single crystal diffraction and also Maxence Vandewalle, Daria Spiridonova, Elena Sukharzhevskaya with other issues. I would also like to say thank to all my friends for supporting me during the compilation of this dissertation: Anastasia Zadoya, Olga Chabanenko, Artem Belonosov, Artem Borisov, Jennifer Sarelly Gómez, Olga Tyumentseva, Mishel Markovski, Victoria Ginga (Vladimirova), Elena Zhitova, Margarita Avdontseva, Batoul Almoussawi, Reseda Ismagilova, Ilya Kornyakov, Bastien Leclercq.

The study was carried out under the framework of the international cotutorial thesis project between Saint Petersburg State University, department of crystallography (Russia), and Lille University of science and technology (France). This work was done thanks to a scholarship of the Embassy of France in Russia (la bourse doctorale Vernadski), the French Government, and managed by the Agency Campus France. I am very grateful for this invaluable international experience to the French Government and people who managed my dossier and helped to solve many bureaucratic issues (Sebastien Broyart, Arthur Langlois, Anaelle Durand, Olivier Dubert, Elizaveta Pereyaslova and Daria Miskarova).

This work was financially supported by the Russian Science Foundation, grant no. 16-17-10085. For technical support I express my gratitude to the St. Petersburg State University Resource Centers: Research Centre for X-ray Diffraction Studies, Centre for Optical and Laser Materials Research, Thermogravimetric and Calorimetric Research Centre, Centre for Diagnostics of Functional Materials

for Medicine, Pharmacology and Nanoelectronics, Centre for Microscopy and Microanalysis and I would also like to express my gratitude to the laboratory of the University of Lille.

I would like to thank my parents, Oleg and Patimat, for supporting and helping me throughout my life and my sister Marina for her kind words of support and faith in me, and finily, heartfelt thank to my husband Roman for his love and care for our daughter Valery while I was preparing my thethis.

Abstract

This thesis aims to the synthesis of new materials inspired by geological minerals, focusing on parent crystal structures with specific properties. This work was carried out under the framework of the international cotutorial thesis project between St. Petersburg State University (Russia) and the University of Lille (France). This work was done thanks to a scholarship of the Embassy of France in Russia (la bourse doctorale Vernadski), the French Government, and managed by the Agency Campus France. The significance of these studies is determined by the position between geology, such as the study of crystal growth processes in nature, and inorganic chemistry, in the modelling of natural processes, the production of synthetic compounds and study of physical properties (magnetic and electrochemistry mainly).

The crystal structural types met in minerals cover the complete panorama from 0 to 3-Dimensionnal characters and offer unexploited potentialities in terms of innovating properties. This work is dedicated to the investigation of sulfates compounds, its crystal structures and physical properties. The main methods of the crystal structures study are single crystal and powder X-Ray diffraction. Special attention is paid to the description of crystal structures, since all the compounds are new. A significant part of this work is devoted to experiments aimed to study magnetic properties.

Most of the new compounds that have been obtained are anhydrous sulfates. Keeping in mind that most of anhydrous sulfates are unstable under ambient conditions and easily hydrated, the synthesis and investigation of new anhydrous sulfates remain a challenge. Contrary, the hydrated sulfates have been shown to be earth-abundant mineral species and can be relatively easily prepared in a laboratory.

Résumé

Ce travail de thèse porte sur la synthèse de nouveaux matériaux « géo-inspirés » issus de l'étude de minéraux présentant des structures crystallines et des propriétés spécifiques. Il a été réalisé dans le cadre d'une cotutelle internationale de thèse entre les universités de Saint Petersbourg (Russie) et de Lille (France) et financé par l'ambassade de France en Russie (bourse doctorale Verndaski), le gouvernement français et mis en place par Campus France. L'étude réalisée se situe à l'interface entre différents domaines spécifiques que sont: la géologie de part la modélisation des processus naturels, la chimie inorganique au travers de la croissance cristalline, de la production de composés synthétiques et de l'étude des propriétés physiques (magnétiques et électrochimiques principalement) associées.

Les structures cristallines des minéraux sont relativement complexes, présentant des dimensionnalités variées, de 0D à 3D, offrant ainsi un large champ de possibilités en termes de propriétés physiques associées. Ce travail concerne la synthèse de composés sulfatés, l'étude de leurs structures cristallines et des propriétés physiques qui en découlent. Les structures cristallines ont été étudiées par diffraction des rayons X sur monocristal et sur poudre. La majeure partie des composés mis en évidence durant cette thèse présentent des propriétés magnétiques intéressantes.

La plupart des nouveaux composés ont été obtenus lors de synthèses solide-solide réalisées à partir de sulfates anhydres. Sachant que la plupart des sulfates sont instables dans les conditions ambiantes et s'hydratent facilement, la synthèse et l'étude de sulfates anhydres demeure un challenge contrairement aux sulfates hydratés qui sont naturellement abondant sur terre et facilement synthétisables en laboratoire. Au total 19 nouveaux composés ont pu être étudiés durant ce travail.

Table of contents

1. Introduction

This thesis was carried out under the framework of the international cotutorial thesis project between St. Petersburg State University (Russia) and the University of Lille (France). It took place at the interface between solid-state chemistry (France) and mineralogy (Russia). It is devoted to the study of sulfate inorganic materials and mineral-like phases, as applicant has experience in the field of Geosciences.

Relevance of the topic

This work is devoted to prospection and investigation of new perspectives in inorganic materials study. The main focus of this work is the carry out of investigations between minerals and their synthetic analogues, to obtain new "mineral-inspired" synthetic compounds. The interest of current research has shifted from the creation of new innovative compounds with unique structural architectures to the purpose of innovative properties, towards the detailed study, modification and tuning of the properties of inorganic materials. Many of them are used in a wide variety of technological fields, such as optics, electronics, energy, catalysis, nanotechnology, biotechnology etc …. Despite the ongoing work of scientists in materials science today, we observe a lack of new compounds with fundamentally new structural architectures that determine the physical and chemical properties of materials for industrial purposes. In another hand, there is also a critical need to obtain new materials with innovating or optimized properties for future usage in various domains. The new structural architectures found in complex minerals are very diverse: from zero-dimensional frameworks to three-dimensional complex structures. Compounds created by nature are mostly thermodynamically stable, so it is possible to imagine producing new "mineral-inspired" synthetic compounds with advanced properties simply by doping, coating and shaping after successfully determing the accurate synthesis conditions. From mineralogical point of view, the most interesting and relatively well studied objects are the fumaroles with highly oxidizing conditions on the scoria cones of the Tolbachik volcano (Igor V Pekov et al., 2018). Tolbachik volcano is a great example of the presence of a wide variety of mineral species. A large number of exhalation minerals were found there in high-temperature volcanic fumaroles (Vergasova and Filatov 2012; Siidra et al. 2017). One mineral, glikinite, (Nazarchuk et al., 2020)) was found and studied together with author. Most of these minerals are sulfates of alkali (Na, K, Rb, Cs) and transition (Cu, Mg, Co, Ni, Zn) metals (Nazarchuk et al., 2018; I V Pekov et al., 2018; Scordari & Stasi, 1990). Minerals containing sulfate anions constitute one of the most diverse groups in terrestrial environments ((Alpers et al., 2000)). About 400 species bearing sulfate (SO_4^{2-}) groups are known to date. Transition metals including element with *d* orbitals are of the greatest interest in this context.

Chapters

This thesis is divided in 9 different chapters.

The **first chapter** is dedicated to the relevance of the thesis, practical significance, aim, individual tasks, methods of thesis and its scientific novelty.

The **second chapter** is about all synthesis routes and methods.

The **third chapter** gathered information on new mineral glikinite, $Zn_3O(SO_4)_2$, how and where it was found, what kind of crystal structure there is, its chemical and physical properties. The crystal structure of glikinite is based on OZn_4 tetrahedra sharing common corners, thus forming $[Zn_3O]^{4+}$ chains. Sulfate groups interconnect $[Zn_3O]^{4+}$ chains into a 3*D* framework.

The **fourth chapter** involved synthesis of an analogue of saranchinaite $Na_2Cu(SO_4)_2$, crystal structure and physicochemical properties. The structural analysis revealed unusual heptahedral CuO_7 coordination [4+1+2] of Cu^{2+} cations in its crystal structure. Electrochemical tests showed a limited electrochemical performance and low mobility of Na ions in the structure. The magnetic properties of $Na_2Cu(SO_4)_2$ reflect its crystal structure with one half of copper cations as mainly paramagnetic and the other half as strongly engaged in antiferromagnetic dimer interactions.

The **fifth chapter** is dedicated to the synthesis, crystal structure and properties of Zn and Mg analogs of itelmenite, $Na_2CuMg_2(SO_4)_4$ (Nazarchuk et al., 2018) and synthetic analog of glikinite, $Zn_3O(SO_4)_2$ (Nazarchuk et al., 2020). Synthetic analogues of both minerals were obtained during studies of phase formation in the Na_2SO_4-$CuSO_4$-$MgSO_4$-($ZnSO_4$) systems which lead to essentially different results. The mineral itelmenite, ideally $Na_2CuMg_2(SO_4)_4$, a new structure type, with novel stoichiometry for anhydrous sulfates with alkali and transition metals: $A^{+2}M_2^{+3}(SO_4)_4$ where (*A* = alkali metal, *M* = transition metal). $Na_2CuMg_2(SO_4)_4$ and $Na_2CuZn_2(SO_4)_4$ were evaluated for Na^+ ion diffusion. For the Zn compound, several by-products were observed which are synthetic analogs of puninite $Na_2Cu_3O(SO_4)_2$ (Siidra et al., 2017), as well as hermannjahnite $CuZn(SO_4)_2$ (Siidra et al., 2018) and glikinite-type $(Zn,Cu)_3O(SO_4)_2$. All of them were prepared via solid-state reactions in open systems. The $Na_2CuMg_2(SO_4)_4$, $Na_2CuZn_2(SO_4)_4$ and $(Zn,Cu)_3O(SO_4)_2$ were structurally characterized by the single-crystal XRD. In the Zn-bearing system, the admixture of Cu^{2+} likely controls the formation of itelmenite-type and glikinite-type phases.

The **sixth chapter** is about synthesis, crystal structure characterization and magnetic properties of synthetic analogs of puninite $Na_2Cu_3O(SO_4)_3$ (Siidra et al., 2017), euchlorine $NaKCu_3O(SO_4)_3$ (Scordari & Stasi, 1990), fedotovite $K_2Cu_3O(SO_4)_3$ (Starova et al., 1991) and the related $Rb_2Cu_{3.07}O_{1.07}(SO_4)_3$, $Cs_2Cu_{3.5}O_{1.5}(SO_4)_3$. $A_2Cu_3O(SO_4)_3$ (*A* = Na, K) compounds have been described by (S=1) square lattice topology. Also this part shows the lattice relaxation after the replacement of alkali

by bigger Rb and Cs alkali is accompanied by the insertion of neutral CuO species into $(Rb,Cs)_2Cu_3O(CuO)_x(SO_4)_3$ phases.

The **seventh chapter** is showing results of remarkable polymorphism in a family of $A_2M_3(SO_4)_4$ (A = Rb, Cs M = Co, Ni). This series of compound were synthesized by inspiration of mineral itelmenite, $Na_2CuMg_2(SO_4)_4$. New compounds were obtained by solid-state synthese and structurally characterized by single and powder X-ray diffraction. In order to establish the temperature of crystallization of synthetic phases differential thermal analysis combined with thermogravimetric analyses were directly performed on mixtures of precursors. The synthesis conditions are investigated and the stability and complexity of the three polymorphs are discussed.

The **eighth chapter** shows the result of synthesis, crystal crystal structure characterization of new 5 Rb copper sulfates: $Rb_2Cu(SO_4)Cl_2$, $Rb_4Cu_4O_2(SO_4)_4{\cdot}(Cu_{0.83}Rb_{0.17}Cl)$, $Rb_2Cu_2(SO_4)_3$, $Rb_2Cu_5O(SO_4)_5$ and $Rb_2Cu_2(SO_4)_3(H_2O)$. Moreover, in view of the fact that this work is also carry out under geological approach, in this part is discussed the geochemistry of rubidium in volcanic environments.

And last **ninth chapter** is about two novel anhydrous sulfates $Cs_2Cu(SO_4)_2$ and $Cs_2Co_2(SO_4)_3$. Both of compound were synthesized by the solid-state reactions in vacuum, crystal structure characterization is discussed. Both new compounds have no structural analogs and add to the family of anhydrous alkali transition metal sulfates. The first representative of this family, with determined structure, was saranchinaite $Na_2Cu(SO_4)_2$. In the crystal structure of $Cs_2Cu(SO_4)_2$ Cu-centered CuO_5 polyhedra and SO_4 tetrahedra form $[Cu(SO_4)_2]^{2-}$ layers with large voids. Unique structural feature of $Cs_2Cu(SO_4)_2$ is the edge-sharing of CuO_5 polyhedra and $S2O_4$ tetrahedra. This type of interpolyhedral connectivity has not been described before. In general, the structural topology of the $Cs_2Co_2(SO_4)_3$ is similar to $Cs_2Cu(SO_4)_2$. The interconnection of Co-centered polyhedra with sulfate tetrahedra occurs via common vertices as well as via common edges with the formation of $[Co_2(SO_4)_3]^{2-}$ corrugated layers with elliptical large cavities.

Practical significance

In the frame of this thesis we mainly focused on transition metals from rows number two and three of the periodic table. Over the rows, their specifications change, following the Z number: atomic radius, stable oxidation states, ionization energy, electronegativity, hardness ... etc are modified. They usually formed coloured compounds especially concerning cobalt, copper or chromium due d → d electronic transitions. Most of them offer interesting properties due to variable oxidation states, returning compounds with interesting catalytic activity or magnetic properties. Playing with the modification of the oxidation states is a challenge to overpass to tackle innovative properties. For instance, even if

titanium is stable at the oxidation state 3+ nor 4+, manganese and iron show a larger variety, ranging from 2+ to 7+ for Mn and from 2+ to 6+ for Fe depending on their chemical surrounding. The versatility of oxidation state of a transition metal gives the redox potential to a material which is very interesting in several domains as magnetism or batteries, mainly based on lithium and sodium. Especially, the combined use of transition metals and polyanions (XO_4) increase the redox potential of the metal through a lowering of the position of the Fermi level (Lander et al., 2017). Historically, in the field of Li^+ ions,, after working on the well-known Li*M*O_2 (*M* = Mn, Co) other materials were tested: phosphates with $LiFePO_4$ or sulfates, largely studied because of its low weight, because its high electronegativity favours the formation of fluorosulfates or hydroxysulfates (Subban et al., 2013). Several groups intensively investigated chemical systems based on transition metal sulfates as well as lithium/sodium/rubidium/potassium transition metal sulfates.

Another interesting fact concerning synthetic material is the possibility to tune crystal structures via "intercalation", a specific point that I will describe for the $Rb_2Cu_{3.07}O_{1.07}(SO_4)_3$ and $Cs_2Cu_{3.5}O_{1.5}(SO_4)_3$ (see Section 6). Intercalation in inorganic chemistry refers to reversible ion insertion in host materials, the working principle of rechargeable batteries at both the positive and negative electrodes. However, plethora of other so-called topochemical routes have been conducted tailoring for instance mixed anion compounds in extended solids at low temperature by rational anionic exchange (Oben et al., 2021). Dealing with the cationic part of the crystalline network itself, (reversible) exsolution enables the creation of cationic-depleted lattices under reduction, for instance after the exsolution of nanometric nickel clusters from perovskites phases (Neagu et al., 2015) with catalytic insights, but also more rarely in oxidizing media as observed after exsolution of nano-scaled hematite in $LiFe_{2-x}(PO_4)_2$ (Hamelet et al., 2009) or $BaFe_{2-x}(PO_4)_2$ (David et al., 2014), this latter example giving rise to a variety of original ordered Fe-vacancy depleted 2D triangular lattices (Alcover et al., 2015). However, as for most intercalation methods, in this last example the driving force is electrochemical and relies on well-adapted redox couples in which the Fe^{2+}/Fe^{3+} emerge efficiently in standard laboratory conditions. In Section 6 of this thesis an original series of topologically related with incorporation of various amount of neutral CuO by depleted Cu^{2+} chains are discussed.

Most of the new obtained compounds and minerals of this thesis are described in terms of anion-centered tetrahedral. Using an anion centered approach to describe this structure, the presence of "additional" oxygen atom was recognized. For example, Puninite (Siidra et al., 2017), euchlorine (Palache et al., 1951), fedotovite (Vergasova et al., 1988) with the general formula $A_2Cu_3O(SO_4)_3$, where (*A* = K, Na), these 'euchlorine group' of minerals belong to a large family of structures with so-called 'additional' or 'extra' oxygen atoms, which are coordinated only by copper atoms to form oxocentred

$(OCu4)^{6+}$ tetrahedral (Krivovichev, Mentré, et al., 2013). These anion-centered tetrahedral could form 0D units with $[O_2Cu_6]^{8+}$ dimers (Siidra et al., 2017), 1D units with $[O_2Cu_4]^{4+}$ chains (Effenberger & Zemann, 1984), 2D units with the $[OCu_2]^{2+}$ layer (Palache et al., 1951) and 3D units with [OCu] framework (Åsbrink & Norrby, 1970).

There are also several other fields where sulfates have found their practical application: sulfate process for the production of cellulose is one of the most economically effective in the industry in our days (Chen et al., 2013). The simplest sulfates are also well known, industrially used as pigments ($BaSO_4$) (Mikhailov et al., 2019), cements (Na_2SO_4) (Donatello et al., 2013), or more rarely for X-Ray dosimetry ($FeSO_4$) (Back & Miller, 1957), or clinical chemistry (Cole & Evrovski, 2000).

The practical relevance is also reflected in the fact that the results of the refinement of the crystal structures are included in the structural databases and the mineral samples studied in this work are selected from private collections, which is important in terms of systematization of these collections.

Aim of thesis

This study deals with the synthesis of new materials inspired by geological minerals, focusing on parent crystal structures and expecting specific properties. The significance of these studies is determined by the position between geology, such as the study of crystal growth processes in nature, and inorganic chemistry, for example, in the modelling of natural processes and the production of synthetic compounds in the laboratory. The crystal structural types met in minerals cover the complete panorama from 0 to 3-Dimensionnal characters and offer unexploited potentialities in terms of innovating properties. Concretely, we aim to design new compounds with various dimensionality working in various chemical systems, mainly based on sulfate groups assembled into a structuring framework, the empty spaces being filled by groups of various natures, for which the structural/physical specificities (electronic, magnetic, optical) will be fully rationalized.

Keeping in mind that most of anhydrous sulfates are unstable under ambient conditions and easily hydrated, the synthesis and investigation of new anhydrous sulfates remain a challenge. Contrary, the hydrated sulfates have been shown to be earth-abundant mineral species and can be relatively easily prepared in a laboratory (Kovrugin et al., 2019).

Individual tasks of thesis

(1) Development of methods for the synthesis of sulfate compounds of copper, zinc, cobalt and nickel with alkali metals.

(2) X-ray diffraction characterization of obtained materials (mainly single crystals), determination of crystal structures, description of the crystal-chemical features;

(3) Attempts to prepare single phase of the corresponding polycrystalline materials, by the best adapted route;

(4) Crystal chemical analysis of available data on structural chemistry of sulfate compounds: i.e. analysis of geometrical parameters (bond distances and angles), coordination geometry and their frequency of occurrence in natural and synthetic materials, stability of sulfate compounds under different physical-chemical conditions;

(5) Measurements of physical properties (i.e. magnetic, conducting, optical etc. depending on cation and architectures) if accurate and theoretical studies of the chemical bonding by means of quantum chemical (1st principle) calculations.

Methods

In order to study the crystal structure, composition and properties of synthetic compounds different methods were used:

- *Diffraction techniques*: X-rays on single crystals and/or powder, at room temperature or in temperature.
- *Spectroscopy*: Infrared.
- *Elemental analysis*: (1) Microprobe analysis, (2) Electron dispersive Spectroscopy
- *Others:* (1) Magnetic properties, (2) Optical properties, (3) Electrochemical properties.

Chapter 2 will describe in more detail all the methods used.

Scientific novelty

Scientific novelty is reflected in the approach used in this thesis: minerals as a source of ideas for creating new materials. This approach was already successfully used in a previous joint PhD between two labs and is at the intersection of earth sciences and inorganic chemistry. I would like to point out that in my work I perform the complete cycle of research from study of fumarolic minerals (including field works) to structural characterization, prediction of properties and synthesis conditions of minerals, synthesis of new fumarolic minerals-inspired materials and novel compounds, then structural characterization of this synthetic compounds, and finaly - study physical and physical-chemical properties of “geo-inspired materials”. The novelty of thesis is reflected in the combination of geology and chemistry approaches to the study of minerals and inorganic compounds containing sulfate anions. In that sense, this “geo-inspired materials” approach is innovative and placed in the frame of the renewal of inorganic chemistry, delivering complex functional materials.

Approbation of the study

The main results of the work were reported at the following congresses, conferences and meetings: The 31rd European Crystallographic Meeting "ECM31" (Oviedo, Spain, 2018); IX National Conference on Crystal Chemistry (Suzdal, 2018); XIX International Meeting on Crystal Chemistry, X-ray Diffraction and Spectroscopy of Minerals, dedicated to the memory of E.S. Fedorov (1853 - 1919) (Apatity, 2019).

Publications

As a result of the work, 8 articles were written and published, all of them are included in the international citation systems Web of Science and Scopus. 5 abstracts of the international scientific conferences were published.

2. Experimental part and methodology

2.1 X-ray diffraction analysis

Single-crystal X-ray analysis were necessary to establish the crystal structure, while powder X-ray analysis were necessary to validate the pure phase.

2.1.1 Single-crystal X-ray analysis

Single-crystal X-ray analysis were used in this work to identify and determine the crystal structure of our products. For each measurement, crystals of samples were selected after separation under the microscope and further used for diffraction measurements via goniometer head collar. All crystal structures were carried out using a Bruker SMART diffractometer equipped with an APEX II CCD detector operating with MoKa radiation at 50 kV and 40mA. More than a hemisphere of three-dimensional XRD data was collected with frame widths of 0.5° in ω, and a 10 - 45 s count time for each frame depending on the crystal size (the smallest, the longest). Then, the collected data were integrated and corrected for absorption using a multi-scan type model using the APEX2, APEX3 and X PREP Bruker programs (Bruker 2014, Bruker 2018). The crystal structures were solved by direct methods and refined using the SHELXL program implemented in the WinGX program package (Sheldrick, 2015). The program CELL_NOW (Sheldrick, 2015) was employed to find a cell and orientation matrix despite the presence of several twin domains or other junk. This program very helped to check and solve twining problems of some crystals.

2.1.2 Powder X-ray diffraction

Typical powder XRD analyses of the compounds were collected at room temperature in the 2θ range of 10−60 ° with a scan step width of 0.02 ° and a scan rate of 0.5 s/step using the Bruker D8 diffractometer on the glass sample holder with an automated sample feed system.

High quality diffraction patterns were recorded in the 2θ range of 8° and 110° by steps of 3.0 s/0.02° using a Rigaku Smart lab diffractometer equipped with a 9-kW rotating anode and Rigaku «Ultima IV». The advantages of this method are: (1) perfect quality of measuring, (2) high speed and (3) possibility to use very small amounts of powder (5-10 mg) what can be prepared on background-free holders.

In the case of samples containing only few crystals, powder X-ray studies were carried-out using a Rigaku R-Axis Rapid II diffractometer with cylindrical image plate detector, using CoKα radiation.

These crystals were crushed and mounted in an epoxy ball with R ~0.5 mm on a glass fiber. For the powder-diffraction study, a Gandolfi-like motion on the φ and ω axes was used to randomize the sample and observed *d* values and intensities were derived using osc2xrd software (Britvin et al., 2017).

The XRD-patterns were analyzed using the DIFFRAC.EVA V4.0 software (Bruker). The Profile-matching refinement, if done, were carried out using the single crystal structural model for each compounds imported in the JANA2006 crystallographic system (Petrícek et al., 2014). The background was fitted using Chebyshev polynomial function, and the peak shapes were described by a Pseudo-Voigt function.

2.1.3 *High-Temperature X-ray Diffraction*

The temperature stability of the materials was carried out using HTXRD techniques on a Rigaku Smart Lab X-ray diffractometer equipped with a 9 kW rotating-anode X-ray generator (CuKα1 = 1.54059 Å). XRD patterns were collected in the 8−80° 2θ range, heating with a step size of 20 °C or 10 °C depending on the phases. Calculations of the unit-cell parameters were performed using the program package Topas 4.2. (Bruker 2009), whereas visualization and calculation of the thermal expansion parameters tensor were performed using the TTT program package (Bubnova et al., 2013).

2.2 DTA- TGA analysis

DTA and TGA were performed using a two equipment's with different methods of sample preparation. TGA 92-1600 SETARAM and STA 429 CD NETZSCH analyzers from room temperature to 700-900 °C. For the first method, the sample used was a powder, and for the second, a pellet. The powders (ca. 20-30 mg) were pressed into pellets (~5 mm diameter and 0.7 – 0.8 mm height) using a steel die (pressure 1 kg/mm^2). This technique, in comparison with the use of powder samples, provides a better reproducibility and precision of results. After weighing with a precision of ± 10 μg, each pellet was loaded into a Pt-Rh crucible and mounted on a holder, after which TGA study was run at the heating rate of 20°C/min in a dynamic atmosphere (air flow at 50 cm^3/min) from 40 to 800-900°C; cooling was performed down to 25-200°C at the same rate. The gaseous decomposition products were analyzed on a QMS 403 C NETZSCH quadrupole mass spectrometer operating in a 1 – 121 *m*/*z* range.

2.3 Magnetic measurements

Magnetization and heat capacity were measured with small amounts of sample mass (10 to 50 mg) over the temperature range from 2 to 400 K using the PPMS Dynacool (9T) from Quantum Design and MPMS SQUID-VSM (Quantum Design). For temperature-dependent magnetization measurements both zero-field-cooling (ZFC) and field-cooling (FC) protocols were used. Powder sample were used for magnetization measurement and pellet for heat capacity measurement.

2.4 Electron spin resonance

X-band EPR experiments were carried out with a Bruker ELEXYS E580E spectrometer. Microwave power and modulation amplitude were respectively 1 mW and 5 G. The spectra were recorded between 300 and 4 K using helium ITC503 oxford temperature regulation.

2.5 Electrochemical measurements

Electrochemical tests were operated in a galvanostatic mode. The charge (or discharge) rate is generally given using the nomenclature C/*n*, where *n* = hours. Complete charge (or discharge) corresponds to the removal (or uptake) of 1 Li^+ or 1 Na^+ per Cu^{2+}. Electrochemical tests were performed in Swagelok®-type cells assembled in an argon-filled glovebox. Electrodes were prepared by ball-milling (15 minutes) in air of polycrystalline sample with carbon C_{sp} as a conductive additive (83.3 : 16.7 wt. %). About 8 mg of the as-prepared composite was studied as a cathode separated from either Na or Li metal as a negative electrode by two sheets of Whatman® GF/D borosilicate glass fiber soaked in a liquid electrolyte. 1M molar solutions of $NaPF_6$ or $LiPF_6$ in EC : DMC (1 : 1 weight ratio) were used as the electrolytes. 3 % in mass of fluoroethylene carbonate (FEC) was added to the Na-based electrolyte. Galvanostatic tests were conducted with an Apple® Mac Pile II potentiostat.

2.6 Infrared spectroscopy (FTIR)

The infrared (IR) spectrum of polycrystalline materials were measured using a PerkinElmer Spectrum Two FTIR spectrometer equipped with a diamond attenuated total reflectance (ATR) accessory with a resolution of 4 cm^{-1} and 16 scans.

2.7 Chemical compositions

To determine the chemical composition of the synthetic itelmenite and glikinite two methods were used to prepare the samples. For the first one, a selected area with crystals was filled with epoxy resin and in the second one, just one crystal (290x100 μm in size) was mounted in epoxy resin. Both of

them were polished with successively decreasing oil suspensions of diamond powders with the finishing size of 0.25 μm. The minerals or synthetic compounds were then analyzed by energy-dispersive (EDS) or wavelength-dispersive (WDS) spectrometry.

We used EDS for for quick chemical determination, while WDS was used only in case of work out the exact values, this analysis is time-consuming but more accurate.

The analyses were obtained using a Hitachi S-3400N scanning electron microscope equipped with an Oxford Instruments X-Max 20 Energy Dispersive Spectrometer, and Oxford Instruments Inca Wave 500 Wavelength Dispersive Spectrometer.

The ED spectra usually were obtained under following conditions: 20 kV accelerating voltage, 1.8 nA beam current; defocused beam (10 μm spot size); acquisition time 30 seconds per spectrum. The spectra were processed automatically using the AzTecEnergy software package using the TrueQ technique. The WD spectra were obtained under following conditions: 20 kV accelerating voltage, 4 nA beam current, 60 seconds per element acquisition time, matrix correction using the XPP method. Synthetic $CaSO_4$ (S *Kα*), Cu metal (Cu *Kα*), Zn metal (Zn *Kα*) and Mo metal (Mo *Lα*) were used as standards for both EDS and WDS analyses.

2.8 Calculations

2.8.1 Bond valence calculation

The bond valence s_{ij}, were calculated from the bond lengths d_{ij}, using expression:

$$s_{ij} = \exp\left[(r_0 - d_{ij})/b\right] \quad (1)$$

where *s* is the bond valence (in valence units), *d* is the observed bond length, and r_o and *b* are fitted constants called bond-valence parameters, the values of r_0 and *b* were taken from (Gagne & Hawthorne 2015). In the case of low atoms occupation, the occupation of each individually. S^{ij} multiplies was taken into account by the coefficient of *s.o.f.*

2.8.2 Distortion parameter

The Δ_{oct} bond-length distortion parameter Δ_{oct}, was calculated according to Wildner 1992, using following formula:

$$\Delta_{oct}=\frac{1}{6}\sum_{i=1}^{6}\left[\frac{(d_i-d_m)}{d_m}\right]^2 \quad (2)$$

where :

d_i = (*M*-O) bond-length,

d_m = <*M*-O> average bond-length (*M* = transition metal or alkaline earth).

All of the *M*-O bonds ≤3 Å were taken into consideration.

2.8.3 First-principle calculations

Exchange couplings between the Cu^{2+} ions were obtained by density-functional-theory (DFT) band-structure calculations performed in the FPLO code (Opahle et al., 2000) with the Perdew-Burke-Ernzerhof flavor of the exchange-correlation potential (Perdew et al., 1996). Mapping procedure (Xiang et al., 2011) was used to calculate parameters J_{ij} of the spin Hamiltonian,

$$H = \sum_{<ij>} J_{ij} S_i S_j \quad (3)$$

where the summation is over lattice bonds <*ij*>, and S = ½ for individual Cu^{2+} ions or S = 1 for the Cu_6 hexamers. Correlations effects in the Cu 3*d* shell were treated on the mean-field level using the DFT+*U* procedure with the on-site Coulomb repulsion U_d = 9.5 eV, Hund's coupling J_d = 1 eV, and double-counting correction in the atomic limit (Nath et al., 2013, 2015).

2.8.4 Quantum Monte-Carlo simulations

Magnetic susceptibility and magnetization for the aforementioned spin Hamiltonians was calculated using the *loop* and *dirloop_sse* algorithms of the ALPS simulation package (Albuquerque et al., 2007; Todo & Kato, 2001) on finite lattices with periodic boundary conditions and up to L = 48 or L = 12x12 sites for 1D and 2D interaction geometries, respectively.

2.8.5 Structural complexity calculations

Structural-complexity parameters were calculated using the Shannon information content per atom ($^{str}I_G$) and per unit cell ($^{str}I_{G,\,total}$) according to the following formulae (Krivovichev, 2012):

$$^{str}I_G = -\sum_{i=1}^{k} p_i \log_2 p_i \quad (4)$$

where k is the number of crystallographic orbits in the structure and p_i is the random-choice probability for an atom from the ith crystallographic orbit:

$$p_i = \frac{m_i}{v} \quad (5)$$

where m_i is the multiplicity of the ith crystallographic orbit in the reduced unit cell and v is the number of atoms in the reduced unit cell. Naturally,

$$^{str}I_{G,total} = 20 \times 2.322 = 46.439 \quad (6)$$

The parameters have been calculated using the TOPOS program package (Blatov et al., 2014).

2.9 Synthesis

2.9.1 Problems with the preparation of synthetic analogues of anhydrous sulfate minerals

It is difficult to prepare a synthetic mineral without impurities. As we know, every mineral is not homogenous and contains a certain percentage of impurities that are often impossible to remove. In order to be able to study the physical properties of minerals, it is necessary to obtain a pure synthetic analogue. These impurities can significantly modify the physical properties, inducing false results, not only due to magnetic impurities which are included phases with the cations like Co^{2+}, Ni^{2+}, but also due to non-magnetic phases with Zn^{2+} (Bag et. all., 2018). Sometimes, non-magnetic impurities drastically affect the properties as shown in the article of (Sidis et al., 2010).

The synthesis of anhydrous sulfates is quite a challenging task and the following lines will explain why.

– First of all, they are unstable in air and hydrated by air moisture very quickly (Siidra et al., 2019).

– Secondly, they are very soluble (Kovrugin et al., 2019).

– Thirdly, sulfates demonstrate a relatively low thermal stability accompanied by decomposition of sulfate groups to SO_3 or $SO_2 + O_2$ above 600 - 750 °C (Nekrasova et al., 2021).

As a consequence, the work under the synthesis of analogues of anhydrous sulfate minerals could requires working in glovebox, desiccator, muffle furnace and a unit for evacuating quartz ampoules, in fact, the presence of quartz ampoules themselves. That is why the experimental part is one of the most important and demanding part of this work.

In order to study the crystal structure, composition and properties of synthetic compounds, different methods were used. Keeping in mind that sulfate alkali-based minerals can usually be found in fumarolic sublimates, chemical vapor transport reactions method (CVT-method) was chosen due to similarity with natural conditions of mineral formation from volcanic gases. In our case, most reactions did not produce essential sublimates such that the conventional solid-state synthesis in evacuated silica tubes was preferred. For some samples, coprecipitation-type synthesis process was used.

In some instances, an inert atmosphere or vacuum is used to keep the stability of sulfate anions during the chemical reaction. For example, alluaudite-type $Na_{2.32}Co_{1.84}(SO_4)_3$ (Dwibedi et al., 2017) and $Na_{2.5}Fe_{1.75}(SO_4)_3$ (Goñi et al., 2017) compounds were synthesized in Ar/N_2-regulated furnaces by low temperature solid state reactions at 350°C. Crystal growth from melt in the temperature range of 460–500 C in an artificial inert-flow reactor was used for preparation of V-containing sodium sulfates $NaV(SO_4)_2$ (Fehrmann et al., 1991), $Na_3V(SO_4)_3$ (Boghosian et al., 1994), $Na_8(VO)_2(SO_4)_6$ (Nielsen et al., 1999), and $Na_2VO(SO_4)_2$ (Fehrmann et al., 1990). Similar experiments carried out in sealed Ag-containers or quartz ampoules leading to the crystallization of $Na_5(CuO_2)(SO_4)$ (Amann & Möller, 2003), $Na_{11}(CuO_4)(SO_4)_3$ (Amann et al., 2004), $Na_8(CoO_3)(SO_4)_2$ (Möller et al., 2002) or $Na_4(MoO_2)(SO_4)_3$ (Schäffer & Berg, 2008).

In this work we used precursors containing water molecules such as $CuSO_4,\cdot 5\ H_2O$, $CoSO_4,\cdot 7\ H_2O$, $NiSO_4,\cdot 7\ H_2O$, etc… But since our research involved only anhydrous sulfates, it was necessary to use non-hydrated reagents. As consequences, all hydrated precursors were previously dried at 400 °C during 12 h and further rapidly placed into glovebox.

The experimental details of synthesis methods of all compounds obtained during this thesis are summarized in **Table 1** for the reader's convenience.

Table 1. The list of new synthetic compounds and their method of preparation.

Formula		Preparation method
$Na_2Cu(SO_4)_2$	Chapter 4	a) Evaporation from an aqueous solution containing nearly equimolar quantities of Na_2SO_4, and $CuSO_4\cdot 5H_2O$. b) Slow cooling of the melt containing equimolar quantities of $CuSO_4$ and Na_2SO_4 in an evacuated ampoule from 950 °C.
$Na_2CuMg_2(SO_4)_4$	Chapter 5	Solid state synthesis in air from a mixture of Na_2SO_4, $CuSO_4$ and $MgSO_4$. Reagents were taken in 1:1.09:1.91 ratio and were loaded into a gold/platinum crucible and kept at 600 °C for 3 hours in air and subsequently cooled for 9 hours to room temperature.
$Na_2CuZn_2(SO_4)_4$	Chapter 5	Solid state synthesis in air from a mixture of Na_2SO_4, $CuSO_4$ and $ZnSO_4$. Reagents were mixed in 1:1.09:1.91 ratio. The mixture

		was loaded into a gold/platinum crucible and kept at 550°C (in accordance with thermal analysis data described below) for 1 hour in air, followed by cooling for 9 hours to room temperature.
$Na_2Cu_3O(SO_4)_3$	Chapter 6	a) Solid state synthesis in air from a mixture of Na_2SO_4, $CuSO_4$ and CuO in 1:2:1 ratio. Mixtures of precursor were loaded into gold plates and kept at 560 °C during 3 hours in air and subsequently cooled for 9 hours to room temperature. b) Slow cooling of the melt containing of Na_2SO_4, $CuSO_4$ and CuO in an evacuated ampoule from 700 °C in 1:2:1 ratio.
$NaK_2Cu_3O(SO_4)_3$	Chapter 6	a) Solid state synthesis in air from a mixture of Na_2SO_4, K_2SO_4, $CuSO_4$ and CuO in 0.5:0.5:2:1 ratio. The condition of synthesis was the same like for $Na_2Cu_3O(SO_4)_3$. b) Slow cooling of the melt containing of Na_2SO_4, K_2SO_4, $CuSO_4$ and CuO in an evacuated ampoule from 700 °C in 0.5:0.5:2:1 ratio.
$K_2Cu_3O(SO_4)_3$	Chapter 6	a) Solid state synthesis in air from a mixture of K_2SO_4, $CuSO_4$ and CuO in 1:2:1 ratio. The condition of synthesis was the same like for $Na_2Cu_3O(SO_4)_3$. b) Slow cooling of the melt containing of K_2SO_4, $CuSO_4$ and CuO in an evacuated ampoule from 700 °C in 1:2:1 ratio.
$Rb_2Cu_{3.07}O_{0.07}(SO_4)_3$	Chapter 6	a) Solid state synthesis in air from a mixture of Rb_2SO_4, $CuSO_4$ and CuO in 1:2:1 ratio. The condition of synthesis was the same like for $Na_2Cu_3O(SO_4)_3$. b) Slow cooling of the melt containing of Rb_2SO_4, $CuSO_4$ and CuO in an evacuated ampoule from 700-750 °C in 1:2:1 ratio.
$Cs_2Cu_{3.5}O_{1.5}(SO_4)_3$	Chapter 6	a) Solid state synthesis in air from a mixture of Cs_2SO_4, $CuSO_4$ and CuO in 1:2:2 ratio. The condition of synthesis was the same like for $Na_2Cu_3O(SO_4)_3$. b) Slow cooling of the melt containing of Cs_2SO_4, $CuSO_4$ and CuO in an evacuated ampoule from 700-750 °C in 1:2:2 ratio.
$Cs_2Ni_3(SO_4)_4$	Chapter 7	a) Slow cooling of the melt containing of Cs_2SO_4, $NiSO_4$ in equimolar quantities in an evacuated ampoule from 700 °C. b) Solid state synthesis in air from a mixture of Cs_2SO_4, $CuSO_4$ in equimolar quantities. Mixtures were kept at 600 °C during 3 hours in air and subsequently cooled for 9 hours to room temperature. c) Evaporation from an aqueous solution containing equimolar quantities of Cs_2SO_4 and $NiSO_4$.
$Cs_2Co_3(SO_4)_4$	Chapter 7	Solid-state reaction in air using stoichiometric ratio of Cs_2SO_4, and $CoSO_4$. The mixture was ground and loaded into a gold crucible and heated to 600 °C for 3 hours and then cooled for 12 hours to room temperature.
$Rb_2Ni_3(SO_4)_4$	Chapter 7	a) Slow cooling of the melt containing of Rb_2SO_4, $NiSO_4$

		in stoichiometric ratio in an evacuated ampoule. The quart ampule was placed into the furnace and heated at 750 °C during 18 hours and then slowly cooled to room temperature for 99 hours. b) Evaporation from an aqueous solution containing equimolar quantities of Rb_2SO_4, $NiSO_4$. c) Solid state synthesis in air from a mixture of Rb_2SO_4 and $NiSO_4$. Mixtures were kept at 600 °C during 3 hours in air and subsequently cooled for 9 hours to room temperature.
$Rb_2Co_3(SO_4)_4$	Chapter 7	a) Slow cooling of the melt containing of Rb_2SO_4 and $CoSO_4$ in stoichiometric ratio in an evacuated ampoule. The quart ampule was heated at 750 °C during 34 hours and then slowly cooled to room temperature for 99 hours. b) Evaporation from an aqueous solution containing equimolar quantities of Rb_2SO_4, $CoSO_4$. c) Solid state synthesis in air from a mixture of Rb_2SO_4, $CoSO_4$. Mixtures were kept at 600 °C during 3 hours in air and subsequently cooled for 9 hours to room temperature.
$Rb_2Cu_2(SO_4)_3$ $Rb_2Cu_5O(SO_4)_5$	Chapter 8	Solid state synthesis in the evacuated quartz ampoule from Rb_2SO_4 and $CuSO_4$ in ratio 3:1. From this mixture was prepared pellet (ca. 5 × 3 mm) and loaded into a quartz ampoule. The ampoule was heated up to 700 °C for 3 hours and kept for 10 h. Then they were cooling during 96 h until 500 °C and further cooling during 12 hours to room temperature.
$Rb_2Cu_2(SO_4)_3H_2O$	Chapter 8	This phase was synthesized accidentally. The mixture of precursors Rb_2SO_4 and $CuSO_4$ were keep in the air during one week. The mixture was sorbeted the H_2O molecules. From this mixture was prepared pellet (ca. 5 × 3 mm) and loaded into a quartz ampoule. The ampoules were heated up to 750 °C for 5 hours and kept for 10 h. Then they were cooling during 40 h until 500 °C and further cooling to room temperature. The products consisted of green crystals of $Rb_2Cu_5O(SO_4)_5$ and light-blue crystals of $Rb_2Cu_2(SO_4)_3{\cdot}H_2O$.
$Rb_2Cu(SO_4)Cl_2$ $Rb_4Cu_4O_2(SO_4)_4{\cdot}(Cu_{0.83}Rb_{0.17}Cl)$	Chapter 8	Single crystals of $Rb_2Cu(SO_4)Cl_2$ and $Rb_4Cu_4O_2(SO_4)_4$ ($Cu_{0.83}Rb_{0.17}Cl$) were grown by slow cooling of melt containing of anhydrous $CuSO_4$ and RbCl in ratio 1:2 in an evacuated quartz ampoule. The ampoules were heated up to 700 °C for 3 hours and kept for 10 h. Then it was cooling during 72 h until 550 °C and further cooling during 12 hours to room temperature.
$Cs_2Cu(SO_4)_2$	Chapter 9	Solid state synthesis in vacuum from a mixture of Cs_2SO_4, $CuSO_4$ and CuO in 1:2:2 ratio. The ampoule was heated up to 700 °C for 3 hours and kept for 10 h. Cooling to 500 °C was performed in 96 h, and in more 12 hours to room temperature.
$Cs_2Co_2(SO_4)_3$	Chapter 9	Solid state synthesis in vacuum from a mixture of Cs_2SO_4, $CoSO_4$ and CuO in 1:2:2 ratio. The ampoule was heated up to 700 °C for 3 hours and kept for 10 h. Cooling to 500 °C was performed in 96 h, and in more 12 hours to room temperature.

2.9.2 DTA- TG and HTXRD analyses for precursors

In order to optimize the temperature of crystallization of synthetic phases DTA and TGA analyses were performed for mixtures of precursors. This procedure was performed for each synthesis to see the crystal formation process. HTXRD studies were performed up to 550° to avoid melting of the sample in the sample holder. Here we will see the example for phases from Chapter 7: $Cs_2Ni_3(SO_4)_4$ and $Cs_2Co_3(SO_4)_4$.

$Cs_2Ni_3(SO_4)_4$

A mixture of Cs_2SO_4, $NiSO_4$/$CoSO_4$ (just dehydrated) in 1:3 ratio was prepared and the TGA and DTG analysis were performed using a thermoanalyzer TGA 92 SETARAM working under air atmosphere. The samples were heated at 10°C/min form 30°C up to 1000°C. For *M* = Ni, the TGA curve presented on **Figure 1a** evidenced several accidents at 90 and 110 °C consistent with the loss of water molecules of the precursors as already detailed (Boyanov, 2002). Keeping in mind the preliminary dehydration stage and short time of contact in air, it shows the well known extreme reactivity of the sulfate precursors to moisture. In agreement with HTXRD results (see **Figure 1b**), the removal of water molecules occurr between 50 and 150°C. A first uncomplete reaction is observed by XRD at 350°C corresponding to the growth of $Cs_2Ni_3(SO_4)_4$ accompanied with residual Cs_2SO_4 and $NiSO_4$ (**Figure 1c**). At 700°C, a weight loss is observed on TGA analysis corresponding to the decomposition through the removal of sulphate molecules. Details of patterns identification for all stages are given in Figure 1c.

$Cs_2Co_3(SO_4)_4$

For the compound $Cs_2Co_3(SO_4)_4$ TGA and HTXRD are shown on **Figure 1d** and **Figure 1e**. A similar trend was observed: first, the dehydratation of precursors where the these low-temperature peaks (from 91 °C to 330 °C) occur due to the a two-stage dehydration processes: in the first stage at 91 °C the six molecules of water are dismissed and at the temperature of 329 °C (second stage of the process) the last seventh molecule is discharged. The event at 146 °C may be related to partial melting of the sample, at 531 °C correspond to the recrystallization and forming of $Cs_2Co_3(SO_4)_4$, $Cs_2Co_2(SO_4)_3$. Endothermic peak at 850 °C belongs to decomposition process of sulfates compounds. Details of patterns identification for all stages are given in **Figure 1f**.

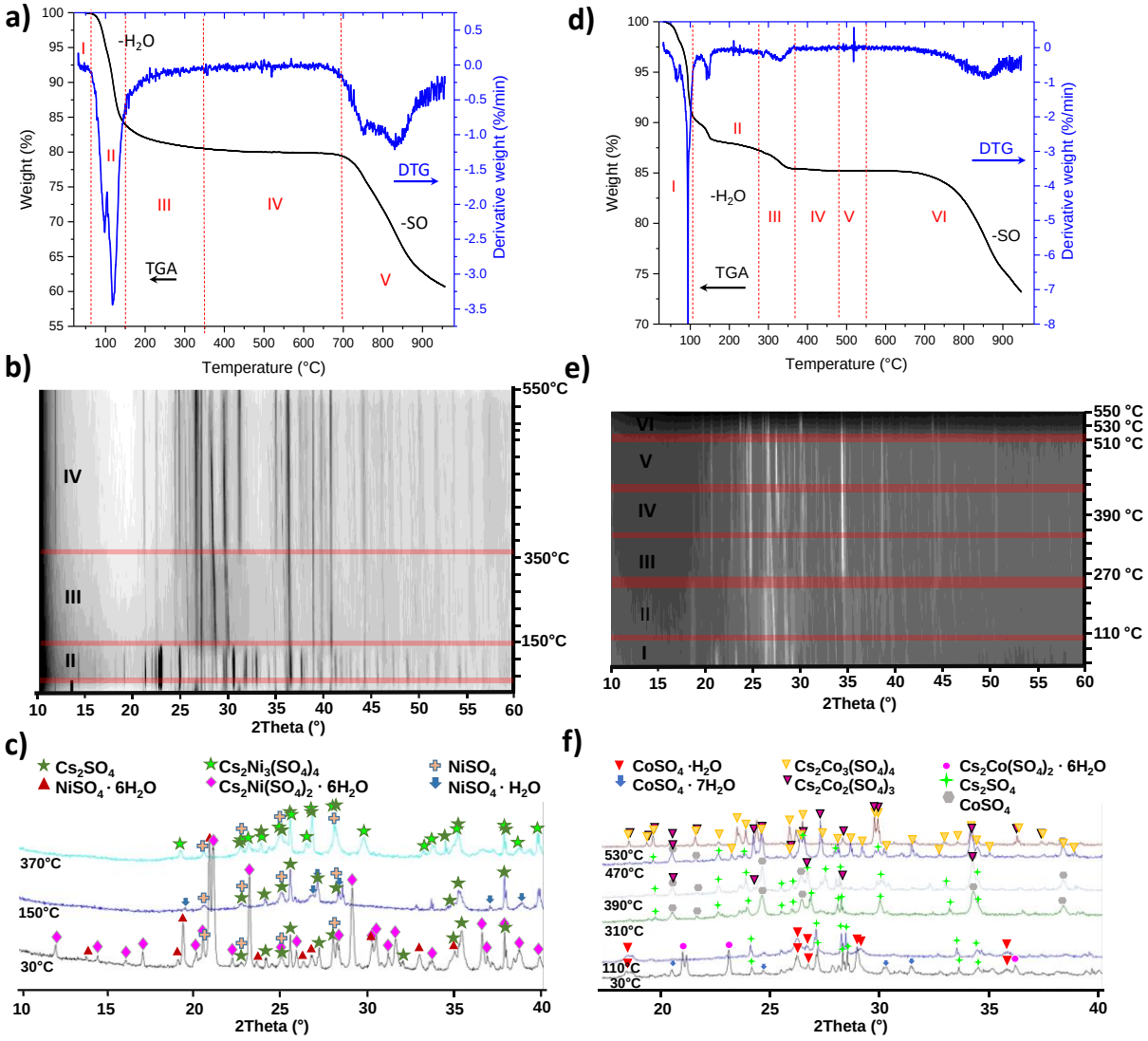

Figure 1 TGA-DTA curves from 30 °C to 1000 °C for the mixture of precursors for $Cs_2Ni_3(SO_4)_4$ (a) Cs_2SO_4, $NiSO_4$ and for $Cs_2Co_3(SO_4)_4$ (d) Cs_2SO_4, $CoSO_4$ in 1:3 ratio, an HTXRD study explained the transitions of in the case of (b) $Cs_2Ni_3(SO_4)_4$ and (e) $Cs_2Co_3(SO_4)_4$. For $Cs_2Ni_3(SO_4)_4$, step I- II correspond to the dehydratation process, step III - IV to the formation of $Cs_2Ni_3(SO_4)_4$ and step V to the collapse of the sample by sulfate removal (a, b). For $Cs_2Co_3(SO_4)_4$, step I - II correspond to the dehydratation process, where sixth water molecule is discharged, step III to lost seventh molecule, IV-V - formation of $Cs_2Co_3(SO_4)_4$ and $Cs_2Co_2(SO_4)_3$, VI – decomposition process (HTXRD from 30 °C to 350 °C with step 40 °C, 350-550 °C - step 20 °C). Phase identification on some selected patterns registered at different temperatures on mixtures of precursors for (c) $Cs_2Ni_3(SO_4)_4$ and (e) $Cs_2Co_3(SO_4)_4$.

3. Glikinite, $Zn_3O(SO_4)_2$, a new mineral species

3.1 Introduction

Since this work is half done in the Department of Geology, one of the tasks was to establish the mineral species. And now the first chapter on the results of the work, I want to start with the mineral glikinite. As part of a scientific expedition to the Tolbachik volcano, Kamchatka, Russia the mineral glikinite was found (Nazarchuk et al., 2020).

In general, anhydrous sulfates of transition metals (Cu, Zn, Mn, Ni, Co) are very common in the minerals of the exhalative fumaroles of the Tolbachik volcano (Vergasova and Filatov, 2012; Siidra et al., 2017; Pekov et al., 2018; Siidra et al., 2019). These minerals are characterized by a large quantity of anion-centered tetrahedral complexes surrounded by sulfate tetrahedrons and forming the various crystal structural architectures. Zinc, along with copper, is one of the predominant metals in arc volcanic emissions (Edmonds et al., 2018). Fumarolic mineral assemblages enriched in zinc have been described from many localities in the world, as in Vulcano (Bernauer, 1936) and Santiaguito (Stoiber and Rose, 1974). Additionally, zinc oxide and zinc silicate condensate particles were detected in considerable amounts in the ashes of Mt. St. Helens (Thomas et al., 1982). Zinc, as an impurity, is very characteristic for many copper sulphate minerals (Pekov et al., 2018). Surprisingly, till recently (Siidra et al., 2018; Siidra et al., 2020), no anhydrous sulfate minerals with Zn-dominated sites in the structure were known and the occurrence of zinkosite $ZnSO_4$ is doubtful to date (Wildner and Giester, 1988). Glikinite is a new mineral named in honor of professor at the Department of Crystallography, Saint-Petersburg State University Arkady Glikin (1943-2012).

3.2 Occurrence and association

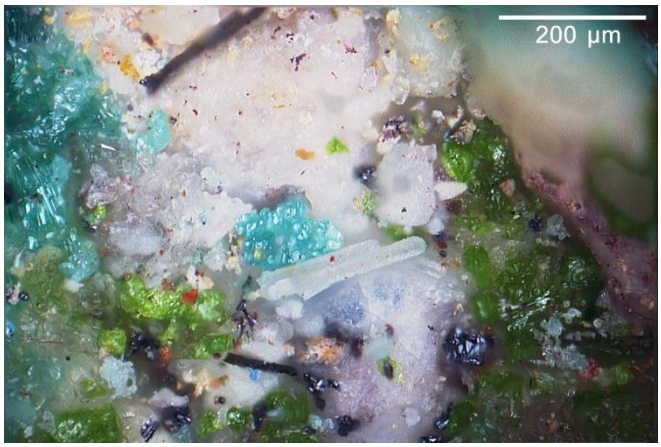

Figure 2. Glikinite (white with bluish tint prismatic crystals in the center) associating with lammerite-β (sky blue), langbeinite (white matrix), euchlorine (grass green) and tenorite (black).

Glikinite is a fumarolic mineral that is deposited directly from volcanic gas emissions as a sublimate. It was found in 2017 in the Arsenatnaya fumarole (Pekov *et al*., 2018), Second scoria cone, Northern Breakthrough (North Breach), Great Fissure eruption, Tolbachik volcano, Kamchatka, Russia. The Second Scoria Cone is located approximately 18 km SSW of the active shield volcano Ploskiy Tolbachik (Fedotov and Markhinin, 1983). Associated minerals are langbeinite, lammerite-β, bradaczekite, euchlorine, anhydrite, chalcocyanite and tenorite (**Figure 2**). The temperature of gases at the sampling location was approximately 250°C. All the recovered samples were packed and isolated when collected to avoid any contact with the external atmosphere.

Glikinite crystals are colorless and transparent. The streak is white. The lustre is vitreous. The mineral is non-fluorescent under UV light or an electron beam. Glikinite is brittle. No cleavage and parting were observed, the fracture is uneven. Hardness corresponds to 2 – 3 on the Mohs' scale. The density could not be measured due to the small sample size. The density calculated from the empirical formula is 3.98 g cm^{-3}.

Glikinite is optically biaxial (+), α = 1.737(2), β = 1.686(2), γ (calc.) = 1.671(2) (589 nm) and $2V_{calc}$=54°. Dispersion of optical axes is distinct, r>v. In plane-polarized light, the mineral is non-pleochroic, colourless or with a slight bluish hue.

The mineral was analysed by energy-dispersive and wavelength-dispersive spectrometry. The mineral is stable under the electron beam; no surface damage was observed after analysis. The empirical formula calculated on the basis of O = 9 *apfu* is $Zn_{2.07}Cu_{0.97}S_{1.98}O_9$ (**Table 2**). The simplified

formula is $(Zn,Cu)_3O(SO_4)_2$ or $Zn_3O(SO_4)_2$, which requires ZnO = 60.40 and SO_3 = 39.60, total 100.00 wt%.

Table 2. Analytical data (wt%) (n=12) for glikinite

Constituent	Mean	Range	Stand. Dev.	Probe Standard
ZnO	42.47	42.12-43.29	0.345	metal Zn
CuO	19.50	18.70-20.31	0.182	metal Cu
SO_3	39.96	38.63-41.28	0.121	Synthetic $CaSO_4$
Total	101.93			

3.3 X-ray crystallography

The powder data are presented in **Table S1**. Unit-cell parameters refined from the powder data are: a = 7.287(7) Å, b = 6.595 (8) Å, c = 7.841 (7) Å, β = 117.24 (9)º, V = 335.0(5) Å^3, Z = 2. A prismatic crystal of glikinite was crushed under the microscope in order to separate thin single crystal fragments. The crystal studied was twinned, and the twinning matrix [1 0 0, 0 -1 0, -1 0 -1] was employed during the crystal structure refinement. The crystallographic data and refinement parameters for glikinite shown in **Table 3**. The unit cell of glikinite is similar to that reported for the (apparently isomorphous) synthetic phase $Zn_3O(SO_4)_2$ by Bald and Grühn (1981) ($P2_1/m$, a = 7.937(2) Å, b = 6.690(2) Å, c = 7.851(2) Å, β = 124.39(1)º, V = 344.01 Å^3, R_1 = 0.085). There is a significant difference in both the a-dimension and the monoclinic angle which presumably relates to the significant Cu content in glikinite (**Table 2**). Atom coordinates, thermal displacement parameters and bond distance are given in **Table S2** and **Table S3** and **Table S4**.

3.4 Description of the crystal structure

The crystal structure of glikinite contains three symmetrically independent Zn sites with two types of different coordination environments (**Figure 3**). The Zn1 site is coordinated by six oxygen ligands thus forming ZnO_6 distorted octahedra. The Zn2 and Zn3 sites have a strongly distorted trigonal bipyramidal coordination environment consisting of five oxygen atoms each. There are two symmetrically independent S sites in the crystal structure of glikinite. The S^{6+} cations have typical but distorted tetrahedral coordination. Generally, coordination environments of atoms in glikinite are very similar to those in synthetic $Zn_3O(SO_4)_2$ (Bald and Grühn, 1981). The significant amount of copper

determined by microprobe in the structure of glikinite does not significantly influence the bond length and angle values in comparison with the structure of synthetic $Zn_3O(SO_4)_2$. Crystal structure of glikinite is an example of a quenched high-temperature structure. Equal distribution of Cu^{2+} over three symmetrically independent Zn sites in glikinite can be hypothesized. Thus, glikinite is a Zn, Cu analogue of synthetic $Zn_3O(SO_4)_2$ (**Table 4**) (Bald and Grühn, 1981).

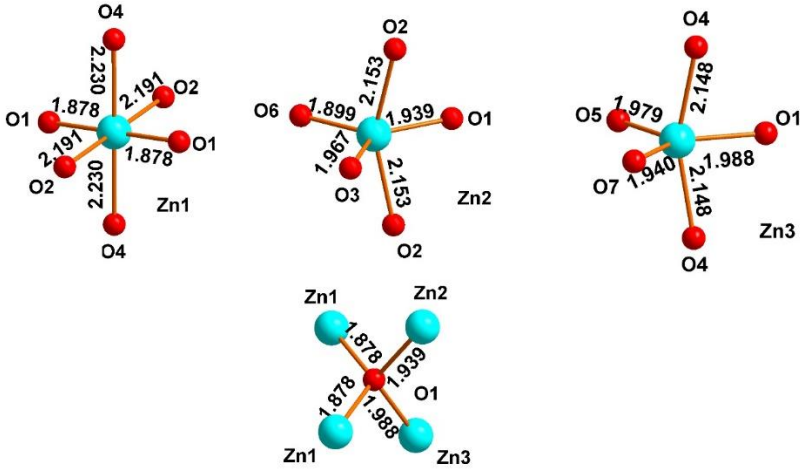

Figure 3. Coordination of zinc atoms in glikinite

The structure of glikinite contains seven O^{2-} anions. The O2-O7 atoms belong to the sulfate groups. The O1 atoms are tetrahedrally (**Figure 3**) coordinated by four Zn atoms forming short and strong O-Zn bonds. From the viewpoint of the bond-valence theory, these bonds are the strongest in the structure and thus it makes sense to consider the O^{2-} anions as coordination centers for oxo-centered OZn_4 tetrahedra (Krivovichev et al., 2013). OZn_4 tetrahedra share common corners thus forming $[Zn_3O]^{4+}$ chains (**Figure 4**). A similar topology of chains $[Cu_3O]^{4+}$ was described previously in the structures of vergasovaite $Cu_3O((Mo,S)O_4SO_4)$ (Berlepsch et al., 1999) and kamchatkite $KCu_3OCl(SO_4)_2$ (Siidra et al., 2017) (**Table 4**). Sulfate groups interconnect $[Zn_3O]^{4+}$ chains into 3*D* framework (**Figure 5**) in glikinite.

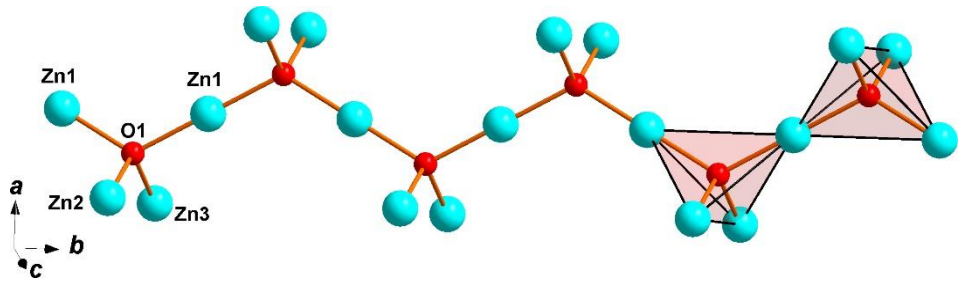

Figure 4. $[Zn_3O]^{4+}$ chain in the structure of glikinite.

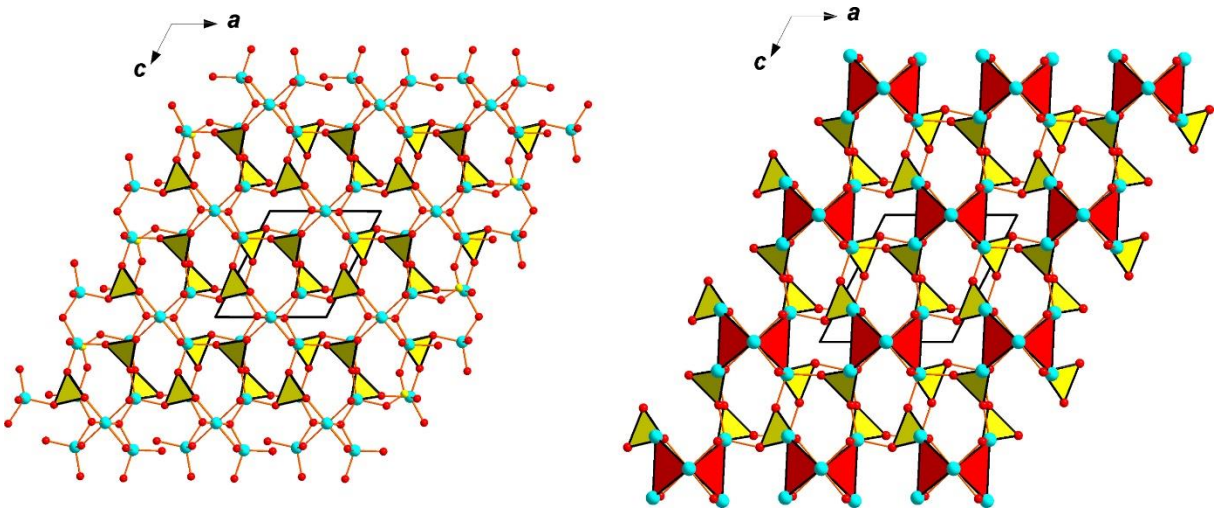

Figure 5. General projection of the crystal structure of glikinite along the *b* axis. OZn_4 polyhedra are added on the right (SO_4 = yellow, OZn_4 = red).

Table 3. Crystallographic data and refinement parameters for glikinite

Crystal data	
Formula	$Zn_3O(SO_4)_2$
Space group	$P2_1/m$
Unit cell dimensions *a*, *b*, *c* (Å);	7.298(18), 6.588(11), 7.840(12)
β (°)	117.15(3)
Unit-cell volume ($Å^3$)	335.4(11)
Z	2
Calculated density ($g \cdot cm^{-3}$)	4.00
Absorption coefficient (mm^{-1})	11.29
Crystal size (mm)	0.03×0.03×0.15
Data collection	
Temperature (K)	293

Radiation, wavelength (Å)	MoKα, 0.71073
θ range (°)	2.920 – 27.914
h, *k*, *l* ranges	−9→9, −6→5, −10→9
Total reflections collected	1135
Unique reflections (R_{int})	621 (0.041)
Unique reflections $F > 4\sigma(F)$	518
Structure refinement	
Refinement method	Full-matrix least-squares on F^2
Weighting coefficients *a*, *b*	0.08020, 0.0000
Twin fractions	39:61
Data/restraints/parameters	621/18/80
R_1 [$F > 4\sigma(F)$], wR_2 [$F > 4\sigma(F)$]	0.046, 0.115
R_1 all, wR_2 all	0.058, 0.121
Gof on F^2	1.02
Largest diff. peak and hole (*e* Å^{-3})	1.130, -1.450

Table 4. Crystal chemical data of glikinite, related synthetic compound and vergasovaite.

Mineral/compound	Glikinite	-	Vergasovaite
Formula	$Zn_3O(SO_4)_2$	$Zn_3O(SO_4)_2$	$Cu_3O((Mo,S)O_4SO_4)$
Crystal system	Monoclinic	Monoclinic	Orthorhombic
Space group	*P*2$_1$/*m*	*P*2$_1$/*m*	*Pnma*
Unit cell data			
a, Å	7.298(17)	7.937(2)	7.421(2)
b, Å	6.588(11)	6.690(2)	6.754(3)
c, Å	7.840(12)	7.851(2)	13.624(5)
β, º	117.14(3)	124.39(1)	
V, Å^3	335.4(11)	344.01(10)	682.85(11)
Z	2	2	4
R_1	0.045	0.085	0.067
Reference	this work	Bald and Grühn, 1981	Berlepsch et al., 1999

3.5 Conclusion

A new mineral glikinite, was found in high-temperature exhalative mineral assemblages in the Arsenatnaya fumarole, Second scoria cone of the Great Tolbachik Fissure Eruption (1975–1976), Tolbachik volcano, Kamchatka Peninsula, Russia. The crystal structure of glikinite is based on OZn_4 tetrahedra sharing common corners, thus forming $[Zn_3O]^{4+}$ chains. Sulfate groups interconnect $[Zn_3O]^{4+}$ chains into a 3*D* framework. Despite the fact that zinc is an impurity component of many copper minerals, no sulfate minerals where zinc would dominate have been known so far, except of zinkosite $ZnSO_4$.

The discovery of new minerals helps us better understand the nature of crystal formation (mineral formation) and find ways to use these minerals as materials. In the following, we will consider an example of obtaining a synthetic analogue of saranchinaite, another representative of the Tolbachik volcano mineral.

4. Synthesis of an analogue of saranchinaite $Na_2Cu(SO_4)_2$, crystal structure and physicochemical properties

4.1 Introduction

Saranchinaite $Na_2Cu(SO_4)_2$ is also mineral of Tolbachik volcano (Siidra et al., 2018). This mineral is formed as a product of fumarolic activity located at the Naboko scoria cone. The temperature of the gas at the sampling location was about 600 ºC. At the type locality saranchinaite is associated with euchlorine, $KNaCu_3(SO_4)_3O$ (Scordari & Stasi, 1990), itelmenite $Na_2CuMg_2(SO_4)_4$, (Nazarchuk et al., 2018), hermannjahnite $CuZn(SO_4)_2$ (Siidra et al., 2018), chalcocyanite CuSO4, thénardite Na_2SO_4, aphthitalite $K_3Na(SO_4)_2$, and hematite Fe_2O_3. Saranchinaite is anhydrous form of the mineral kröhnkite $Na_2Cu(SO_4)_2(H_2O)_2$ (Siidra et al., 2018). Kröhnkite was first described 130 years ago (Domeyko 1879) from samples found in the famous Chuquicamata Mine in Chile.

In this chapter we will go deeper not only on crystal structures investigation but also into magnetic properties and electrochemistry. For the second issue, we demonstrated the electrochemical behaviour of $Na_2Cu(SO_4)_2$ either vs Na or vs Li to understand of principle of battery working (Kovrugin et al., 2019).

4.2 General statement about batteries

Sulphate materials (minerals) are largely used as a cathode or anode materials. During the last decade, many articles dedicated to the electrochemistry of sulfates were published. If searching on the SCOPUS database using the key words like «sulphate» and «batteries» 122 articles were found in 2017, 154 in 2018, 179 in 2019, 252 in 2020 and already 110 in 2021 implying a great increase. The mineral-inspired eldfellite-type $NaFe(SO_4)_2$ phase has been recently considered as a low-cost electrode cathode in a rechargeable Na-ion battery demonstrating about 80 mAh/g of reversible capacity with a discharge voltage of 3.0 V vs Na^+/Na for a relatively long life (Singh et al., 2015; Ri et al., 2018).

Experimentally, the electrochemical behavior was examined using an electrochemical cell. It is a device that can (1) generate electrical energy from the chemical reactions occurring in it, or (2) use the electrical energy supplied to it to facilitate chemical reactions in it.

There are two types of cells: electrolytic cells and galvanic cells (Gasteiger et al., 2013). In the case of electrolytic cells, electrical energy has to be supplied to initiate the reaction, electric energy is converted into chemical energy (charge) (**Figure 6a**), the redox reaction is not spontaneous. In the case of galvanic cells. It converts chemical energy into electrical energy (discharge) (**Figure 6b**). The redox reaction is spontaneous and is responsible for the production of electrical energy. An electrochemical cell consists of one positive electrode and a negative one, having different chemical potentials and

separated by an ionically conductive and electronically insulating electrolyte. In each case, the electrolyte is selected individually, depending on the chemical composition of the test material. The electrode can be a liquid imbibed into a porous matrix, and an ionomeric polymer or solid. An incorrectly selected electrolyte can lead to negative results during electrochemical tests. When the electrodes are connected by means of an external circuit, electrochemical reactions take place concomitantly at both sides, with electrons running spontaneously through external circuit and ion transport in the electrolyte to ensure electroneutrality. During the discharge cycle, an oxidation or anodic reaction occurs at the negative electrode, and a reduction or cathodic reaction occurs at the positive electrode. For rechargeable (secondary) batteries, this process can be reversed during the charge process (Palacín, 2009). The term "battery" refers to a stack of cells or a single cell. In this electrochemical reactor, the nature of different redox reactions in the electrolyte provides different electrochemical performance.

The electrochemical properties of $Na_2Cu(SO_4)$ were obtained in collaboration with the Laboratoire de Réactivité et de Chimie des Solides (LRCS) Amiens, France during the internship under the Travel Research Grant № 3.41.315.2017 of Saint-Petersburg State University. The electrochemical properties of $Na_2Cu(SO_4)$ were probed in lithium and sodium half-cells, when each half-cell consists of an electrode and an electrolyte. It was found to be electrochemically active, although a very limited amount of lithium (or sodium) could be effectively inserted and extracted in these compounds. This is mostly due to the fact that their structures cannot accommodate extra alkali cations and to the difficulty of oxidizing Cu^{2+} into Cu^{3+}. This therefore reminds that choosing open 3D frameworks favoring the ionic diffusion is a good but not sufficient criterion to make good alkali hosts.

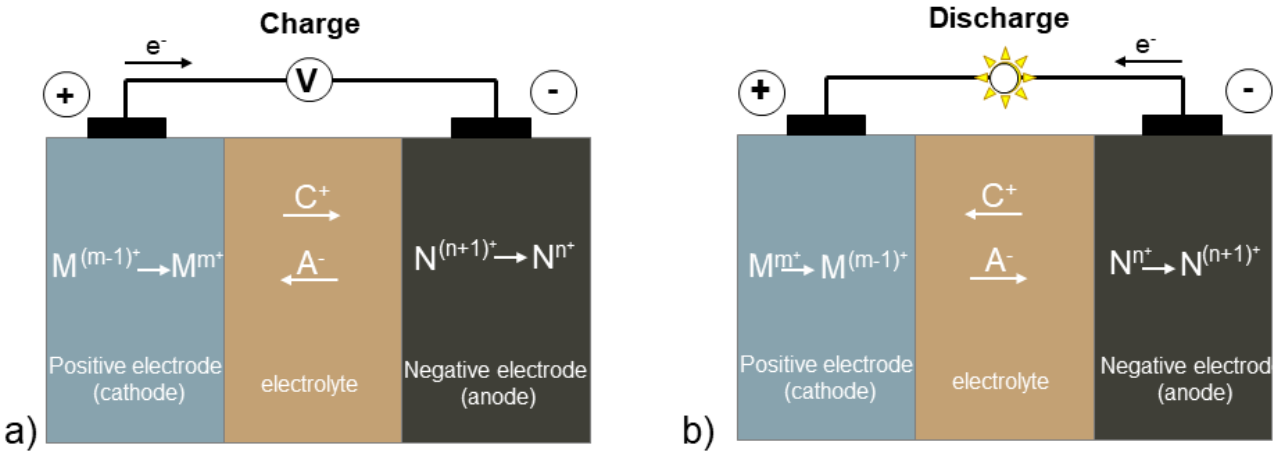

Figure 6. The schematic operation principle of an electrochemical cell on charge (a) and on discharge (b), respectively.

4.3 Synthesis of $Na_2Cu(SO_4)_2$

As noted earlier, to study the physical properties of minerals, it is necessary to obtain a pure synthetic analogue. Because of it, anhydrous $Na_2Cu(SO_4)_2$ were obtained from hydrated phase of $Na_2Cu(SO_4)_2(H_2O)_2$. By analogy with a formation of saranchinaite as a result of high-temperature exhalative processes occurring in the fumarole fields of Tolbachik volcano (Siidra et al. 2018), single crystals of $Na_2Cu(SO_4)_2$ were grown by slow cooling of melt containing equimolar quantities of $CuSO_4$ and Na_2SO_4 in an evacuated ampoule from 950 °C. The resulted solid products in the evacuated ampoule are shown in **Figure 7.**

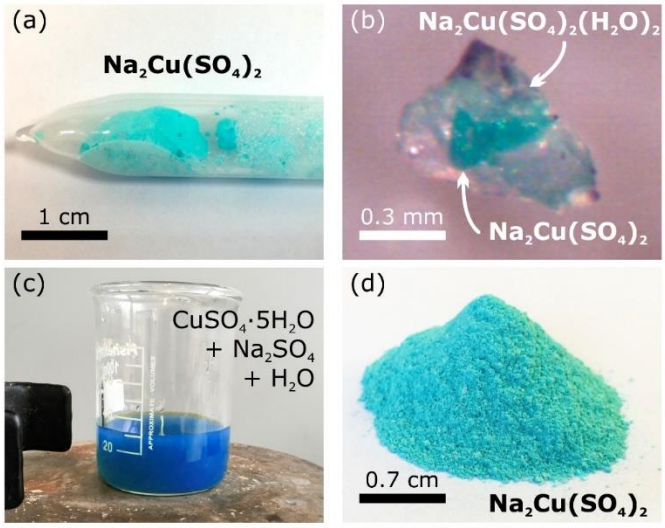

Figure 7. Evacuated ampoule with $Na_2Cu(SO_4)_2$ (a); single crystal of $Na_2Cu(SO_4)_2$ in kröhnkite-based matrix (b); homogenous aqueous precursor for $Na_2Cu(SO_4)_2$ (c); pure powder sample of $Na_2Cu(SO_4)_2$(d).

The as-prepared $Na_2Cu(SO_4)_2$ is sensitive to air moisture and starts to transform into the hydrated kröhnkite-type $Na_2Cu(SO_4)_2(H_2O)_2$ composition after 12 hours of exposition in air, which is accompanied by a color change to pale blue material. Single crystals of $Na_2Cu(SO_4)_2$ inside a crystalline matrix of $Na_2Cu(SO_4)_2(H_2O)_2$ are shown in (**Figure 7b**). Note, that the observed hydration process is reversible, and the solids may be easily dehydrated by heating of the crystalline sample up to 300°C for 2 hours.

Powder samples of $Na_2Cu(SO_4)_2$ were prepared by a coprecipitation-type synthesis process. The precursors used as starting materials while distilled water was used as solvent. Resulted powder of a light blue color contains both saranchiniate-type $Na_2Cu(SO_4)_2$ and kröhnkite-type $Na_2Cu(SO_4)_2(H_2O)_2$ phases identified by powder X-ray diffraction analysis. Finally, the obtained mixture was heated up to 300 °C for two hours to produce a polycrystalline sample of anhydrous $Na_2Cu(SO_4)_2$ (**Figure 7d**). A high-purity (99%) of the sample was confirmed by X-ray powder diffraction analysis. Note however several small peaks of unidentified impurity as illustrated in **Figure 8**. The equimolar amounts of starting precursors resulted in a preparation of $Na_2Cu(SO_4)_2$ with a small amount of Na_2SO_4 as an admixture. A probable hydration of starting precursors may serve as an explanation for the observed impurity of sodium sulfate.

4.4 Single crystal X-ray diffraction

Initial atomic coordinates for the crystal structure of synthetic $Na_2Cu(SO_4)_2$ were taken from the structure of the previously reported mineral phase (Siidra *et al.,* 2018). The crystal structure was further refined in the non-centrosymmetric $P2_1$ space group to $R_1 = 0.020$. Main crystallographic information for the synthetic and mineral phases is summarized in **Table 5**. Selected interatomic distances and results of bond valence calculations for Cu^{2+} are given in **Table S10**. Fractional atomic coordinates, atomic displacement parameters, and a comparison of Na–O bonds in the structures of synthetic and mineral phases are listed in **Table S8**, **Table S9**.

Table 5. Single crystal and structure refinement data for synthetic $Na_2Cu(SO_4)_2$ and its 'natural' analogue saranchinaite

Crystal data	$Na_2Cu(SO_4)_2$	$(Na,K)_2Cu(SO_4)_2$
sp. gr.	$P2_1$	$P2_1$
a [Å]	8.9711(3)	9.0109(5)
b [Å]	15.5482(5)	15.5355(8)
c [Å]	10.1421(3)	10.1507(5)
β [°]	107.155(1)	107.079(2)
V [Å^3]	1351.73(7)	1367.06(12)
Z	2	2
ρ_{calc} [g·cm^{-3}]	2.964	2.970
μ [mm^{-1}]	3.987	3.982
Data collection		
F(000)	1176	1181
θ range [°]	2.1 – 31.6	2.1 – 22.7
hkl limits	–13 → 13 –15 → 22 –14 → 14	–9 → 9 –16 → 16 –11 → 11
total refln.	16018	10024
unique refln. (R_{int})	6585 (0.0238)	3642 (0.0394)
unique refln. $F > 4\sigma F$	6263	3236
Refinement		

R_1 [$F > 4\sigma F$], wR_2 [$F > 4\sigma F$]	0.0204, 0.0436	0.0295, 0.0580
R_1 all, wR_2 all	0.0224, 0.0443	0.0381, 0.0610
GoF	1.009	0.965
$\Delta\rho_{max}$, $\Delta\rho_{min}$ [e·Å^{-3}]	0.549, –0.437	0.459, –0.465

4.5 Powder X-ray diffraction

The refined unit-cell parameters in the space group $P2_1$ are: a = 8.9655(1) Å, b = 15.5366(1) Å, c = 10.1384(1) Å, β = 107.07(1)°, V = 1350(1) Å^3. The final observed, calculated, and difference powder XRD patterns resulting from the profile matching procedure are plotted in **Figure** 8.

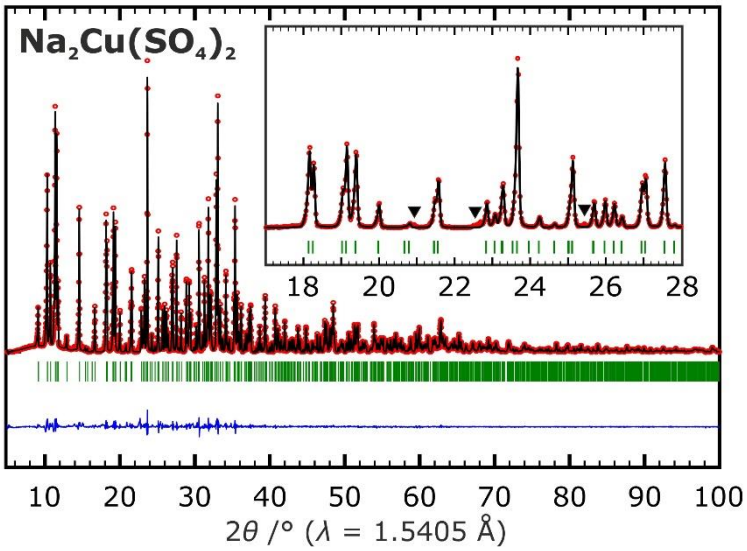

Figure 8. Results of the profile matching analysis of $Na_2Cu(SO_4)_2$ from the powder XRD data. Impurities are shown by black triangles.

4.6 Infrared spectroscopy (FTIR)

Absorption bands in the IR spectrum of $Na_2Cu(SO_4)_2$ and their assignments are (cm^{-1}): 1248–955 [ν_4 S–O stretching vibrations], 684–605 [ν_1 and ν_3 S–O bending vibrations], 520 [ν Cu–O stretching vibrations] (**Figure 9a**). The split of all bands in the range 900–1250 cm^{-1} is due to the presence of eight symmetrically independent $(SO_4)^{2-}$ anions with distorted tetrahedral geometry. The band assignments were done according to (Berger 1976; Hezel *et al.*,1966; Takahashi *et al.*, 1975; Ross *et al.*, 1962; Decius *et al.*, 1963; Bakhtiari *et al.*, 2011; Usoltseva *et al.*, 2011). Note that after several hours exposure on open air, $Na_2Cu(SO_4)_2$ starts to hydrate with appearance of intensive band at 860 cm^{-1} (Cu···O–H bending vibrations).

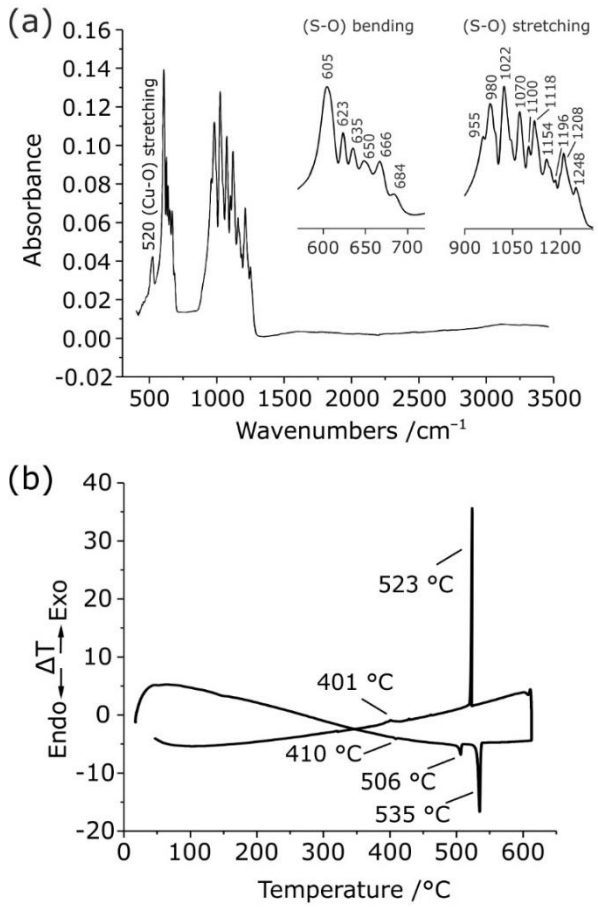

Figure 9. Infrared (FTIR) spectrum (a) and DTA curves (b) for $Na_2Cu(SO_4)_2$.

4.7 Thermal analysis (DTA)

Thermal evolution of synthetic $Na_2Cu(SO_4)_2$ occurs in three steps upon heating (**Figure 9b**). The observed thermal phenomena are consistent with the temperature values of the phase transformations for the natural phase (mineral) determined recently by our high-temperature powder XRD (HTPXRD) study (Siidra *et al.,* 2018). Thus, the powder XRD patterns collected for the mineral $(Na,K)_2Cu(SO_4)_2$ phase were used for further comparative thermal analysis. The first small endothermic peak centered at 410 °C is related to the formation of an unidentified phase, which disappears at around 500 °C. The second endothermic peak observed at 506 °C indicates the total disappearing of synthetic $Na_2Cu(SO_4)_2$ assorted with the formation of $Na_2Cu_3O(SO_4)_3$ (synthetic analogue of puninite (Siidra *et al.,* 2017), which remains stable until ~535 °C. The third endothermic intense peak centered at 535 °C can be associated with the final decomposition of polyanionic $Na_2Cu_3O(SO_4)_3$ into Na_2SO_4, CuO, and unidentified phase(s). Exothermic peaks at 523 °C and 401 °C found on the reverse DTA curve are related to recrystallization processes.

4.8 Optical properties

The green color of $Na_2Cu(SO_4)_2$ corresponds well to optical reflection spectrum with an intense maximum in the region of 500–550 NT (**Figure 10**). The optical bandgap E_g can be estimated to *ca.* 580 nm. The most powerful peak in the spectrum is precisely the second harmonic radiation at $\lambda_{2\omega}$ = 0.532 nm, which may be exited in a non-centrosymmetric substance under neodymium laser radiation with λ_{ω} = 1.064 nm. Such an adverse match complicates to some degree a neodymium laser application for determination of the nonlinear optical activity of $Na_2Cu(SO_4)_2$ in usual transmitted light scheme (Kurtz *et al.,* 1968).

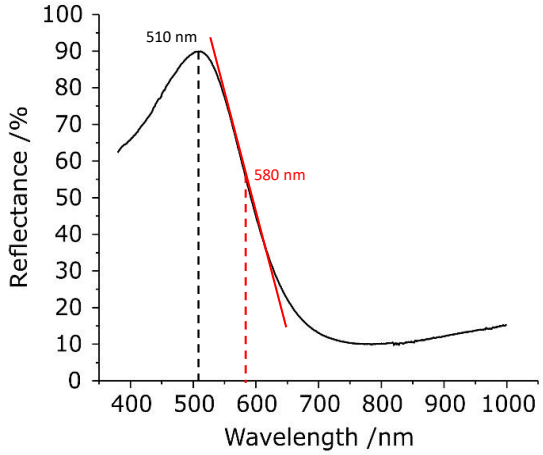

Figure 10. Light reflectivity from $Na_2Cu(SO_4)_2$ powder measured with PerkinElmer Lambda 1050 spectrophotometer at room temperature.

An intense impulse YAG:Nd-laser was used as a source of radiation at wavelength λ_{ω} = 1.064 nm while second harmonics (SH) was registered in the reflection mode. Generated in the powder sample green light of SH ($\lambda_{2\omega}$ = 0.532 nm) was selected in the backward using colored glass filters. Then SH signal was registered with a photomultiplier and its intensity $I_{2\omega}$ measured by a lock-in integrator. Measured signal from the sample under investigation was calibrated in relation to quartz standard. Thin $Na_2Cu(SO_4)_2$ powder was nearly of the same dispersion as α-quartz powder used as a reference. The value $Q = I_{2\omega} / I_{2\omega}(SiO_2) = 0.2$ was found to present the SHG activity of $Na_2Cu(SO_4)_2$ on both heating and cooling in between RT and 400 °C. In order to correct this value for the SH emission in the colored substance it is necessary to multiply it by a factor of 10 corresponding to the share 1/10 of light at $\lambda_{2\omega}$ = 0.532 nm penetrating through $Na_2Cu(SO_4)_2$ particles. Because nonlinear coefficients of two materials are related as square roots of Q, we estimate averaged nonlinear coefficient for $Na_2Cu(SO_4)_2$ to be $<d> = 1.4\ d_{14}(SiO_2) \sim 0.5$ pm/V. This is very close to nonlinearities of earlier investigated sulfates such as $LiKSO_4$ and $Li_2SO_4 \cdot H_2O$ with nonlinear coefficients d_{33} = 0.71 pm/V and d_{22} = 0.4 pm/V, respectively (Weber 2003).

4.9 Description of the crystal structure of $Na_2Cu(SO_4)_2$

$Na_2Cu(SO_4)_2$ crystallizes in the non-centrosymmetric monoclinic space group $P2_1$. The structural data for the synthetic phase are in good agreement with the data reported for natural saranchinaite containing a small amount of potassium (Siidra *et al.,* 2018). Nevertheless, one interesting point is worth a special discussion. Unusual structural feature of its crystal structure is an atypical coordination environment of O around Cu^{2+} sites. In the structure, there are four crystallographically independent Cu positions. Each Cu site forms four short Cu–O_{eq} bonds in its equatorial plane that define regular CuO_4 squares (average <Cu–O_{eq}> = 1.978, 1.952, 1.945, and 1.970 Å for Cu1, Cu2, Cu3, and Cu4, respectively). Each square is complemented by one longer apical Cu–O_{ap} bond, thus, forming rather regular CuO_5 tetragonal pyramids (<Cu–O_{ap}> = 2.287, 2.264, 2.352, and 2.260 Å for Cu1, Cu2, Cu3, and Cu4, respectively) typical for copper oxide compounds.

All Cu^{2+} cations have also additional weaker and longer (2.8–3.1 Å) contacts with two O_{add} each, which should be taken into consideration. Bond valence calculations for Cu–O_{add} bonds dictate that they should be taken into consideration and included into the coordination sphere of Cu^{2+} cations. A Cu–O distance of ≈3.03 Å provides 0.03 valence units and contributes about 1.5% of the overall bond valence sum (BVS). Therefore, Cu–O distances with bond valence ≥ 0.03 vu were considered.

Accordingly, the coordination spheres of the Cu1 and Cu4 sites can be described as distorted octahedra with one additional sixth O ligand each (Cu–O_{sixth} = 2.839 Å [0.04 vu] and 2.942 Å [0.03 vu] for Cu1 and Cu4, respectively), which is common for minerals and synthetic compounds (Burns and Hawthorne 1995). The most remarkable observation concerns the coordination of the Cu2 and Cu3 sites adopting scarce heptahedral CuO_7 coordination (**Figure 11**) with two additional oxygen atoms O located at distances of 2.882 Å [0.04 vu], 2.954 Å [0.03 vu] and 2.938 Å [0.03 vu], 3.012 Å [0.03 vu] from Cu2- and Cu3-centers, respectively. Each pair of these additional O anions is located geometrically strictly below two O corners of one the diagonals of square bases of the CuO_5 pyramids with $O_{eq}\cdots O_{add}$ distances of 2.39–2.42 Å for the Cu1–Cu4 sites. The O_{add}–Cu–O_{add} angles are in the range between 64 and 74°. This unusual relatively regular 7-fold coordination of Cu^{2+} is very rare for inorganic compounds at ambient conditions (Siidra et al., 2018; Yoshiasa et al., 2000; Nadeem et al., 2010). Coordination of Cu^{2+} sites in the crystal structure of $Na_2Cu(SO_4)_2$ is shown in **Figure 11**.

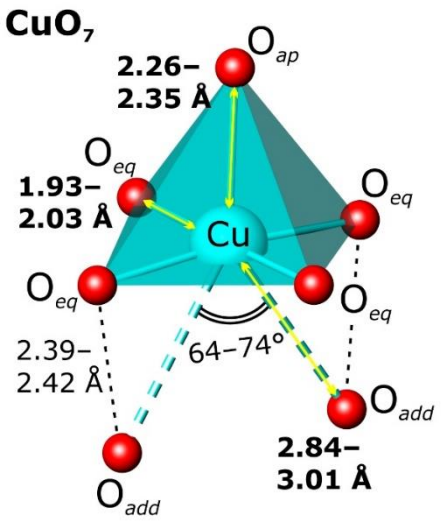

Figure 11. Heptahedral coordination of Cu^{2+} in the structure of $Na_2Cu(SO_4)_2$.

The atomic environment of eight Na^+ cations in the structure of synthetic $Na_2Cu(SO_4)_2$ does not change significantly from the ones reported for saranchinaite **Tables S7-S10**. Note only differences in the coordination of the Na5 site in both structures (**Figure 12**) caused by the partial substitution of Na^+ by K^+ in the structure of the mineral phase.

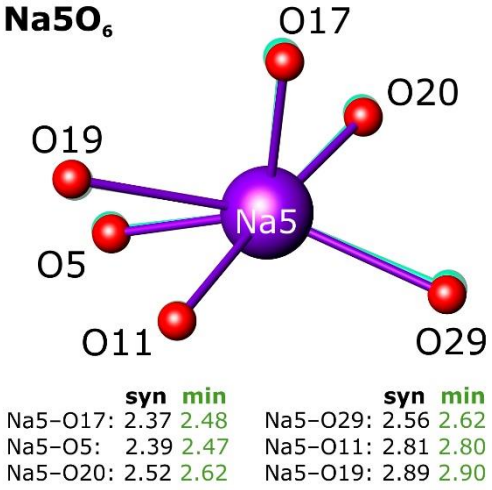

Figure 12. Geometrical environment of the Na5 site in the structure of synthetic $Na_2Cu(SO_4)_2$. Projections of the O positions in the structure of saranchinaite are shown by green color for comparison. Distances are given in Å.

In the crystal structure of $Na_2Cu(SO_4)_2$, all copper polyhedra are connected to each other *via* medium/long Cu--O_{add}----Cu bridges and polymerized into polar chains running along the *c*-direction as shown in **Figure 13**. Thus, the non-centrosymmetric symmetry of the structure is justified by the "up" only orientation of CuO_5 pyramids along [001]. Note that Cu2 and Cu3 metal centers are located

relatively close to each other (Cu2···Cu3 = 3.36 Å; *cf.* Cu3···Cu4 = 4.90 Å) and share a common O corner of their square O bases forming a dimer. Such close arrangement of the two neighboring Cu2 and Cu3 polyhedra may be responsible for overall slight shortening of the Cu–O contacts and, thus, favoring an unusual heptahedral $Cu2O_7$ and $Cu3O_7$ coordination polyhedra. Indeed, the average Cu–O distances to the seven closest O ligands for Cu2 (2.273 Å) and Cu3 (2.297 Å) are slightly smaller than those for Cu1 (2.300 Å) and Cu4 (2.312 Å). The terminal oxygen atoms of every copper polyhedron are bridged by sulfate SO_4 anions to form a complex 3D framework with large system of pores and cavities filled by Na^+ cations (**Figure 14**).

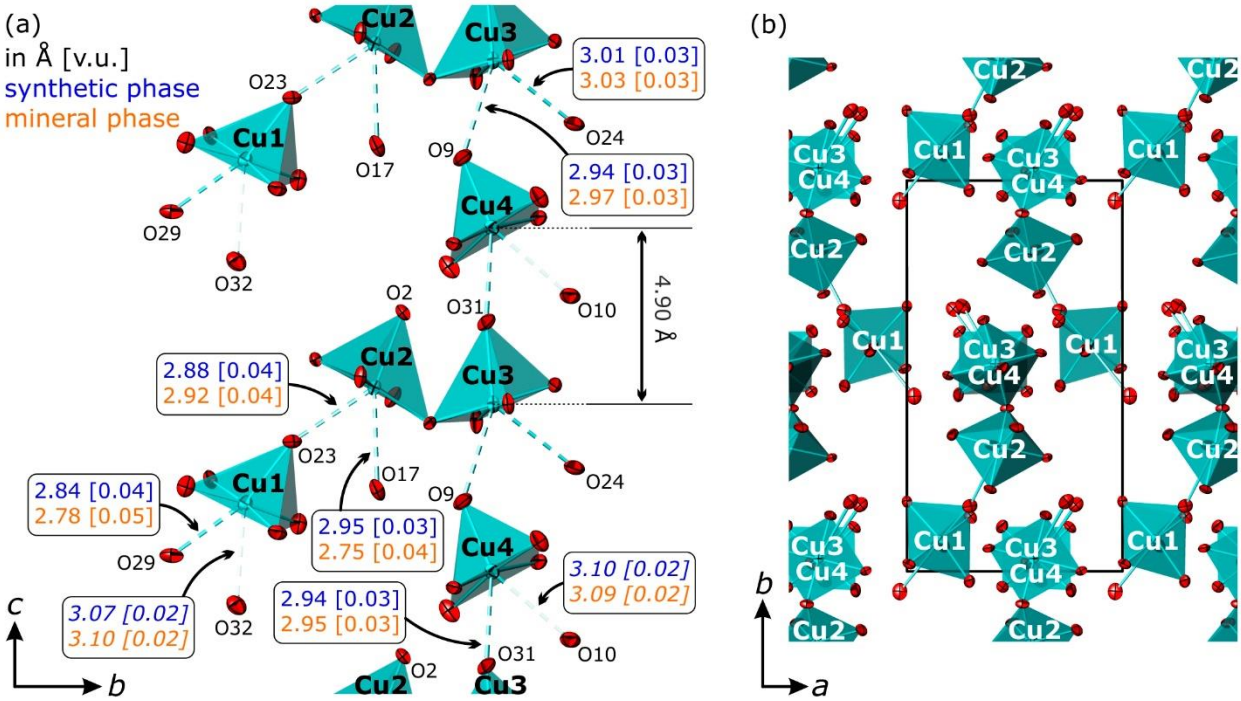

Figure 13. Interconnection of CuO_5 pyramids and comparison of bond lengths and valence values for long Cu–O distances in the structures of synthetic (blue) and mineral (orange) phases. Cu–O contacts < 0.03 vu are italicized. Displacement ellipsoids are drawn at 80% probability level.

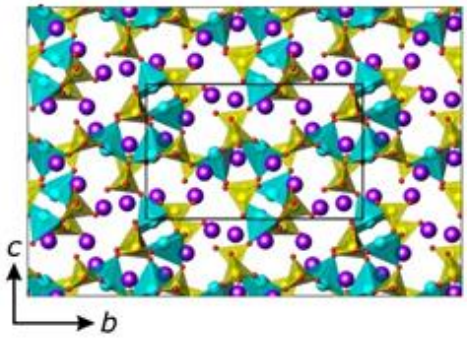

Figure 14. Projections of the crystal structures of $Na_2Cu(SO_4)_2$ along *a* axis, where Na – purple color, CuO_5 pyramids – blue and SO_4 anions - yellow.

4.10 Electrochemistry

The $Cu^{2+/}Cu^{3+}$ redox potential has been predicted to provide a high operating voltage in rechargeable battery systems (Sun et al., 2015). However, this phenomenon still lacks further studies and overall understanding. For example, a recent report revealed a very limited electrochemical performance for $K_2Cu_2(SO_4)_3$ and $K_2Cu_3O(SO_4)_3$ (Lander, Batuk, et al., 2017). Nevertheless, it has been also demonstrated that $Li_2Cu_2O(SO_4)_2$ is able to offer a reversible electrochemical activity at 4.7 V vs Li^+/Li corresponding to the $Cu^{2+/3+}$ redox transition associated with the reversible change of 0.3 Li (Sun et al., 2015). Hence, as a further attempt to explore the oxidation of Cu^{2+} to Cu^{3+} in course of an electrochemical reaction, several tests were performed using $Na_2Cu(SO_4)_2$ as a cathode material providing a theoretical capacity of ~89 mAh/g (for one e^- transfer per Cu cation).

The electrochemical behavior of $Na_2Cu(SO_4)_2$ either *vs* Na or *vs* Li was examined using Swagelok®-type cells assembled in an argon-filled glovebox and cycled at room temperature. Unfortunately, difficulties for Na^+ extraction have been encountered during the electrochemical cycling in Na- and Li-based types of the cells, and the removal of significant amount of Na^+ from the structure $Na_2Cu(SO_4)_2$ failed. As seen from **Figure 15a**, the irreversible extraction is limited to a value of only 0.04 Na^+ per formula unit at ~4.0 V *vs* Li^+/Li. The cycling of the $Na_2Cu(SO_4)_2$-based cathode *vs* Na reveals an occurring of a probable redox process at higher voltage of around 4.7 *vs* Na^+/Na (**Figure 15b**), which is beyond the voltage stability window of the electrolytes available up to now. Thus, $Na_2Cu(SO_4)_2$ is not suitable as a cathode material.

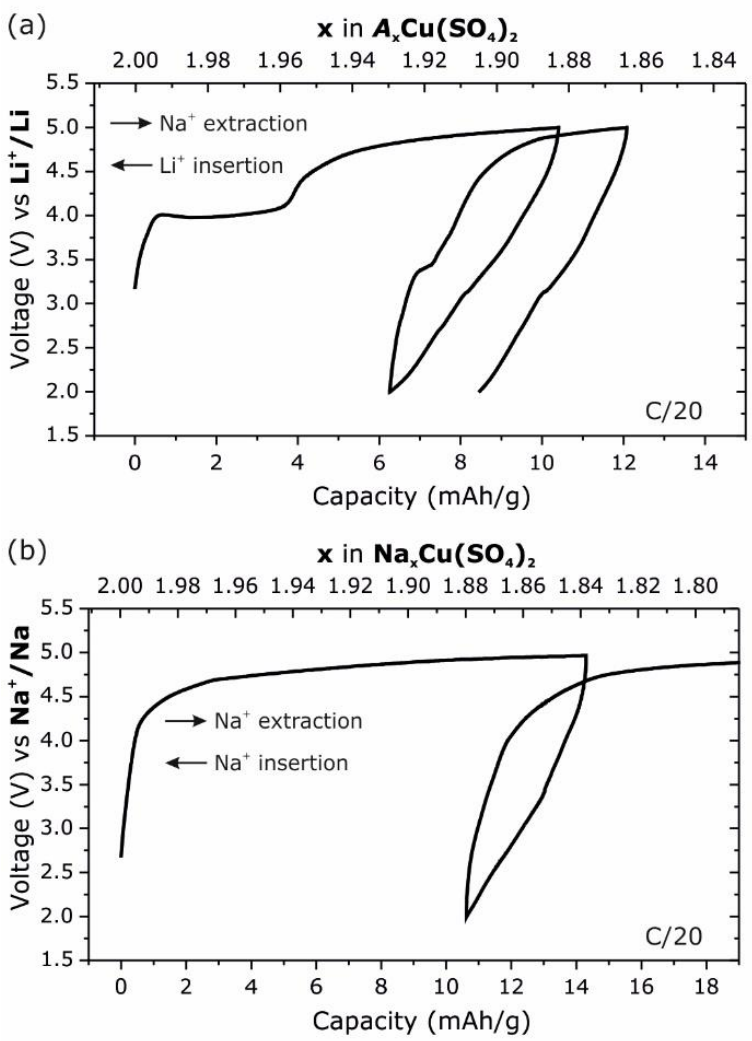

Figure 15. Electrochemical curves for $Na_2Cu(SO_4)_2$ as a cathode. *A* in $A_2Cu_2(SO_4)_2$ (on fig. *a*) corresponds to Na^+ upon charging and to Li^+ upon discharging.

A prerequisite for Na-based materials to be used as electrodes in Na-ion batteries is the existence of Na-diffusion paths within the structure. To get more information on how Na ions can travel inside the framework, it was generated Bond Valence Energy Landscapes (BVEL) using the BondStr program (FullProf Suite (Rodríguez-Carvajal, 1993)). The bond valence energy landscape (BVEL) also demonstrates that there is no interconnected pathways for sodium migration in the structure of $Na_2Cu(SO_4)_2$ (**Figure 16**) considering a percolation energy of 1.6 eV reported for the movement of Na^+ in polyanionic compounds (Boivin et al., 2017).

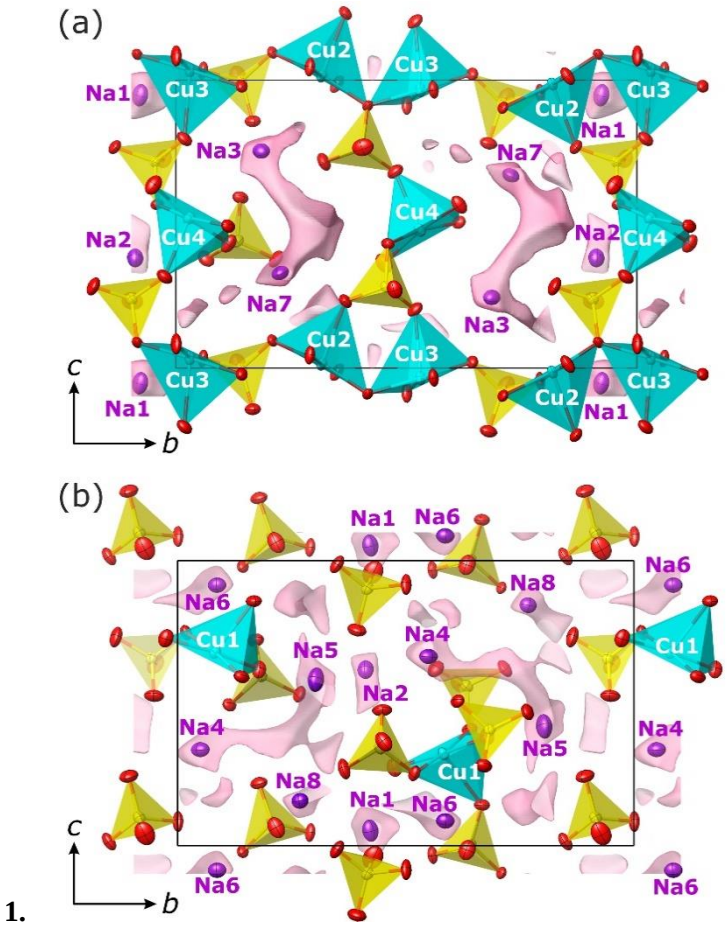

1.

Figure 16. Two cross-sections at ½ translation along the *a*-axis demonstrating sodium diffusion pathways shown in pink inside the structure of $Na_2Cu(SO_4)_2$ defined from BVEL with a percolation energy of 1.6 eV. Displacement ellipsoids are drawn at 80% probability level.

The synthetic saranchinaite phase is of interest not only in terms of electrochemistry, but also in terms of magnetism. The magnetic properties will be described below.

4.11 Magnetism of $Na_2Cu(SO_4)$

The magnetic properties of $Na_2Cu(SO_4)_2$ reflect well its crystal structure in that sense that according to the orientation of the $d_{x^2-y^2}$ magnetic orbitals (Cu^{2+}, d^9, S=1/2) roughly assigned to the CuO_4 square planes, only no magnetic overlap is achieved apart in the dimers formed by Cu2 and Cu3. Here, the Cu2–O3–Cu3 angle is 118.3°, which suggests significant super-exchange contribution. Accordingly, we considered half of copper atoms as mainly paramagnetic and the other half as strongly engaged in antiferromagnetic dimers interactions. The Curie-Weiss fit shown in **Figure 17a** gives $\mu_{eff} = 1.85\mu_B$/Cu and $\theta_{CW} = -17.2$ K, which validate predominant antiferromagnetic exchanges. The accident observed below *ca.* 50 K is mainly occurred due to the intra-dimer interactions, as detailed below. It was fitted using χT(T) plot (**Figure 17b**) through the susceptibility equation:

$$\chi_{Cu}=(\rho)\frac{Ng^2\beta^2}{kT(3+e^{-J/kT})}+(1-\rho)\frac{Ng^2\beta^2}{4k(T-\theta)}+\chi_{dia}, \quad (7)$$

where the first term represents the intra-dimer susceptibility of the Cu fraction ρ following the Bleaney-Bowers equation (Bleaney & Bowers, 1952), while the second term is the complementary Cu^{2+} paramagnetism with interaction quantified by θ, N, g, β, k and χ_{dia} having their usual meanings.

The fit was first constrained to ρ = 50 % but then greatly improved relaxing $g = 2.237(3)$, $J/k = 138.7(7)$ K (96.4 cm^{-1}), $\theta = -0.95(1)$ K, $\chi_{dia} = -21.10^{-6}$ emu/mol and ρ = 45.8(2) %. The g value is in good agreement with the effective moment greater than the "spin-only" value ($\mu_{eff} = 1.74\mu_B$), while θ and J/k confirm strong AFM dimer in a nearly paramagnetic matrix. The ratio ρ suggests few percent of extra paramagnetic impurities intrinsic and/or extrinsic, not revealed by XRD.

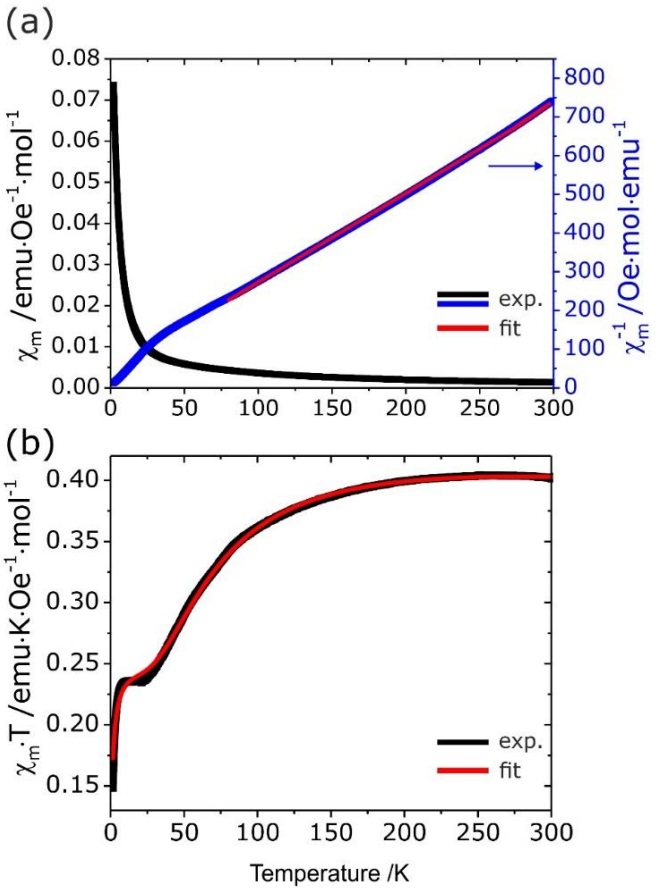

Figure 17. Thermal evolution of the magnetic susceptibility, invert magnetic susceptibility (a) and temperature dependence of χT (b) for $Na_2Cu(SO_4)_2$.

4.12 Conclusion

The novel anhydrous sulfate $Na_2Cu(SO_4)_2$ has been synthesized by two different methods for the first time and structurally characterized. A unusual structural feature of the new synthetic $Na_2Cu(SO_4)_2$ phase is the presence of heptahedral CuO_7 polyhedra with two additional long and weak Cu−O distances,

which are interconnected through common O corners in polar chains. Electrochemical, magnetic, thermal, and optical behaviors of $Na_2Cu(SO_4)_2$ have been also determined. The $Na_2Cu(SO_4)_2$ demonstrates a very limited electrochemical activity and highly stable Na sublattice (that is, low mobility of Na ions) in its crystal structure. The magnetic behavior of $Na_2Cu(SO_4)_2$ reflects its crystal structure with half of the copper cations as mainly paramagnetic and the other half as strongly engaged in antiferromagnetic dimer interactions.

We believe that the preparation of synthetic analogues of known minerals is able to serve fundamental science well. It can help to solve complex crystal structures or to make a model system for an investigation of various physical properties in the laboratory, when it is difficult to obtain samples with a good crystallinity and sufficient amount in nature (e.g., zeolites (Cundy & Cox, 2005)). Also the investigation of synthesis route could help to better understand the crystallization process of the minerals. In the next part of this work we will consider a detailed example of crystal formation of synthetic phases of the minerals itelmenite $Na_2CuMg_2(SO_4)_4$ (Nazarchuk et al., 2018) and glikinite $Zn_3O(SO_4)_2$ (Nazarchuk et al., 2020).

5. Synthesis, crystal structure and properties of Zn and Mg analogs of itelmenite and synthetic analog of glikinite

5.1 Intoduction

The mineral itelmenite, ideally $Na_2CuMg_2(SO_4)_4$, containing isomorphous admixture of Zn, was first described in 2018 (Nazarchuk et al., 2018). It was found in the fumarole on the Naboko scoria cone formed during the recent 2012-2013 eruption. Glikinite, ideally $Zn_3O(SO_4)_2$ (Nazarchuk et al., 2020), was collected from the sulfate zone of the arsenic-rich (or As-containing) Arsenatnaya fumarole as was described in Section 3, on the Second scoria cone of the 1975-1976 eruption. Itelmenite exhibits not only a new structure type, but also a new stoichiometry for anhydrous sulfates with alkali and transition metals: $A^{+}_2M^{2+}_3(SO_4)_4$. Glikinite has a synthetic structural analogue (Bald and Grühn, 1981); however, the mineral (Nazarchuk et al., 2020) contains essential amount of copper impurity. Synthetic analogs of both these mineral species were obtained and were investigated a new possible material for Na^+-based batteries.

Despite the low conductive ability of the itelmenite-type $Na_2Cu\mathit{M}_2(SO_4)_4$ framework, the results on phase formation in the Na_2SO_4-$CuSO_4$-$MgSO_4$-($ZnSO_4$) system appeared interesting with implications to mineralogy and geochemistry. Identified phases mimic fumarolic minerals assemblages, which allowed to deduce some of the secrets of the mineral formation in active fumaroles in scoria cones of Tolbachik volcano.

In order to study the crystal structure, composition and properties of synthetic itelmenite-type $Na_2Cu\mathit{M}_2(SO_4)_4$ and glikinite, $Zn_3O(SO_4)_2$ were used solid-state synthesis in air.

5.2 Synthesis of $Na_2CuMg_2(SO_4)_4$ and $Na_2CuZn_2(SO_4)_4$

$Na_2CuMg_2(SO_4)_4$ was prepared by solid state synthesis in air from a mixture of Na_2SO_4, $CuSO_4$ and $MgSO_4$. Reagents were taken in 1:1.09:1.91 ratio and were loaded into a gold/platinum crucible and kept at 600 °C for 3 hours in air and subsequently cooled for 9 hours to room temperature.

$Na_2CuZn_2(SO_4)_4$ phase was prepared by solid state synthesis in air from a mixture of Na_2SO_4, $CuSO_4$ and $ZnSO_4$. Reagents were mixed in 1:1.09:1.91 ratio. The mixture was loaded into a gold/platinum crucible and kept at 550°C (in accordance with thermal analysis data described below) for 1 hour in air, followed by cooling for 9 hours to room temperature.

Since it is impossible to separate the positions of copper and zinc for the phase $Na_2CuZn_2(SO_4)_4$ by single X-ray diffraction, a chemical analysis was performed, which will be described below.

5.2.1 DTA- TG and HTXRD analyses for precursors of $Na_2CuMg_2(SO_4)_4$ and $Na_2CuZn_2(SO_4)_4$ phases

In order to optimize the temperature of crystallization of synthetic phases DTA and TGA analyses were performed for mixtures of precursors. This procedure was done before each synthesis.

$Na_2CuMg_2(SO_4)_4$. Figure 18 represents TG, DSC, and IC (ionic currents at *m*/*z* = 18 and 48, which correspond to H_2O^+ and SO^+) registered for a pelletized mixture of Na_2SO_4, $CuSO_4$, and $MgSO_4$ taken with the ratio 1:1.09:1.91 and first heated from 40 to 850°C and then cooled to 720°C.

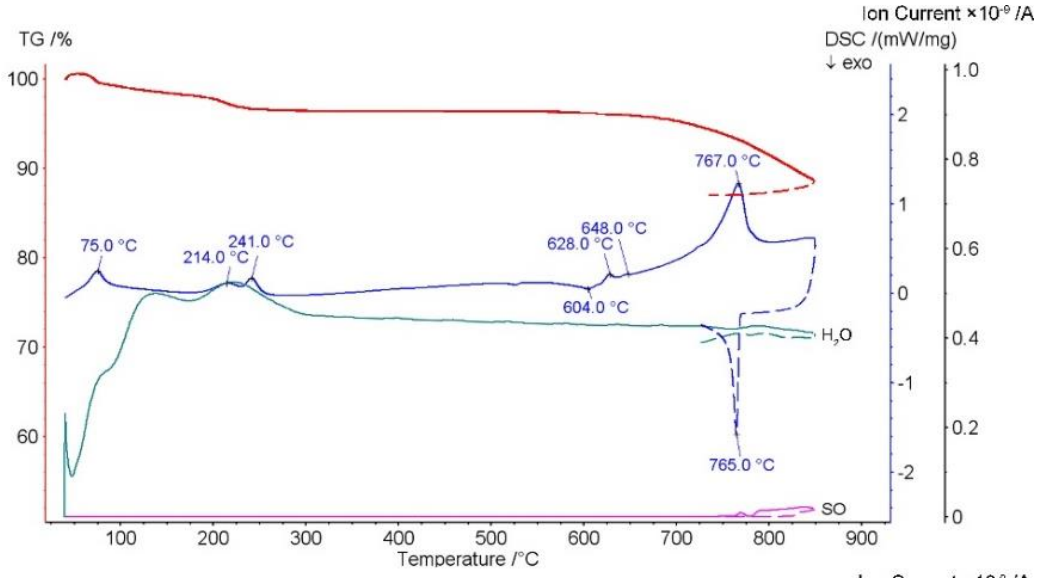

Figure 18. TG (red), DSC (blue) and IC (green) curves for the mixture of Na_2SO_4, $CuSO_4$ and $MgSO_4$ in 1:1.09:1.91 ratio

The low-temperature part of TG curve exhibits two kinks due to mass loss: 1.33% at 56 - 95°C, and 1.70% at 172-276°C which correspond to endothermic effects on the DSC curve with one maximum at 75°C for the first one and two maxima at 214 and 241°C for the second one, respectively. These are accompanied by the maxima for the *m*/*z* = 18 IC curve. Between the kinks, a monotonous mass loss of 1.04% is observed. The event at 214°C may be related to partial melting of the sample.

These low-temperature effects clearly occur due to the dehydration processes. We note that the starting material rapidly absorbs water from humid air, most likely with formation of crystalline hydrates (Siidra et al. 2019), even if briefly exposed during opening the container and mounting onto the holder to the TGA apparatus. Note that water is an essential constituent of fumarolic gases (Chaplygin et al. 2016) therefore the experimental conditions still mimic the natural ones.

Further heating the sample proceeds eventless from 276 to 560°C, after which an exothermic weak effect is observed with a maximum at 604°C. At 617 - 653°C, two endothermic effects are observed with maxima at 628 and 648°C, which are accompanied by weight losses of 0.22%. We attributed a complicated series of effects to crystallization of $Na_2CuMg_2(SO_4)_4$. HT X-ray diffraction study of the reagent mixture (not represented herein) also confirms the appearance of itelmenite in this temperature range. Thus, the crystallization temperature of this compound is in a good agreement with the temperature of gases (600-620°C) in Saranchinaitovaya fumarole where itelmenite was discovered in 2014 (Nazarchuk et al. 2018) yielding a good emulation of natural fumarolic processes.

The rate of mass loss increases essentially above 653°C; further heating to 850°C results in loss of 7.26% accompanied by a strong endothermic effect on the DSC curve (with a maximum at 767°C and completion at 799°C. The IC for m/z = 48 is observed only above 767°C when the sample is almost completely melted. After that, the content of sulfur oxides in the decomposition products increases; this indicates that decomposition of sulfates occurs only after complete melting of the sample. It is reasonable to assume that the endothermal effect is due to the sample melting accompanied by the partial decomposition and evolution of sulfur oxides.

Cooling from 850 to 690°C results in additional mass loss of 1.94%; the DSC curve shows a strong peak at 765°C due to crystallization, after which evolution of sulfur oxides had stopped. It is possible that some decomposition products (e.g. polysulfuric acids) condense below 195°C and do not enter the analyzing chamber of the mass-spectrometer.

$Na_2CuZn_2(SO_4)_4$. We used a similar synthetic approach as described above for the Zn compound (**Figure 20**), Zn substituting Mg. The mixture of precursors was loaded into a platinum crucible and kept at 550°C (in accordance with thermal analysis data described below) for 1 hour in air, followed by cooling for 9 hours to room temperature. Visual inspection under an optical microscope revealed four crystalline phases different in color and morphology (**Figure 19**).

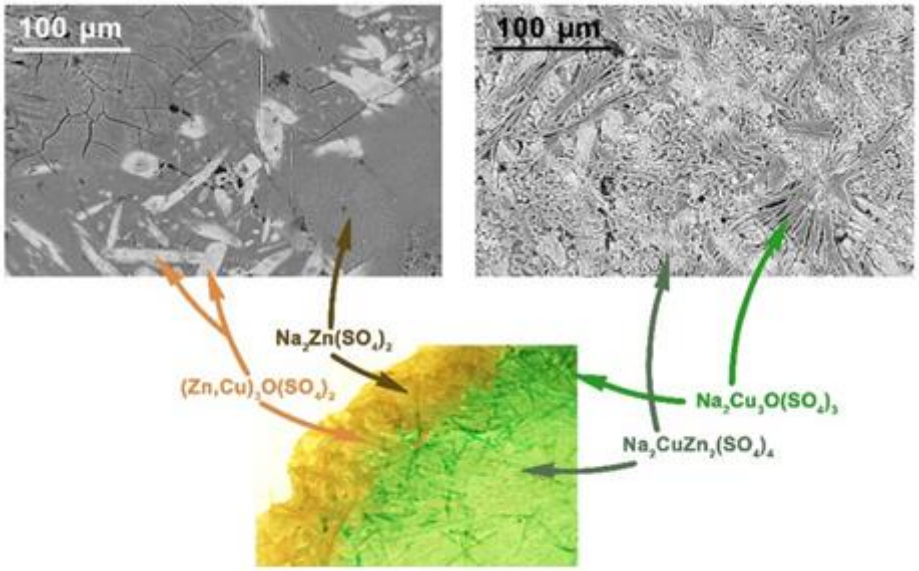

Figure 19. An image of the crucible bottom and wall covered by the various anhydrous sulfates obtained in Na_2SO_4-$CuSO_4$-$ZnSO_4$ system. Two back-scattered electron microscope images of different colored zones are shown above: an orange-colored zone (orange arrows point on light prismatic and isometric crystals of $(Zn,Cu)_3O(SO_4)_2$; a dark-grey matrix consists of $Na_2Zn(SO_4)_2$ and marked by brown arrows) and green zone (sheaf-like dark-grey aggregates of $Na_2Cu_3O(SO_4)_3$ are marked by light-green arrows and dark-green arrows point on multiple irregularly shaped crystals of $Na_2CuZn_2(SO_4)_4$). Ideal formulas are given

Each of them was identified by the means of the single-crystal X-ray diffraction and SEM-EDX. Light-green crystalline matrix consisting of the irregularly shaped crystals (**Figure 19**) and formed on the bottom of the crucible was determined as the targeted $Na_2CuZn_2(SO_4)_4$. Unit-cell parameters of the grass-green prismatic crystals corresponded to the mineral puninite, $Na_2Cu_3O(SO_4)_3$ (Siidra et al., 2017). Closer to the crucible walls and upward, a well-crystallized zone of an orange-brown color (**Figure 19**) is observed. Unit-cell parameters of the two types of crystals in this zone correspond to recently discovered glikinite and synthetic $Zn_3O(SO_4)_2$ (Nazarchuk et al., 2020; Bald and Grühn 1981) and previously known synthetic $Na_2Zn(SO_4)_2$ (Berg and Thorup 2005). Different heating regimes were tried and none of them resulted in the single-phase sample of the $Na_2CuZn_2(SO_4)_4$. Crystal structure description and chemical compositions are reported below only for $Na_2CuZn_2(SO_4)_4$ and $(Zn,Cu)_3O(SO_4)_2$.

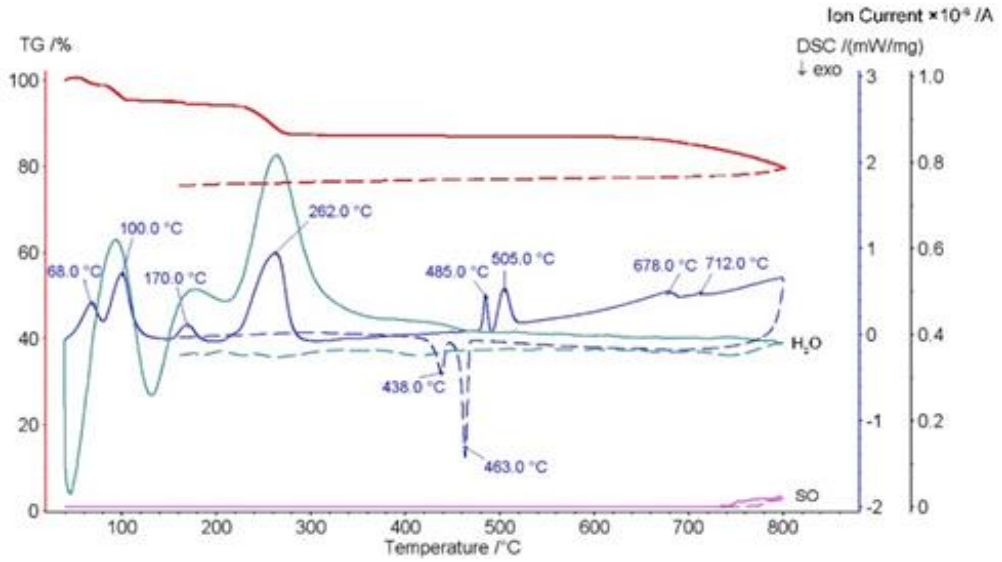

Figure 20. TG-DSC-IC curves for the mixture of Na_2SO_4, $CuSO_4$ and $ZnSO_4$.

Figure 20 shows the thermal analysis results for the pelletized mixture of Na_2SO_4, $CuSO_4$, and $ZnSO_4$ taken in the ratio listed above. The sample was heated from 40 to 800°C and cooled to 150°C at the same conditions as the previous one. HT X-ray diffraction study of the reagent mixture also confirms the appearance of Zn-itelmenite in this temperature range 30°C -550°C (**Figure 21**).

The initial heating stage is also accompanied by several essential thermal effects which are accompanied by maxima of the *m*/*z* = 18 ionic current, *i.e.* they also correspond to release of absorbed water. Next essential endothermal effects are observed in the 477-526 °C range (corresponding maxima at 485 and 505 °C) accompanied by the mass loss of 0.05%. Crystallization of a multiphased sample (**Figure 19**), containing the desired $Na_2CuZn_2(SO_4)_4$, proceeds at essentially lower temperatures compared to its magnesium-based analog (485 °C *versus* 628 °C) . This process is reflected by two very strong thermal effects. The 526 - 570°C range is featureless, and monotonous mass loss is as low as 0.05%. No IC at *m*/*z*=48 was observed.

An endothermal event starts at 583 °C, reaching its maximum at 678 °C and completing at 691°C; the mass loss is 1.40%. This is rather common for decomposition processes, yet no peaks were observed on the IC curves. Most likely, the decomposition products had condensed before the analyzing chamber. Another endothermal process commences between 691 and 718 °C with a maximum of 712 °C and mass loss of 0.98%. Further heating from 718 to 800 °C resulted in weight loss of 4.63%. No essential effects are observed on the DSC curve while an ionic current at *m*/z = 48 was registered indicating release of sulfur oxides. It is possible that the decomposition mostly proceeded on the bottom of the Pt crucible.

Upon cooling, the DSC curve features two strong exothermal effects in the 471 - 417°C (the corresponding maxima at 463 and 438°C). These effects may indicate first-order transitions (most likely

crystallization of several compounds formed upon heating). As in the previous case, weight loss continued upon cooling from 800 to 700°C (2.23%).

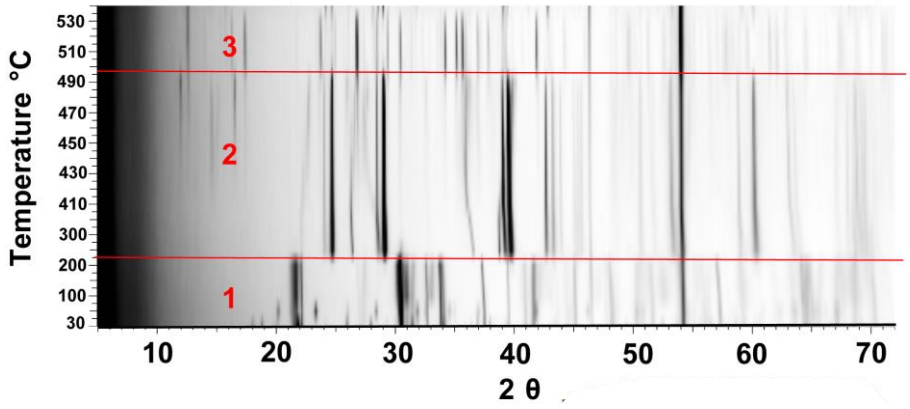

Figure 21. 2D-plot high-temperature X-ray diffraction pattern of the mixture of Na_2SO_4, $CuSO_4$ and $ZnSO_4$ from RT to 550 °C, where 1 step corresponds to dehydration of precursors, 2 step corresponds to Na_2SO_4, $CuSO_4$ and $ZnSO_4$ and the phase formation process, 3 step corresponds to growing of a multiphase sample ($Na_2CuZn_2(SO_4)_4$, $(Zn,Cu)_3O(SO_4)_2$, $Na_2Zn(SO_4)_2$ and $Na_2Cu_3O(SO_4)_3$.

5.3 Chemical composition

The $Na_2(Cu,Zn)_3(SO_4)_4$ compound contains 9.4-10.5 wt.% Na_2O, 25.7-29. wt.% ZnO, 9.2-12.8 wt.% CuO and 50.3-51.8 wt.% SO_3. Hence, the average composition of the phase (13 spot analyses, **Table 6)**, calculated for S = 4, corresponds to $Na_{2.03}Cu_{0.89}Zn_{2.10}(SO_4)_4$ with variation of Zn between 2.00 and 2.24 a toms per formula unit (apfu) and Cu between 0.72 and 1.00 apfu. The general formula can be written as $Na_2(Cu_{1-x}Zn_x)Zn_2(SO_4)_4$ with x = 0-0.24 (**Figure 22**).

The $(Zn,Cu)_3O(SO_4)_2$ phase, which occurs along with $Na_2CuZn_2(SO_4)_4$, is Na-free and contains 30.3-36.2 wt.% ZnO, 23.6-28.3 wt.% CuO and 39.4-41.4 wt.% SO_3. Its average composition (11 spot analyses, **Table 6**), calculated for S = 2, is $(Zn_{1.68}Cu_{1.31})O(SO_4)_2$ and general phase formula can be written as $(Zn_{3-x}Cu_x)O(SO_4)_2$, with x = 1.20-1.45.

In addition, the studied samples contain another Zn-Cu-S phase (ZnO = 26.3-27.6 wt.%, CuO = 21.3-22.6 wt.% and SO_3 = 49.1-49.7 wt.%, 5 spot analyses (**Table 6**) with average formula of $Zn_{1.08}Cu_{0.90}(SO_4)_2$ and a Na-Zn-Cu sulfate (Na_2O = 18.5-20.0 wt.%, ZnO = 21.0-24.0 wt.%, CuO = 3.2-5.7 wt.% and SO_3 = 52.4-53.0 wt.%, 6 spot analyses, **Table 6**) with average formula of $Na_{1.95}(Zn_{0.85}Cu_{0.20})(SO_4)_2$. Both phases were not studied using XRD or single crystal analysis; the former probably corresponds to mineral hermannjahnite $CuZn(SO_4)_2$ (Siidra et al. 2018) and the latter has no analogue among known minerals. $Na_2Zn(SO_4)_2$ (Berg and Thorup 2005) is known for synthetic compounds only.

Table 6. Average compositions (wt. %) of $Na_2CuZn_2(SO_4)_4$, $(Zn,Cu)_3O(SO_4)_2$, $CuZn(SO_4)_2$ and $Na_2Zn(SO_4)_2$.

Component	$Na_2CuZn_2(SO_4)_4$	$(Zn,Cu)_3O(SO_4)_2$	$CuZn(SO_4)_2$	$Na_2Zn(SO_4)_2$
Na_2O	10.01	bld	bld	19.07
ZnO	27.20	34.20	27.11	21.83
CuO	11.21	26.11	21.92	5.16
SO_3	50.90	40.12	49.37	52.66
Total	99.32	100.43	98.40	98.72

Bld – below detection limit.

Figure 22. Back-scattered electron image of the sample containing $Na_2(Cu,Zn)Zn_2(SO_4)_4$ (NaCuZn, gray), $(Zn,Cu)_3O(SO_4)_2$ (ZnCu, white), $CuZn(SO_4)_2$ (CuZn, light gray) and $Na_2Zn(SO_4)_2$ (NaZn, dark gray).

5.4 Powder X-ray diffraction

The X-ray powder diffraction pattern of $Na_2CuMg_2(SO_4)_4$ polycrystalline sample was collected at room temperature. The unit-cell parameters of:

- $Na_2CuMg_2(SO_4)_4$ refined in *Pbca* space group are: a = 9.5506(1) Å, b = 8.7643(1) Å, c = 28.7100(1) Å and V = 2403.2(1) Å^3, R_P = 2.84%;

- $Na_2CuZn_2(SO_4)_4$ in the space group *Pbca* are: $a = 9.4568(1)$ Å, $b = 8.8051(1)$ Å, $c = 28.8605(1)$ Å and $V = 2403.2(1)$ Å^3;

- $(Zn,Cu)_3O(SO_4)_2$ in the space group $P2_1/m$ are: $a = 7.2986(1)$ Å, $b = 6.5698(1)$ Å, $c = 7.7927(1)$ Å, $\beta = 117.360(1)°$,and $V = 331\ .9(1)$ Å^3.

In the powder pattern of $(Zn,Cu)_3O(SO_4)_2$ there is an impurity phase : $Na_2Zn(SO_4)_2$ included to the refinement. Despite a manual selection of crystals of $(Zn,Cu)_3O(SO_4)_2$ we determined around 15% of $Na_2Zn(SO_4)_2$. The crystals of the sodium phase intergrow with $CuZn_2O(SO_4)_2$, as we can see on the **Figure 19** and **Figure 22**, making their separation impossible. The final observed, calculated, and difference powder XRD patterns resulting from the profile-matching procedure were plotted in **Figure 23** for the 3 samples.

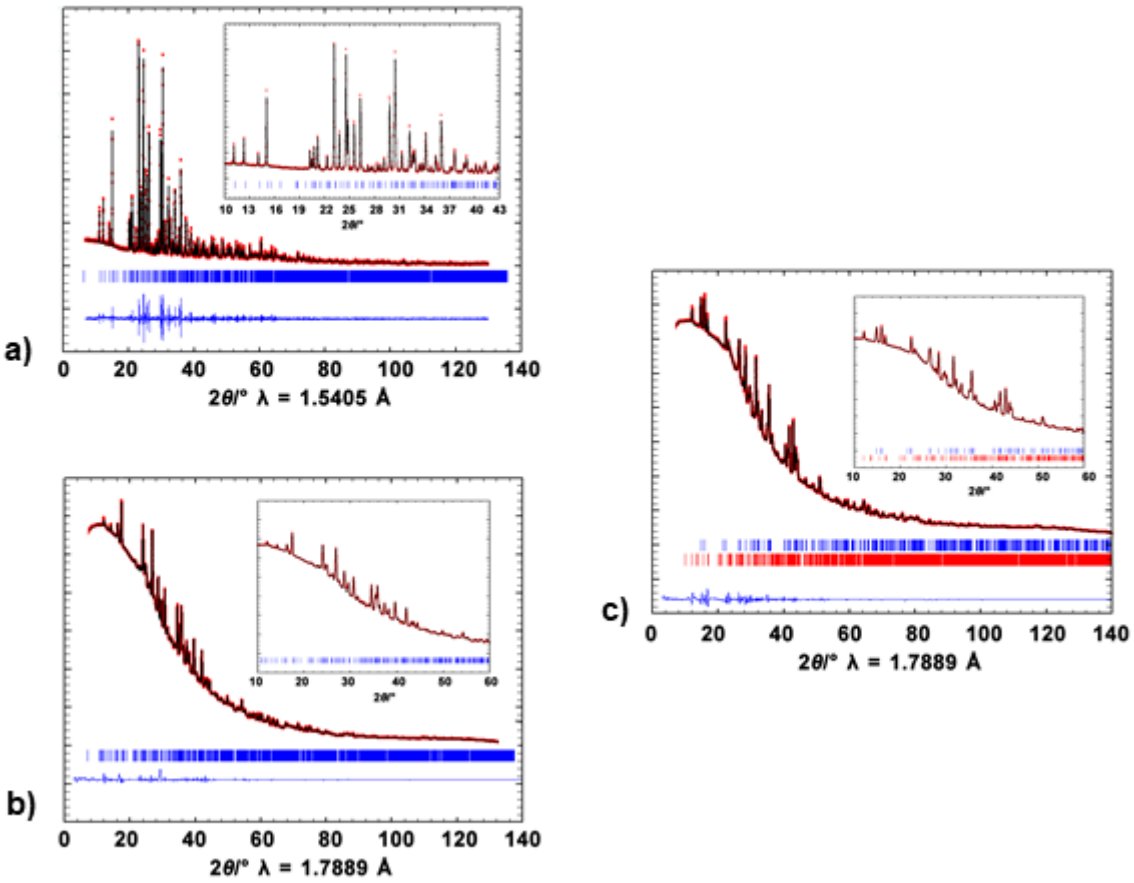

Figure 23. Results of the Profile-matching refinement from the powder XRD data of $Na_2CuMg_2(SO_4)_4$ (a), $Na_2CuZn_2(SO_4)_4$ (Gandolfi) (b) and $(Zn,Cu)_3O(SO_4)_2$ (Gandolfi) (c).

To study the thermal stability of phase $Na_2CuMg_2(SO_4)_4$, the method of high-temperature X-ray diffraction was used. Phase $Na_2CuMg_2(SO_4)_4$ was studied here, as it was the only one that could be obtained in its pure form.

5.1 High-Temperature X-ray Diffraction of $Na_2CuMg_2(SO_4)_4$

The temperature step was 50°C in the range 50-400°C and 20°C in the range of 400-680°C. HTXRD data (**Figure 24a**) are consistent with thermal analysis data reported above. In general, the pattern does not undergo significant changes. $Na_2CuMg_2(SO_4)_4$ starts to decompose at 620°C and peaks of CuO start to appear. Using data up to the decomposition we found a volumic dilatation coefficient $\alpha = 53 \cdot 10^{-6}$ °C^{-1} which is rather high, in accordance with the rather "soft" framework offered by sulfates. However, this dilation is strongly anisotropic, as verified plotting the temperature dependence of the cell parameters (**Figure 24b**) of $Na_2CuMg_2(SO_4)_4$ in the appropriate thermal range. They can be expressed by the following functions after fitting, where the temperature T is expressed in °C:

$a_t = 9.55759(59) + 0.1235(14) \times 10^{-3}T$

$b_t = 8.7675(10) + 0.0717(23) \times 10^{-3}T$

$c_t = 28.7345(86) + 0.330(58) \times 10^{-3}T + 0.885(84) \times 10^{-6}T^2$

$V_t = 2407.39(49) + 82(3) \times 10^{-3}T + 70(5) \times 10^{-6}T^2$

It is noteworthy that the most expanding direction is the *c*-axis giving the first experimental clue about a rather anisotropic and complex structural framework, as detailed below.

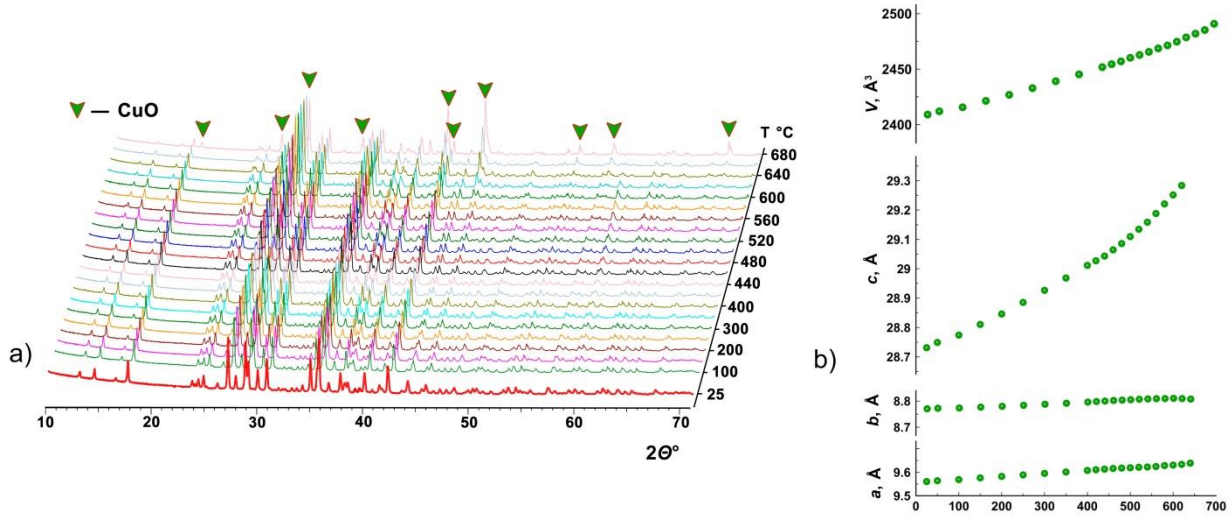

Figure 24. Three-dimensional perspective plot showing all diffractograms for $Na_2CuMg_2(SO_4)_4$ over 10-75° 2Θ with increasing temperature (a). The temperature dependences of the unit cell parameters and volume for $Na_2CuMg_2(SO_4)_4$ (b).

5.2 Single-crystal X-ray diffraction analysis

Single crystals data were refined in the *Pbca* space group to R_1 = 0.036 and R_1 = 0.053 for $Na_2CuMg_2(SO_4)_4$ and $Na_2CuZn_2(SO_4)_4$, respectively. Atomic coordinates reported for glikinite (Nazarchuk et al. 2020) were refined to R_1 = 0.053 in the crystal structure of $(Zn,Cu)_3O(SO_4)_2$. The main crystallographic information for all three new synthetic phases is summarized in **Table 7**.

Table 7. Crystallographic data for $Na_2CuMg_2(SO_4)_4$, $Na_2CuZn_2(SO_4)_4$ and $(Zn,Cu)_3O(SO_4)_2$.

	$Na_2CuMg_2(SO_4)_4$	$Na_2CuZn_2(SO_4)_4$	$(Zn,Cu)_3O(SO_4)_2$
Crystal system	Orthorhombic	Orthorhombic	Monoclinic
Space group	Pbca	Pbca	$P2_1/m$
Unit cell dimensions			
a (Å)	9.531(7)	9.458(5)	7.3156(6)
b (Å)	8.745(6)	8.811(4)	6.6004(5)
c (Å)	28.71(2)	28.850(15)	7.8941(7)
β (°)			117.424(5)
Unit-cell volume ($Å^3$)	2393(3)	2404(2)	338.34(5)
Z	4	4	2
Calculated density ($g·cm^{-3}$)	3.032	3.450	3.968
Absorption coefficient (mm^{-1})	2.966	6.581	11.194
Crystal size (mm)	0.15×0.15×0.10	0.18×0.18×0.10	0.10×0.10×0.10
Data collection			
Temperature (K)	296(2)	296(2)	296(2)
Radiation, wavelength (Å)	Mo*K*α, 0.71073	Mo*K*α, 0.71073	Mo*K*α, 0.71073
θ range (°)	1.418 - 26.757	1.412 - 27.997	2.907-27.466
h, k, l ranges	-8→12	-12→10	-12→10
	-11→8	-11→8	-11→8
	-36→36	-36→38	-36→38
Total reflections collected	10945	12574	848
Unique reflections (R_{int})	2532 (0.06)	2894 (0.12)	844(0.02)
Unique reflections $F > 4\sigma(F)$	1857	1679	783
Structure refinement			

Refinement method	Full-matrix least-squares on F^2	Full-matrix least-squares on F^2	Full-matrix least-squares on F^2
Weighting coefficients *a*, *b*	0.034500	0.048500	0.000200, 11.927700
Data/restraints/parameters	2532/0/230	2894/0/230	844/12/80
R_1 [$F > 4\sigma(F)$], wR_2 [$F > 4\sigma(F)$]	0.036, 0.074	0.053, 0.107	0.053, 0.105
R_2 all, wR_2 all	0.059, 0.083	0.113, 0.133	0.059, 0.108
Gof on F^2	1.006	0.958	1.144
Largest diff. peak and hole (*e* Å^{-3})	0.538, -0.487	1.104, -0.941	1.747,-1.698

5.3 Structure description of $Na_2CuMg_2(SO_4)_4$ and $Na_2CuZn_2(SO_4)_4$

There are three *M* sites (**Figure 25**a), all coordinated by distorted octahedral arrays of O atoms with average *M*–O distances in the range 2.08-2.17 Å (**Table S5**) in $Na_2CuMg_2(SO_4)_4$, $Na_2CuZn_2(SO_4)_4$ and itelmenite $Na_2CuMg_2(SO_4)_4$ (Nazarchuk et al., 2018). *M*1O_6 polyhedron has five *M*1-O bonds in the range 1.95-2.16 Å and sixth significantly longer *M*1-O bond ~2.8 Å. The similar coordination environments are also observed for *M*2 site. Thus, both *M*1 and *M*2 can be described as Jahn-Teller-distorted MO_{5+1} coordinations. *M*3 site has symmetrical [6O] octahedral coordination with two slightly elongated apical bonds of 2.15-2.29 Å. In general, substitution of Mg^{2+} (r = 0.72 Å) by Zn^{2+} (r = 0.74 Å) slightly increases *M*-O bond-lengths. *M*O_6 polyhedra are characterized by the different degree of distortion (**Table 8**). The following Δ_{oct} $\mathbf{\Delta_{oct}}$ bond-length distortion parameter, suggested in Wildner 1992, was used for octahedrally coordinated *M* sites in both $Na_2CuMg_2(SO_4)_4$ and $Na_2CuZn_2(SO_4)_4$:

$$\mathbf{\Delta_{oct}} = \frac{1}{6}\sum_{i=1}^{6}\left[\frac{(d_i - d_m)}{d_m}\right]^2 \quad (8)$$

where d_i = (*M*-O) bond-length, d_m = <*M*-O> bond-length (*M* = Cu, Mg, Zn). All of the *M*-O bonds ≤3 Å were taken into consideration (**Table S5**). Dealing with Mg^{2+} alkali earth against Cu^{2+} transition metal, the values correlate rather well with the content of Cu^{2+} cation in *M* sites due to the Cu^{2+} Jahn-Teller distortion. Cu:Mg ratio in *M* sites was obtained during the refinement of the crystal structure of

$Na_2CuMg_2(SO_4)_4$ (**Table 8**) Cu^{2+} cation dominates in *M*1 site, whereas only 22.5% of copper is present in *M*2. The *M*3 site is almost completely occupied by Mg^{2+} cations in $Na_2CuMg_2(SO_4)_4$ in agreement with very symmetrical coordination environment.

Table 8. *M* site populations and $\Delta_{oct}\times10^3$ in the structures of itelmenite, $Na_2CuMg_2(SO_4)_4$ and $Na_2CuZn_2(SO_4)_4$.

	Itelmenite (Nazarchuk et al. 2018)	$\Delta_{oct}\times10^3$	$Na_2CuMg_2(SO_4)_4$	$\Delta_{oct}\times10^3$	$Na_2CuZn_2(SO_4)_4$	$\Delta_{oct}\times10^3$
*M*1	$Cu_{0.71}Mg_{0.09}Zn_{0.2}$	20.62	$Cu_{0.820(5)}Mg_{0.180(5)}$	19.98	Cu>Zn	20.92
*M*2	$Mg_{0.55}Cu_{0.39}Zn_{0.06}$	16.55	$Mg_{0.775(4)}Cu_{0.225(4)}$	17.64	Zn>Cu	17.48
*M*3	$Mg_{0.91}Zn_{0.09}$	1.11	$Mg_{0.949(3)}Cu_{0.051(3)}$	1.38	Zn>Cu	2.18

It can be only qualitatively **(Table 8**) partially answered on the basis of the different octahedral distortions of the Cu and Zn sites. Despite similar ionic radii, intuitively the Cu^{2+} Jahn-Teller effect is responsible for strong octahedral distortion. However, the second order Jahn-Teller effect which occurs for Zn^{2+} with a completely filled $3d^{10}$ shell (Boucher et al 1994) can also lead to strong polyhedral distortion, such that Cu^{2+} for Zn^{2+} substitution in similar sites is possible. The strongest distortion is observed for $M1O_{5+1}$ octahedron in the crystal structures of both the mineral and its two synthetic analogues reported herein. The $M3O_6$ octahedron is obviously the least distorted preserving its main octahedral shape. Its $\Delta_{oct}\times10^3$ value is close to 1 for $M3O_6$ in itelmenite and synthetic $Na_2CuMg_2(SO_4)_4$. Importantly is preserved for $M1O_{5+1}$ and $M2O_{5+1}$ despite distance changes in the latter and significantly increased for $M3O_6$ in $Na_2CuZn_2(SO_4)_4$, where it is expected to be mostly occupied by Zn^{2+}. According to these coordination changes after replacing Zn^{2+} for Mg^{2+}, Cu^{2+} cations are expected dominant in *M*1 site in $Na_2CuZn_2(SO_4)_4$, and in minor amount in *M*2 and *M*3.

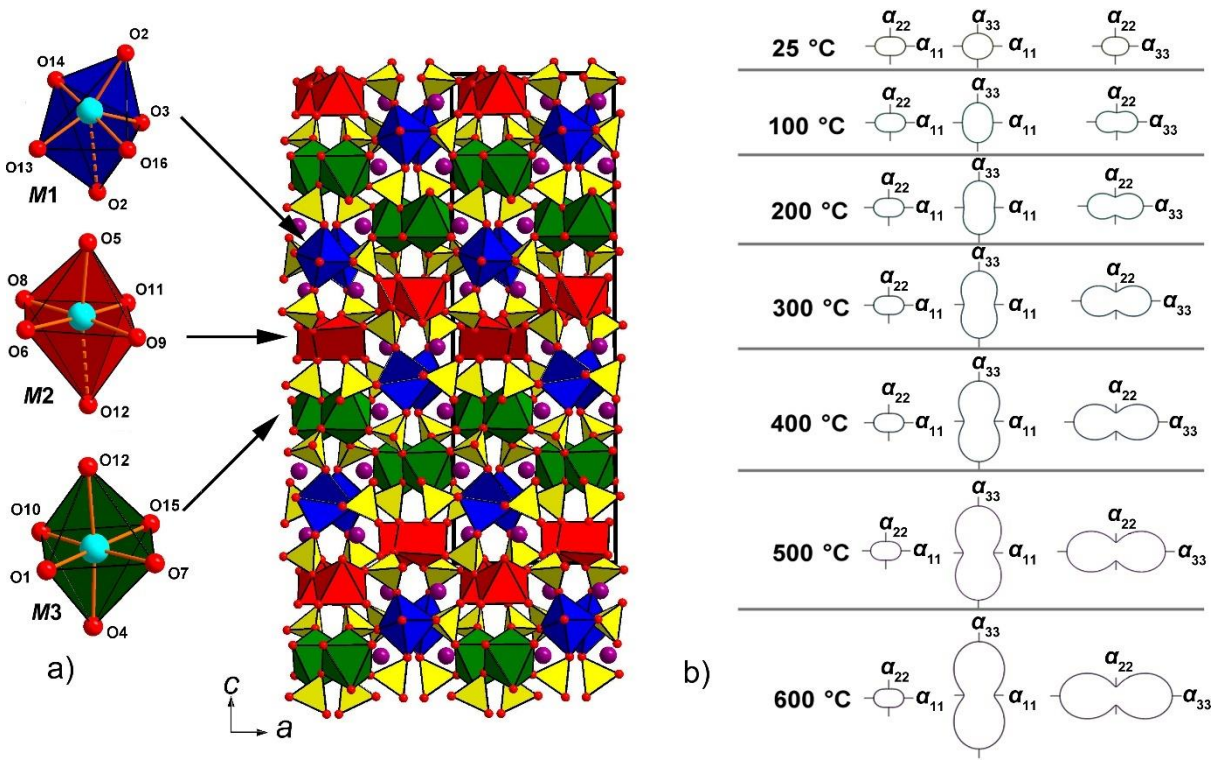

Figure 25. Coordination of *M* sites in $CuMg_2O(SO_4)_2$ and $CuZn_2O(SO_4)_2$ (distances <2.5Å are shown by dashed lines) (left) and general projection of the crystal structure of $Na_2CuMg_2(SO_4)_4$ along the *b* axis (weak Cu-O bonds >2.5Å are omitted for clarity) (a). Pole figures of the thermal expansion coefficients of $Na_2CuMg_2(SO_4)_4$ at different temperatures (b).

There are two positions fully occupied by Na in $Na_2CuMg_2(SO_4)_4$ and $Na_2CuZn_2(SO_4)_4$. Na1 atom forms ten Na-O bonds in the range 2.38 - 3.25 Å, whereas Na2 is coordinated by the eight O atoms in the range 2.38-2.87 Å. In the crystal structure of natural itelmenite (Nazarchuk et al., 2018), admixture of K is concentrated in Na1 site with the larger coordination sphere.

Four symmetrically independent S^{6+} cations show very similar S-O bond lengths in itelmenite and $Na_2CuMg_2(SO_4)_4$, $Na_2CuZn_2(SO_4)_4$. The <S-O> distances demonstrate very similar values of ~1.47 Å.

The structural architecture of $Na_2CuMg_2(SO_4)_4$ and $Na_2CuZn_2(SO_4)_4$ is simple, where each of the vertices of the SO_4 tetrahedron is common with one of the vertices of the MO_6 octahedron. Resulted system of channels in the framework is filled by Na^+ cations (**Figure 25b**). Itelmenite-type structural topology is unknown in synthetic compounds.

High-temperature powder X-ray diffraction studies **(Figure 24)** show that $[CuMg_2(SO_4)_4]^{2-}$ framework upon heating expands anisotropically (**Figure 25b**). Note that, at room temperature expansion is almost isotropic. The thermal expansion occurs mostly in the direction of α_{33}.

5.4 Structure description of $(Zn,Cu)_3O(SO_4)_2$

There are three *M* sites (**Table S6**) in the structure of synthetic analogue of glikinite. Refinement of the crystal structure is complicated by the presence of the significant amount of Cu^{2+} (see chemical composition above **Table 6**) distributed over *M* sites. *M*1 site has slightly distorted octahedral coordination with $\Delta_{oct} \times 10^3 = 5.87$. Relatively small value indicates only minor presence of Cu^{2+} in $M1O_6$ octahedron. *M*2 and *M*3 sites are 5-coordinated (**Figure 26a**). Addison tau-parameter has been used to describe the distortion around *M*2 and *M*3 sites. Values of $\tau = 0.41$ and $\tau = 0.35$ for *M*2 and *M*3 sites, respectively, were calculated. Thus, coordination environments of both sites are intermediate from square pyramidal to trigonal bipyramidal geometry. $M2O_5$ and $M3O_5$ coordinations are more typical for Cu^{2+} rather than to Zn^{2+}. The question of the distribution of Cu^{2+} and Zn^{2+} in glikinite and its synthetic analogue remains a debate.

Average S-O bond lengths show typical values of 1.441 and 1.466 Å for the $S1O_4$ and $S2O_4$ tetrahedra, respectively.

The structure of $(Zn,Cu)_3O(SO_4)_2$ contains seven O^{2-} anions. The O2-O7 are strongly bonded in SO_4^{2-} groups. The O1 atom is tetrahedrally coordinated by four Zn^{2+}, Cu^{2+} cations, forming short and strong O-Zn bonds. From the viewpoint of bond-valence theory, these bonds are the strongest in the structure and thus it makes absolute sense to consider the O1 atoms as centers of oxocentered $O(Zn,Cu)_4$ tetrahedra. The mean O-Zn length in the $O1Zn_4$ tetrahedron is 1.926 Å, which is typical for such units (Krivovichev et al., 2013) taking into account high content of Cu^{2+}. The $O(Zn,Cu)_4$ tetrahedra link together via common vertices to form $[(Zn,Cu)_3O]^{4+}$ single chains (**Figure 26b**). In this unit, each tetrahedron shares two of four vertices with adjacent tetrahedra. The $[(Zn,Cu)_3O]^{4+}$ single chains extend along the *b* axis. Oxocentered chains are interconnected via SO_4 groups into framework projected in **Figure 26c**.

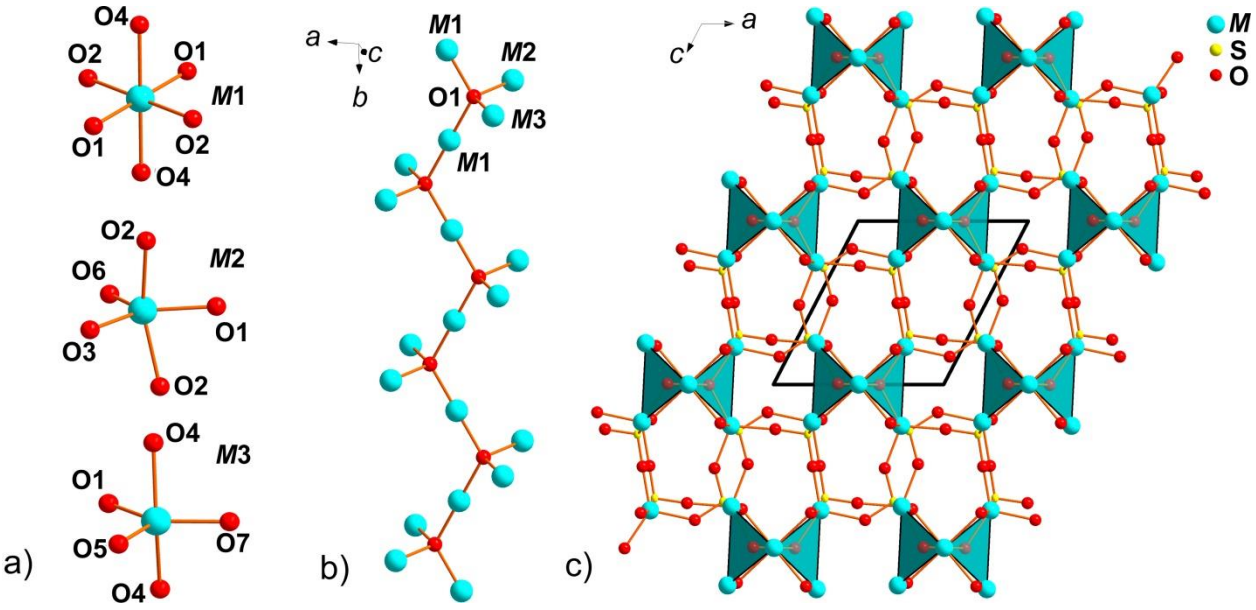

Figure 26. Coordination of *M* sites in $(Zn,Cu)_3O(SO_4)_2$ (a). $[M_3O]^{2+}$ chain elongated along the *b* axis (b). General projection of the crystal structure of $(Zn,Cu)_3O(SO_4)_2$ (c). $[M_3O]^{2+}$ chains are highlighted by blue.

5.5 Evaluation of Na^+ ion diffusion in $Na_2Cu\mathit{M}_2(SO_4)_4$ (*M* = Mg, Zn)

A prerequisite for Na-based materials to be used as electrodes in Na-ion batteries is the existence of Na-diffusion paths within the structure. To get more information on how Na ions can travel inside the framework, it was generated Bond Valence Energy Landscapes (BVEL) using the BondStr program (FullProf Suite (Rodríguez-Carvajal, 1993)). **Figure 27** demonstrates calculated possible Na^+ diffusion pathways in $Na_2Cu\mathit{M}_2(SO_4)_4$ considering all counterions at distances up to 8 Å and the polarizability of Na^+. An energy of 1.6 eV is usually considered as required percolation energy for the diffusion of Na^+ in conducting polyanionic compounds (Boivin et al., 2016; Kovrugin et al., 2018; Sun et al., 2015). In the framework of $Na_2Cu\mathit{M}_2(SO_4)_4$, the iso-energy surface of 1.6 eV represents a non-interconnected ion diffusion path (**Figure 27**a) indicating a limited Na^+ diffusion inside the structure. The energy level leading to an infinitely connected surface for Na^+ diffusion in $Na_2Cu\mathit{M}_2(SO_4)_4$ corresponds only to 3.0 eV above the minimum energy level (**Figure 27**b), which is a rather high energy barrier far above the expected BVEL calculations of E_m< 1.5 eV for any fast ion conductor (Katcho et al 2019) and, thus, the $Na_2Cu\mathit{M}_2(SO_4)_4$ framework cannot be considered as a good Na^+ conductor. Meanwhile, it should be noted that a lithiated analogue of the structure can probably induce a higher ionic conductivity (Boivin et al., 2017).

Low conductive ability of the $Na_2Cu\mathit{M}_2(SO_4)_4$ framework is not surprising, since there is a number of works reporting a limited ion diffusion inside sulfate polyanionic structures (Lander et al. 2017; Kovrugin et al. 2019). However, we believe that the sulfate-based cathodes have a commercial potential in future considering a higher electronegative nature of sulfur, which may deliver the highest redox potential and lead to formation of cathode materials offering high voltage operation and, thus, competitive energy density overcoming weight penalties and lower theoretical capacity in comparison with conventional oxide cathodes.

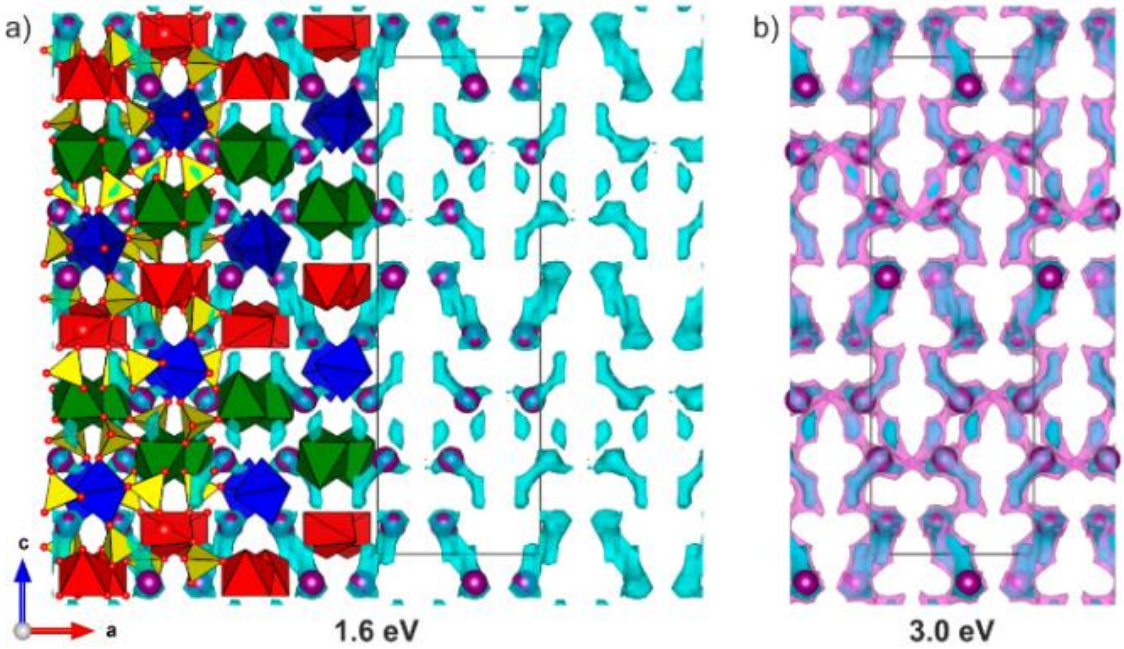

Figure 27. Na^+ ion diffusion pathways obtained using bond valence energy landscapes with an iso-energy surface value of 1.6 eV (*a*) and 3.0 eV (*b*) above the minimum energy level. The iso-energy surfaces of 1.6 eV and 3.0 eV are shown by cyan and pink, respectively. Legend for the unit-cell content see in **Figure 25**

5.6 Infrared spectroscopy of $Na_2CuMg_2(SO_4)_4$

To study the IR spectra, it is necessary to have a pure polycrystalline sample. Since only for phase $Na_2CuMg_2(SO_4)_4$ was possible to obtain a pure powder, and it was investigated. The IR spectrum of preliminary heat treated (to avoid hydration) $Na_2CuMg_2(SO_4)_4$ contains three groups of strong bands (in the ranges 464 to 496, 605 to 674 and 993 to 1277 cm^{-1}) (**Figure 28**). Most of the observed peaks correspond to optically active modes of the three symmetrically independent SO_4 tetrahedra (Smith and Seshadri 1999). The peaks from 464 to 496 cm^{-1} can be tentatively assigned to Mg-O vibrations. The frequencies of the Cu-O stretching and O-Cu-O bending modes are out of the investigated region, i.e. 150-350 cm^{-1} (Secco 1988).

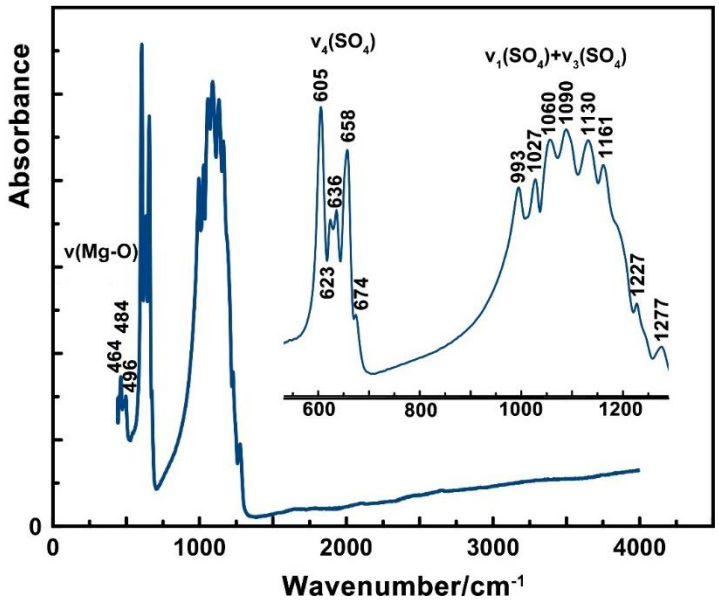

Figure 28. Infrared (FTIR) spectrum of $Na_2CuMg_2(SO_4)_4$.

5.7 Thermal analysis of $Na_2CuMg_2(SO_4)_4$

TGA curve demonstrates the stability up to 650 °C. However, one should note at ~50°C a 7-8 weight % loss, assigned to adsorbed H_2O, a systematic drawback dealing with sulfates (**Figure 29**).

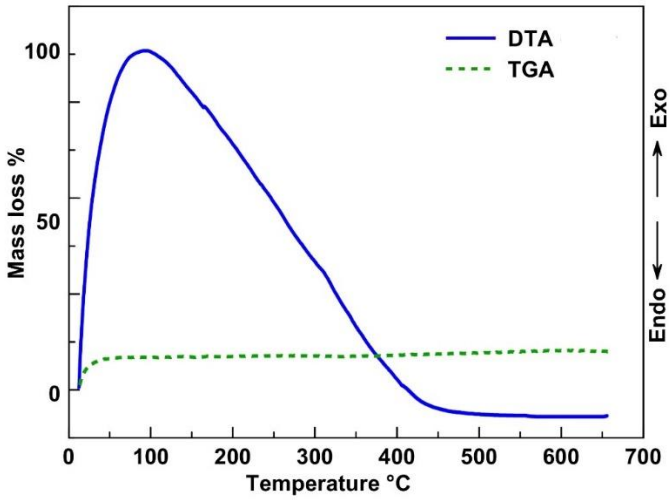

Figure 29. TGA-DTA curves for $Na_2CuMg_2(SO_4)_4$ from 25°C to 650°C.

5.8 Mineralogical and chemical synthesis approach

Our experiments indicate that investigation of anhydrous sulfate systems reproduces many compounds known before as mineral species only. It appeared possible to obtain the Zn- and Mg-analogues of itelmenite. Moreover, the latter was obtained as a pure phase which allowed the study of thermal expansion. The possibility of the formation of synthetic analogues of puninite $Na_2Cu_3O(SO_4)_2$ (Siidra et al., 2017), hermannjahnite $CuZn(SO_4)_2$ (Siidra et al., 2018) and glikinite $Zn_3O(SO_4)_2$ (Nazarchuk et al., 2020) as side products has been shown. On the other hand, the presence of $Na_2Zn(SO_4)_2$ compound (Berg and Thorup 2005) among the crystallized phases, unknown to date as a mineral, shows a high probability of finding such a mineral species in the fumaroles of the scoria cones of the Tolbachik volcano. Note that all the compounds synthesized in this thesis were obtained by the method of solid-state reactions in open air, and not from gas as in natural mineral forming fumarolic environments.

Earlier, in Nazarchuk et al. (2018), we have suggested that itelmenite may form as a result of the interaction between gas and basalt scoria. This hypothesis is confirmed by the syntheses and phase-formation described above. Mg and possibly Na components in the fumarole come from the scoria, not from the gases. The concentrations of metals in the Tolbachik gases, during recent 2012-2013 eruption, are higher than the corresponding concentrations in high-temperature fumaroles worldwide (Zelensky et al., 2014). The hot Cu, Zn and sulfate bearing fumarolic gases condense on the surfaces of the scoria, forming a liquid which dissolves Na and Mg species from the basaltic scoria which then crystallize once the temperature is sufficiently low. Our study shows that outstanding mineralogical diversity observed in the fumaroles of scoria cones is not only due to the formation from the gas enriched by transition metals and involves also intensive exchange with the host basaltic scoria. The similar processes seem also to be responsible for the recrystallization of silicates described from deep and hot zones of Arsenatnaya fumarole (Shchipalkina et al., 2020).

The phase formation in the system with Mg turned out to be interesting and very different from the system with Zn. Apparently, such a difference can be explained by much lower melting point of $ZnSO_4$ (680°C) compared with $MgSO_4$ (1137°C). In addition, zinc has crystal chemical affinity with divalent copper, which leads to a greater structural diversity of the newly formed phases and more complex phase diagrams not available to date.

$Zn_3O(SO_4)_2$ phase was previously described by Bald and Grühn (1981). Interestingly, the polyhedra of zinc in the previously described Cu-free synthetic compound and the polyhedra with a significant admixture of copper in the $(Zn,Cu)_3O(SO_4)_2$ described above and glikinite demonstrate

very similar bond-lengths and overall geometry. Jahn-Teller effect of Cu^{2+} in octahedral environment and the second order Jahn-Teller effect of Zn^{2+} result in distortions of similar magnitude (Halcrow 2013).

In our opinion, a significant amount of copper is important for the stabilization of this structure type and the formation of oxocentered $[(Zn,Cu)_3O]^{4+}$ units. Admixture of Cu^{2+} also controls the formation of itelmenite-type phases.

5.9 Conclusion

This chapter is dedicated to the synthesis, crystal structure and properties of Zn and Mg analogs of itelmenite, $Na_2CuMg_2(SO_4)_4$ (Nazarchuk et al., 2018) and synthetic analog of glikinite, $Zn_3O(SO_4)_2$ (Nazarchuk et al., 2020). Synthetic analogues of both minerals were obtained during studies of phase formation in the Na_2SO_4-$CuSO_4$-$MgSO_4$-($ZnSO_4$) systems which lead to essentially different results.

The mineral itelmenite, ideally $Na_2CuMg_2(SO_4)_4$, a new structure type, with novel stoichiometry for anhydrous sulfates with alkali and transition metals: $A^{+2}M_2^{+3}(SO_4)_4$ where (A = alkali metal, M = transition metal). $Na_2CuMg_2(SO_4)_4$ and $Na_2CuZn_2(SO_4)_4$ were evaluated for Na^+ ion diffusion.

For the Zn compound, several by-products were observed which are synthetic analogs of puninite $Na_2Cu_3O(SO_4)_2$ (Siidra et al., 2017), as well as hermannjahnite $CuZn(SO_4)_2$ (Siidra et al., 2018) and glikinite-type $(Zn,Cu)_3O(SO_4)_2$. All of them were prepared via solid-state reactions in open systems. The $Na_2CuMg_2(SO_4)_4$, $Na_2CuZn_2(SO_4)_4$ and $(Zn,Cu)_3O(SO_4)_2$ were structurally characterized by the single-crystal XRD. In the Zn-bearing system, the admixture of Cu^{2+} likely controls the formation of itelmenite-type and glikinite-type phases.

A further example of why it is important to study crystal formation will be discussed in the next chapter, which deals with minerals of the euchlorine group. An example of interaction of hexamers $[Cu_6O_2]$ in synthetic analogs of the euchlorine group and their link between crystal structure and magnetic properties will be discussed.

6. Interaction of magnetic hexamers [Cu_6O_2] in synthetic analogs of puninite $Na_2Cu_3O(SO_4)_3$, euchlorin $NaKCu_3O(SO_4)_3$, fedotovite $K_2Cu_3O(SO_4)_3$ and the related $Rb_2Cu_{3.07}O_{1.07}(SO_4)_3$, $Cs_2Cu_{3.5}O_{1.5}(SO_4)_3$

6.1 Inroduction

Copper compounds, including abundant minerals (Pekov et al., 2018) and their synthetic analogs, are fertile grounds for research on low-dimensional magnetism (Inosov 2018). In low-dimensional magnets exist the interplay between various magnetic exchanges which may create exotic quantum magnetic states, in absence of 3D magnetic ordering of the spins such as in quantum spin liquids (QSL). Dimension and topology of the magnetic subsystem, and also its interactions with others - elastic, charge, orbital - magnetic subsystems have a decisive influence on the formation of the main state of matter and can lead to unusual physics.

For example, Cu_2OSeO_3 with a chiral lattice built by the Cu_4 tetrahedra hosts several skyrmion phases (Chacon et al., 2018; Qian et al., 2018) tunable by electric field (Seki et al., 2012; White et al., 2014) reveals nonreciprocal propagation of phonons, and shows topological magnon states. Skyrmions are small magnetic vortices that occur in an astonishingly wide range of materials and they were first discovered about a decade ago (Skyrme, 1962; Sondhi et al., 1993). They can be imagined as 2D knots in which the magnetic moments rotate about 360° within a plane. They could form the basis of future magnetic data storage technologies that have a higher density than today's disk drives. This is because they can be made much smaller than the magnetic domains used in these devices and they can be controlled efficiently with spin currents. Developing microscopic magnetic models of such complex systems is far from trivial, though. In Cu_2OSeO_3, the presence of Cu_4 tetrahedra acting as single magnetic units was hardly appreciated until pointed out by ab initio calculations (Janson et al., 2014) and further confirmed spectroscopically (Ozerov et al., 2016). The interplay between, such super-spins are very interesting at the fundamental viewpoint, but are hardly achieved in true materials. Indeed, this chapter is addressed to study some interesting fact concerning intercalation: incorporation of various amount of neutral CuO by depleted Cu^{2+} chains. Also here will be discussed crystal structures characterization of $A_2Cu_3O(SO_4)_3$ (A = Na, K), and the related $Rb_2Cu_{3.07}O_{0.07}(SO_4)_3$, $Cs_2Cu_{3.5}O_{1.5}(SO_4)_3$, twining problems, IR- spectroscopy, thermodynamic and magnetic properties.

6.2 Synthesis

Single-phase and polycrystalline sulfate materials were prepared by the solid state technique. For establish the temperature of crystallization of synthetic phases was used differential thermal (DTA) and thermogravimetric (TGA) analyses and high-temperature X-ray diffraction for mixtures of precursors from room temperature to 700 °C, we will show the DTA and TGA graphs only for mixture of precursors of $Na_2Cu_3O(SO_4)_3$ and $NaKCu_3O(SO_4)_3$ (**Figure 30)**. In DTA curves the first three endothermic peaks are attributed to the dehydration of precursors. The endothermic peaks 464 °C and 532 °C are referent of recrystallization of $NaKCu_3O(SO_4)_3$ and $Na_2Cu_3O(SO_4)_3$. And last endothermic peak 656 °C is corresponded the decomposition into CuO and other not identified transformation products. The temperature stability also was proofed by HTXRD techniques. The crystallization temperature for each compound is summarized in **Table 9**. The resulting solid products are often inhomogeneous in texture but contain single crystals (typical crystal size 0.15×0.15×0.10 mm) (**Figure 31**).

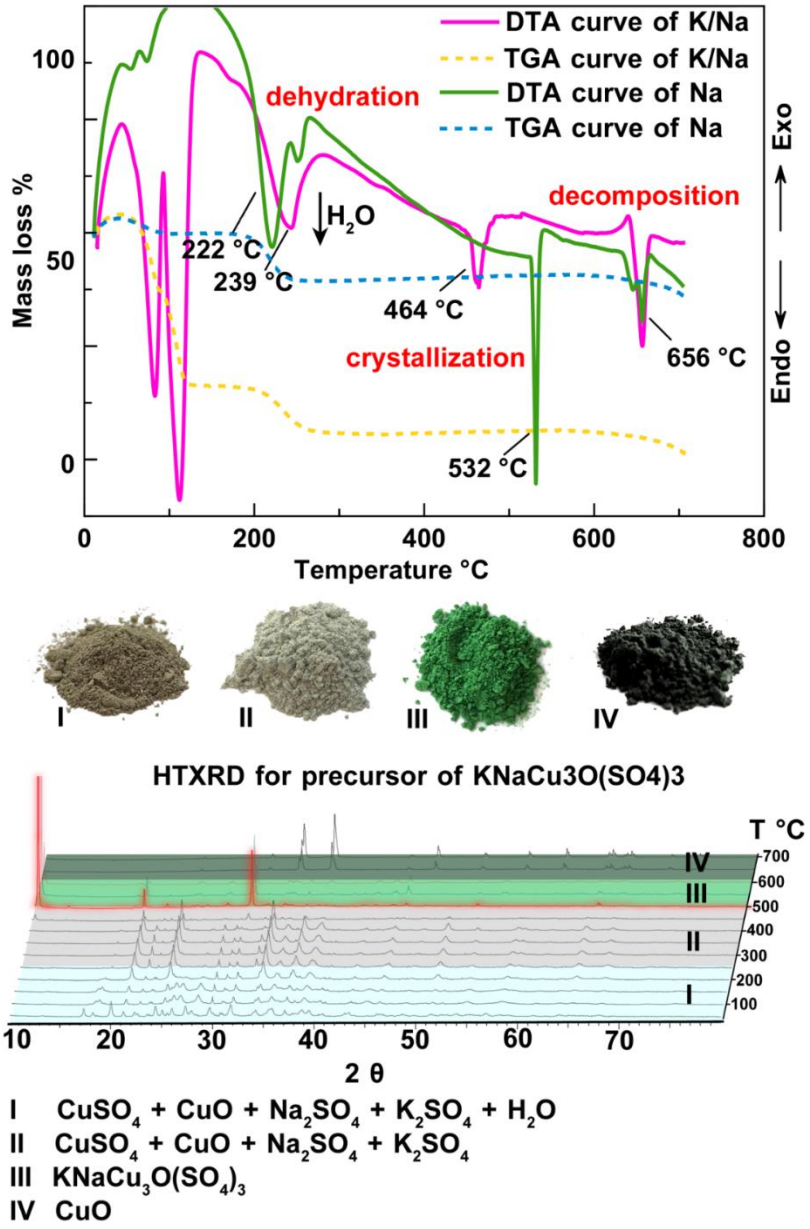

Figure 30. TGA and DTA curves for a mixture of Na_2SO_4, K_2SO_4, $CuSO_4$ and CuO (a) and photographs showing the color change from gray to black during heating (b). High-temperature X-ray diffraction for a mixture of reagents Na_2SO_4, K_2SO_4, $CuSO_4$ and CuO at 10-80º 2Θ in the temperature range 25-700 ° C, the XRD pattern of the $NaKCu_3O(SO_4)_3$ is highlighted in red. Numbers indicate the zones of existence of the advising phases: I - dark gray mixture of Na_2SO_4, K_2SO_4, $CuSO_4$, CuO + absorption H_2O; II - anhydrous mixture of light gray Na_2SO_4, K_2SO_4, $CuSO_4$, CuO; III crystallized green phase $NaKCu_3O(SO_4)_3$; IV - decomposition product of black color - synthetic tenorite, CuO.

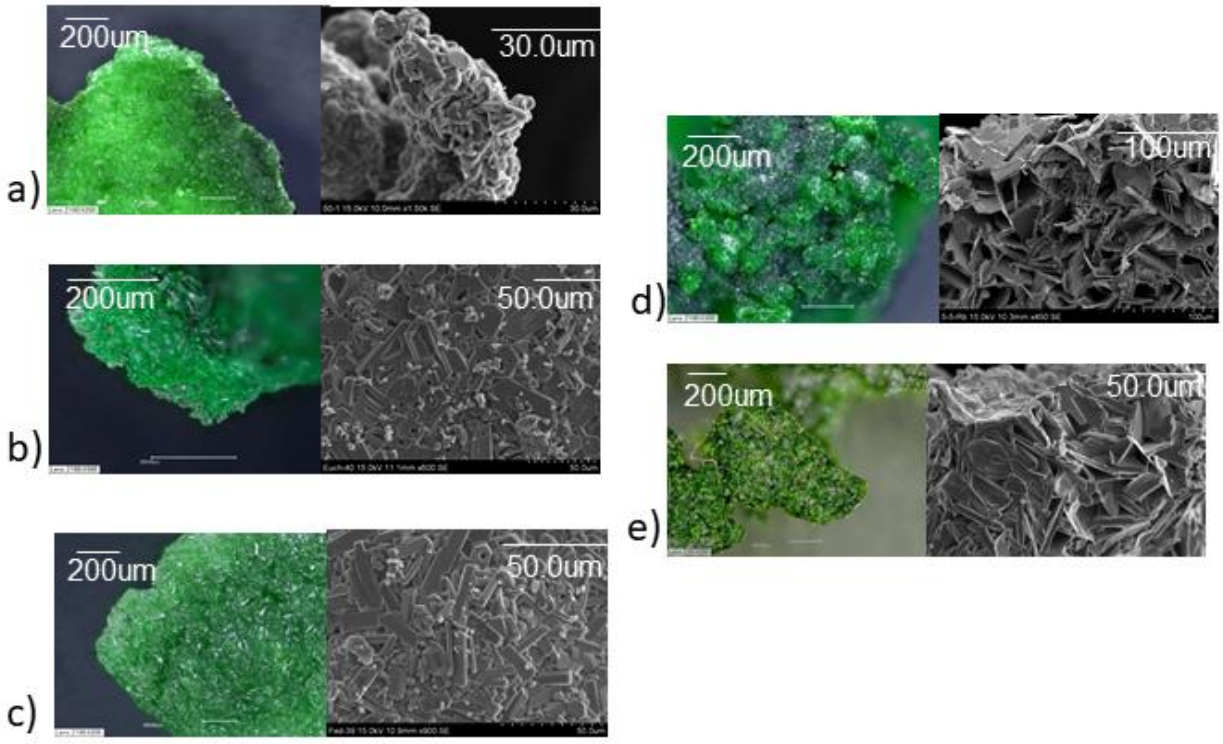

Figure 31. The photo of crystals from an optical electron microscope and SEM of $Na_2Cu_3O(SO_4)_3$ (a), $KNaCu_3O(SO_4)_3$ (b), $K_2Cu_3O(SO_4)_3$ (c), $Rb_2Cu_{3.07}O_{1.07}(SO_4)_3$ (d) and $Cs_2Cu_{3.5}O_{1.5}(SO_4)_3$ (e)

Table 9. Temperature crystallization of $A_2Cu_3O(SO_4)_3$ (A = Na, K), $Rb_2Cu_{3.07}O_{1.07}(SO_4)_3$, $Cs_2Cu_{3.5}O_{1.5}(SO_4)_3$.

Compound	Ratio $A_2(SO_4)$ (A = Na, K, Rb, Cs), $CuSO_4$ and CuO	Crystallization temperature
$Na_2Cu_3O(SO_4)_3$	1:2:1	from 533 to 658 °C
$NaKCu_3O(SO_4)_3$	1:2:1	from 464 °C to 656 °C
$K_2Cu_3O(SO_4)_3$	1:2:1	from 532 °C to 664 °C
$Rb_2Cu_{3.07}O_{0.07}(SO_4)_3$	1:2:1	from 464 °C to 685 °C
$Cs_2Cu_{3.5}O_{1.5}(SO_4)_3$	1:2:1 (x=0) 1:2:1.25 (x=0.25) 1:2:1.5(x=0.5) 1:2:1.75(x=0.75) 1:2:2(x=1) 1:2:2.25 (x=1.25)	from 551 °C to 691 °C

6.3 Single-crystal and powder X-ray analysis

6.3.1 Twinning, a problem to overcome in these series

Single-crystal X-ray analysis sometimes can be complicated due to the presence twinned crystals. Typically, in some of the samples investigated here, the synthetic compounds have very small size and it is hard to select untwinned specimen, because crystals are composed of several twin domains. All of the crystal structures expected of Na-phase were collected and refined from twinned samples. The problem is complicated by the fact of the presence of non-merohedral twinning (i.e. non-superposition of the R* lattices of the multi-components) often leading to low quality R values, ill-defined thermal parameters, etc. . For establish the unit cells for twinned or split crystals, their orientation matrices and the twin laws were used program Cell_Now able to separate in the real space multiple domains and their orientation matrices. In the K, Na/K and Rb compounds, the twin law used to improve the structure was (-1 0 -1) (0 -1 0) (0 0 1).

Main crystallographic information for the synthetic phases is summarized in **Table 11**. Atom coordinates, thermal displacement parameters and selected interatomic distances for all crystal structures are provided in **(Table S12, S14, S16).**

6.3.2 Validation of the single-phase materials

High quality diffraction patterns were collected in the 2θ range of 8° and 110° by steps of 3.0 s/0.02°. Results are shown in **Figure 36** and validate the preparation of single-phase materials. Pure polycrystalline samples were obtained after refinement of the crystal structures and using corrected stoichiometry 1:2:1 for $A_2(SO_4)$ (*A* = Na, K, Rb, Cs), $CuSO_4$ and CuO.

The main problem was to find good conditions to synthesize pure phase ~1 gr mass (for DTA-TGA, IR analysis and magnetic properties). After several syntheses, it was noticed that the synthesis at stoichiometry does not give a pure phase, while if we add more copper oxide, we have a pure powder. This fact was proved by a series of syntheses for the cesium phase, where each time was increase the amount of CuO. We prepared the $Cs_2Cu_{3+x}O_{1+x}(SO_4)_3$ (x = 0, 0.25, 0.5, 0.75, 1, 1.25) series. XRD patterns, refined parameters are given in **Table 10** and (**Figure 32**).

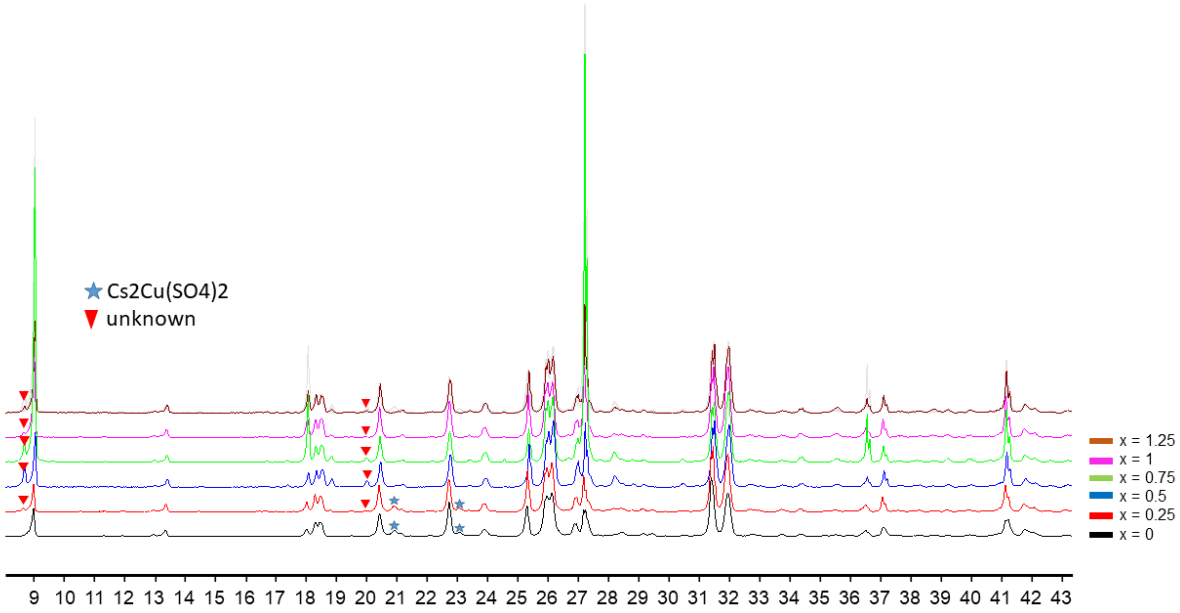

Figure 32. Black pattern correspond to x=0 $Cs_2Cu_3O(SO_4)_3$, red pattern - x= 0.25 $Cs_2Cu_{3.25}O_{1.25}(SO_4)_3$, blue - x = 0.5 $Cs_2Cu_{3.5}O_{1.5}(SO_4)_3$, green - x = 0.75 $Cs_2Cu_{3.75}O_{1.75}(SO_4)_3$, purple - x = 1 $Cs_2Cu_4O_2(SO_4)_3$ and brown - x = 1.25 $Cs_2Cu_{4.25}O_{2.25}(SO_4)_3$.

Table 10. The unit cell parameters for phase $Cs_2Cu_3O(CuO)_x(SO_4)_3$ (x = 0, 0.25, 0.5, 0.75, 1, 1.25) refined in JANA2006.

	a, Å	***b,*** Å	***c,*** Å	***β,*°**	***V,*** Å^3
CIF $Cs_2Cu_{3.5}O_{1.5}(SO_4)_3$	20.8687(16)	9.6967(7)	14.0548(11)	109.484(4)	2681.2(4)
x=0	20.8215	9.6702	14.0528	109.447	2668.1
x=0.25	20.8430	9.6807	14.0437	109.459	2671.8
x=0.5	20.8474	9.6864	14.0472	109.465	2674.5
x=0.75	20.8527	9.6844	14.0414	109.412	2674.4
x=1	20.8498	9.6891	14.0445	109.441	2675.5
x=1.25	20.8433	9.6876	14.0445	109.441	2674.2

The amount of CuO was increased each new synthesis. if we consider in more detail the diffractogram x = 0 and x= 0.25 we will see solid solution between two phases:

$Cs_2Cu_3O(SO_4)_3$ = **0.8** $Cs_2Cu_{3.5}O_{1.5}(SO_4)_3$ + **0.2** $Cs_2Cu(SO_4)_2^{i}$ + 0.2 SO_3

This equation means that we cannot get a pure phase of $Cs_2Cu_3O(SO_4)_3$, all the times we have impurity in the form of $Cs_2Cu(SO_4)_2$ and unknown phase - X-phase. And in fact, XRD data and refinement in JANA2006 of x = 0 and x = 0.25 patters show the presence of $Cs_2Cu(SO_4)_2$ (**Figure 33**) and (**Figure 34**).

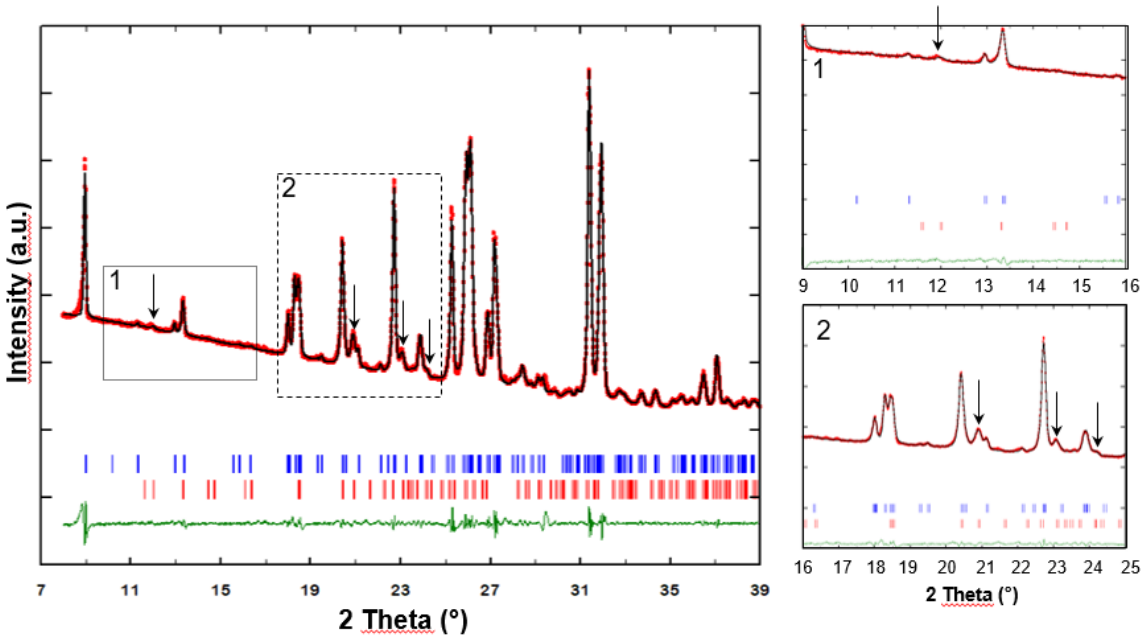

Figure 33. Profile-matching refinement for $Cs_2Cu_3O(SO_4)_3$ (x=0), where the experimental (red) and calculated (black) patterns are superimposed; the difference curve and Bragg positions are respectively represented in blue $Cs_2Cu_{3.5}O_{1.5}(SO_4)_3$ and red $Cs_2Cu(SO_4)_2$

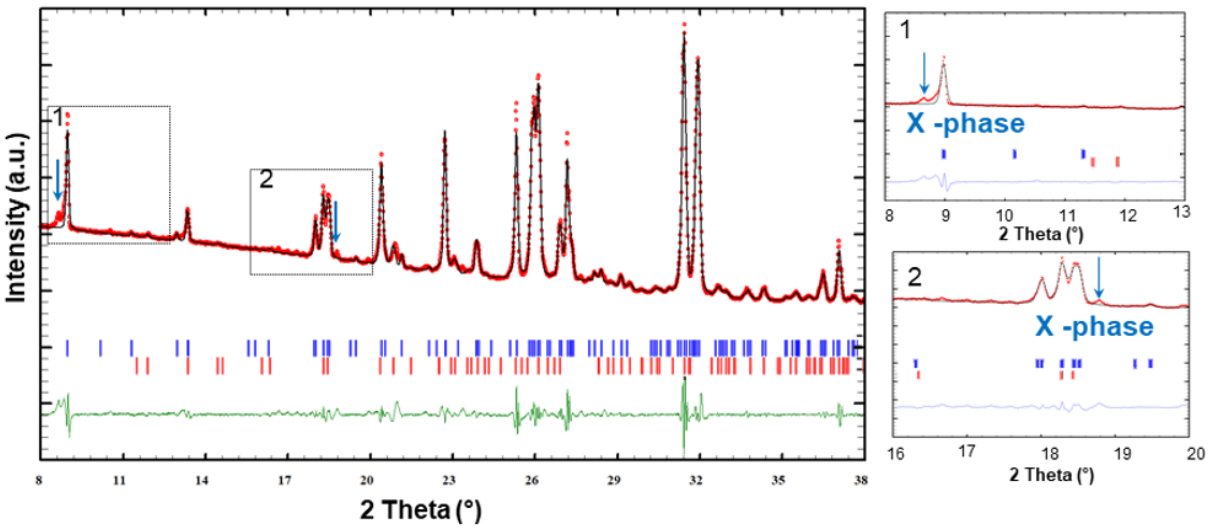

Figure 34. Profile-matching refinement for $Cs_2Cu_3O(SO_4)_3$ (x=0.25), where the experimental (red) and calculated (black) patterns are superimposed; the difference curve and Bragg positions are respectively represented in blue $Cs_2Cu_{3.5}O_{1.5}(SO_4)_3$ and red $Cs_2Cu(SO_4)_2$

In the case of others diffractogram we also have impurities unknown peaks. It is worth pointing out that the most cloth UC parameters for x = 1 - $Cs_2Cu_4O_2(SO_4)_3$. But the purest phase is x = 0 (**Figure 33**). At any rate, we know exactly what kind of impurity we have, which means we can take this fact into account and "subtract" it from the magnetic analysis data.

Consequently, the ratio was change from 1:2:1 to 1:2:2. The excess of CuO can be explained by the fact that a part is not reacting and may segregate in another part of the sample. The main conclusion is that we never managed to obtain an ideally 100%- pure phase, but in the case of cesium, we will further show that this impurity can be taken into account in magnetic analysis, and as for other unidentified phases, we can neglect them, they constitute less than 2%.

Moreover we know that $CuSO_4$ not stable and decompose at ~650 °C in air (**Figure 35**) (Nandi et al., 1979). We cannot create ideal synthesis conditions in the laboratory to take into account the hydroscopicity of sulfates or control their decomposition at high temperatures. The products of decompositions shows at **Figure 30**. The profile matching patterns for all compounds (**Figure 36**) were obtained using the experimental cells.

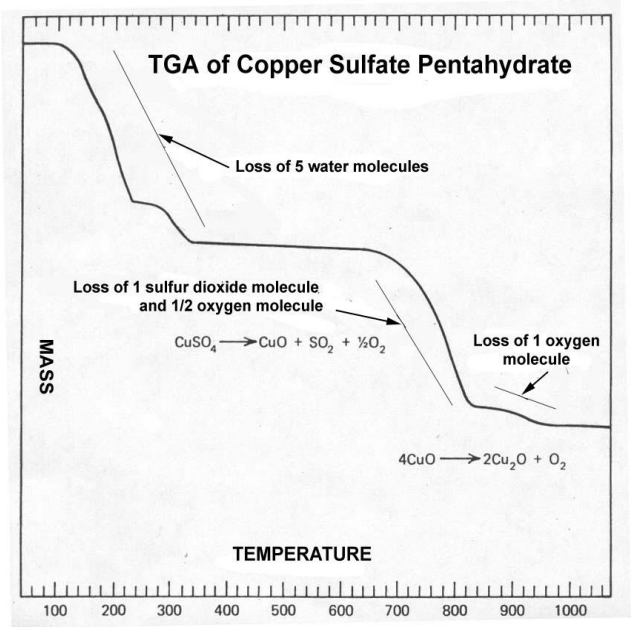

Figure 35. The TGA curve of $CuSO_4\,5H_2O$ (Nandi et al., 1979).

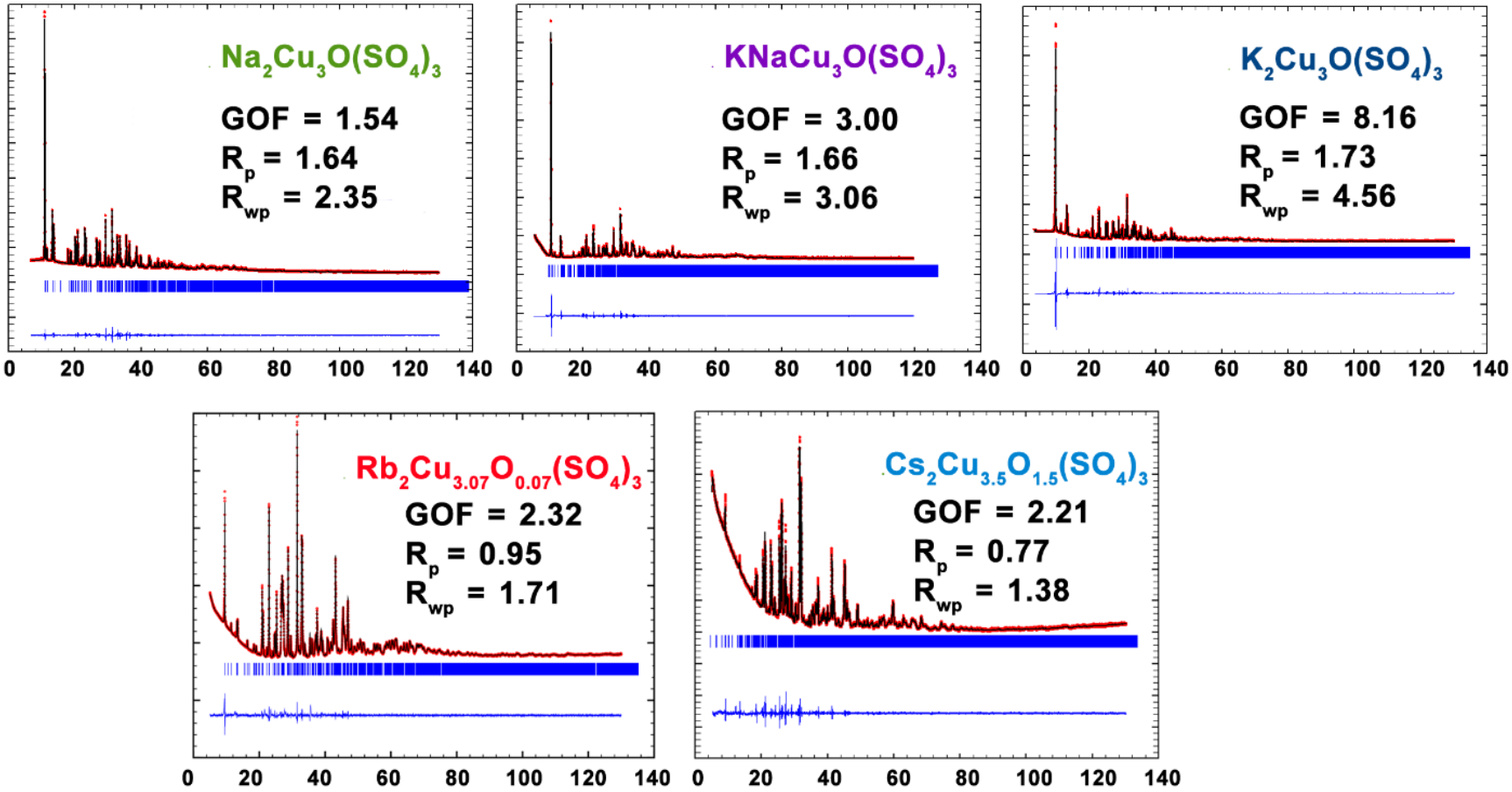

Figure 36. The powder XRD Rietveld refinement for $A_2Cu_3O(SO_4)_3$ and $Rb_2Cu_{3.07}O_{1.07}(SO_4)_3$, $Cs_2Cu_{3.5}O_{1.5}(SO_4)_3$: the experimental (red) and calculated (black) patterns are superimposed; the difference curve and Bragg positions are respectively represented in blue.

Table 11. Single crystal and structure refinement data for synthetic $(Na,K)_2CuO(SO_4)_3$ series and $Rb_2Cu_{3.07}O_{1.07}(SO_4)_3$

Crystal data	Na	K/Na	K	Rb
sp. gr.	*C*2/*c*	*C*2/*c*	*C*2/*c*	*C*2/*c*
a [Å]	17.3097(9)	18.575(11)	19.117(12)	19.820(3)
b [Å]	9.3982(5)	9.399(4)	9.535(6)	9.5757(12)
c [Å]	14.3982(7)	14.370(10)	14.235(9)	14.1374(15)
β [°]	111.9360(10)	113.97(6)	110.68(3)	110.193(7)
V [Å^3]	2172.72(19)	2293(3)	2428(3)	2518.3(5)
Z	8	8	8	8
ρ_{calc} [Mg/m^3]	3.30	3.23	3.14	3.54
μ [mm^{-1}]	6.55	6.534	6.478	13.382
Data collection				
F(000)	2088	2152	2216	2525
θ range [°]	2.5 – 28.8	2.3 – 24.9	1.5 – 23.8	1.5 – 28.0
hkl limits	–23 → 23 –12 → 12 –19 → 19	–20 → 21 –10 → 11 –16 → 16	–19 → 21 –9 → 10 –16 → 13	–26 → 26 –12 → 12 –18 → 18
total refln.	13044	8374	4651	12395
Unique refln*.	2837	1946	1795	3041
(R_{int})	0.06	0.14	0.06	0.07
*unique refln.criteria $F > 4\sigma F$				
Refinement				
R_1 [$F > 4\sigma F$],	0.03	0.06	0.05	0.04
wR_2 [$F > 4\sigma F$]	0.07	0.15	0.12	0.08
R_1 all,	0.05	0.12	0.10	0.08
wR2 all	0.08	0.19	0.15	0.09
GoF	1.00	1.03	0.98	1.01
$\Delta\rho_{max}$,	0.90	1.96	1.41	1.41
$\Delta\rho_{min}$ [e·Å^{-3}]	– 0.77	-1.44	–0.86	-1.08

6.3.3 Description of the crystal structures for synthetic $(Na,K)_2CuO(SO_4)_3$ series

The structural data for the synthetic phases correspond to the data reported for natural puninite $Na_2Cu_3O(SO_4)_3$ (Siidra et al., 2017), euchlorine $KNaCu_3O(SO_4)_3$ (Scordari and Stasi 1990) and fedotovite $K_2Cu_3O(SO_4)_3$ (Vergasovaet al., 1988).

Cationic preference: The *A* sites include the main differences between minerals and synthetic compounds.

- As for puninite structure the *A* sites are occupied exclusively by Na cations, with the minor amount of K is in *A*(1).

- The *A* sites in the mineral euchlorine $KNaCu_3O(SO_4)_3$ have solid solution between Na and K (Siidra et al., 2017): *A*(2) site is occupied exclusively by K while *A*(1) is occupied by Na (0.80) and K (0.20) simultaneously.

- In the crystal structure of fedotovite $K_2Cu_3O(SO_4)_3$ the dominant *A* belongs to potassium and minority belongs to sodium with $(K_{1.65}Na_{0.28})$ Σ=1.93.

There is no solid-solution in synthetic phases: *A* sites are occupied only Na for $Na_2Cu_3O(SO_4)_3$, only K for $K_2Cu_3O(SO_4)_3$ and only by Na and K in ration *A*(1):*A*(2) equal to 1:1 for $KNaCu_3O(SO_4)_3$. All distances of alkali cations with oxygens correspond to the minerals puninite, euchlorine and fedotovite.

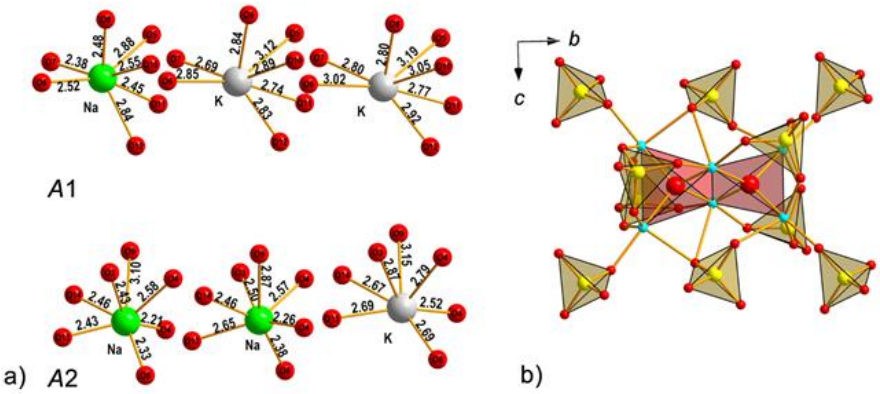

Figure 37. Coordination of alkali *A*1 sites in the structure of $A_2Cu_3O(SO_4)_3$ (*A* = Na, K) (up) and *A*2 (down) (a); the O-centred OCu_4 tetrahedra share a common edge thus forming $[O_2Cu_6]^{8+}$ dimers and OCu_4 chains surrounded by SO_4 tetrahedra (b)

In the crystal structures of Na-, K-, K/Na- -analogues there are three symmetrically independent Cu sites with different coordination environments (**Table 12S**). The Cu(1) site forms four short Cu-O bonds producing CuO4 square pyramids (**Figure 38**). The Cu(2) and Cu(3) sites have a distorted square pyramidal (4+1) coordination environment. All respect the strong Jahn-teller distortion active around the Cu^{2+} (d^9) ions. There are three symmetrically independent sulphate sites in the $A_2Cu_3O(SO_4)_3$ (A = Na, K). The S^{6+} cations have typical $(SO_4)^{2-}$ tetrahedral coordination with standard distances about 1.47Å.

Using an alternative model, the crystal structures can also be described in terms of oxo-centered OCu_4 polyhedral (Krivovichev, Mentre, et al., 2013). The O(1) and O(2) atoms are tetrahedrally coordinated by four Cu cations with formation $[O_2Cu_6]^{8+}$ dimers (Cu^{2+} hexamers) in the $A_2Cu_3O(SO_4)_3$ (A = Na, K) (**Figure 38**). This hexamer unit are connected in chains along the crystallographic *b* direction. In the bc plane they form layers (while isolated by sulfate groups), as shown **Figure 38** .We will investigate how these 6xS=1/2 units form clusters with a nominal S=1 macro-spin, and their

interactions in pseudo Haldane chains (**Figure 38**) (Fujihala *et al.*, 2018). Alkali atoms are in the interlayer, leaving inter layer distances of 7.7 Å.

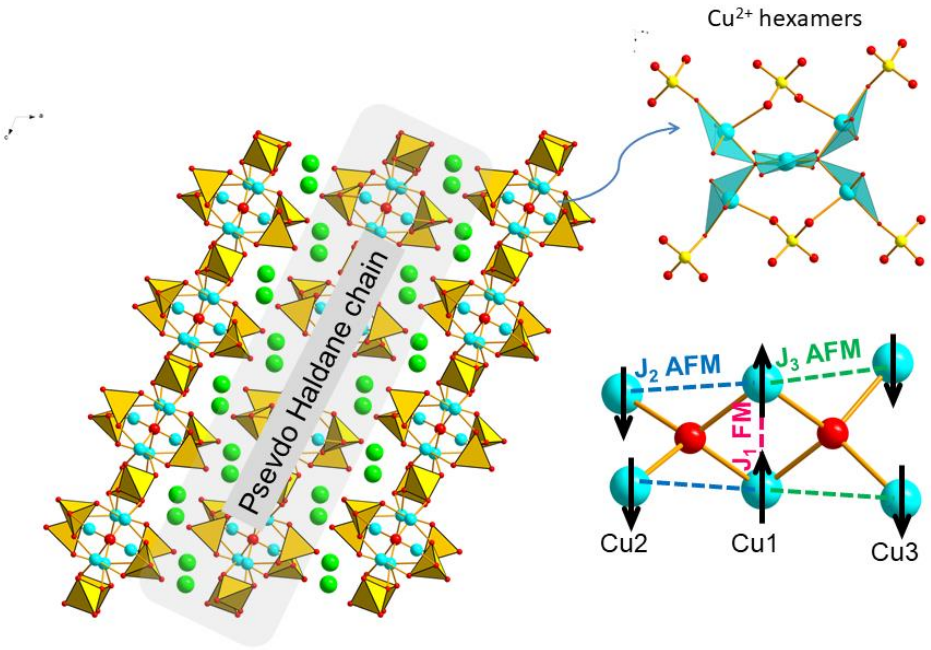

Figure 38. General projections of the crystal structure of $A_2Cu_3O(SO_4)_3$ (*A* = Na, K) and figures of the Cu^{2+} hexamers (SO_4 = yellow, Cu = blue and dark blue, O = red and pink, Na = green, Cs = purple) along the b axis.

6.3.4 Description of the crystal structures of $Rb_2Cu_{3.07}O_{1.07}(SO_4)_3$

After isolating single crystal out of the Rb-preparation, the structure refinement using the parent model (*A* = Na, K; monoclinic, *C2/c*) returns R_1 = 4.11%. However, Cu and O over-stoichiometry was detected by significant residual electronic peak on extra positions (leaving 7% of interstitial CuO) in the empty sites separating the original Cu_6 hexamers, see **Figure 42b**. Three new atoms were introduced into the model one Cu^{2+} and 2 O^{2-}. After the refinement of these atoms, it was found that they are low occupied with s.o.f. 0.07 for Cu^{2+} and 0.035 for O^{2-}. The final $Rb_2Cu_{3.07}O_{1.07}(SO_4)_3$ stoichiometry was systematically refined on several crystals. The CuO over-stoichiometry implies locally, the junction of two separated Cu_6 hexamers into Cu_{14} tetradecameric ones in a random manner. The full occupation of Cu^{2+} interstitials require severe local re-organization of the sulfate groups better understood in the following well-ordered *A* = Cs. Rb phase crystalize in monoclinic symmetry with space group *C*2/*c* with unit cell parameters: a = 19.820(3) Å, b = 9.5757(12) Å, c = 14.1374(15) Å, β = 110.193(7), V = 2518.3(5) $Å^3$ (**Figure 39**).

It leads in the crystal structures of the Rb–phase to four symmetrically independent Cu sites with square pyramidal coordination. In the case of rubidium, one additional position of copper appears in the crystal structure with Cu(4) site s.o.f. 0.07, as we mentioned before. In general, the crystal structure has the same arrangement of atoms with the exception of additional copper and oxygen groups. *A1 and A2* sites are occupied only by Rb. Finally, the refined model pictures a disorder between the hexameric units of the A/K samples, and a longer one. This latter probably requests strong rearrangement locally, but at this stage it is difficult to go further. However, the following Cs-study will give us all necessary information about the possibility to create longer units and their local structures.

6.3.5 Description of the crystal structures of $Cs_2Cu_{3.5}O_{1.5}(SO_4)_3$

The refinement of the crystal structure has shown similar features as in the Rb case dealing with extra Cu and O but in greater expense, returning the refined $Cs_2Cu_{3.5}O_{1.5}(SO_4)_3$ formula.

It was refined 2 models: the first one was the same like for Rb, but with s.o.f. 0.5 for Cu^{2+} and 0.25 for each O^{2-} with unit cell parameters: *C*2/*c*, *a* = 21.0412(1), *b* = 9.7311(3), *c* = 14.2009(1), Å β = 109.201(7)°, *V* = 2658.58(22) Å^3. And second one with the super cell: *P*2/*a*, *a* = 20.874(5), *b* = 19.406(4), *c* = 14.042(3), Å β = 109.577(12)°, *V* = 5359(2) Å^3. We also found evidences of extra atoms like in the Cs-case, and the first one was the same as for Rb, but with s.o.f. 0.5 for Cu^{2+} and 0.25 for each O^{2-} with unit cell parameters: *C*2/*c*, *a* = 21.0412(1), *b* = 9.7311(3), *c* = 14.2009(1), Å β = 109.201(7)°, *V* = 2658.58(22) Å^3. In this subcell the resulting structure is disordered similarly to the Rb-case and *in fine*, it became clear that it was impossible to refine a proper structure, highlighted for instance by abnormally distorted SO_4 groups. Moreover, some oxygen atoms had high thermal displacement parameters and, as a consequence, a high R_1 factor (R_1 = 7.6%).

6.3.6 The supercell ordering for A=Cs: The supercell ordering for A=Cs

In a second stage, we used the space group and the super cell: *P*2/*a*, *a* = 20.874(5), *b* = 19.406(4), *c* = 14.042(3), Å β = 109.577(12)°, *V* = 5359(2) Å^3. In our opinion, the more correct model turned out to be with a supercell. After checking the precession images in *hk1* we found evidences of weak extra peaks of two kinds i) In the basic cell, some reflexions are breaking the C-centering adopted for other members of the series (**Figure 39**), the ii) Others are doubling the b-cell parameter. Finally, intensities were re-integrated using the supercell refined with the following parameters: *a* = 20.874(5), *b* = 19.406(4), *c* = 14.042(3), Å *β* = 109.577(12)°, *V* = 5359(2) Å^3. This cell is to compared to the one for Na: is *C*2/*c*, *a* = 17.3097(9), *b* = 9.3982(5), *c* = 14.3982(7), Å β = 111.936(1)°, *V* = 2172.72(19) Å^3. The extinctions have been scrupulously examined on the built-precession frames which suggest only the a-glide perpendicular to *b* as active. The space groups *P*2/a, *P*2, *Pa* and others sometimes in contradiction

with the extinctions have been tested where only the *P*2/*a* space group offered an acceptable fully ordered solution. In the best model (R_1= 7.6 %), we used restraints on thermal parameters and O-O distances within one of the 12 independent sulfate groups. We also used different possibilities offered in the *C*-centered pseudo-orthorhombic cell built from the super cell by the matrix (001) (201) (010) leading to the unit cell 14.0436(2), *b*=39.341(8), *c*=19.405(5), α,β,γ =90° after refinement. All solutions in this space group leads to disordered solutions (best model in $C222_1$).

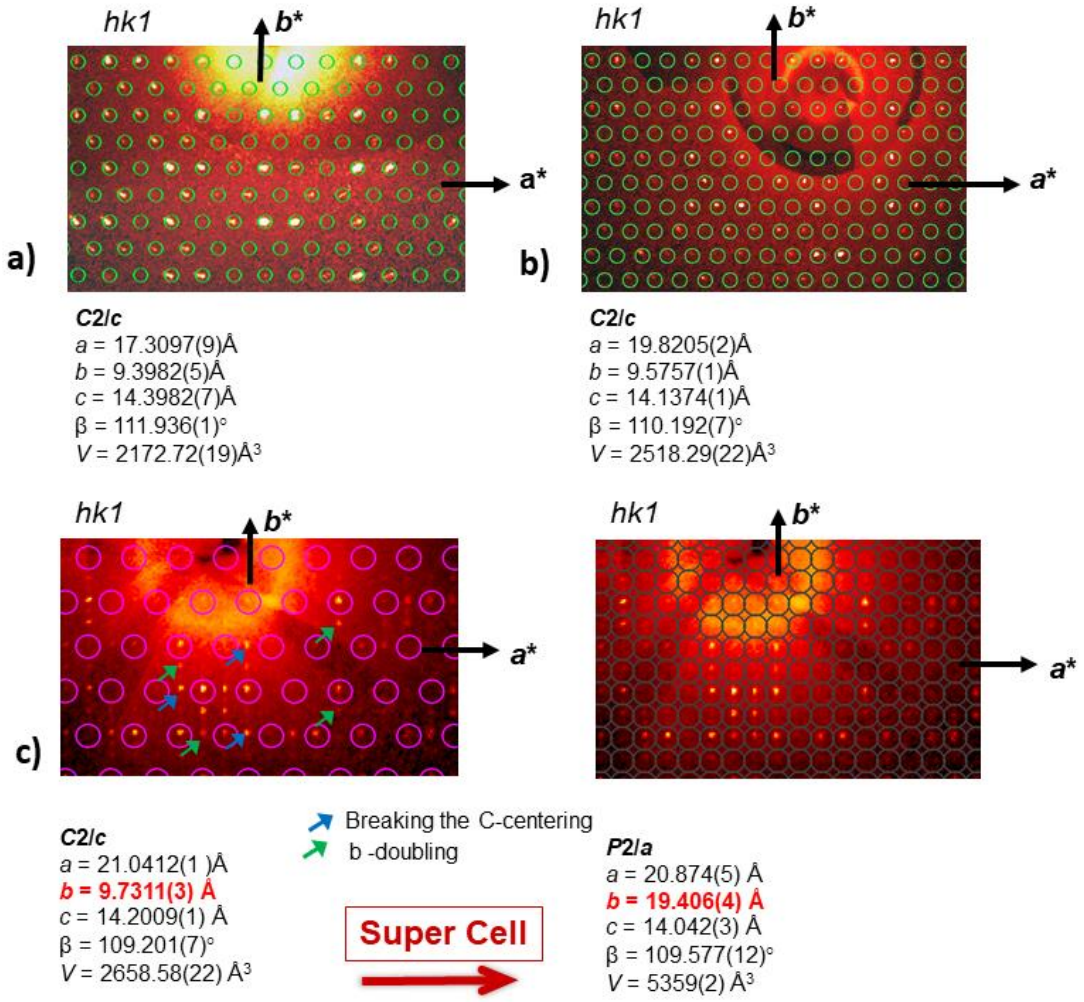

Figure 39. The precession images for $Na_2Cu_3O(SO_4)_3$(a), $Rb_2Cu_{3.07}O_{1.07}(SO_4)_3$ (b) and $Cs_2Cu_{3.5}O_{1.5}(SO_4)_3$(c).

6.3.7 Description of the crystal structure of $Cs_2Cu_{3.5}O_{1.5}(SO_4)_3$ (P2/a space group)

In the crystal structures of $Cs_2Cu_{3.5}O_{1.5}(SO_4)_3$ there are 14 Cu sites with full occupancies. All Cu cations have a distorted square pyramidal coordination (4+1) or octahedral (4+2) environments. Dealing

with a crystal structure including 94 atoms (335 refined parameters) the solution is far from perfect, and the following details are given after optimizing the refined model by DFT using ionic relaxation, giving a very close model with more realistic polyhedral in the problematic cases. The average distance Cu-O 1.94 Å for square-planes and 2.5-2.8 Å for apical atoms. Cu atoms form $[O_6Cu_{14}]^{16+}$ clusters (= tetradecamers) in which the 10 central ones share edges by pairs, and corners between the dimers. The four end-Cu^{2+} ions share corners with only by pairs and with the central unit, see **Figure 40**. Finally, it look like an extension of the Cu_6 units in the Na/K compounds.

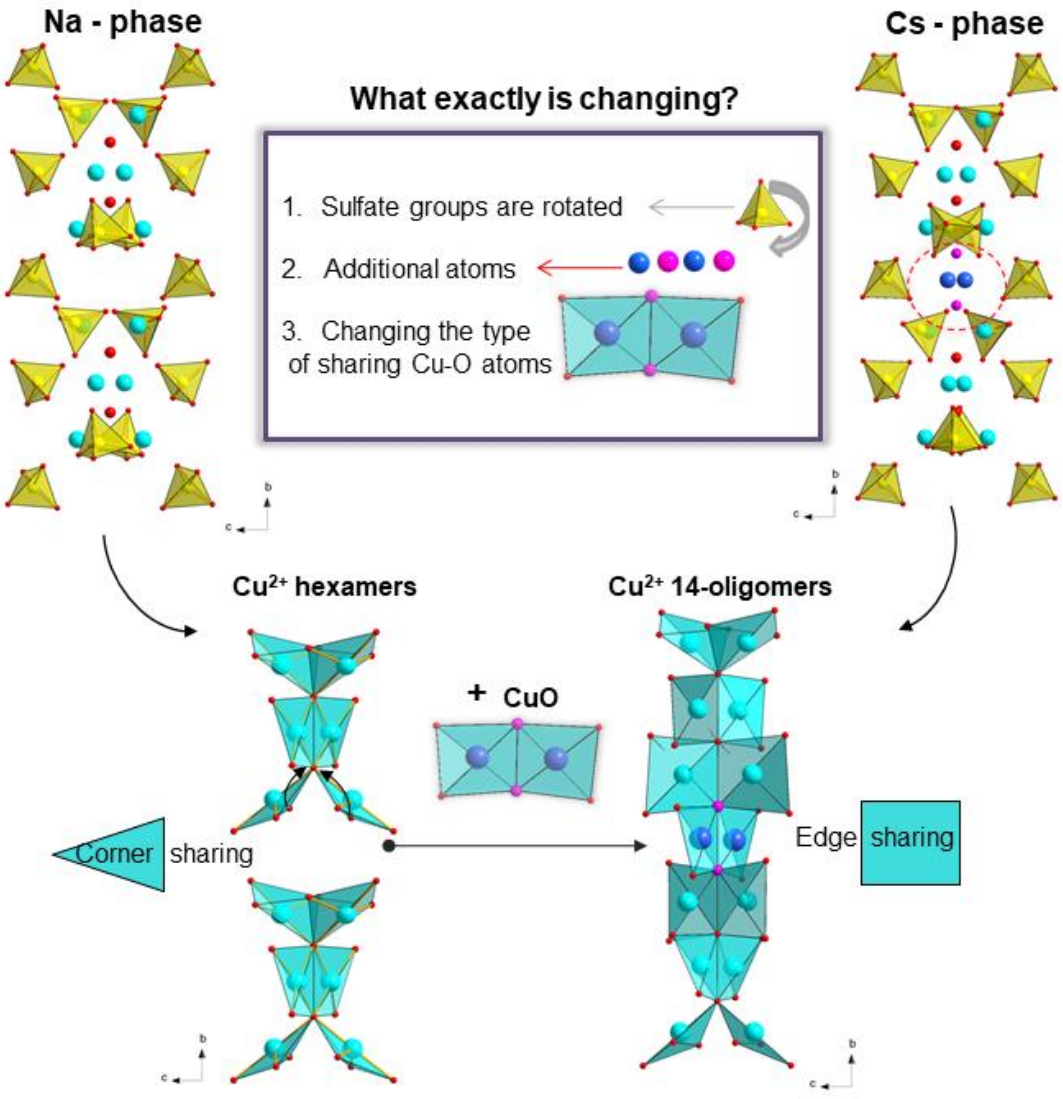

Figure 40. The picture of differences between $Na_2Cu_3O(SO_4)_3$ and $Cs_2Cu_{3.5}O_{1.5}(SO_4)_3$ phases.

The clusters are linked by sulfate groups along chains (see **Figure 41**) themselves arranged within layers, reminiscent of the parent phases.. Some of sulphates groups are rotated (**Figure 40**) .

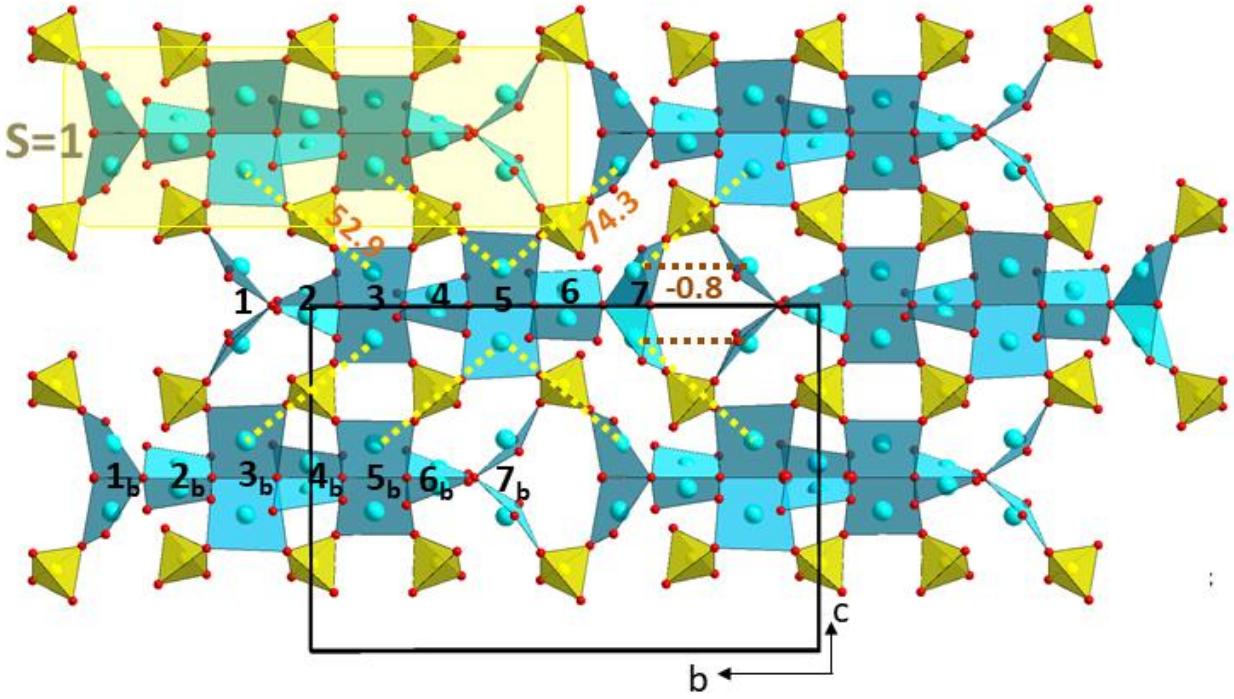

Figure 41. General picture of $[O_6Cu_{14}]^{16+}$ clusters (= tetradecamers) surrounded by sulfate groups. Yellow dash lines show the main intra- and inter-Cu14 exchanges between the **a** and **b** satellite positions.

And thus we can see, the changes in the crystal structure is performed by incorporation of additional CuO units and local rearrangement. In terms of crystallographic principles one can write the topotactic equation $A_2Cu_3O_1(SO_4)_3$ + x CuO → $A_2Cu_{3+x}O_{1+x}(SO_4)_3$, x = 0.07 for *A*=Rb, x=0.5 for *A*=Cs.

If we consider how the crystal structures change in terms of architecture between anion-centered tetrahedra, one can see that additional anion-centered copper dimers are inserted randomly between the dimers (with a *s.o.f* of only 7% for the rubidium phase) (**Figure 42**). In the case of cesium, ongoing to the supercell (to make all copper positions fully occupied), we can observe the formation of a cluster consisting of 14 copper atoms arranged between them in-plane as shown on the **Figure 42**. Our formula is $Cs_2Cu_{3.5}O_{1.5}(SO_4)_3$.

6.4 Preparation of the polycrystalline samples

We already explained earlier that Na and K compounds were prepared using an excess of $CuSO_4$ reagent (x=1). The preparation of $Cs_2Cu_{3.5}O_{1.5}(SO_4)_3$ was achieved as a single phase with difficulties between the Cs:Cu ratio. We have also attempted to synthesize the $Cs_2Cu_4O_2(SO_4)_3$ phase, with full

chain, but our attempts were unsuccessful. Possibly due to the distance between Cs-O what are maximum is 3.8 Å, if we want incorporate one more dimer we need more space between 14-oligomers, but we do not have it. We could not achieve more long distains, the structure is controlled by Cs atoms (**Figure 43**). Between tetradecamers the distain is 4.39 Å, while the size of dimer is equal 5.12 Å. Such a structural rearrangement with the incorporation of additional clusters among sulfates was not previously observed.

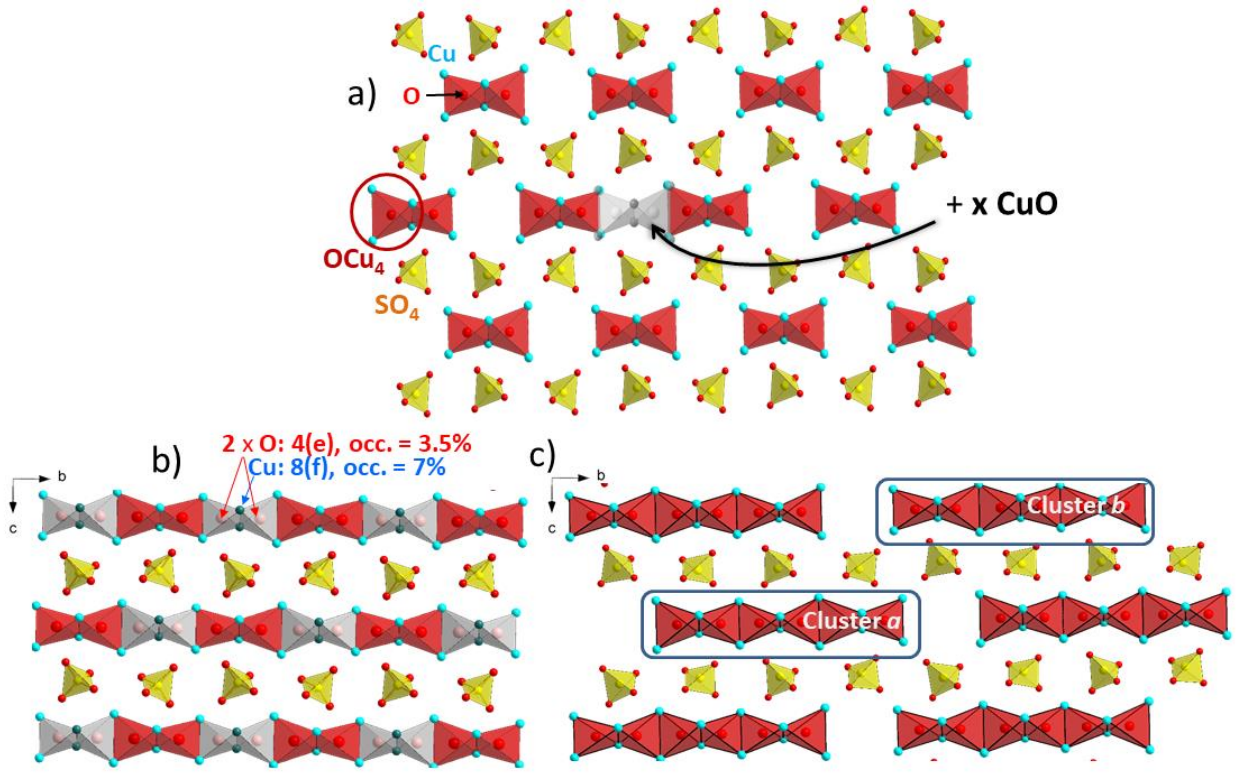

Figure 42. The picture of evolution changing of a) $A_2Cu_3O(SO_4)_3$ (A = Na, K), b) $Rb_2Cu_{3.07}O_{1.07}(SO_4)_3$ and c) $Cs_2Cu_{3.5}O_{1.5}(SO_4)_3$.

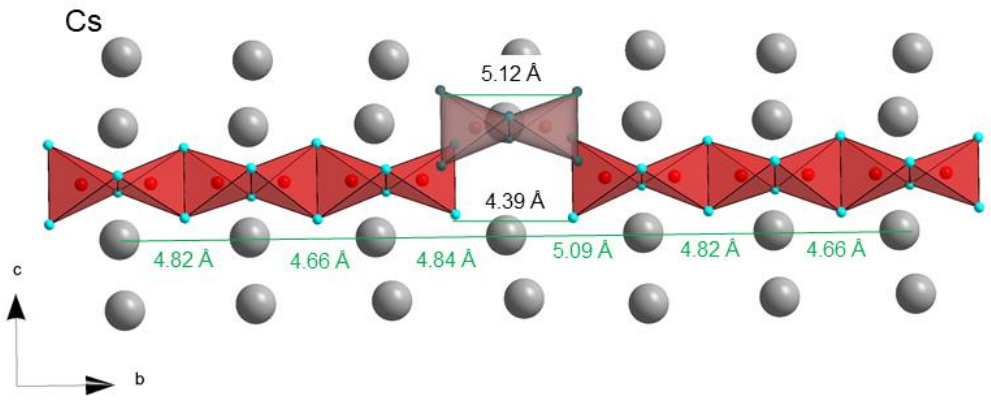

Figure 43. The picture of copper tetradecamers in $Cs_2Cu_{3.5}O_{1.5}(SO_4)_3$.

6.5 DTA and TGA analysis for $Na_2Cu_3O(SO_4)_3$

In DTA curves the first endothermic peak 406 °C is attributed to the first step of decomposition into CuO and then with peak 673 °C is referent to the structure collapsing, loss of sulfates base and transformation into CuO that corresponds with the high temperature powder X-ray analysis. The peak 572 °C may be related into the first step of decomposition (**Figure 44**).

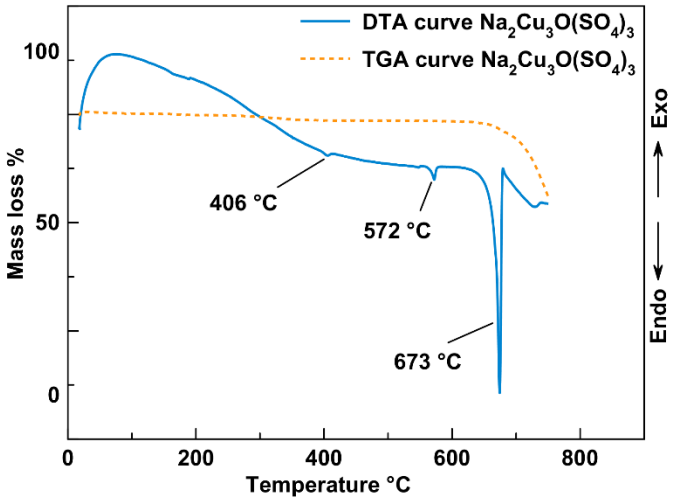

Figure 44. TGA-DTA curves for $Na_2Cu_3O(SO_4)_3$ from 25°C to 800°C.

6.6 High-Temperature X-ray Diffraction analysis of $Na_2Cu3O(SO_4)_3$

It is of interest to look at the thermal behavior of $Na_2Cu3O(SO_4)_3$ from the viewpoint of its temperature stability and mineralization from volcanic gases. The temperatures of the phase transformations found from HTXRD data suggest with data determined by DTA and TGA study (**Figure 30**). The experiment demonstrates that the synthetic mineral of puninite starts to decompose at about 400 °C forming CuO (**Figure 45**). In general, the pattern does not undergo significant changes. The temperature dependence of the cell parameters of $Na_2Cu_3O(SO_4)_3$ can be described by the following functions to prove that there is no transitiuons in the course (**Figure 45**):

a_t=17,3234(21)+ 0,515(14) × 10^{-3}T + 0,186(21)× $10^{-6}T^2$

b_t=9,41449(34) + 0,1328(24) × 10^{-3}T + 0,0456(35) × $10^{-6}T^2$

c_t= 14,4277(11) + 0,0653(29) × 10^{-3}T

β_t= 111,909(14) + 0,805(10) × 10^{-3}T- 0,36(15)× $10^{-6}T^2$

V_t= 2179,99(49) + 120(1)× 10^{-3}T

The strongest expansion of $Na_2Cu_3O(SO_4)_3$is observed in the direction of α11 axis. This thermal behavior can be explained on the basis of the considerations of the respective rigidity of structural units $Na_2Cu_3O(SO_4)_3$. SO_4 tetrahedra and CuO_n polyhedra are strong and solid.

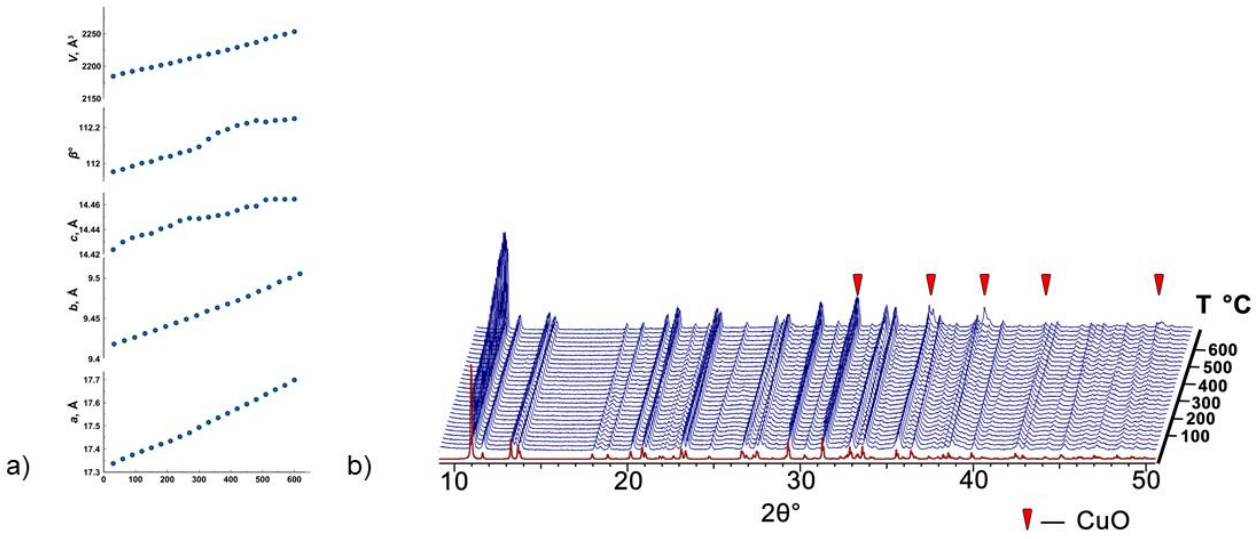

Figure 45. a) dependence of the cell parameters from temperature b) diffractogram for $Na_2Cu_3O(SO_4)_3$ over 8-50º 2Θ with increasing temperature.

Table 12. Values ($\times 10^{-6}$ °C^{-1}) of the principal eigenvalues of thermal expansion tensor of unit cell of $Na_2Cu_3O(SO_4)_3$ at different temperatures (T°C).

T°	α11	α22	α33	μ1a	μ2b	μ3c	αa	αb	αc	αβ	αV
0	29,9	14,1	1,4	5,1	0	27,0	29,72(83)	14,10(25)	7,31(56)	7,20(89)	45(1)
100	31,8	15,0	1,2	2,4	0	24,4	31,77(60)	15,05(18)	6,46(40)	6,55(64)	48,11(74)
200	33,8	16,0	0,9	0,1	0	22,2	33,80(37)	15,99(11)	5,62(25)	5,91(40)	50,73(46)
300	35,8	16,9	0,6	1,9	0	20,2	35,80(21)	16,931(64)	4,77(14)	5,26(22)	53,32(26)
400	37,9	17,9	0,1	3,6	0	18,6	37,79(26)	17,865(79)	3,93(18)	4,62(28)	55,90(32)
500	40,1	18,8	-0,4	5,1	0	17,1	39,75(45)	18,79(14)	3,09(31)	3,98(49)	58,46(57)
600	42,2	19,7	-1,0	6,4	0	15,8	41,69(68)	19,72(21)	2,25(46)	3,34(73)	60,99(85)
700	44,4	20,6	-1,6	7,6	0	14,7	43,61(91)	20,64(28)	1,41(62)	2,70(10)	63(1)

6.7 Infrared spectroscopy (FTIR)

The infrared spectrum for all phases have been obtained from 4000 to 400 cm^{-1} with a PerkinElmer SpectrumTwo spectrometer equipped with a diamond attenuated total reflectance (ATR) accessory. Stretching frequencies within the range 1255-956cm^{-1}, and bending frequencies within the range 696 -605 cm^{-1} (**Figure 46**). All IR spectra are summarize in **Table S11**. The three sulfate ion has tetrahedral symmetry. The bending frequencies with 599 - 696 cm^{-1} belong to ν_4 mode (Berger 1975). The symmetric stretching mode ν_1 occurring at 956 - 996 cm^{-1}. The peaks from 1022 cm^{-1} to 1255 cm^{-1} are assigned to ν_3 (A. Hezel, L and S. D. Ross 1966; Takahashi et al., 1974; Ross 1962; Decius 1963). The peaks from 452 cm^{-1} to 593 cm^{-1} are assigned to ν stretching Cu–O vibrations (Bakhtiari 2011, Usoltseva et al., 2016).

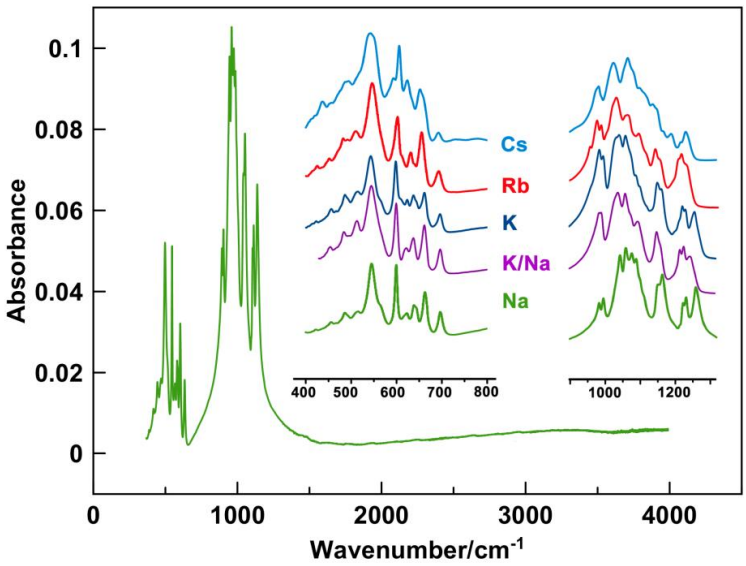

Figure 46. IR spectra of $A_2Cu_3O(SO_4)_3$ (A = Na, K), $Rb_2Cu_{3.07}O_{1.07}(SO_4)_3$, $Cs_2Cu_{3.5}O_{1.5}(SO_4)_3$.

6.8 Magnetic properties

6.8.1 Main magnetic generalities

Let me first summarize the classical magnetic behaviors in the solid compounds. When the magnetic energy related to the ordering is lower than the thermal screening, we are then in the paramagnetic state (at high temperature, the magnetic spins are disordered) up to the ordering temperature (**Figure 47**). Cooperative parallel ordering of long-distance spins within the structure corresponds to the ferromagnetic state (FM), in opposition to the antiferromagnetic state (AFM). When we have magnetic correlations in low-D units (for instance AFM layers) while these units are not coupled we call it low dimensional antiferromagnetic state, symbolized in (**Figure 47).** The ordering temperature in an FM case is called the temperature of Curie (noted Te), the ordering temperature in an AFM case of Néel temperature (noted Tn).

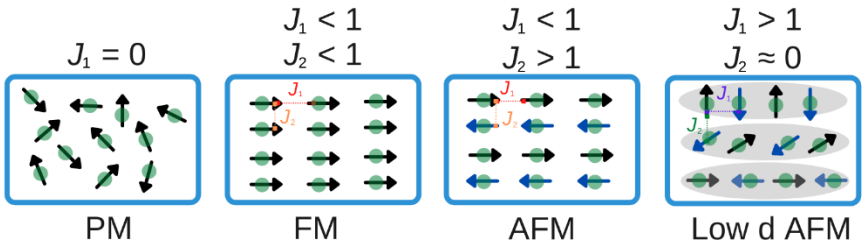

Figure 47. Illustration of the spin configuration in the paramagnetic state (PM), ferromagnetic state (FM), antiferromagnetic state (AFM) and low dimensional antiferromagnetic state (low d AFM).

6.8.2 Magnetic interactions

The magnetic interactions between atoms is mainly by exchange interactions (marked *J*) between two magnetic centers, i.e. the spin of the unpaired *d* / electrons of our metallic centers couple by overlap with the orbitals of a neighboring site. If the overlap between two metallic sites, we say that the exchange is direct. But usually we are talking about more complex ways of exchange, where the *d* orbital of our cation couples by overlap with the *p* orbital of an intermediate anion (in our case oxygen). We are talking about superexchange in the case when the intermediate atom is oxygen (M-O-M) or super-superexchange in the case of a path involving two oxygen (M-O-O-M). These types of overlap go ahead to local FM or AFM interactions, depending on the configuration of electrons, angle or type of bond. Based on Goodenough-Kanamori rules, an M-O-M angle of 90 ° or 180 ° angle enable to predict the type of intrecations. Therefore, it is easy to understand that you can change magnetic properties by

manipulating the spin to cations, the type of atoms in the crystal structure and the interactions between atoms.

6.8.3 $A_2Cu_3O(SO_4)_3$ and magnetic problematic

As mentioned above, Cu^{2+} magnetic centers correspond to individual S= 1/2 sites, but in a few cases these ions build clusters – magnetic molecules – that at low temperatures act as new magnetic ions with various spins (Janson et al., 2014) depending of the internal Js in the clusters. This feature gives access to interesting physics beyond spin – 1/2. This is typically the case of the mineral fedotovite, $K_2Cu_3O(SO_4)_3$ (Starova et al., 1991) concerned in this chapter.

On the structural level, as already mentioned $K_2Cu_3O(SO_4)_3$ entails Cu_6 hexamer units that behave at high temperature (paramagnetic regime) as 6 individual S = 1/2 spins. At lower temperature (~100K) , the deviation of the Curie-Weiss law match the realization of S = 1 macrospin (Furrer et al., 2018), naively understood as four spins up and two spins down. This was verified by fitting inelastic neutron scattering spectra, assigning the *Js* inside the Cu_6 hexamers. The hexamer units are connected into chains, as described above (**Figure 42**) along the crystallographic *b* direction and may then form S = 1 chains (**Figure 48**). Due to the absence of magnetic ordering firstly deduced from specific heat data and to the observation of a spin-gap between the fundamental and first excited states, such chains between clusters have been assigned to Haldane S = 1 AFM chains, as recently put forward (Fujihala et al., 2018). According to Haldane's conjecture, there is a spin gap of the excitation spectrum in integer Heisenberg AFM spin chains whereas half-integer AFM spin chains have a gapless excitation spectrum. In other words, a regular S = 1/2 chain is expected gapless due to a continuum of magnetic excitation contrarily to S = 1 spins giving a gap of energy Δ=0.41 J. The significance of this model lies in its unique quantum ground state that can be approximated by dimers of S = 1/2 interconnected by the exchange J (**Figure 49**) (Affleck 1989; Haldane et al., 1983).

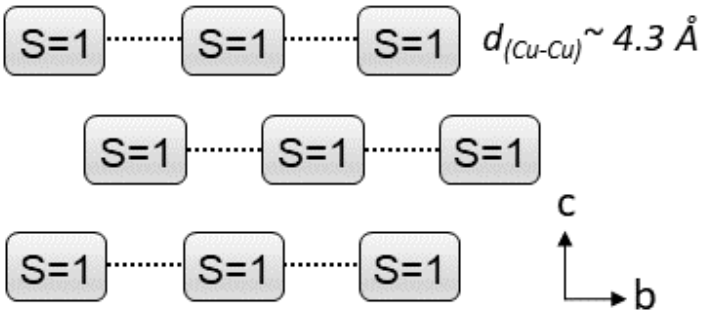

Figure 48. Possible magnetic models for $A_2Cu_3O(SO_4)_3$ represented by the Haldane chains (Fujihala et al., 2018)

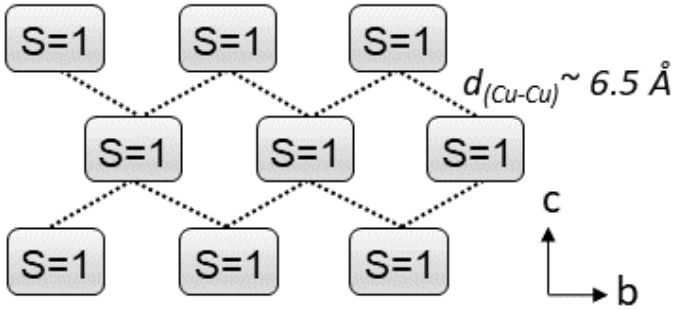

Figure 49. S = 1 square lattice magnetic models for $A_2Cu_3O(SO_4)_3$.
Each S = 1 is the Cu6 hexamer unit.

Any experimental contribution to this kind physics in new materials is relevant, especially in the case where S = 1 units are simulated by large macrospins such as in our family. In details about the literature of these series, the hypothesis of this conjecture was supported by the experimental observation of a finite spin gap of about 0.6 meV via inelastic neutron scattering (INS), as predicted for S = 1 Haldane chains. It goes together with a Schottky like Cp-anomaly consistent with a magnetically disordered ground state (White et al., 2014), which would indicate that the chains are isolated from each other and do not order magnetically in a Néel-like AFM 3D state.

On the other hand, very recently a magnetic ordering was observed around T_N = 3.0 K by subsequent magnetic susceptibility measurements and neutron diffraction (Furrer et al., 2018). This would indicate a conventional antiferromagnetic state at very low temperature and not the quantum ground state predicted by Haldane, although it does not refute totally the Haldane physics (T_N would result from interactions between the Haldane chains). However, it also suggests another topology, i.e.

the possibility for 2D-AFM units, for which small field, or very weak interactions or magnetic anisotropy can create an antiferromagnetic ordering below T_N.

The following work has essentially consisted in the demonstration of this 2D magnetic topology, in contrast to the proposed 1D-haldane one.

6.8.4 Analysis of the magnetic exchanges in the $A_2Cu_3O(SO_4)_3$ systems

Here rather than spectroscopic characterizations, we have used DFT calculations to estimate all Js in the system, keeping in mind that even if often scaled by interatomic Cu-Cu distances, the exchanges can be very misleading and super-super exchanges (SSE) by Cu-O-O-Cu can predominate. As mentioned earlier, the crystal structure is based on the clusters of $[O_2Cu_6]^{8+}$ which are linked by sulfate groups via Cu-O-O-Cu super-exchanges (SSE) along the b-axis forming 1D units, the aforementioned spin chains but also in the (bc) plane forming 2D-layers, shown in **Figure 50**. Along the a-axis, the layers are separated by about 8 Å with no obvious exchange pathways.

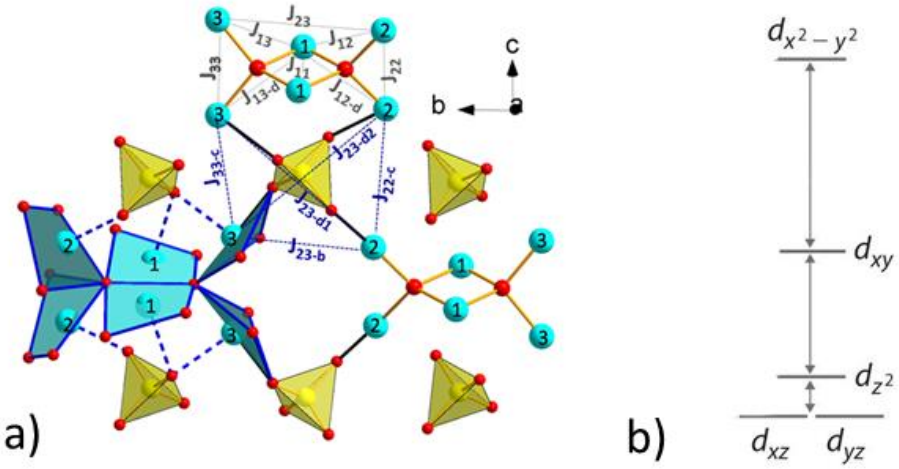

Figure 50. a) Crystal structure and main exchange couplings (intra-hexamer: blue lines, inter-hexamer: grey lines). The longest apical Cu-O_{4+1} bonds are shown by the dotted blue lines. b) ideal square plane crystal field image for Cu^{2+}

As we noticed earlier the Cu^{2+} coordination is strongly distorted for CuO_{4+1} square pyramids. It leads to a sizable mixing between d_{x2-y2} and d_{z2} as magnetic orbitals. In the case of the d^9 Cu^{2+} ions, the magnetic orbital and superexchange pathways are usually restricted to the dz^2 , i.e. towards the four oxygen atoms in the basal plane (see the blue O_4 plaquettes in (**Figure 50**), i.e. in the Cu_6 hexamers, but in the present case one should additionally consider the "long" apical Cu2-O13 (2.19 Å) and Cu3-O12(2.32 Å) bonds with a degree of magnetism,. On the other hand, the longer apical Cu1-O12 (2.56

Å) contacts should not play any significant role in the superexchange, because they are well above the sum of the Van der Waals radii.

Intra-hexamers: Magnetic couplings within the hexamers were analyzed in some of the previous studies (Furrer *et al.*, 2018). They used energies of local magnetic excitations probed by inelastic neutron scattering to quantify 7 exchange parameters listed in **Table 13** for both $K_2Cu_3O(SO_4)_3$ and $Na_2Cu_3O(SO_4)_3$. In this work, ferromagnetic nature of J_{22} and J_{33} was assumed to avoid frustration, whereas the second-neighbor coupling J_{23} was neglected. It allowed a good simulation of the INS spectra (**Figure 51**).

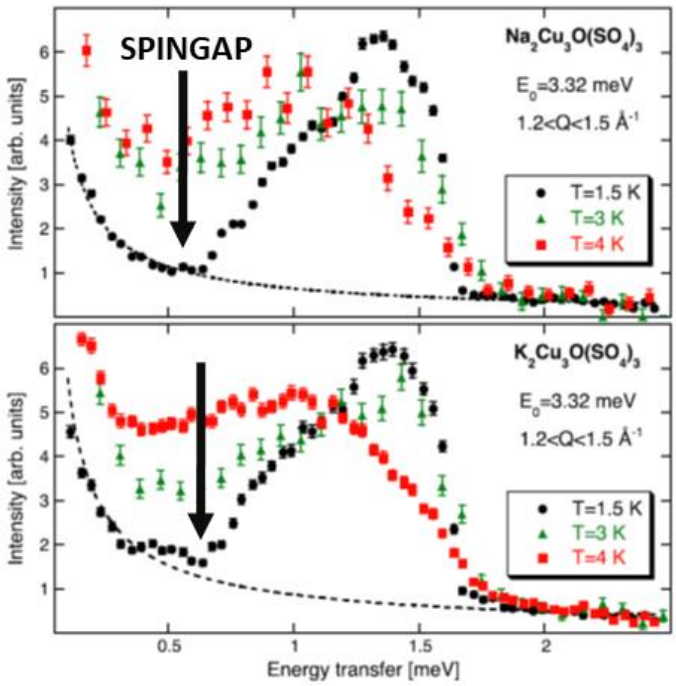

Figure 51. Energy spectra of neutrons scattered from $A_2Cu_3O(SO_4)_3$ (A = Na, K). The dashed curves correspond to the tail of the elastic line (Furrer *et al.*, 2018).

Table 13. Unit cell parameters, results of the Curie-Weiss fitting, and magnetic exchanges parameters from DFT in the three studied compounds of the $(Na,K)_2Cu_3O(SO_4)_3$ series. When available, the intra-hexamer exchange parameters from (Furrer et al., 2018) (fits to excitations energies determined by inelastic neutron scattering) and(Fujihala et al., 2018) (fits to the experimental susceptibility data) are given for comparison. Zero values indicate exchange couplings that are below 0.05 K and can't be resolved by DFT.

		$Na_2Cu_3O(SO_4)_3$		$KNaCu_3O(SO_4)_3$		$K_2Cu_3O(SO_4)_3$	
Compound							
Space group		*C*2/*c*		*C*2/*c*		*C*2/*c*	
Lattice parameters		*a* = 17.3097(9)Å *b* = 9.3982(5)Å *c* = 14.3982(7)Å *β* = 111.936(1)° *V* = 2172.72(19)Å3		*a* = 18.5753(1)Å *b* = 9.3994(4)Å *c* = 14.3701(1)Å β = 113.969(1)° *V* = 2292.62(31)Å^3		*a* = 19.6125(9)Å *b* = 9.7712(5)Å *c* = 14.4903(7)Å β = 110.485(1)° *V* = 2578.32(17)Å^3	
μ_{eff} per Cu^{2+} (S=1/2) High Temp.		1.93 μ_B, -235.2 K		1.73 μ_B, -187.2 K		1.80 μ_B, -216.3 K	
μ_{eff} per hexamer/θ_{CW} (S=1) Low Temp.		2.84 μ_B, -7.3 K		2.71 μ_B, -8.4 K		2.80 μ_B, -10.7 K	
χ(T) $_{QMC}$: J_{fit}, D_{fit}		2.45 K, 0.74 K		3.05 K, 0.92 K		2.48 K, 0.74 K	
M(*H*) $_{QMC}$: $T_{N\ calc}$, $_{exp}$		~ 3.3 K, 3.4 K		4.3 K, 4.7 K		3.3 K, 2.9 K	
J label	*atoms*	Distances, Å	J/k_B (K)	Distances, Å	J/k_B (K)	Distances, Å	J/k_B (K)
Intra- hexamer							
$J_{11\ this\ work}$ Fujihala et al., 2018 Furrer et al., 2018	Cu1-Cu1	2.8196(7)	-159 - 116	2.807(2)	-164	2.818(2)	-157 -35 -93
$J_{12\ this\ work}$ Fujihala et al., 2018 Furrer et al., 2018	Cu1-Cu2	3.3940(8) x2	171 - 110	3.167(1) x2	170	3.190(2) x2	171 125 93
$J_{12\text{-}d\ this\ work}$ Fujihala et al., 2018 Furrer et al., 2018	Cu1-Cu2	3.1796(7) x2	170 - 188	3.391(1) x2	141	3.401 (2) x2	153 125 197
$J_{13\ this\ work}$ Fujihala et al., 2018 Furrer et al., 2018	Cu1-Cu	3.1114(8) x2	118 - 88	3.393(2) x2	145	3.416 (2) x2	139 125 86
$J_{13\text{-}d\ this\ work}$ Fujihala et al., 2018 Furrer et al., 2018	Cu1-Cu3	3.4185(7) x2	230 - 115	3.135(1) x2	190	3.117 (1) x2	198 125 220
$J_{22\ this\ work}$ Fujihala et al., 2018 Furrer et al., 2018	Cu2-Cu2	3.0141(9)	26 - 46	2.999(2)	36	2.977 (2)	42 -35 -44
$J_{33\ this\ work}$ Fujihala et al., 2018 Furrer et al., 2018	Cu3-Cu3	3.0069(8)	-2 - 38	3.019(2)	29	2.977(2)	19 -35 -39
$J_{23\ this\ work}$ Fujihala et al., 2018	Cu2-Cu3	5.1332(7) x2	16 -	5.124(2) x2	14	5.165 (3) x2	14 -

Furrer et al., 2018			-				-
Inter- hexamers							
$J_{11\text{-}a}$	Cu1-Cu1	7.8335(8) x2	0	8.299(3) x2	0	8.544(4) x2	0
$J_{12\text{-}a}$	Cu1-Cu2	6.8707(8)	0	7.498(4)	0	7.785(5)	0
$J_{13\text{-}a}$	Cu1-Cu3	7.4259(8)	0	8.015(5)	0	8.340(5)	0
$J_{23\text{-}b}$	Cu2-Cu3	4.3434(7) x2	0	4.313(2) x2	0	4.444(3) x2	0
$J_{22\text{-}c}$	Cu2-Cu2	4.3616(8)	0	4.288(3)	0	4.289(3)	0
$J_{33\text{-}c}$	Cu3-Cu3	4.2728(8)	0	4.281(3)	0	4.231(2)	0
$J_{23\text{-}d2}$	Cu3-Cu2	6.3316(8)	9	6.375(3)	11	6.378(3)	9
$J_{23\text{-}d1}$	Cu2-Cu3	6.3485(8)	7	6.270(3)	9	6.333(3)	9

These results are also in reasonable agreement with the susceptibility fits of (Fujihala *et al*., 2018). Our DFT calculations return similar values, although we found weakly antiferromagnetic J_{22} and J_{33}, as well as J_{23}. Only J_{11} is ferromagnetic but reaches almost *ca.* 60% of the maximal AFM exchanges. Its ferromagnetic nature is typical for the edge-sharing geometry of the two $Cu1O_5$ units with the Cu1-O-Cu1 angles close to 90°. Interactions between the hexamers are detailed later but found, for the significant ones, even weaker than J_{22}, J_{33}, and J_{23}, so at higher temperatures magnetic behavior should be determined by individual hexamers, which show quite similar exchange parameters for $K_2Cu_3O(SO_4)_3$, $Na_2Cu_3O(SO_4)_3$, and the mixed $NaKCu_3O(SO_4)_3$ compound. This similarity for all alkali is reflected in the comparable INS spectra reported for fedotovite and puninite (Fujihala *et al*., 2018; Furrer *et al*., 2018) but also in very similar temperature dependence of the magnetic susceptibility. All three compounds show a characteristic bend of the inverse susceptibility around 100 K (**Figure 52**) that marks the transition from the paramagnetic regime with individual Cu^{2+} ions to the collective regime, where each hexamer acts as a single spin. Curie-Weiss fits return effective magnetic moments of 1.73-2.20 μ_B/Cu above 100 K and 2.71-2.84 μ_B/hexamer below 100 K (**Table 13**), suggesting, respectively, the anticipated S = ½ state of individual Cu^{2+} ions and the S = 1 state of the Cu_6 hexamer at low temperatures. In details, with the exception of weak antiferromagnetic interactions J_{22}, J_{33}, and J_{23}, all intra-hexamer interactions tend to align the Cu2 and Cu3 spins parallel to each other and antiparallel to Cu1, thus giving rise to the S = 1 state of the hexamer.

This behavior indicates the separation of energy scales, with strong couplings within the hexamers and weak couplings between the hexamers. The evolution of the hexamers is independently tracked by ESR on $Na_2Cu_3O(SO_4)_3$ that shows powder-averaged paramagnetic resonance with two components, $g_\perp$ = 2.1 and $g_\parallel$ = 2.4, down to 100 K, with respect to the mixing of magnetic orbitals noted above. Below 100 K, the line broadens around g = 2.2 indicating the development of local fields on individual Cu^{2+} ions (**Figure 51**). The inverse of the ESR intensity shown in (**Figure 52**). tracks magnetic susceptibility and also shows the slope change around 100 K.

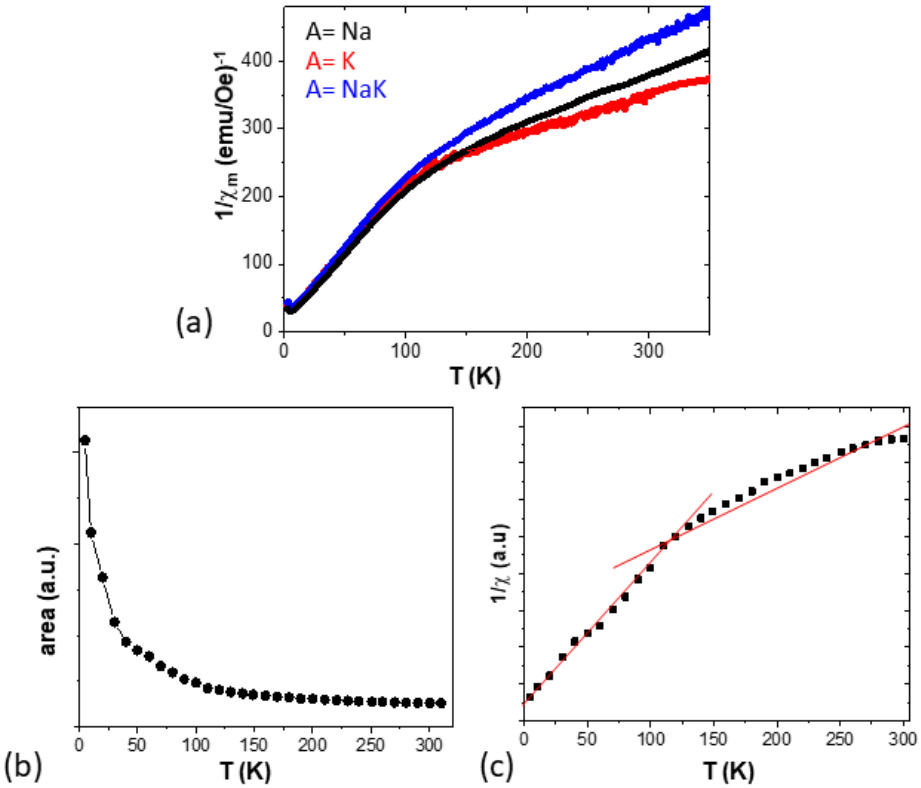

Figure 52. (a) χ^{-1}(T) plots measured at 1000 Oe for the $A_2Cu_3O(SO_4)_3$ series. The K sample is resented corrected from an important fitted temperature-independent contribution (b) the integrated ESR intensity tracking the magnetic susceptibility and (c) its inverse versus temperature with evidence of the slope change around 100 K.

Interactions between hexamers: We now analyze the inter-hexamer interactions that cause this magnetic order. All *J*'s corresponding to the Cu-Cu distances of less than 8 Å were calculated, but only two interactions, $J_{23\text{-}d1}$ and $J_{23\text{-}d2}$, are found to be significant. On the other hand, the interaction $J_{23\text{-}b}$ proposed in (Fujihala et al., 2018) is well below 1 K and, therefore, negligible. Which refute interaction in 1D chains. Both $J_{23\text{-}d1}$ and $J_{23\text{-}d2}$ connect the hexamers in the *bc* plane.

At lower temperatures, interactions between the hexamers become important, and it is these interactions that underlie the supposed Haldane physics of $K_2Cu_3O(SO_4)_3$ (Fujihala et al., 2018). Indeed, all three compounds show broad susceptibility maxima around 5-6 K indicative of low-dimensional magnetic behavior (**Figure 53**). No other features, except for the weak upturn caused by paramagnetic impurities, are seen in the magnetic susceptibility.

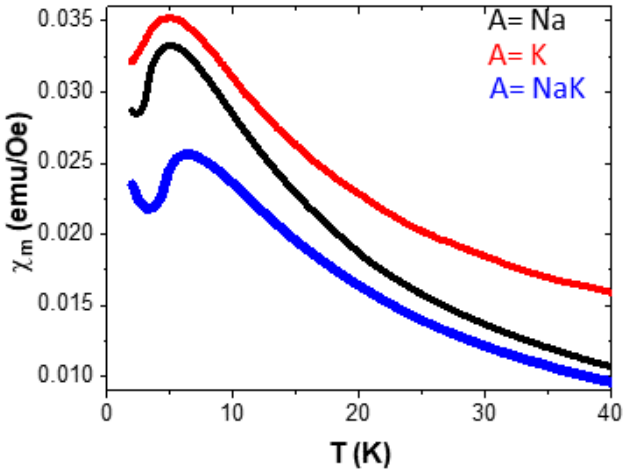

Figure 53. Evidence of the low-T χ(T) bump typical of low-dimensional magnetism in the $A_2Cu_3O(SO_4)_3$ (A = Na, K).

The diagonal couplings $J_{23\text{-}d1}$ and $J_{23\text{-}d2}$ are similar in size in all three compounds and build an effective square lattice of S = 1 magnetic moments associated with the hexamers (Figure 54). In the following, we juxtapose this square-lattice model with the experimental data.

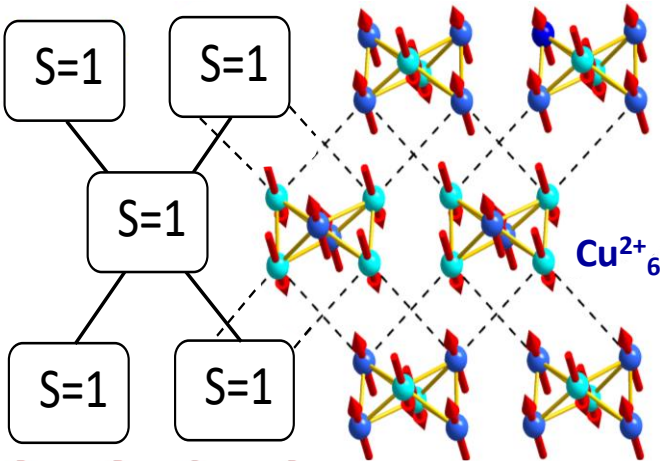

Figure 54. Two-dimensional square lattice of S=1 hexamer units with the hypothetical magnetic structure for the (u,0,u) spin components. Dotted lines denote the leading magnetic interactions between the hexamers.

6.8.5 Heat capacity of $A_2Cu_3O(SO_4)_3$ (A = Na, K)

Magnetic specific heat of $Na_2Cu_3O(SO_4)_3$ reveals a two-peak structure corresponding to the inter-hexamer and intra-hexamer interactions (**Figure 55**). It was obtained from the experimental specific heat by subtracting the phonon contribution roughly estimated using two Debye contributions (i = 1 to 2) via $C_{latt} = 9R\ (\theta)^3$

with $C_1 = 11(1)$, $\theta_{D,1} = 310(20)$ K, $C_2 = 18(1)$, $\theta_{D,1} = 1502(50)$ K. Full magnetic entropy of $3R*\ln 2$ is recovered around 100 K (**Figure 54)**, most of it contained in the second (higher-temperature) peak, whereas the first peak contains only 20% of the magnetic entropy.

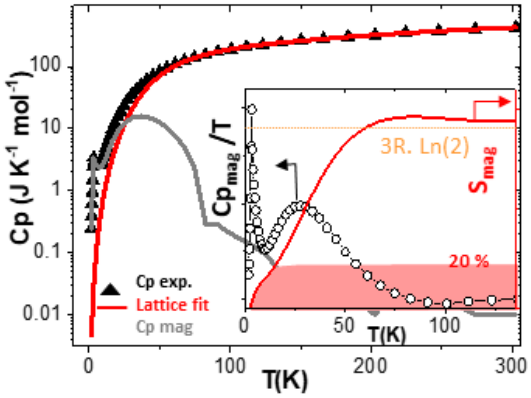

Figure 55. Phonon and magnetic contributions to the specific heat of $Na_2Cu_3O(SO_4)_3$. The inset shows magnetic entropy S_{magn} obtained by integrating $Cp_{magn.}/T$, with about 20% of the total entropy recovered at T_N.

Concurrently, specific heat shows λ-type transition anomalies at 3.4 K for $Na_2Cu_3O(SO_4)_3$ and 4.7 K for $NaKCu_3O(SO_4)_3$ indicating the onset of long-range magnetic order in both compounds. No clear anomaly can be seen in the case of $K_2Cu_3O(SO_4)_3$, although a broad feature is clearly present at 3-4 K and was previously interpreted as a Schottky anomaly (Fujihala et al., 2018). On the other hand, Fisher's heat capacity of (Hase et al., 2019) indicated a magnetic transition, found in our work at 2.9 K. The observation of magnetic Bragg peaks below this temperature (Hase et al., 2019) also shows that $K_2Cu_3O(SO_4)_3$ develops long-range magnetic order, at odds with earlier expectations of the Haldane physics in this compound. The broadened feature in the specific heat may be caused by a lower crystallinity of the potassium compound in possible relation with its fastest reactivity with moisture, due to the potassium-driven lattice dilatation.

6.8.6 2D topology proved by QMC simulations

Another argument supporting our scenario can be derived by fitting magnetic susceptibility data with an effective spin model, where hexamers are represented by S = 1 units. At first glance, Haldane spin chain with J = 3.9 K gives a decent description of the magnetic susceptibility of $Na_2Cu_3O(SO_4)_3$ below 60 K (**Figure 56**), but the associated spin gap of 0.41J ~ 1.6 K is clearly too small to account for the spin gap of 4-5 K observed experimentally Furrer et al., 2018).

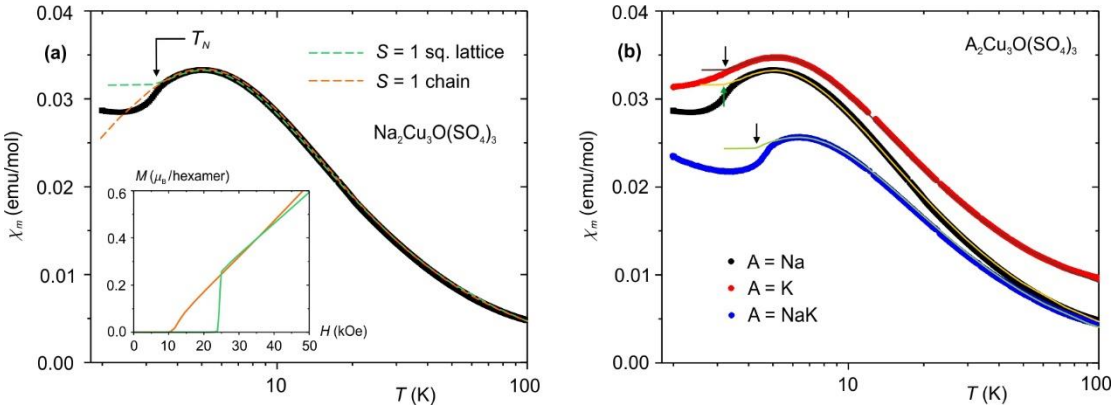

Figure 56. (a) Comparison of the susceptibility fits for $Na_2Cu_3O(SO_4)_2$ using the S = 1 chain (Haldane chain) and S = 1 square-lattice models, with the latter model revealing magnetic ordering at T_N = 3.3 K. The inset shows magnetization curves calculated with the same parameters and depicted using the same color code at a low temperature of about 0.2 K to highlight field-induced transitions caused by the closing of the spin gap in the S =1 chain and the closing of the magnon gap in the S = 1 square-lattice antiferromagnet. In the latter case, the field is applied along the easy direction, hence the spin-flop transition is much sharper than in the powder-averaged data. Susceptibility fits for all three compounds using the S = 1 square-lattice model with the parameters described in the text. The arrows mark the *transition temperatures* T_N.

lattice model proposed in our work leads to a susceptibility fit of comparable quality if the exchange coupling of J = 2.45 K is supplied with the single-ion anisotropy of D = 0.74 K (Figure 56a). This single-ion anisotropy represented by the $D(S^z)^2$ term in the spin Hamiltonian is essential to explain two features of $Na_2Cu_3O(SO_4)_3$. First, the anisotropy triggers magnetic order even in the absence of magnetic couplings between the square planes. Our DFT calculations suggest that such couplings along the crystallographic *a* direction are very weak, below 0.05 K, and can be excluded to a first approximation. Incidentally, even a purely 2D model without *any* interlayer couplings leads to T_N ~ 3.3 K in excellent agreement with the experimental value of 3.4 K, so it is mostly the anisotropy that is responsible for the long-range ordering in these materials. Single-ion anisotropy of the hexamers implies zero-field splitting of the ground-state S = 1 triplet, which is likely caused by anisotropic interactions between the S = 1/2 Cu^{2+} ions.

Second, the excitation gap depends now not only on *J*, but also on *D* and can be much larger than in the Haldane scenario. We illustrate this by calculating the low-temperature *M*(*H*) curves for the exchange parameters obtained from the susceptibility fits (**Figure 56a**, inset). Haldane chain shows an anomaly of *M*(*H*) around 10 kOe where the spin gap is closed. On the other hand, the *S* =1 square lattice reveals a spin-flop transition around 25 kOe that corresponds to the closing of the excitation gap and manifests itself in the change of slope of the experimental *M*(*H*) curve (**Figure 57**). Indeed, for the three samples, the gap closing at 2 K takes place at the critical fields H_c of ~4.5T (~0.57 meV) for $K_2Cu_3O(SO_4)_3$, ~3.5T (~0.44 meV) for $Na_2Cu_3O(SO_4)$ and ~5.8T (~0.73 meV) for $NaKCu_3O(SO_4)_3$, as estimated by the maximal dM/dH inflection and the mean-field spin energy $E=\mu_B$ g SH, *S*=1 and *g*=2.2 from ESR low-T experiments. These values match rather well the direct measures of the excitation gap by INS (Fujihala et al., 2018; Furrer et al., 2018). In addition, only the square-lattice model would allow the field-induced transition at H_c to be observed at 2 K. In the chain scenario, the gap is so small that at 2 K it is fully overcome by thermal fluctuations.

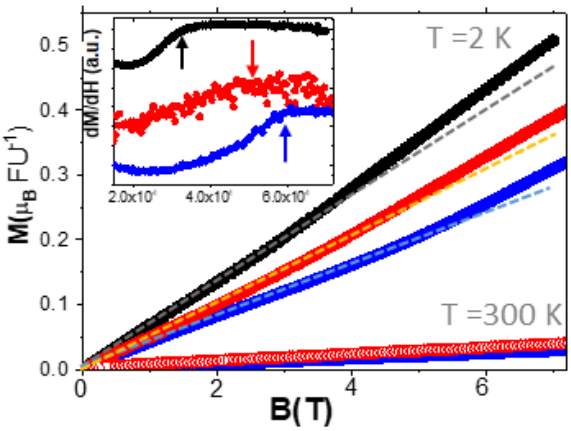

Figure 57. Raw M(H) data at 2K and 300K with the spin-flop transition highlighted via dM/dH in the inset.

Similar fits with the *S* = 1 square-lattice model return *J* = 3.05 K, *D* = 0.92 K in $NaKCu_3O(SO_4)_3$ with the expected T_N = 4.3 K (experiment: 4.7 K) and *J* = 2.48 K, *D* = 0.74 K in $K_2Cu_3O(SO_4)_3$ with the expected T_N = 3.3 K (experiment: around 3.0 K), see **Figure 56b**. These *J* values apply to the spin Hamiltonian with *S* = 1 and are thus lower than $J_{23\text{-}d1}$ and $J_{23\text{-}d2}$ of about 10 K from DFT (**Table 13**), which describe interactions between the *S* = ½ Cu^{2+} ions.

Discussion 1: Magnetic structure stabilized by $J_{23\text{-}d1}$ and $J_{23\text{-}d2}$ fully respects the magnetic Shubnikov group *C*2’/*c* with k = (0,0,0) proposed for $K_2Cu_3O(SO_4)_3$ on the basis of both the S=1 clustering and the observed magnetic satellites in the neutron powder pattern (Hase et al., 2019).

According to (Hase et al., 2019) the (*u*,*v*,*w*) spin components are dominated by the *u* and *w* terms. In **Figure 57** we arbitrarily choose *u*=*w* for better visualization and demonstrate that the magnetic order associated with *C*2'/*c* complies with the antiferromagnetic nature of $J_{23\text{-}d1}$ and $J_{23\text{-}d2}$. On the other hand, antiferromagnetic $J_{23\text{-}b}$ of (Fujihala et al., 2018) should lead to a different type of magnetic order and would not be consistent with neutron diffraction.

Discussion 2: These unexpected magnetic properties arise from the complex crystal structures of anhydrous copper oxysulfates, which are among the most common minerals in volcanic fumaroles with highly oxidizing conditions (e.g. Vesuvius, Italy; Tolbachik, Kamchatka Peninsula, Russia) (Vergasova et al., 2016). The impossibility of studying magnetism in natural mineral samples due to the presence of impurities requires new approaches to the synthetic procedures, which mimic natural geological processes on volcanoes (Kovrugin et al., 2015; Siidra et al., 2020). Until recently, synthetic analogues were practically unknown, due to the instability of anhydrous sulfates in air and their proclivity to hydration (Siidra et al., 2019). A specific structural feature of fumarolic copper oxysulfate minerals is the formation of complex copper-oxygen substructures, i.e. the hexamers responsible for the magnetism that we analyzed in this work. The formation of hexamers leads to manifestations of interesting, often new, unusual magnetic phenomena (Prša et al., 2009). In that sense, the $(Na,K)_2Cu_3O(SO_4)_3$ mineral series opens further perspectives concerning exotic magnetic compounds. Practically, in the lab we achieved the realization of novel synthetic compounds of this family, and their characterization is now in progress.

6.8.7 Analysis of the magnetic exchanges in the $Rb_2Cu_{3.07}O_{1.07}(SO_4)_3$ and $Cs_2Cu_{3.5}O_{1.5}(SO_4)_3$ phases

As was discussed earlier the magnetic data for Cs-phase include impurity $Cs_2Cu(SO_4)_2$. Because of that the magnetic data discussed below have been corrected from 6.6% of Cu^{2+} ions of the solid $Cs_2Cu(SO_4)_2$ impurity assumed paramagnetic in absence of experimental magnetic data.

Concerning the preservation of Cu_{14} hexamers and their ordering in the prepared samples, the lattice parameters refined for all members show only minor deviations from those of the Cu-ordered x = 0.5 single crystalline specimen, which by its own validate the nominal composition of the major phase. Structurally, their alternation in 1D chains is also mandatory due to their specific coordination by SO_4 groups. Low angle-XRD powder patterns reveal systematic broad and weak supercell peaks (1 ½ 0) and (0 ½ 1) with intensities growing with x (**Figure 32**). Similar to single crystal, one expects minor deviation from the $Cs_2Cu_{3.5}O_{1.5}(SO_4)_3$ over-stoichiometry and long-range Cu^{2+} ordering in-plane and/or between layers.

All compounds of the series show a characteristic bend of the inverse susceptibility around 100 K (**Figure 58a**) that marks the transition from the paramagnetic regime with individual Cu^{2+} ions to the collective regime, where each clusters acts as a single spin . This behavior indicates the separation of energy scales, with strong couplings within the clusters and weak couplings between them. Between 400 and 150 K, Curie-Weiss fits results in μ_{eff} = 1.77 and 1.97 μ_B/Cu for A = Rb and Cs, respectively, in agreement to the expected value for *S* = 1/2. However, in the low temperature part, the effective moment is reduced to 0.84 μ_B/Cu for Cs ,significantly lower than those for Na and K (1.11 and 1.16 μ_B/Cu respectively), but intermediate for *A*= Rb (1.01 μ_B/Cu). This suggests a weaker contribution of individual spins in the Cu_{14} tetradecamers than in the Cu_6 hexamers.

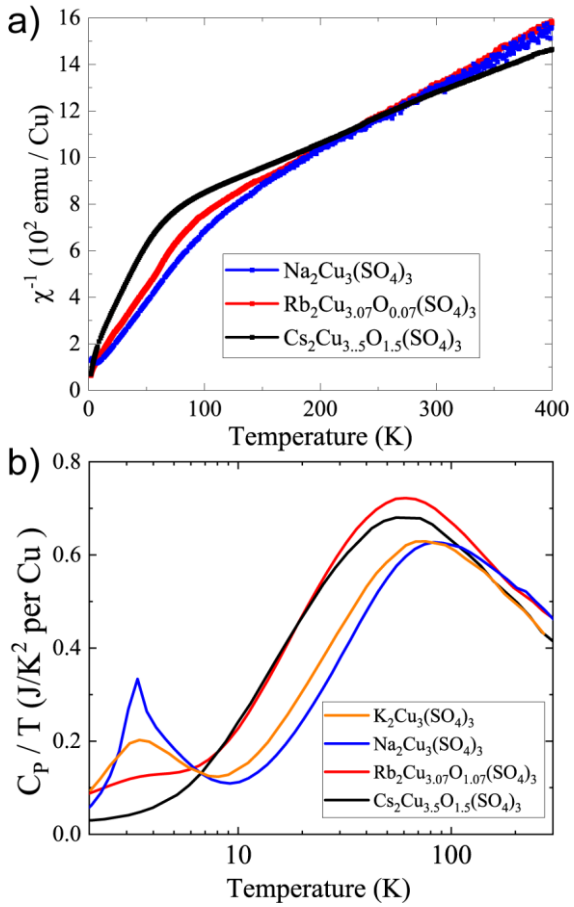

Figure 58. (a) inverse susceptibility and (b) Cp/T versus temperature normalized per one Cu^{2+} units for pertinent members of the series

For *A* = Na, K, the magnetic couplings within the hexamers were preliminary analyzed in several previous studies, by means of the energies of local spin excitations probed by inelastic neutron scattering (Furrer et al., 2018; Hase et al., 2019), and later confirmed by us using systematic DFT calculations (Nekrasova et al., 2020). They present a strong ferromagnetic central Cu-Cu exchange (rung like) across a shared edge due to Cu-O-Cu angles close to 90°, while both the *leg-like* and *diagonal* ones are found

also strong and antiferromagnetic (AFM). Most of the intra-hexamer interactions tend to align the external four spins parallel to each other and antiparallel to the two central ones, thus giving rise to the $S = 1$ fundamental state of the hexamer, (see **Figure 50** and **Figure 59**).

We obtained similar DFT-results for the Cu_{14} oligomers of $Cs_2Cu_{3.5}O_{1.5}(SO_4)_3$ where the two independent crystallographic Cu_{14} sub-units a and b were considered equivalent for simplicity. The main calculated intra- exchanges are shown in **Figure 59**c, and listed exhaustively in **Table 14**, the inter Cu_{14} exchanges are shown in **Figure 41** and **Table 15**. All exchanges (along legs, diagonal and next-nearest neighbor ones) are antiferromagnetic with calculated values up to $J_{1\text{-}2}$= 359 K using the relaxed crystal structure and GGA+U. Similar to the A = Na, K cases edge-sharing rung-like ones are ferromagnetic with values up to -96 K for $J_{3\text{-}3}$ due to Cu-O-Cu angles near orthogonality. Apart the next-nearest neighbor (NNN) $J_{2\text{-}4}$ and $J_{4\text{-}6}$ bringing frustration in the $Cu_{2\text{-}3\text{-}4}$ and $Cu_{4\text{-}5\text{-}6}$ triangles, the overall contribution of the J exchanges largely play for the stabilization of $S = 1$ spin-clusters with ideal spin configuration highlighted in (**Figure 59b**).

Table 14. The unit cell parameters and magnetic exchanges parameters from DFT in the $Cs_2Cu_{3.5}O_{1.5}(SO_4)_3$. The intra-hexamer exchange parameters.

Compound		**$Cs_2Cu_{3.5}O_{1.5}(SO_4)_3$**	
Space group		*P*2/*a*	
Lattice parameters		*a* = 17.3097(9)Å *b* = 9.3982(5)Å *c* = 14.3982(7)Å *β* = 111.936(1)° *V* = 2172.72(19)Å3	
J label	*Atoms*	distances (Å) refined, (*relaxed*)	J/k_B (K)
$J_{11\text{-rung}}$	Cu1-Cu1	2.900 (2.947)	-14
$J_{12\text{-leg}}$	Cu1-Cu2	3.2309 (3.396)	359
$J_{12\text{-diag}}$	Cu1-Cu2	3.3621 (3.141)	192
$J_{22\text{-rung}}$	Cu2-Cu2	2.8258 (2.820)	-82
$J_{23\text{-leg}}$	Cu2-Cu3	3.3554 (3.207)	175
$J_{23\text{-diag}}$	Cu2-Cu3	2.9682 (3.299)	168
$J_{33\text{-rung}}$	Cu3-Cu3	2.9161 (2.886)	-96
$J_{34\text{-leg}}$	Cu3-Cu4	3.3217 (3.068)	98
$J_{34\text{-diag}}$	Cu3-Cu4	3.0523 (3.270)	280

$J_{44\text{-rung}}$	Cu4-Cu4	2.8647 (2.836)	-67
$J_{45\text{-leg}}$	Cu4-Cu5	3.1065 (3.270)	283
$J_{45\text{-diag}}$	Cu4-Cu5	3.2577 (3.145)	117
$J_{55\text{-rung}}$	Cu5-Cu5	2.912 (2.921)	-52
$J_{56\text{-leg}}$	Cu5-Cu6	3.2063 (3.354)	187
$J_{56\text{-diag}}$	Cu5-Cu6	3.3281 (3.026)	131
$J_{66\text{-rung}}$	Cu6-Cu6	2.8471 (2.828)	-95
$J_{67\text{-leg}}$	Cu6-Cu7	3.4552 (3.180)	215
$J_{67\text{-diag}}$	Cu6-Cu7	3.1443 (3.367)	232
$J_{77\text{-rung}}$	Cu7-Cu7	2.9080 (2.957)	48
$J_{13\text{-leg}}$	Cu1-Cu3	5.0682 (5.125)	31
$J_{13\text{-diag}}$	Cu1-Cu3	5.7837 (5.869)	4
$J_{24\text{-NNN}}$	Cu2-Cu4	4.8825 (4.995)	114
$J_{24\text{-diag}}$	Cu2-Cu4	5.6478 (5.737)	2
$J_{35\text{-NNN}}$	Cu3-Cu5	4.9127 (4.934)	39
$J_{35\text{-diag}}$	Cu3-Cu5	5.6734 (5.701)	3
$J_{46\text{-NNN}}$	Cu4-Cu6	4.9971 (4.948)	133
$J_{46\text{-diag}}$	Cu4-Cu6	5.7555 (5.693)	1
$J_{57\text{-NNN}}$	Cu5-Cu7	5.1825 (5.056)	27
$J_{57\text{-diag}}$	Cu5-Cu7	5.9011 (5.788)	1

Table 15. The inter Cu_{14} exchanges (J/K_b in K) with calc. and relaxed distances (see **Figure 41**).

$J_{71 \text{ along b}}$	Cu7-Cu1	4.368 (4.400)	-0.8
J_{55}	Cu5-Cu5b	6.411 (6.373)	52.9
J_{33}	Cu3-Cu3b	6.318 (6.3811)	52.9
J_{37}	Cu3-Cu7b	6.482 (6.1524)	74.3
J_{73}	Cu7-Cu3b	6.150 (6.5699)	74.3
J_{51}	Cu5-Cu1b	6.246 (6.5905)	74.3
J_{75} (=J_{13})	Cu7-Cu5b	4.157 (4.214 A)	-2.0 K
J_{53}	Cu5-Cu3b	4.178 (4.145 A)	2.3 K

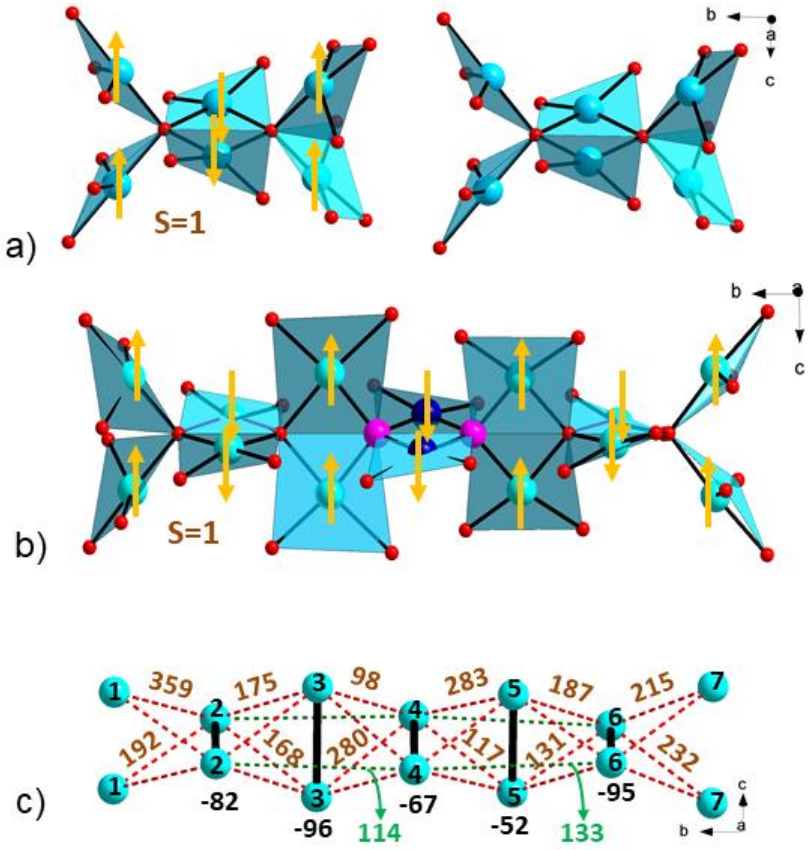

Figure 59. (a) two subsequent S = 1 hexamers with idealized local S = ½ spins and (b) S = 1 tetradecamers after 2xCuO incorporation. (c) and main intra-Cu_{14} exchanges.

DFT calculations are in reasonable agreement with the susceptibility fits performed using full diagonalization or QMC in the high temperature region. **Figure 60** highlights the best fit considering significant frustrated J_{NNN} exchanges (= 350 K) additionally to the "ideal "S = 1 topology with J_{legs} = J_{diag} = 250K, and J_{rung} =250K. These values for a simplified three-J-model are in agreement with the magnitude of those calculated by DFT.

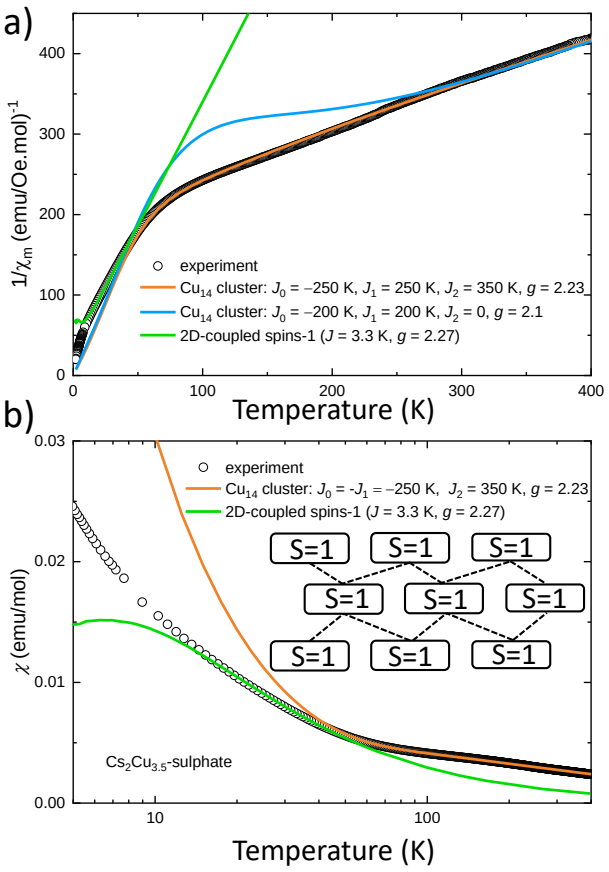

Figure 60. (a) χ^{-1}(T) and (b) χ(T) QMC-fits using adapted models along the temperature range. The best low-T fit returns a square lattice of S = 1 clusters depicted in (b).

For A = Na and K, spin gaps of less than 1 meV were observed and wrongly related to a Haldane S = 1 spin chain (Fujihala et al., 2018; Furrer et al., 2018). Our revised model (Nekrasova et al., 2020) for a S = 1 square lattice explains this gap as a Cu_6 hexamer inter-cluster interaction below 100 K with a magnetically ordered state and a magnon gap as experimentally observed (Hase et al., 2019).

For the Cs-system, similar results were found and agree well with the isothermal magnetization M(H) plot, displaying an unsaturated plateau around 1.2 μ_B/Cu_{14} expected for coupled S = 1 spins. Indeed the Js between the terminal Cu^{2+} of the Cu_{14} clusters along b are calculated very weak and ferromagnetic (-0.8 eV) along SSE's due to unfavorable nearly perpendicular Cu-O bonds (Cu-O-O-Cu dihedral angles ~ 80°). On the opposite, all in-plane SSEs with σ-type overlap between the two Cu-O bonds (45°<Cu-O-O-Cu <2°) and short O-O distances promote significant Js between 53 and 74 K, see **Figure 59d**, despite longueur Cu-Cu distances above 6.13 Å. We count ~23 Cu-Cu distances (> 6.5 Å) between two Cu_{14} units, including only two significant calculated ones giving roughly a main inter-exchange of ~5.5 K. Indeed, the QMC simulation of χ(T) using a square lattice of S = 1, with g = 2.23 and J = 3.3 K

reproduces well our experimental data below 45 K and with values in good agreement with our DFT calculations, see **Figure 59b**. Note that the slope of $\chi^{-1}(T)$ returns $\mu_{eff} = 3.15\ \mu_B$ per Cu_{14}, i.e. $g\sqrt{S(S+1)}$.

Below 10 K, the data are spurred by the correction of secondary phase ideally considered as paramagnetic, and should not be taken into account. In the *A* = K, Na, Na/K compounds the need of the $S = 1$ single ions anisotropy $D(S^z)^2$ is essential in order to

i) trigger the experimentally observed magnetic ordering (Hase et al., 2019), even in absence of inter-layer exchanges, these latter being calculated below 0.05 K, and expected even lower in the Rb and Cs system, as dropping exponentially with the layer-layer separation distance and

ii) to match the experimental excitation gap within the $S = 1$ square-lattice scenario strongly influenced by *D* and *J*.

Here single-ion anisotropy implies zero-field splitting of the ground-state $S = 1$ triplet, which is likely caused by anisotropic (likely Dzyaloshinskii-Moriya) interactions on individual Cu-Cu bonds. It is expected effective also in the Cu_{14} case. It is responsible for the $\chi(T)$ upturn calculated at $T_N \sim 4.5$ K. The occurrence of this magnetic ordering of anisotropic origin is probable at least for an ideal ordering although not observed in the $\chi(T)$ nor in Cp/T(T) plots, see **Figure 58b**. Here one should keep in mind that the magnetic correlation across the [A] interleave is fragile, and that even in the magnetically ordered K-case (Hase et al., 2019), Cp/T mainly denote a Schottky-anomaly for similar reason, see **Figure 58b**.

6.9 Conclusion

This part was devoted not only to the synthesis and description of the compositional and topological changes of the crystal structures but also to a detailed description and study of the magnetic properties of synthetic analogs of euchlorine-type minerals.

In the first part of the chapter have been showed that $A_2Cu_3O(SO_4)_3$ (*A* = Na, Na/K, K) compounds contain magnetic Cu_6 hexamer units, which at temperatures below about 100 K carry an overall spin-1 and represent magnetic molecules. Weak interactions between such molecules lead to long-range magnetic order below T_N = 3.4 K (A = Na), 4.7 K (A = Na/K), and 2.9 K (A = K). The formation of the magnetic order is rationalized by *ab initio* calculations that reveal predominant inter-hexamer interactions forming a $S = 1$ square lattice within crystallographic *bc* planes, and challenge previous description of these minerals in terms of Haldane spin chains. We emphasize the role of the

anisotropy inherent to the $S = 1$ molecules in the formation of a magnetically ordered ground state with a magnon gap instead of a Haldane gap expected previously.

In the second part of the chapter have been discussed the lattice relaxation after the replacement of alkali by bigger Rb and Cs alkali is accompanied by the insertion of neutral CuO species into $(Rb,Cs)_2Cu_3O(CuO)_x(SO_4)_3$ phases. The structural principles allow for the passage from 1D-like Cu_6 hexamers ($x = 0$, A = Na, K) to longer Cu_{14} tetradecamers ($0.07<x<0.5$, A = Cs, Rb) after topochemical insertion of neutral CuO species.

The compositional and topological changes are driven by the variation of the internal chemical pressure and cell volume dependent on the A alkali size. It is striking that the scheme of FM and AFM magnetic exchanges effective in the individual sub-units return $S = 1$ magnetic clusters in both cases, themselves interacting in 2D layers, rather than in 1D chains due to specific Cu-O-O-Cu magnetic paths.

Ideally one could imagine for $x = 1$ the occurrence of infinite chains, not observed experimentally, as probably hampered by the mismatch between such 1D-units and the coordination of all Cu^{2+} ions by the sulfate groups. The exact nature of the magnetic ground state in $Cs_2Cu_{3.5}O_{1.5}(SO_4)_3$ remains an open question and requires additional studies using neutron scattering or local probes. While an AFM order in the bc-plane may be expected from the similarity to the Na and K compounds, the vanishingly small magnetic interactions between the planes and the incomplete structural order of the intercalated CuO units may cause deviations from this simple scenario. One should keep in mind the similar ambiguity in the A = K compound, where NPD results (Hase et al., 2019) revealed magnetic ordering, not detected by specific heat with a Schottky-like anomaly around T_N. In this compound, it was previously concluded that the role of the magnetic anisotropy of the $S = 1$ clusters is predominant at T_N in absence of inter-layer exchanges, Similarly the anisotropy of the Cu_{14} $S = 1$ clusters may also be significant for A = Cs.

7. Remarkable polymorphism in a family of $A_2M_3(SO_4)_4$ (*A* = Rb, Cs *M* = Co, Ni)

7.1 Introduction

To date, there are only three cesium/rubidium transition metal sulfates compounds referenced on literature: $(Cs,Rb)_2(Ni,Co)(SO_4)_2$, $6H_2O$ (Lim & Kim, 2009) and $Rb_2(Co,Ni)_2(SO_4)_3$. A new family of compounds with a general formula $A_2M_3(SO_4)_4$ where *A* –alkali metal, *M* –transition metal, (*A* = Rb, Cs and *M* = Co, Ni) belong to the prototype mineral itelmenite $Na_2CuMg_2(SO_4)_4$ (Nazarchuk et al., 2018). In the main chemical systems investigated, there is a lack concerning those based on cesium and rubidium. On the next chapter we will discuss in more detail geochemistry of Rb in volcanic environments.

In this chapter we present the results on the obtention and study of the 4 crystal structures $Cs_2Ni_3(SO_4)_4$**(1),** $Cs_2Co_3(SO_4)_4$ **(2),** $Rb_2Ni_3(SO_4)_4$(**3**)**,** $Rb_2Co_3(SO_4)_4$(**4**). Our trials to obtain the corresponding pure powder samples are also detailed through High Temperature X-Ray diffraction analysis and thermal analysis.

7.2 Synthesis

7.2.1 Synthesis of crystals of $Cs_2M_3(SO_4)_4$, M = Ni **1** *and Co* **2**

Crystals of $Cs_2Co_3(SO_4)_4$ and $Cs_2Ni_3(SO_4)_4$ were obtained by solid-state reaction in air using stoichiometric ratio of Cs_2SO_4, and MSO_4 *M* = Co and Ni (dehydrated at 400°Cover the night). The mixture was ground and loaded into a gold crucible and heated to 600 °C for 3 hours and then cooled to 25 °C during 12 hours for the cobalt phase and to 700 °C during 10 hours and further slowly cooled to room temperature for 99 hours for the nickel one. The products consisted of prismatic yellow unshaped crystals of **1** with Cs_2SO_4 and $NiSO_4$ for the nickel one and purple crystals of the new **2** assorted with $Cs_2Co_2(SO_4)_3$ for the cobalt sample.

7.2.2 Synthesis of crystals of $Rb_2M_3(SO_4)_4$ M = Ni **3** *and Co* **4**

Crystals of **3** and **4** were obtained using Rb_2SO_4 and MSO_4(*M* = Ni, Co) (also dehydrated at 400°C during the night) reagents in stoichiometric ratio. The mixtures of precursors were ground, pressed into pellets (ca. 5*3 mm) and loaded into a quartz tube (ca. 8*0.8 mm) which was evacuated and sealed at an approximate pressure of 10^{-2} mbar. The quarts ampules were placed into the furnace and heated at 750 °C during 18 hours for **3** and 34 hours for **4** and then slowly cooled to room temperature during 99 hours. The products consisted of yellow crystals of $Rb_2Ni_3(SO_4)_4$ (this work), $Rb_2Ni_2(SO_4)_3$

(Materials Data on $Rb_2Ni_2(SO_4)_3$) and unreacted $NiSO_4$ and violet crystals of $Rb_2Co_3(SO_4)_4$, $Rb_2Co_2(SO_4)_3$ and $Co(SO_4)$.

7.2.3 Powder synthesis

Several trials to obtain polycrystalline samples were performed from stoichiometric amounts of $(Rb/Cs)_2SO_4$ and MSO_4 (M = Ni, Co) (also dehydrated at 400°C during the night) heated at several temperatures during variable durations. The strategy of synthesis is developed in the text and all attempts are summarized in **Table 1.**

7.3 Single-crystal X-ray analysis

Single crystals of the respective compounds were mounted on thin glass fibers for X-ray diffraction analysis using Bruker APEX II DUO X-ray diffractometer working with a microfocus X-ray tube equipped with Mo Kα radiation and working at 50 kV and 40 mA. The data were integrated and corrected from absorption using a multiscan type model implemented in the Bruker programs APEX3 (version 2018.1-9, Bruker AXS, Madison, Wisconsin, USA) (Adam et al., 2015). More than a hemisphere of X-ray diffraction data was collected for each crystal. The crystal structures of synthetic compounds were solved by direct methods and refined using the SHELXL-2018 program (version 2018/3) implemented in the WinGX software (version 2018.3) (Sheldrick, 2015) program package. Main crystallographic information for the new phases are summarized in **Table 16**. Atom coordinates, bond-valence sums, thermal displacement parameters and selected interatomic distances for all crystal structures are provided in Supporting Information (**Tables S18–S22**).

7.4 Structure description of $Cs_2Ni_3(SO_4)_4$ (1)

The crystal structure of **1** was solved in the monoclinic non-centrosymmetric space group $P2_1/n$ with unit cell parameters: a = 5.410(5), b = 18.444(16), c = 7.618(7) and β = 104.56(3)°. There are two symmetrically independent Ni^{2+} crystallographic sites involved in two NiO_6 octahedra: $Ni2O_6$ sharing edges with another $Ni2O_6$ unit and $Ni2O_6$ sharing corners with $Ni1O_6$, building thus a 2D sheet (see **Figure 61**a)) parallel to the *ac* plane. $Ni1O_6$ is quite regular with average <Ni-O> bond length around 2.08 Å, whereas the other octahedra are relatively distorted not from the point of view of Ni-O bond distances (<Ni-O>= 2.079 Å) but because of O-Ni-O angles deviations (from 67 to 101° although it has to be almost orthogonal), probably induced by the edge pooling (see **Figure 62**a)). The Ni-Ni distances are quite large, mainly between 3.26 and 3.62 Å as shown on **Figure 1a**), but magnetic couplings are possible through Ni-O-Ni connection. There are two different SO_4 tetrahedra, S^{6+}-O bond lengths lying between 1.44 and 1.52Å and O-S^{6+}-O bond angles from 102 to 112°. The sulfates are connected through

corner sharing and also $S1O_4$ sharing edges with $Ni2O_6$. The sulfates are pointing outwards the layer (see **Figure 61**b)). The distance between the two layers is 3.01 Å, measured as the shortest O_3S-O…O-SO_3 distance.

Cesium atoms are located in the interlayer space and balance the charge of the layer. They are surrounded by 8 oxygens forming irregular polyhedral, where the Cs-O bond lengths are in the range of 3.043(5) − 3.449(5) Å.

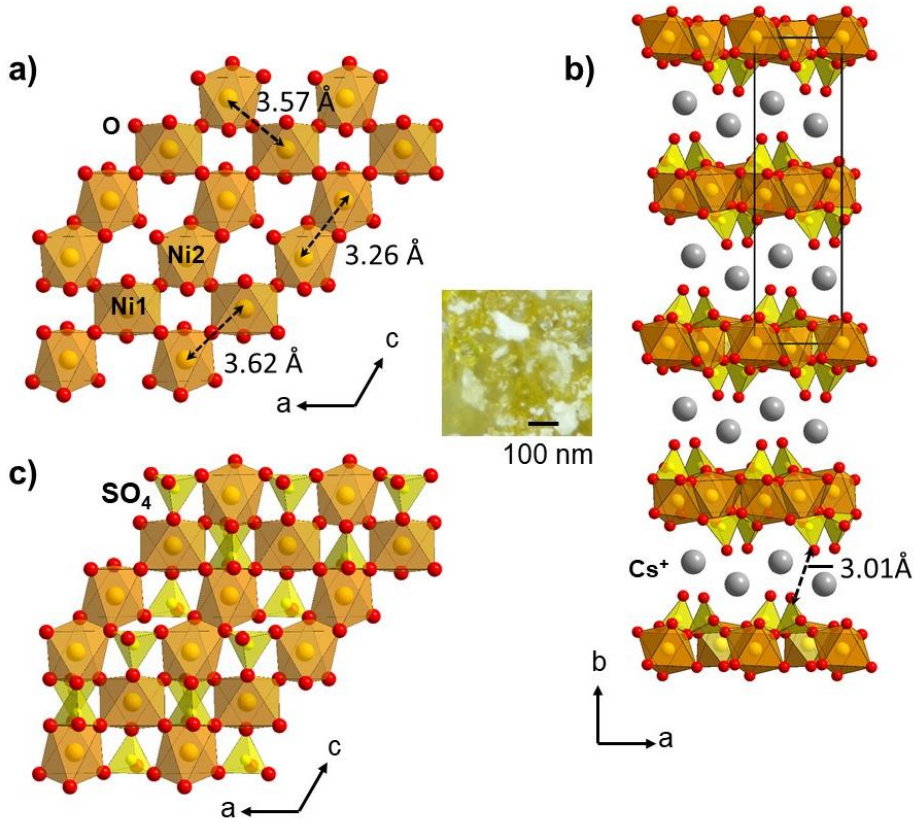

Figure 61. 2D blocks in **1** projected on the *ac* plane with (a) NiO_6 octahedra (in orange) connected to (b) SO_4 tetrahedra (in yellow) and (c) general projection of the crystal structure of **2** along *c*-axis, showing the stacking and the interstitial Cs^+ cations (in grey). The photo in insert shows the color and shape of crystals.

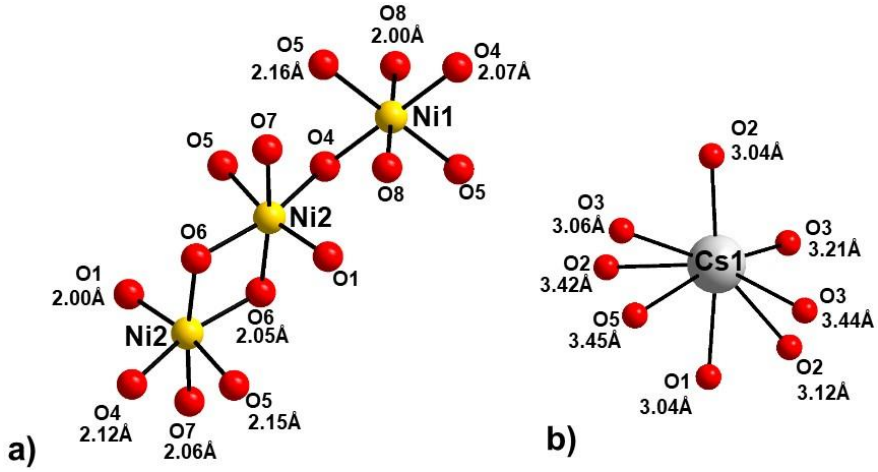

Figure 62. Coordination of a) Ni^{2+} and b) Cs^{+} cations in the crystal structure of **1**.

7.5 Structure description of $Cs_2Co_3(SO_4)_4$ (2)

2 crystallized in an orthorhombic symmetry with unit cell parameters: *a* = 9.0576(8) Å, *b* = 9.9193(7) Å and *c* =15.8622(13) Å (S.G. $P2_12_12_1$). The structure has two symmetrically independent Cs^{+}, three Co^{2+}, and four S^{6+} cations. The atoms Co1 and Co3 have octahedral coordination with the bond lengths ranging from 2.044(4) to 2.200(4)Å for Co1 and from 1.999(4) to 2.240(3)Å for Co3 (**Figure 63** a)). The atom Co2 formed a regular square pyramid CoO_5 with bond lengths going from 1.995(3) to 2.109(3) Å. $Co2O_5$ and $Co3O_6$ polyhedra are connected together through corner pooling (O10) forming $[Co_2O_{10}]^{16-}$ dimers (**Figure 63** a)). The sulfur atoms are tetrahedrally coordinated by oxygen atoms with the S–O distances lying from 1.431(4) to 1.482(3) Å. SO_4 tetrahedra are linked with cobalt polyhedral through common oxygen atoms for S1, S3 and S4 and through edge sharing for S2, forming a final 3D framework (**Figure 64**b) and c)). Cs atoms are located in the empty spaces. Cs^{+} cations are surrounded by ten O^{2-} anions with the Cs-O bond lengths in the range of 3.027(4)–3.482(5) Å for Cs1 and 3.058(4)–3.416(4) Å for Cs2 (**Figure 63**b)). The final crystal structure is shown (**Figure 64**d).

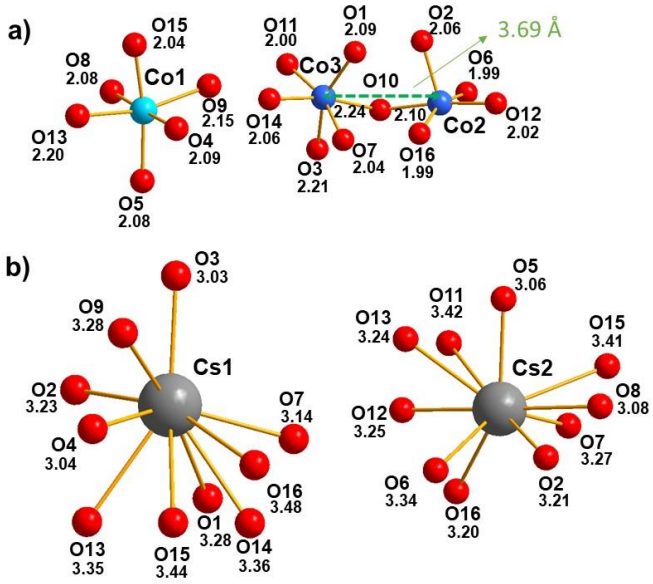

Figure 63. Square pyramid coordination of the Co2 and octahedral coordination of the atoms Co1 and Co3 and (a). Cs1 and Cs2 complex environments (b).

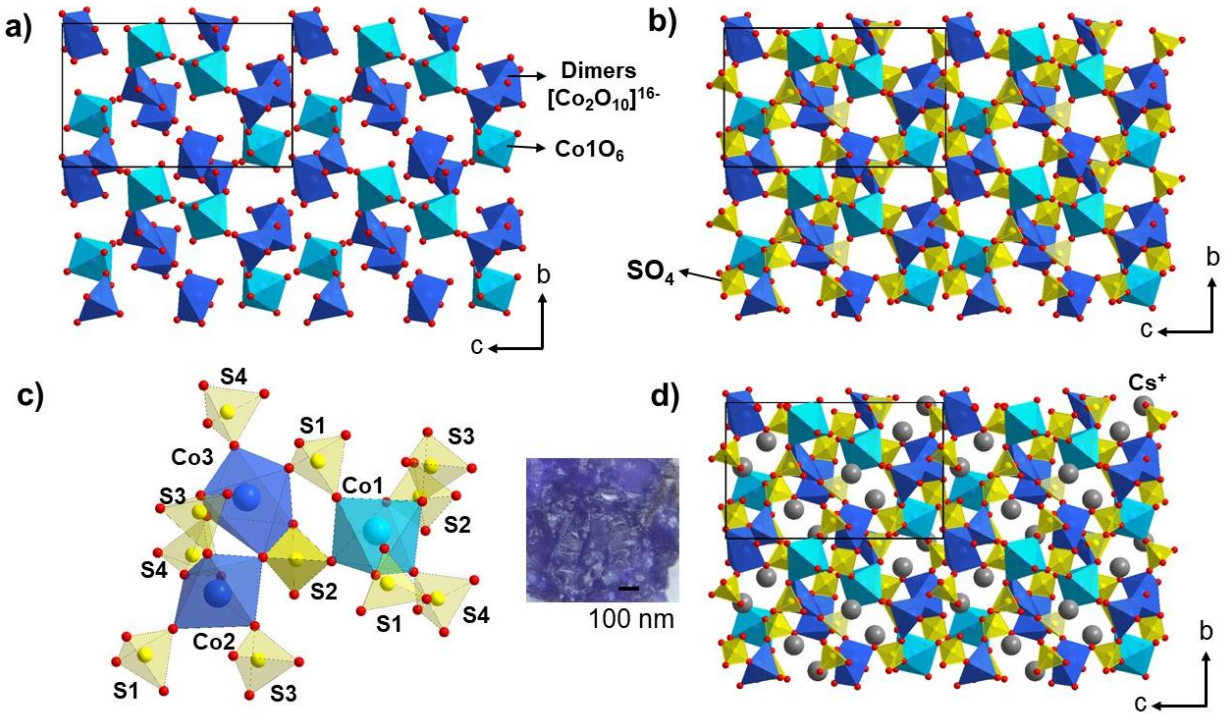

Figure 64. (a) Association between Co_2O_{10} dimers (dark blue) and CoO_6 octahedra (turquoise blue) in bc plane and (b) connected to SO_4 tetrahedra (yellow). (c) the connectivity between the different polyhedral is detailed and (d) the whole structure with the Cs^+ cations (in grey) is shown along *a*-axis.

Table 16. Single crystal and structure refinement data for $A_2M_3(SO_4)_4$(A = Rb, Cs; M = Co, Ni).

Crystal data	$Cs_2Ni_3(SO_4)_4$	$Cs_2Co_3(SO_4)_4$	$Rb_2Ni_3(SO_4)_4$	$Rb_2Co_3(SO_4)_4$
sp. gr.	$P2_1/n$	$P2_12_12_1$	$P2_1/c$	$P2_1/c$
a [Å]	5.399(2)	9.0576(8)	9.2661(15)	9.3678(4)
b [Å]	18.340(7)	9.9193(7)	8.5703(13)	8.6386(3)
c [Å]	7.596(3)	15.8622(13)	9.2865(15)	9.3763(6)
β [°]	104.581(8)		119.009(3)	119.1660(10)
V [Å^3]	727.9(5)	1425.1(2)	644.95(18)	662.57(6)
Z	2	2	2	2
ρ_{calc} [Mg/m^3]	3.769	3.854	3.766	3.669
μ [mm^{-1}]	9.429	4.791	12.577	11.736
Data collection				
F(000)	772	1532	700	694
θ range [°]	2.985 – 26.492	2.026 – 27.999	2.513 – 35.846	2.490 – 47.320
hkl limits	–6 → 6	–15 → 15	–10 → 15	–16 → 18
	–22 → 22	–15 → 16	–14 → 14	–17 → 16
	–9 → 9	–26 → 26	–15 → 12	–17 → 15
totalrefln.	8039	62948	9305	20415
Unique refln. (R_{int})	1498	7020	2939	5064
	0.06	0.07	0.04	0.05
Refinement				
R_1 [$F > 4\sigma F$],	0.04	0.03	0.03	0.04
wR_2 [$F > 4\sigma F$]	0.08	0.05	0.06	0.06
R_1 all,	0.06	0.05	0.06	0.07
wR2 all	0.09	0.06	0.06	0.07
GoF	1.035	1.072	1.047	1.047
$\Delta\rho_{max}$,	0.848	1.071	1.067	1.097
$\Delta\rho_{min}$ [e·Å^{-3}]	-0.847	-1.819	-0.936	-2.108

The two crystal structures show different dimensionality, Ni-based phase being 2D and the cobalt on being 3D.

7.6 Structure description of $Rb_2M_3(SO_4)_4$, *M*= Ni (3) and Co (4)

The crystal structure of **3** and **4** are isotypic and adopts a monoclinic symmetry. The unit cell parameters are a = 9.2661(15) Å, b = 8.5703(13) Å, c =9.2865(15) Å, β =119.01(°) and the space group is $P2_1/c$. The two structures contain one independent crystallographic position for Rb^+, two for S^{6+} and M^{2+} (M = Ni and Co). The specific environments of cations are gathered in **Figure 65**. The rubidium atoms are coordinated by eight O^{2-} with Rb-O bond lengths in the range of 2.7751(18)–3.1300(18) Å in the crystal structure of **3** and of 2.8072(13)–3.1426(14) Å in the crystal structure of **4.** The atoms Co1 and Co2 have an octahedral coordination with bond lengths ranging from 2.0112(13) to 2.1874(13) Å for Co1 and 1.9990(13) to 2.3938(13) Å for Co2. The nickel atoms are also octahedrally coordinated with bond lengths varying from 1.9856(17) to 2.1481(17) Å for Ni1 and from 1.9759(17) to 2.3770(17) Å for Ni2. The MO_6 octahedra are connected together through corners sharing, building isolated $[M_3O_{16}]^{26-}$ trimers (see **Figure 65**a)).

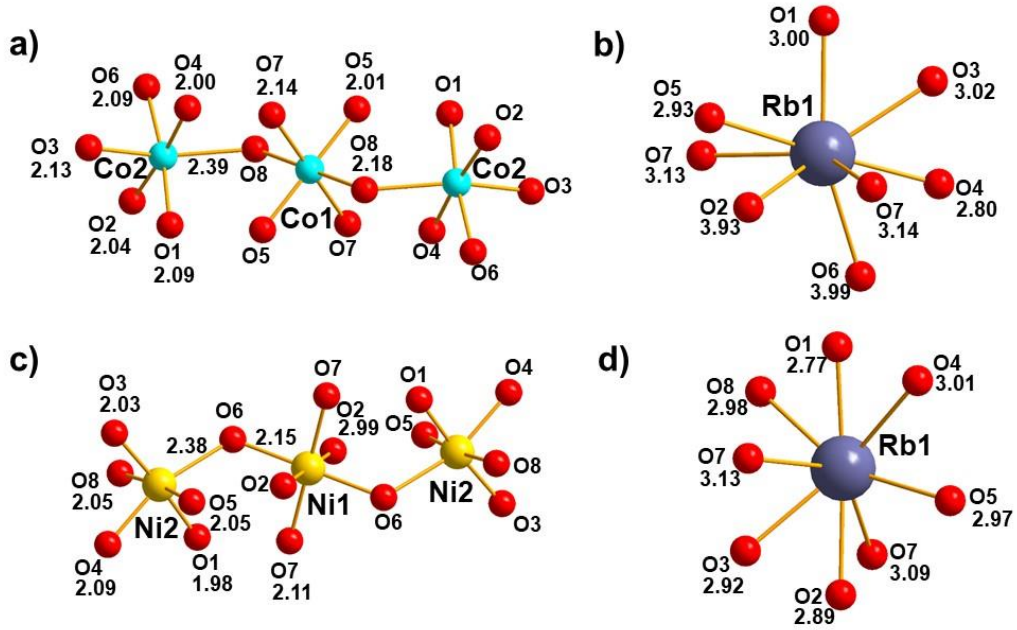

Figure 65. MO_6 octahedra sharing corners giving M_3O_{16} trimers (a) in **4** (M = Co) and (c) in **3** (M = Ni) and Rb^+ environments (b) in **4**, and (d) in **3**. The cation-oxygen bond distances are given.

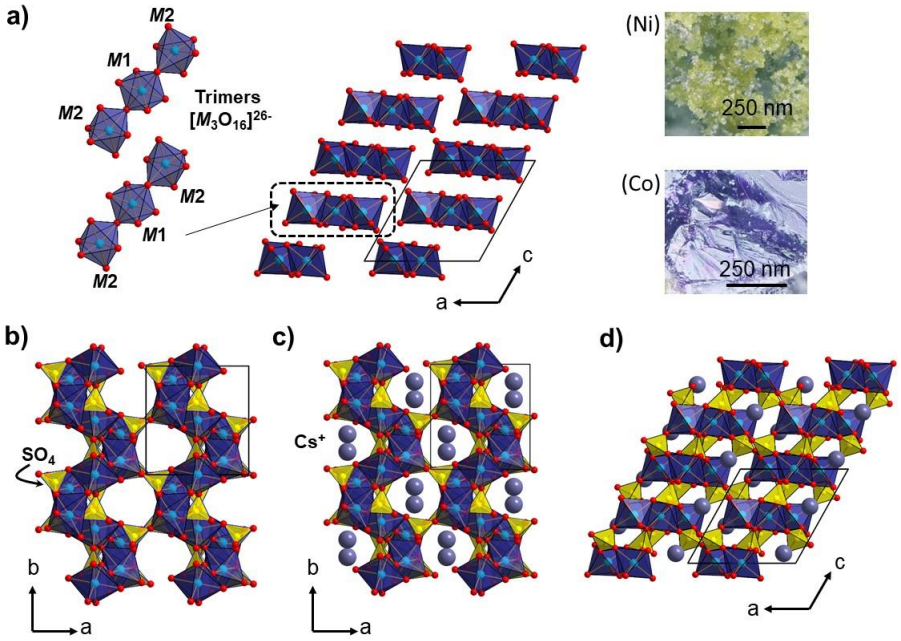

Figure 66. (a) M_3O_{16} trimers (in blue) and their association in the *ac* plane, (b) association of SO_4 tetrahedra (in yellow) to the trimers, building 1D cavities running along *c*-axis, these cavities are hosting Cs^+ cations (in grey) and the final crystal structures are shown along (c) *c*- and (d) *b*-axis. In insert, the photos show the crystal shapes of Co and Ni compounds.

7.7 Comparison of synthetic and natural phases

These new phases are directly inspired from the crystal structures of itelmenite $Na_2CuMg_2(SO_4)_4$ and its synthetic Mg and Zn-analogue (Nekrasova et al., 2021). Both of them have three *M* sites: *M*1 and *M*2 are at the center of MO_5 distorted tetragonal pyramid with *M*-O bonds in the range of 1.95-2.16 Å and *M*3 sites are surrounded by six O atoms octahedrally coordinated and with *M*–O distances in the range 2.08-2.17 Å. *M*1 and *M*2 can be described as Jahn-Teller-distorted MO_{5+1} coordination. *M*3 site has symmetrical octahedral coordination with two slightly elongated apical bonds of 2.15-2.29 Å. MO_6 polyhedra have different distortion depending on the amount and nature of atom sitting on the same site. Indeed, Cu:Mg ratios on the different *M* sites were previously refined in (Nekrasova et al., 2021) (**Figure 67**). Cu^{2+} cation dominates in *M*1 site, whereas only 22.5% of copper is present in *M*2. The *M*3 site is almost completely occupied by Mg^{2+} cations in $Na_2CuMg_2(SO_4)_4$ in agreement with very symmetrical coordination environment. In the case of itelmenite, the distortion is controlled by the composition itself and by the Cu^{2+} Jahn-Teller distortion (**Figure 67**). All polyhedral are linked together through corner sharing, forming a 2D framework running along *b*-axis. To conclude, each crystal structure shows one symmetric polyhedron, the others been distorted from the regular octahedral.

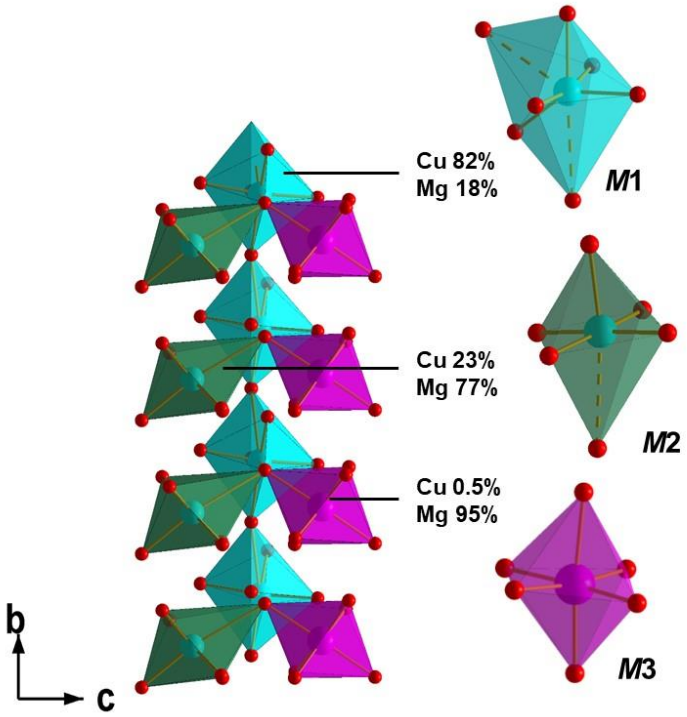

Figure 67. Coordination of *M* sites in the crystal structures of synthetic itelmenite (Nekrasova et al., 2021) and chemical composition for each side.

The different environments of the transition metals are summarized in **Table 17** as well as the frameworks they are building together. In itelmenite the polyhedrons are isolated, linked through corner sharing in **1**, forming dimers in **2** and trimers in **3** and **4**. The tentative of rationalization and establishment of a relation between the nature of alkaline and transition metals is not obvious. No special criteria (ionic radii of alkaline, ionic radii of transition metal) appear to be convincing.

Table 17. Comparison of the environments of transition metals in itelmenite phase and in the new crystal structures of this work.

Crystal structure	Type of polyhedra			Nature of blocks
itelmenite $Na_2M_3(SO_4)_4$	$M1$ $M1O_5$	$M2$ $M2O_5$	$M3$ $M3O_6$	isolated
$Cs_2Ni_3(SO_4)_4$(1)	$Ni1O_6$	$Ni2O_6$		linked into 2D framework.
$Cs_2Co_3(SO_4)_4$ (2)	$Co1O_6$	$Co2O_5$	$Co3O_6$	Co3 and Co2 form $[Co_2O_{10}]^{16}$ dimers
$Rb_2Ni_3(SO_4)_4$ (3)	$Ni1O_6$	$Ni2O_6$		linked into $[Ni_3O_{16}]^{26-}$ trimers
$Rb_2Co_3(SO_4)_4$ (4)	$Co1O_6$	$Co2O_6$		linked into $[Co_3O_{16}]^{26-}$ trimers

Comparing the different structure types, the nature of alkali and transition metal necessarily affect the crystal structure and its complexity. This can be quantified using the calculation developed by Krivovichev (Krivovichev, 2012) and based on the Shannon information theory and depending of the unit cell and its number and nature of atoms. The total structural information amount ($I_{G,total}$ (bits/unit-cell)) of all structures were calculated using ToposPro (Blatov et al., 2014). **1**, **3** and **4** show similar structural complexity with $I_{G,total}$= 184.193 bit/cell. Concerning **2**, $I_{G,total}$ is equal to 464.386 bit/cell which is higher than the three other phases. Of course, this is strongly related to the modification of the crystal system assorted with the more or less doubling of the unit cell volume. Again, there is no obvious relation between the calculated complexity and the nature of alkali or transition metals. This level of complexity is called "intermediate" as mentioned by Krivovichev in (Krivovichev, 2012) as around 23% of inorganic structures.

The presence of dimers and trimers appears to be interesting as it may give rise to interesting magnetic coupling as suggested by the Goodenough-Kanamori rules. Consequently, a strong attention was payed to the obtention of the pure powder samples.

7.8 Phases stability phases 1 and 2

In order to get the pure powder sample, the reactivity of precursors was analyzed using thermogravimetric analysis and HTXRD. HTXRD studies were performed up to 550° to avoid melting of the sample in the sample holder.

A mixture of Cs_2SO_4, $NiSO_4$ in 1:3 ratio was prepared and the TGA and DTG analysis were performed under air atmosphere. The sample was heating at 10°C/min form 30°C up to 1000°C. The TGA curve presented on **Figure 68**a) evidenced several accidents at 90 and 110 °C consistent with the loss of water molecules of the precursors as already detailed in (Boyanov, 2002). Thus, it is almost

impossible to avoid water absorption from humid air, even if precursors are exposed during the shortest time possible. In agreement with HTXRD results (see **Figure 68b**)), there are transitions occurring around 50 and 150°C and corresponding to water molecules removal on precursors of **1**. A phase transition is then observed at 350 °C corresponding to the growth of $Cs_2Ni_3(SO_4)_4$ assorted with unreacted precursors: Cs_2SO_4 and $NiSO_4$. At 700°C, a weight loss is observed on TGA analysis corresponding to the decomposition through the removal of sulphate molecules. Details of patterns identification are given in **Figure 70**a for **1**.

A similar analysis was done on **2** working from a mixture of Cs_2SO_4, $CoSO_4$ in 1:3 ratio (TGA on **Figure 68c**) and HTXRDP **Figure 68d**)). Finally, the same general behaviour was observed: first, the dehydratation of precursors where the these low-temperature peaks (from 91 °C to 330 °C) occur due to the a two-stage dehydration processes: in the first stage at 91 °C the six molecules of water are dismissed and at the temperature of 329 °C (second stage of the process) the last seventh molecule is discharged. The event at 146 °C may be related to partial melting of the sample. Exothermic peak at 531 °C correspond to the recrystallization and forming of $Cs_2Co_3(SO_4)_4$, $Cs_2Co_2(SO_4)_3$. Endothermic peak at 850 °C is belong to decomposition process of sulfates compounds. Details of patterns identification for all stages are given in **Figure 70**b for **2**.

Several trials were performed with temperatures of synthesis chosen on the plateau of the TGA: 600 °C and 700 °C for **1** and 530 °C, 560 °C and 600 °C for **2**. All of them led to the synthesis of the targeted phase but systematically assorted with impurities as detailed on **Table 18**.

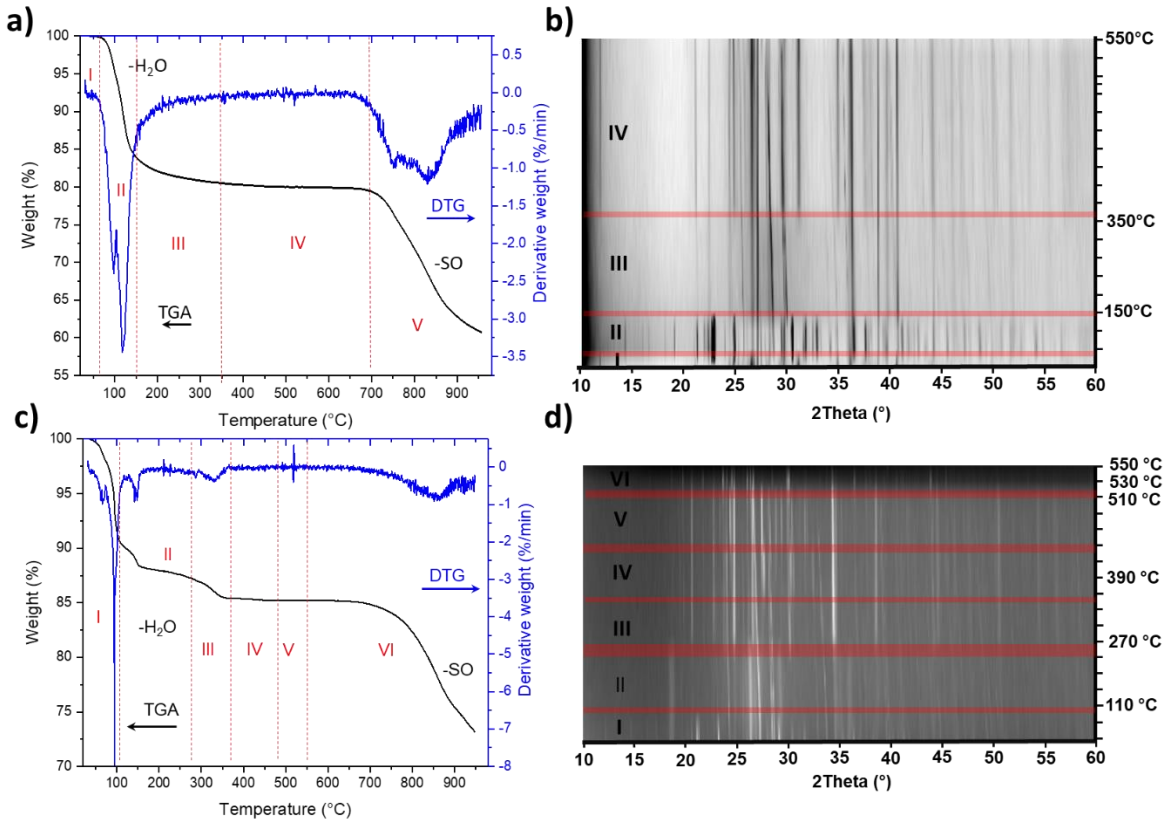

Figure 68. TGA-DTA curves from 30 °C to 1000 °C for the mixture of precursors for **1** (a) Cs_2SO_4, $NiSO_4$ and for **2** (c) Cs_2SO_4, $CoSO_4$ in 1:3 ratio, an HTXRD study explained the transitions of in the case of (b) **1** and (d) **2**. For **1**, step I- II correspond to the dehydratation process, step III - IV to the formation of $Cs_2Ni_3(SO_4)_4$ and step V to the collapse of the sample by sulfate removal (a, b). For **2**, step I - II correspond to the dehydratation process, where sixth water molecule is discharged, step III to lost seventh molecule, IV-V - formation of $Cs_2Co_3(SO_4)_4$ and $Cs_2Co_2(SO_4)_3$, VI – decomposition process (HTXRD from 30 °C to 350 °C with step 40 °C, 350-550 °C - step 20 °C).

Table 18. Summary of the different syntheses attempted to prepare the title compounds and obtained phases.

Formula	Preparation method T(°C)	Duration (h)	Cooling time (h)	XRDP analysis
$Cs_2Ni_3(SO_4)_4$	a) 700	10	96 to 500°C and 5 to 25°C	a) $Cs_2Ni_3(SO_4)_4$, Cs_2SO_4.
	b) 600	2	10 to 100°C	b) $Cs_2Ni_3(SO_4)_4$, Cs_2SO_4, $NiSO_4$
$Cs_2Co_3(SO_4)_4$	a) 600 °C	3	12 to 100°C	a) $Cs_2Co_3(SO_4)_4$, $Cs_2Co_2(SO_4)_3$, $CoSO_4$
	b) 560	3	Quenched	b) $Cs_2Co_3(SO_4)_4$, $Cs_2Co_2(SO_4)_3$
	c) 530	2	60 to 100°C	c) $Cs_2Co_3(SO_4)_4$, $Cs_2Co_2(SO_4)_3$
$Rb_2Ni_3(SO_4)_4$	a) 750 °C	18	96 to 500°C	a) $Rb_2Ni_3(SO_4)_4$, Rb_2SO_4.
		1.5	10 to 100°C	b) $Rb_2Ni_3(SO_4)_4$, $Rb_2Ni_2(SO_4)_3$

	b) 600 c) 600°C d) 600 e) 600	24 24 6	10 to 100°C 70 to 500°C and 10 to 25°C Furnace off	c) $Rb_2Ni_2(SO_4)_3$, $NiSO_4$ d) $Rb_2Ni_3(SO_4)_4$, $Rb_2Ni_2(SO_4)_3$, $NiSO_4$ e) $Rb_2Ni_3(SO_4)_4$, $Rb_2Ni_2(SO_4)_3$, $NiSO_4$
$Rb_2Co_3(SO_4)_4$	a) 750 b) 600 c) 600	34 1.5 24	40 to 200°C 10 to 100°C 10 to 100°C	a) $Rb_2Co_3(SO_4)_4$ $Rb_2Co_2(SO_4)_3$ b) $Rb_2Co_3(SO_4)_4$, $Rb_2Co_2(SO_4)_3$, $CoSO_4$ c) $Rb_2Co_3(SO_4)_4$, $Rb_2Co_2(SO_4)_3$, $CoSO_4$

7.9 Phases stability phases 3 and 4

Again, a similar procedure was used to try to synthesize pure powder samples of **3** and **4** and again, the results highlight for **3**. Dehydratation of precursor $NiSO_4,6H_2O$ is a three-stage process: at 91 °C two molecules of water are dismissed and further another three molecules at about 140 °C (**Figure 70c**). The last last sixth water molecule is discharged at a temperature of 310 °C. Endothermal effects at 420 °C and 435 °C correspond to the formation of $Rb_2Ni_2(SO_4)_3$ and $Rb_2Ni_3(SO_4)_4$ (step IV and V, VI), at 790 °C (step VII) – it is decomposition process in **Figure 70**c.

For the mixture of precursors of **4** we can see four endothermic peaks (**Figure 69**a-b) : at a temperature of 100 °C the six molecules of water from $Rb_2Co(SO_4)_2,6H_2O$ are dismissed and at the temperature of 334°C the one molecule of $CoSO_2,H_2O$ is discharged with the formation of $Rb_2Co_2(SO_4)_3$. An endothermic peak at 521°C correspond to obtention of $Rb_2Co_3(SO_4)_4$. Last Endothermal effects at 816 °C and 888 °C correspond to the two-stage decomposition on simple oxides CoO and undetectable phases. Again, detailed XRD patterns are presented in **Figure 70**d.

At the end, changing the synthesis conditions (temperature in the accurate zone of heating, duration or cooling) never allowed to obtain the pure phase. Also, in the case of **2** and **4** there is like a demixing of a part of $A_2M_3(SO_4)_4$ leading to the presence of the wanted $A_2M_3(SO_4)_4$ assorted with the sub products $A_2M_2(SO_4)_3$ + MSO_4. Despite many attempts, the synthesis of the pure powder samples systematically failed for thermodynamical reasons. Other trials will focus on other type of synthesis, for example using hydrothermal synthesis, inducing other media and other thermodynamical process.

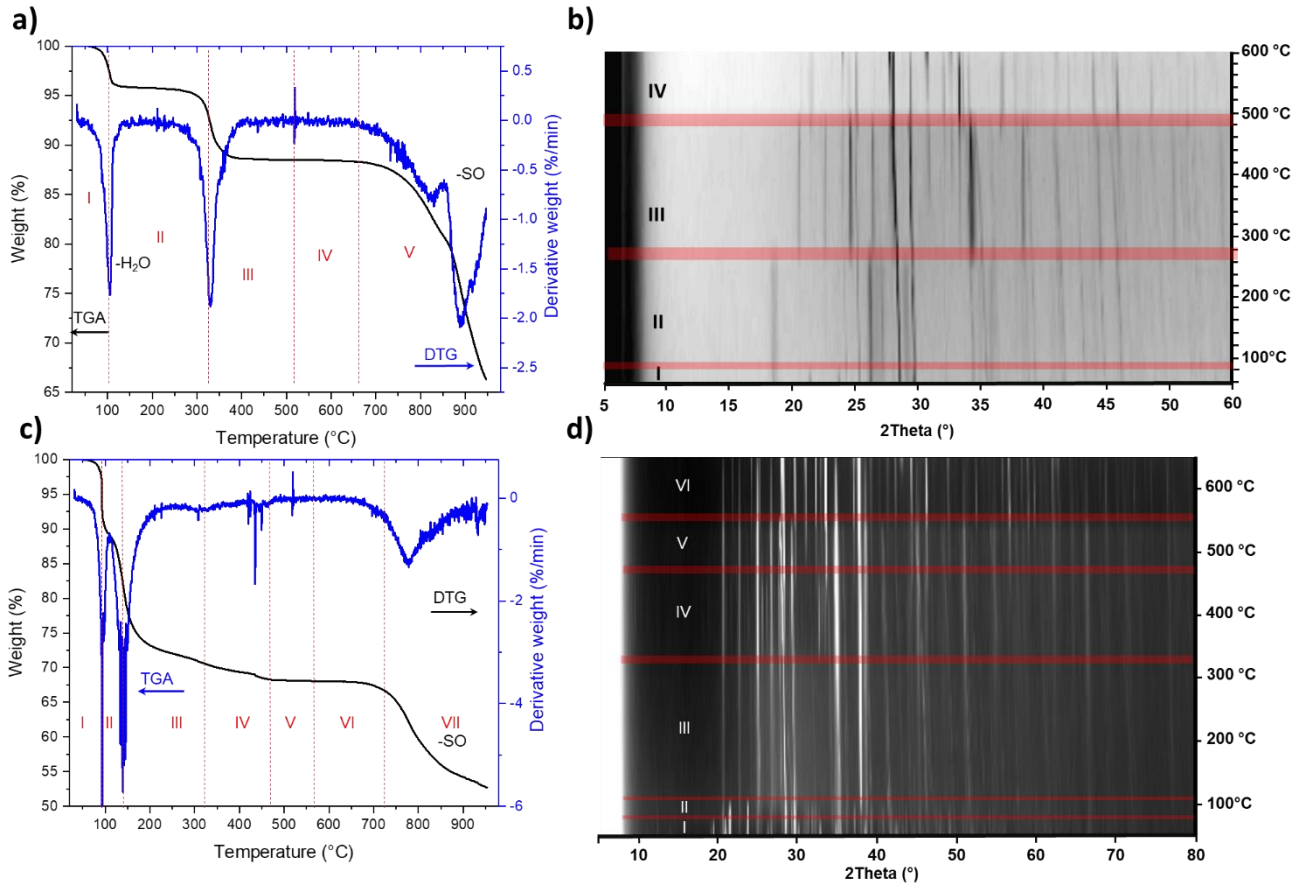

Figure 69. (a) TGA-DTA curves for mixture of precursors for **4** from 30 °C to 1000 °C (Rb_2SO_4, $CoSO_4$ in 1:3 ratio), where I - II - hydrated precursors, III – anhydrous precursors and formation of $Rb_2Co_2(SO_4)_3$, IV – formation of $Rb_2Co_3(SO_4)_4$, V - decomposition (a, b). And for **3** I – III steps correspond to the dehydration of $NiSO_4$, $6H_2O$ as three-stage process, step V-VI – formation of $Rb_2Ni_2(SO_4)_3$ and $Rb_2Ni_3(SO_4)_4$, step VII - decomposition

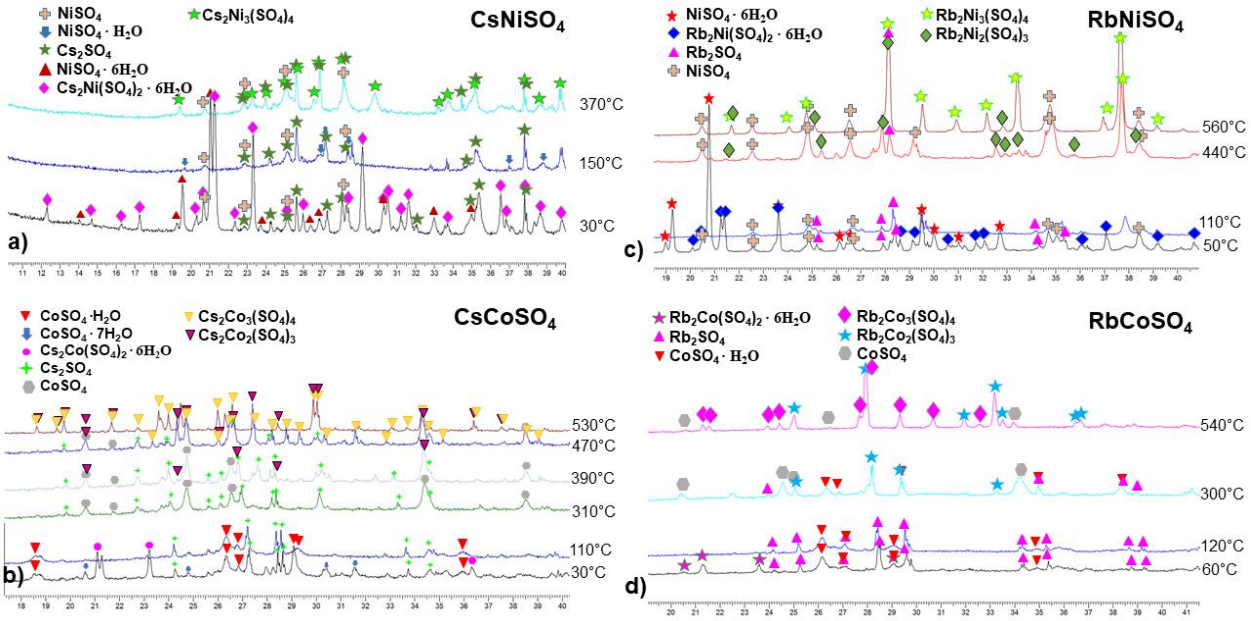

Figure 70. Detailed XRD patterns of a) formation $Cs_2Ni_3(SO_4)_4$ b) formation $Cs_2Co_3(SO_4)_4$ c) formation $Rb_2Ni_3(SO_4)_4$ d) formation $Rb_2Co_3(SO_4)_4$

7.10 Conclusion

In this part we considered the results of remarkable polymorphism in a family of $A_2M_3(SO_4)_4$ (A = Rb, Cs M = Co, Ni). This series of compound were synthesized by inspiration of mineral itelmenite, $Na_2CuMg_2(SO_4)_4$. New compounds were obtained by solid-state synthese and structurally characterized by single and powder X-ray diffraction. In order to establish the temperature of crystallization of synthetic phases differential thermal analysis combined with thermogravimetric analyses were directly performed on mixtures of precursors. Obtaining synthetic analogues of known sulfate minerals helps to understand the principle of mineral formation and to project the synthesis. This is very important from the point of view of fundamental science. It can help to solve complex crystal structures or to make a model system for an investigation of various physical properties in the laboratory, when it is difficult to obtain samples with a good crystallinity and sufficient amount in nature. It is not always possible to synthesize a pure powder sample, as has been demonstrated in this chapter. The formation of one or another phase is controlled by thermodynamic states and phase diagrams, which are only to be studied in the near future. The next part will consider the mechanisms of formation of fumarolic minerals in terms of geochemistry.

8. Anhydrous alkali copper sulfates – a promising playground for new Cu^{2+} oxide complexes: new Rb-analogues of fumarolic minerals related compounds

8.1 Introduction

10 years ago, the amount of structurally characterized anhydrous sulfates of copper and alkali metals was very limited. Most of the known compounds belonged to minerals from volcanic fumaroles. Despite a significant number of articles on copper and alkali metal sulfates that have appeared in the last few years, rubidium sulfates are almost unknown. It is known that, in the series of alkali metals from Na to Cs in the structures of oxides and oxysalts the phenomenon of morphotropism is commonly observed. As a rule, potassium and rubidium representatives are isostructural, while sodium and cesium ones can demonstrate own structure types.

In this chapter we present the results on the obtention and study of the 4 crystal structures (Siidra et al., 2021): $Rb_2Cu(SO_4)Cl_2$, $Rb_4Cu_4O_2(SO_4)_4{\cdot}(Cu_{0.83}Rb_{0.17}Cl)$, $Rb_2Cu_2(SO_4)_3(H_2O)$ and $Rb_2Cu_5O(SO_4)_5$. One of the goals of this work was also an analysis and a brief review of the geochemistry of rubidium in volcanic environments. This is discussed in the chapter below.

8.2 Geochemistry of rubidium in volcanic environments

Quaternary arc volcanism on the Kamchatka peninsula, Russia, produced huge volume of basaltic rocks which form numerous large volcanoes and monogenetic volcanic fields. Among the active volcanoes the most known and well studied is the Tolbachik volcanic complex; it is a part of the Klyuchevskaya Volcanic Group in Central Kamchatka Depression (Churikova et al 2015a and references herein). Tolbachik complex consists of two stratovolcanoes, exctinct Ostry Tolbachik and active Plosky Tolbachik, and monogenetic volcanic field known as Tolbachinsky Dol. The latter was formed during several eruptions including Great Fissure Tolbachik Eruption in 1975–76 and Tolbachik fissure eruption in 2012–2013 (Volynets et al 2015).

The large volume of erupted lavas due to Tolbachik's recent activity are well studied in terms of their mineralogy and geochemistry, including direct sampling during eruptions. (Churikova et al 2015a and references herein). The Tolbachik lavas and scoria consist of basalts and basaltic andesites with subordinate trachybasalts and basaltic trachyandesite. Basalts, on the basis of potassium content, are subdivided into medium- and high-K varieties, and another basalt subdivision is based on MgO/Al_2O_3 ratio into high-magnesian, high-alumina and intermediate rocks. Published whole-rock geochemical data (e.g. Churikova et al 2015b, Volynets et al 2015) show large variations in content of both major and trace elements, e.g. MgO = 2.1-10.7 wt.%, Na_2O = 2.3-4.2 wt.%, K_2O = 0.7-3.1, Cr = 7-745 ppm.

Unusual geochemical feature of the Tolbachik basalts is their enrichment in copper with 100-250 ppm in bulk rock samples (Portnyagin et al 2015). On multi-elements normalizing diagrams (relatively to N-type of mid-ocean ridge basalts) the Tolbachick basaltic rocks show enrichment in large ion lithophile elements (e.g. Cs, Rb, Ba) and depletion in high field strength elements (e.g. Nb, Ta). This is considered to be a typical signature of subduction related magmas (Churikova et al 2001). Mineralogy, trace element geochemistry and data from Sr–Nd–Pb isotopic studies suggest involvement of several components during formation of primary melts including subducted Pacific sediments, oceanic basaltic crust with additional fluid flux from subducted material (Churikova et al 2001; Portnyagin et al 2015) and even assimilation at crustal level of ore-bearing hydrothermal vein (Zelenski et al., 2016).

Tolbachik is also well known due to strong fumarolic activity and remarkable mineralogy of fumarolic deposits. They have been studied since 1976 and hundreds of new minerals with unusual combination of both abundant and trace elements have been found and described in details (Vergasova and Filatov, 2012; Pekov et al., 2018a). Particularly abundant are sulfate minerals with Na and K as major cations. Other alkaline elements, Rb and Cs, are rare in fumarolic minerals. Yet, some species contain these elements in trace to minor amount (up to 1.95 wt.% Rb_2O in cesiodymite and 4.11 wt.% Cs_2O in averievite, Pekov et al., 2018b, Vergasova et al., 1998,) while cesiodymite, contains Cs as the major constituent (Pekov et al., 2018b).

Rb, the element on which this thesis is focused, is a trace element in Tolbachik basaltic rocks with concentration between 13 ppm (primitive high-Mg basalts) and 89 ppm (evolved low-Mg basaltic andesites). Rb_N values (normalized relative to N-MORD) vary from 24 to 159. On Harker-type diagrams, the element exhibits a clear positive correlation with K_2O (Supplementary Fig. 1) and this relationship seems to be common for the Quaternary volcanic rocks from Kurile-Kamchatka region (Popolitov, Volynets 1982). In basalts, Rb is likely to be hosted by plagioclase pheno- and microphenocrysts and possibly by the groundmass glass.

Rb is also present in high-temperature magmatic gases (1030-1060°C) sampled during 2012-13 eruption and considered to be uncontaminated. The measured Rb content in condensate is 1.0±0.2 ppm (Zelenski et al., 2014) and 1.7 ppm (Chaplygin et al., 2016). A slightly lower concentration of Rb (0.78 ppm) was measured in the gases upon 1975-1976 eruption (Menyailov, Nikitina 1980). In contrast, the Rb content in the low-temperature gas (690 °C) from 2012-13 eruption was found as outstandingly high as 16.5 ppm (Chaplygin et al., 2016). However, the strong gas enrichment in trace elements was explained as a secondary feature due to “evaporation at forced pumping during sampling and possible dissolution of earlier precipitated sublimates in the gas conduit” (Chaplygin et al., 2016). Despite the low Rb content in Tolbachik gases, it essentially above that in gases produced by other volcanoes. For

instance, exhalations of Kudryavy (Kurily, Russia), Gorelyi (Kamchatka, Russia), Erta Ale (Afar, Ethiopia), Mount St. Helens USA) and White island (New Zealand) volcanoes exhibit extremely low Rb content in condensate with values between 0.22 and 0.002 ppm (Tedesco and Toutain 1991; Symonds and Reed, 1993; Taran et al 1995; Zelenski et al., 2013; Chaplygin et al., 2015). The high enrichment factor for Rb in Tolbachik gases ($LogEF_{Rb}$ = 2-3, Chaplygin et al 2016, Zelenski et al., 2014) suggests that the element was transported in the form of volatile species from a source and not derived from wall rocks due to contamination.

To date, the compositional data on whole rock basalts with different degree of alteration by fumarolic gases are yet lacking and one can but suggest the tentative mechanisms of gas enrichment by the trace elements to the levels essential for the crystallization of Rb-enriched minerals. For instance, such strong Rb enrichment could be due to its extraction by hot hydrated gases from the plagioclase and glass, and/or dissolution of some earlier precipitated fumarolic minerals, e.g. sulfates, as suggested by Chaplygin et al (2016). In this case, some helpful data can be collected from the results of model experiments, including chemical composition, structure, formation mechanism (chemical transport, crystallization from melt, hydration rate etc.) and other features of synthetic Rb-containing species chemically relevant to the yet few known minerals. As yet, rubidium accumulates mostly in the copper sulfate/oxysulfate/halosulfate family (alumoklyuchevskite $K_3Cu_3AlO_2(SO_4)_4$ (Siidra et al., 2017); belousovite $KZn(SO_4)Cl$ (Siidra et al., 2018); cesiodymite $CsKCu_5O(SO_4)_5$ and cryptochalcite $K_2Cu_5O(SO_4)_5$ (Pekov et al. 2018b); parawulffite $K_5Na_3Cu_8O_4(SO_4)_8$ and wulffite $K_3NaCu_4O_2(SO_4)_4$ (Pekov et al., 2014)) and copper vanadates ($[Cu_5O_2](AsO_4)(VO_4)\cdot(Cu_{0.5}\square_{0.5})Cl$ (Siidra et al., 2019) and averievite $Cu_5O_2(VO_4)_2\cdot n(Cs,Rb,K)Cl$ (Vergasova et al., 1998)). This approach is supported by our recent successful synthesis of Rb- and Cs-based analogs of mineral species, e.g. $M_2Cu_3O(SO_4)_3$ (M = Rb, Cs) as analogs of fedotovite (M = K) (Nekrasova et al. 2020, 2021). The current reports the results of our further studies of multinary Rb – Cu sulfates where no less than 8 new compounds representing 4 new structure types have been observed.

8.3 Experimental Section

Single crystals of $Rb_2Cu(SO_4)Cl_2$, $Rb_4Cu_4O_2(SO_4)_4 \cdot (Cu_{0.83}Rb_{0.17}Cl)$, $Rb_2Cu_2(SO_4)_3(H_2O)$ and $Rb_2Cu_5O(SO_4)$ were grown by solid-state techniques, more details provede in **Table 1**. The products consisted of green $Rb_2Cu_5O(SO_4)_5$, sky-blue $Rb_2Cu_2(SO_4)_3$ crystals, light-blue crystals of $Rb_2Cu_2(SO_4)_3(H_2O)$ (**Figure 71**). Crystallographic information for all obtained phases is summarized in **Table 19.**

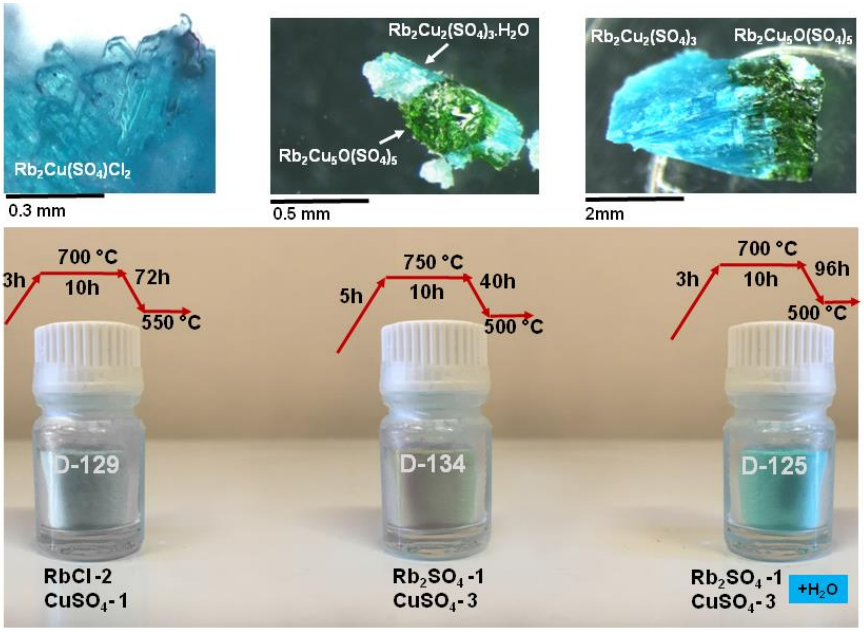

Figure 71. Crystals of blue $Rb_2Cu(SO_4)Cl_2$, green $Rb_2Cu_5O(SO_4)_5$, blue $Rb_2Cu_2(SO_4)_3 \cdot H_2O$ and $Rb_2Cu_2(SO_4)_3$ crystals. Initial reagent mixtures and schemes of the synthesis for each compound.

8.4 Structures descriptions

8.4.1 Structures without additional O^{2-} anions

$Rb_2Cu_2(SO_4)_3$

The crystal structure of another new anhydrous sulfate with langbeinite $A^+_2M^{2+}_2(SO_4)_3$ stoichiometry contains two symmetrically independent Rb sites, two Cu sites and three S atoms (**Figure 72**).

In $Rb_2Cu_2(SO_4)_3$, Rb^+ and S^{6+} cations have typical and similar to the described above coordination environments, whereas coordination of Cu^{2+} cations demonstrate interesting features worthy of discussion. Cu1 atom has four short and strong Cu-O_{eq} bonds thus forming CuO_4 squares. However, it has three additional very long Cu1-O5 = 2.864(12), Cu1-O1 = 2.925(15) Å and Cu1-O10 =

2.981(15) Å bonds, thus forming [4+3] coordination environments. These Cu-O bonds have bond-valence sums of 0.04-0.03 *v.u.* and thus should be taken into consideration. Cu2 atom has CuO_6 [4+1+1] coordination environments described above in $Rb_2Cu(SO_4)_2$. Both, CuO_6 and CuO_7 polyhedra demonstrate bidentate bridging with SO_4 tetrahedra.

$Rb_2Cu_2(SO_4)_3$ is isostructural to $K_2Cu_2(SO_4)_3$ described by Lander et al. (2017). The Cu-centered polyhedra and SO_4 tetrahedra form $[Cu_2(SO_4)_3]^{2-}$ bands depicted in **Figure 72**. The arrangement of sulfate tetrahedra and Cu-centered polyhedra was originally described by Lander et al. (2017) as a herringbone pattern.

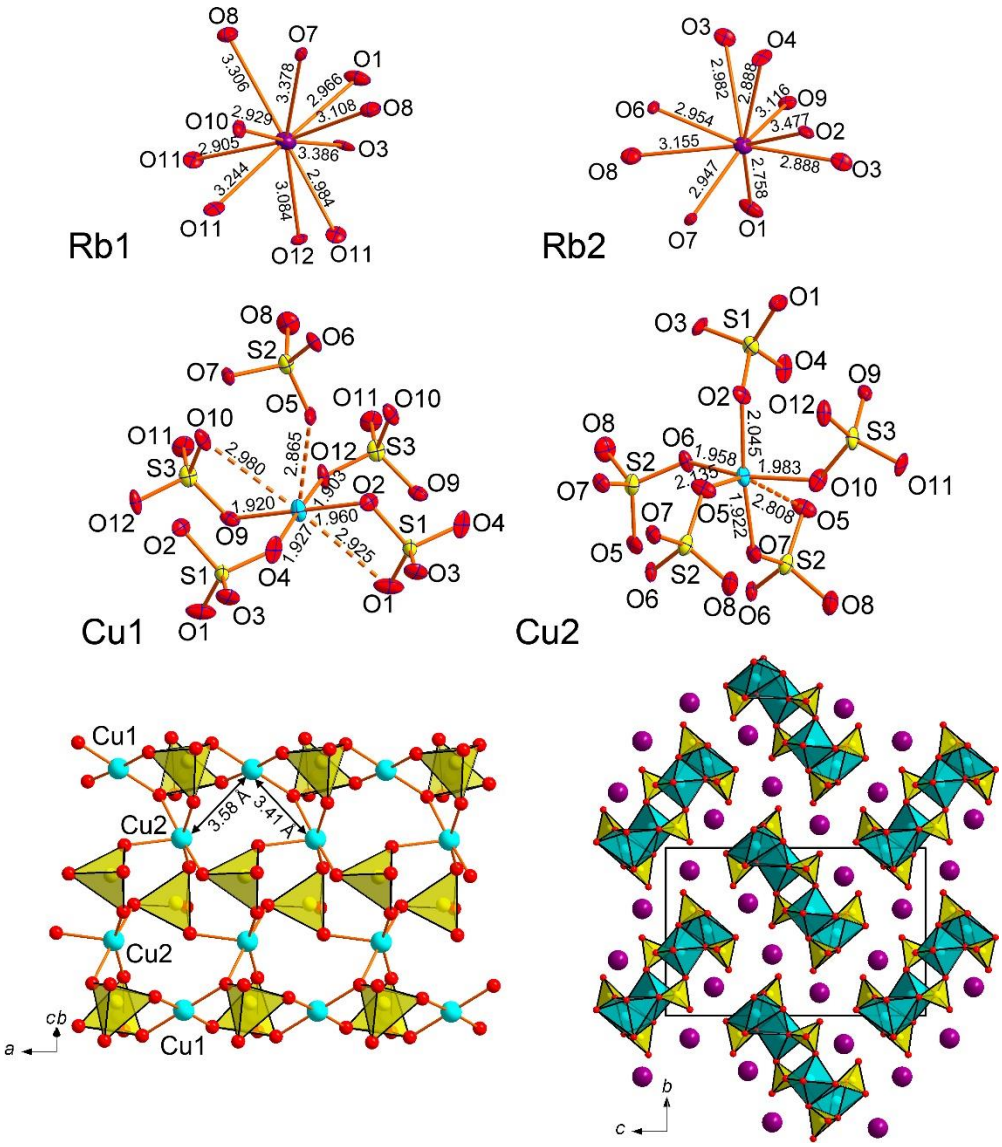

Figure 72. Coordination environments of Rb^+, Cu^{2+} and S^{6+} cations (above) in the crystal structure of $Rb_2Cu_2(SO_4)_3$. $[Cu_2(SO_4)_3]^{2-}$ band (only short and strong Cu-O bonds are shown) (left below) and general projection of the crystal structure of $Rb_2Cu_2(SO_4)_3$ along the *a* axis (right below).

$Rb_2Cu_2(SO_4)_3(H_2O)$ "hydrolangbeinite"

The dominant motif of the $Rb_2Cu_2(SO_4)_3(H_2O)$ structure are layers formed by the corner sharing and edge-sharing between sulfate tetrahedra and copper polyhedra (**Figure 73**). The $[Cu_2(SO_4)_3(H_2O)]^{2-}$ layers are parallel to the *ab* plane. In general, layered character is typical for hydrated copper oxysalt structures. In $Rb_2Cu_2(SO_4)_3(H_2O)$, the layers are linked together by Rb1 and Rb2 atoms coordinated by the eight and ten oxygen anions, respectively. Note, water molecules are bonded exclusively to Rb1 atoms. The Cu1 site shows typical coordination with the formation of CuO_5 tetragonal pyramids with almost planar CuO_4 base. Cu2-centered CuO_6 octahedron demonstrates exceptionally strongly distorted character. Cu2-O5 and Cu2-O6 bonds are strongly inclined (**Figure 73**) relative to the equatorial plane of octahedron. This distortion is again due to the edge-sharing through O5-O6 with $S2O_4$ tetrahedron. The rearrangement of sulfate groups in $Rb_2Cu_2(SO_4)_3(H_2O)$ is provoked by the hydration of one of the Cu-centered polyhedra. The vertex occupied by the water molecule is unshared and projected into the interlayer space.

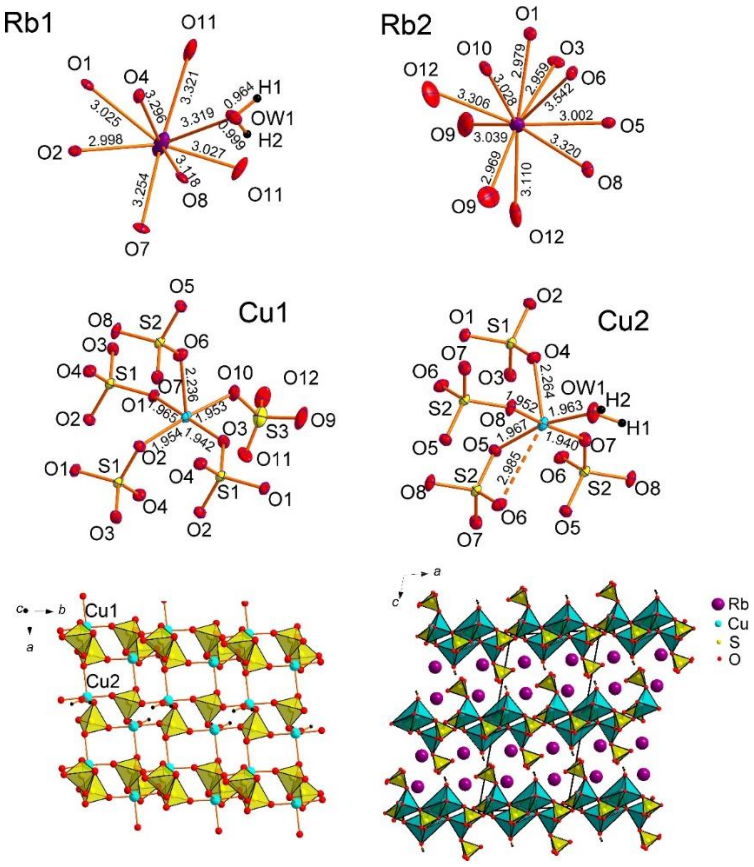

Figure 73. Coordination environments of Rb^+, Cu^{2+} and S^{6+} cations (above) in the crystal structure of $Rb_2Cu_2(SO_4)_3(H_2O)$. $[Cu_2(SO_4)_3(H_2O)]^{2-}$ layer (only short and strong Cu-O bonds are shown) (left below) and general projection of the crystal structure of $Rb_2Cu_2(SO_4)_3(H_2O)$ along the *b* axis (right below).

Table 19. Crystallographic data for $Rb_2Cu(SO_4)_2$, $RbNaCu(SO_4)_2$, $RbKCu(SO_4)_2$, $Rb_2Cu_2(SO_4)_3$, $Rb_2Cu_2(SO_4)_3(H_2O)$, $Rb_2Cu(SO_4)Cl_2$, $Rb_4Cu_4O_2(SO_4)_4{\cdot}(Cu^{+}_{0.83}Rb_{0.17}Cl)$, $Rb_2Cu_5O(SO_4)_5$.

	$Rb_2Cu_2(SO_4)_3(H_2O)$	$Rb_2Cu(SO_4)Cl_2$	$Rb_4Cu_4O_2(SO_4)_4 \cdot(Cu_{0.83}Rb_{0.17}Cl)$	$Rb_2Cu_5O(SO_4)_5$
Crystal system	Monoclinic	Monoclinic	Tetragonal	Triclinic
Space group	$P2_1/n$	$C2/c$	$I4$	P-1
Unit cell dimensions				
a (Å)	10.1158(9)	7.4645(7)	14.171(14)	10.1002(9)
b (Å)	6.1409(5)	16.0377(18)		12.4740(10)
c (Å)	20.3446(19)	7.6580(8)	4.991(5)	14.5961(11)
α (°)				77.227(4)
β (°)	103.564(2)	116.327(6)		81.111(4)
γ (°)				89.880(4)
Unit-cell volume (Å^3)	1228.56(19)	821.68(15)	1002(2)	1770.9(3)
Calculated density (g·cm^{-3})	3.267	3.245	3.695	3.694
Absorption coefficient (mm^{-1})	11.910	15.285	15.752	6.394
Crystal size (mm)	0.13×0.13×0.10	0.13×0.13×0.07	0.08×0.08×0.10	0.08×0.08×0.10
Data collection				
Temperature (K)	296(2)	296(2)	296(2)	296(2)
Radiation, wavelength (Å)	Mo$K\alpha$, 0.71073	Mo$K\alpha$, 0.71073	Mo$K\alpha$, 0.71073	Mo$K\alpha$, 0.71073
θ range (°)	2.059- 27.998	2.540-27.989	2.032-30.000	1.322-26.428
h, k, l ranges	-13→8 -8→8 -26→26	-9→9 -21→21 -10→9	-19→19 -19→19 -7→7	-16→15 -19→19 -23→20
Total reflections collected	11103	5905	6648	68695
Unique reflections (R_{int})	2960 (0.5)	990(0.03)	1455(0.08)	14571(0.09)
Unique reflections $F > 4\sigma(F)$	2005	896	944	7772
Structure refinement				
Weighting coefficients a, b	0.0429, 3.2731	0.0204, 1.4496	0.0000, 13.7767	0.0421, 0.0000
Data/restraints/parameters	2960/1/189	990/0/50	1455/67/81	14571/0/596
R_1 [$F > 4\sigma(F)$], wR_2 [$F > 4\sigma(F)$]	0.041, 0.091	0.019, 0.044	0.042, 0.064	0.050, 0.097
R_1 all, wR_2 all	0.076, 0.107	0.024, 0.046	0.088, 0.077	0.127, 0.127
Gof on F^2	1.012	1.038	1.041	1.004
Largest diff. peak and hole (e Å^{-3})	2.365, -1.352	0.577, -0.787	1.073, -0.904	2.305, -1.816

$Rb_2Cu(SO_4)Cl_2$

The coordination environments of atoms in monoclinic (*C*2/*c*) $Rb_2Cu(SO_4)Cl_2$ are very similar to those described earlier in its natural analog, chlorotionite $K_2Cu(SO_4)Cl_2$ (Giacovazzo et al., 1976) crystallizing in orthorhombic *Pnma* space group. The Cu atom demonstrates mixed-ligand coordination environments with oxygen and chlorine atoms thus forming the CuO_2Cl_2 coordination environments complemented by the two very long Cu-Cl bonds of 3.2020(8) Å (**Figure 74**). These Cu-Cl bonds are much shorter in chlorotionite $K_2Cu(SO_4)Cl_2$ (3.0467(2) Å). The SO_4 tetrahedra in $Rb_2Cu(SO_4)Cl_2$ and $K_2Cu(SO_4)Cl_2$ show very similar S-O bond length values. Two symmetrically independent Rb atoms have strongly dissimilar coordination environments: $Rb1O_4Cl_4$ and $Rb2O_4$. Rb2 has two Rb-Cl distances of 3.6652(10) Å and two of 3.6908(9) Å which are beyond the limit of 3.55 Å for the consideration of bonds. We should note also the unusually low coordination number of K in chlorothionite.

In $Rb_2Cu(SO_4)Cl_2$, the main structural feature of edge sharing between sulfate tetrahedra and CuO_2Cl_4 octahedra remains intact. The Cu-S1 distances are 2.5785(10) Å and 2.593(1) Å in $Rb_2Cu(SO_4)Cl_2$ and chlorotionite $K_2Cu(SO_4)Cl_2$, respectively.

The observed symmetry lowering in $Rb_2Cu(SO_4)Cl_2$ compared to $K_2Cu(SO_4)Cl_2$ is likely due to the replacement of K^+ by larger Rb^+. This causes also the significant elongation of Cu-Cl bonds in the CuO_4Cl_2 octahedra.

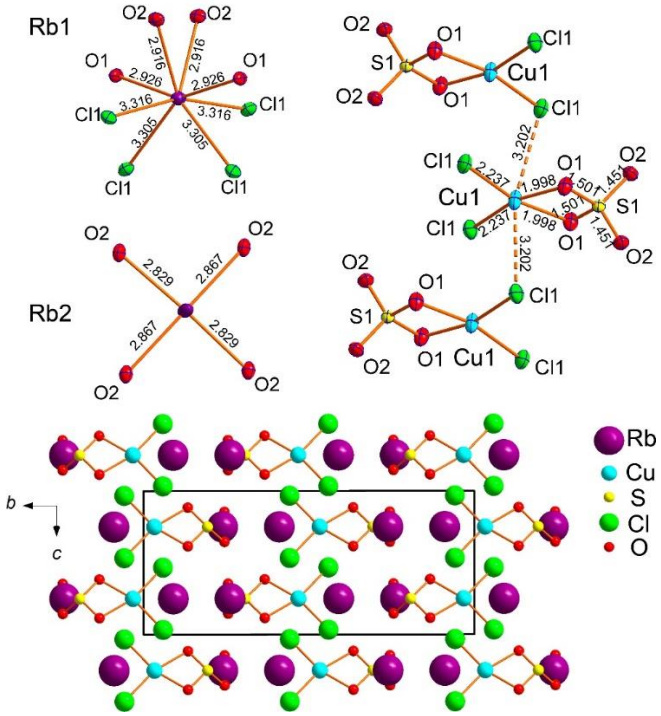

Figure 74. Coordination environments of Rb^+, Cu^{2+} and S^{6+} cations (above) in the crystal structure of $Rb_2Cu(SO_4)Cl_2$. General projection of the crystal structure of $Rb_2Cu(SO_4)Cl_2$ along the *a* axis (below). Weak and long Cu-Cl bonds are not shown for clarity.

8.4.2 Structures with additional O^{2-} anions

$Rb_4Cu_4O_2(SO_4)_4\cdot(Cu^{+}_{0.83}Rb_{0.17}Cl)$, rubidium analogue of piypite

Piypite $K_4Cu_4O_2(SO_4)_4\cdot$(Na,Cu)Cl was described from the fumaroles of the Second scoria cone by Vergasova et al. (1984). The crystal structure was solved (R_1 = 0.035) on a sample of "caratiite" from Mount Vesuvius, Naples, Italy by Effenberger and Zemann (1984). It belongs to the tetragonal symmetry, *I*4, *a* = 13.60(2) Å, *c* = 4.98(1) Å, *V* = 921.1 Å^3. Later, Kahlenberg et al. (2000) solved the structure (R_1 = 0.028) of its synthetic sodium analog, $Na_4Cu_4O_2(SO_4)_4\cdot(M\text{Cl})$ (*M* = Na, Cu, □) in the supercell with *P*4/*n*, *a* = 18.451(1), *c* = 4.9520(2), and *V* = 1685.86 Å^3.

The new compound $Rb_4Cu_4O_2(SO_4)_4\cdot(Cu_{0.83}Rb_{0.17}Cl)$ crystallizes analogous to the potassium compound in space group in *I*4, *a* = 14.171(14), *c* = 4.991(5), *V* = 1002(2) Å^3, R_1 = 0.043. Proceeding from K to Rb, the value of the *a* parameter is affected most. We did not observe indication of the supercell suggested by Kahlenberg et al. (2000). In the structure of $Rb_4Cu_4O_2(SO_4)_4\cdot(Cu_{0.83}Rb_{0.17}Cl)$, chlorine is disordered over two Cl1A (s.o.f. = 0.44(7)) and Cl1B (s.o.f. = 0.55(7)) sites with Cl1A-Cl1B = 0.82(2) Å. All of the atoms except of ClA were refined anisotropically.

The structure of $Rb_4Cu_4O_2(SO_4)_4\cdot(Cu_{0.83}Rb_{0.17}Cl)$ (**Figure 75**) contains one symmetrically unique Rb position, one Cu, one S and one mixed metal site *M*, occupied by $Cu^{+}$and Rb^{+} cations in a ratio indicated above. The Rb^{+} cation is coordinated by seven O atoms and two Cl atoms. The Cu site is coordinated by four oxygens forming a distorted CuO_4 square complemented by one apical O^{2-} anion at a distance of 2.395(8) Å and another one at 3.086(11) Å. As a result, an essentially elongated CuO_6 octahedron is formed.

The mixed *M* site has a refined occupancy of $Cu^{I}_{0.83(7)}Rb_{0.17(7)}$. There are two strong bonds to the Cl atoms (*M*-Cl1A = 2.08(5) Å and *M*-Cl1B = 2.09(3) Å) which correspond to a typical linear $Cu^{I}Cl_2^{-}$ anion. There are also four equivalent *M*-O2 distances of 2.900(9) Å which transform into real bonds around Rb^{+}.

The O1, O2, O3 and O4 oxygens constitute the tetrahedral SO_4^{2-} groups and are further termed as O_t. The "additional" O5 oxygen atom is bonded exclusively to the Cu^{2+} cations (**Figure 75**) and can be designated as O_a. The Cu^{2+}–O_a distances vary in the range of 1.908(15) – 1.922(15) Å, whereas Cu^{2+}–O_t, from 1.908(15) to 3.086(11) Å. Because of the higher strength of the Cu–O_a bonds compared to the weaker Cu–O_t, one can describe the copper-oxide substructure of $Rb_4Cu_4O_2(SO_4)_4\cdot(Cu_{0.83}Rb_{0.17}Cl)$ in the terms of oxocentered OCu^{2+}_4 tetrahedra.

These tetrahedra link together via common edges to form the $[O_2Cu]^{2+}$ single chains (**Figure 75**). In such units, each tetrahedron shares two of six edges with adjacent tetrahedra. The $[O_2Cu]^{2+}$ single chains extend along the *c* axis. The chains are surrounded by SO_4 tetrahedra in a rod-like arrangement. Rb^+ cations fill the space in between the rods. In turn, the channels filled by $CuCl_2^-$ linear complexes, are formed between the rubidium atoms. Formation of "guest" metal-chloride species with copper in the channels is characteristic for fumarolic minerals: averievite $Cu_5O_2(VO_4)\cdot nMCl_x$ (M=Cu, Cs, Rb, K) (Vergasova *et al*., 1998; Kornyakov et al., 2021) and aleutite $[Cu_5O_2](AsO_4)(VO_4)\cdot(Cu_{0.5}\square_{0.5})Cl$ (Siidra et al., 2019). A similar phenomenon was observed in the family of copper-lead selenite bromides (Siidra et al. 2018): the oxocentered $OCu^{2+}{}_nPb_{4-n}$ tetrahedra were present only in the structures containing both Cu^{2+} and Cu^+. Whenever Cu^{2+} was the sole copper species, the anionic sublattice was formed only by SeO_3^{2-} and Br^- with no "extra" O^{2-} present. A possible explanation, which evidently needs to be further verified, is that the Cu^+ form strong covalent bonds to the halide anions. The terminal atoms of the strong halo- and/or oxoanions form weaker bonds to the dications (Pb^{2+} or Cu^{2+}) and the "extra" O^{2-} anions are one of the ways to complete their bond valence sums to saturation.

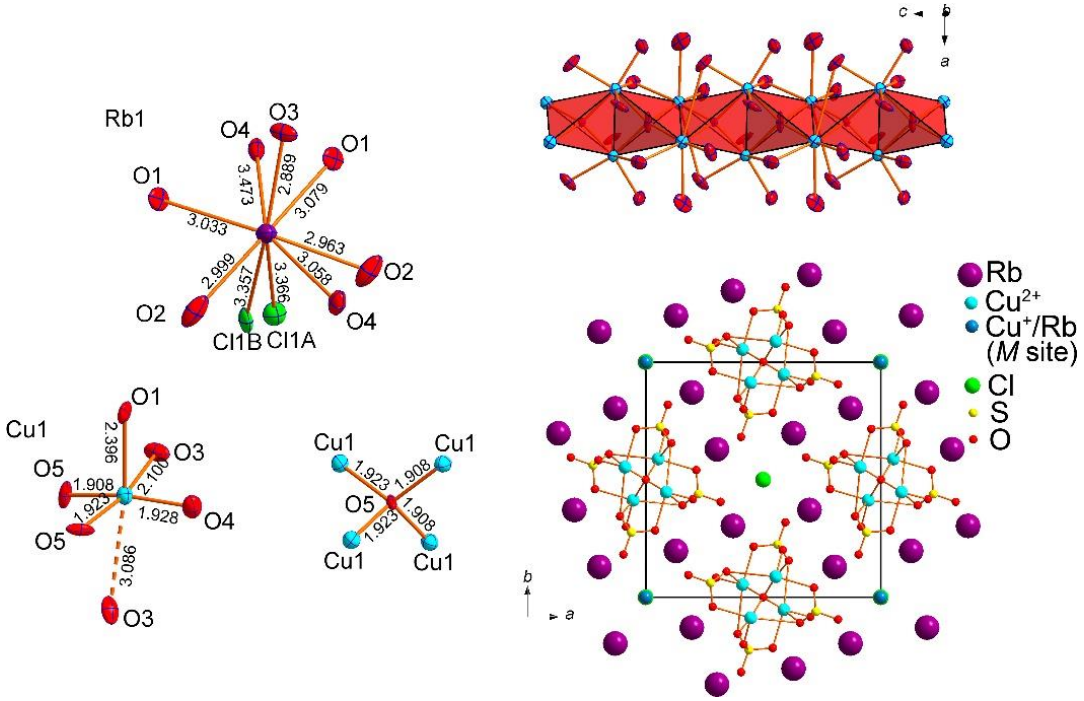

Figure 75. Coordination environments of Rb^+, Cu^{2+} cations and additional O^{2-} anions cations in the crystal structure of $Rb_4Cu_4O_2(SO_4)_4\cdot(Cu_{0.83}Rb_{0.17}Cl)$ (left). Polyhedral representation of the oxocentered $[Cu_2O]^{2+}$ chains surrounded by the oxygen atoms of sulfate groups (right above). General projection of the crystal structure of $Rb_4Cu_4O_2(SO_4)_4\cdot(Cu_{0.83}Rb_{0.17}Cl)$ along the *c* axis (below) (Rb-Cl and *M*-Cl, *M*-O bonds are omitted for clarity).

$Rb_2Cu_5O(SO_4)_5$, rubidium analogue of cryptochalcite and cesiodymite

$Rb_2Cu_5O(SO_4)_5$ is isostructural to the recently described cryptochalcite, $K_2Cu_5O(SO_4)_5$, and cesiodymite $CsKCu_5O(SO_4)_5$ (Pekov et al., 2018). Note, both these fumarolic minerals contain significant amounts of Rb (up to 1.95 wt. % Rb_2O). The new compound $Rb_2Cu_5O(SO_4)_5$ is the first synthetic representative of this structure type. The initial model started from the atomic coordinates provided by Pekov et al. (2018). The unit-cell volume of $Rb_2Cu_5O(SO_4)_5$ (V = 1770.9(3) Å^3) is nearly halfway between those of cryptochalcite (V = 1751.73(10) Å^3) and cesiodymite (V = 1797.52(16) Å^3). The structure of cryptochalcite-type compounds, and $Rb_2Cu_5O(SO_4)_5$ in particular, represents an interesting example of the framework formed by both CuO_n copper-centered polyhedra and oxocentered OCu_4 tetrahedra. The $[Cu_5O(SO_4)_5]^{2-}$ open framework, with Rb^+ in the channels, can be described as consisting of two types of blocks, *A* and *B* (**Figure 76**). The *A*-blocks (in the middle) are formed by O_2Cu_6 dimeric units and sulfate tetrahedral, whereas *B*-blocks (right) are formed by CuO_5 tetragonal pyramids and sulfate tetrahedra.

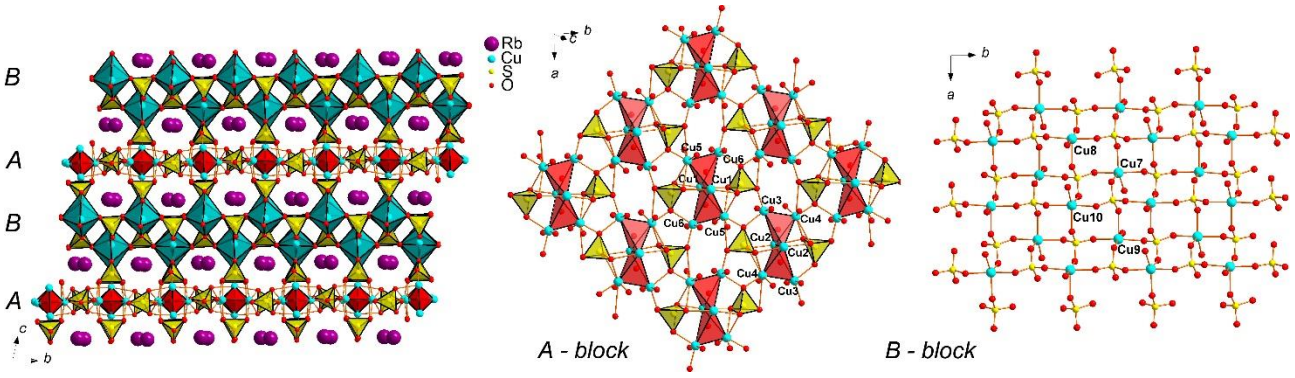

Figure 76. General projection of the crystal structure of $Rb_2Cu_5O(SO_4)_5$ along the *a* axis. The $[Cu_5O(SO_4)_5]^{2-}$ open-framework can be described as consisting of two types of blocks, *A* and *B*. *A*-blocks (in the middle) are formed by O_2Cu_6 dimeric units and sulfate tetrahedral, whereas *B*-blocks (right) are formed by CuO_5 tetragonal pyramids and sulfate tetrahedra. Rb-O bonds are omitted for clarity.

8.5 Discussion on a family of anhydrous copper sulfates

The new compounds obtained for the first time and the determination of their crystal structures significantly expand the family of anhydrous copper sulfates. Some of the obtained anhydrous rubidium copper sulfates turned out to be isostructural to known compounds and minerals. An example of this is $Rb_2Cu_5O(SO_4)_5$, which is completely isostructural to cesiodymite $CsKCu_5O(SO_4)_5$ and cryptochalcite $K_2Cu_5O(SO_4)_5$ (**Table 20**). This fact, as well as the high content of rubidium in natural samples, shows that the discovery of a mineral species with an alkali position, occupied essentially or even

predominantly by rubidium, is highly probable. Our synthesis of a number of mineral analogs also demonstrates the possibility of introducing rubidium cations into the already known structural architectures. A slight symmetry lowering, with the most structural features left intact, is observed for the Rb analog of chlorothionite.

Table 20. Crystallographic parameters of known cryptochalcite-type $A_2[Cu_5O(SO_4)_5]$ compounds.

Mineral/Synthetic Formula	cryptochalcite $K_2[Cu_5O(SO_4)_5]$	cesiodymite $CsK[Cu_5O(SO_4)_5]$	synthetic $Rb_2[Cu_5O(SO_4)_5]$
Space group	*P*-1	*P*-1	*P*-1
a, Å	10.0045(3)	10.0682(4)	10.1002(9)
b, Å	12.6663(4)	12.7860(7)	12.4740(10)
c, Å	14.4397(5)	14.5486(8)	14.5961(11)
α,º	102.194(3)	102.038(5)	77.227(4)
β,º	101.372(3)	100.847(4)	81.111(4)
γ,º	90.008(3)	89.956(4)	89.880(4)
V, Å^3	1751.7(1)	1797.5(2)	1770.9(3)
R_1	0.050	0.090	0.050
Reference	Pekov et al., 2018	Pekov et al., 2018	this work

On the other hand, the minerals and synthetic framework compounds of the $A_2Cu(SO_4)_2$ series demonstrate a vivid example of morphotropism with the formation of structural types depending on the size of the cations residing in the cavities of the $[Cu(SO_4)_2]^{2-}$ open-framework. To date, four versions can be distinguished. We propose to call this series of compounds “saranchinaite-type”, since for the first time such stoichiometry $[M_2Cu(SO_4)_2]$ was revealed during the discovery and description of saranchinaite $Na_2Cu(SO_4)_2$ (Siidra et al. 2018) and shortly thereafter its synthesized synthetic analogue (Kovrugin et al., 2019). Saranchinaite forms a framework with a unique topology (further denoted as type **1**) that has not yet been identified in other anhydrous copper and alkali metal sulfates. Note the presence of only a minor admixture of potassium in one of the positions in the mineral (Siidra et al. 2018). $K(Na,K)Na_2[Cu_2(SO_4)_4]$ (Siidra et al., 2021) with a significant potassium content crystallizes in a completely different structure type (**2**). The $Rb_2Cu(SO_4)_2$ described in this work, containing only rubidium atoms, also forms a new structure type. The recently described family of compounds $KMCu(SO_4)_2$ (*M* = Na, K) (Borisov et al., 2021; Zhou et al., 2020) is substantially supplemented by two rubidium representatives $RbNaCu(SO_4)_2$ and $RbKCu(SO_4)_2$. Attempts to obtain a solely sodium

representative of this structural type (**3**) were unsuccessful. The type **3** compound with channels predominantly occupied by sodium apparently does not exist. Sodium analogues of anhydrous sulfates discussed herein, except of chlorothionite, represent their own structure types. However, euchlorine – type $A_2Cu_3O(SO_4)_3$ (A_2 = Na_2, NaK, and K_2) compounds (Nekrasova et al., 2020) and minerals (Vergasova et al., 1988; Siidra et al., 2017, 2019) demonstrate the same structure type. The dimensionality of Cu-SO_4 backbones may be crucial for the inclusion of Na^+ keeping the same structure type. Framework compounds such as *e.g.* saranchinaite-type and cryptochalcite-type may show different architectures depending on the size of alkali metal, whereas *e.g.* euchlorine-type and chlorothionite-type having layered and chain structures are more flexible to include alkali metals of significantly various ionic radii.

Note that the structural architectures of anhydrous sulfates do not relate exclusively to framework ones. Thus, piypite and its synthetic analogs are based on chain copper oxide-sulfate complexes; chlorothionite and its polymorphs are also based on chain complexes formed via weak Cu-Cl bonds. The discovery of a new $Rb_2Cu(SO_4)Cl_2$ monoclinic polymorph of chlorothionite (**Table 21**) seems to be of particular interest considering the recently discovered interesting magnetic properties on synthetic $K_2Cu(SO_4)X_2$ (*X* = Cl, Br) (Soldatov et al., 2018; Bo et al., 2020) and $Na_2Cu(SO_4)Cl_2$ (Fujihala et al., 2020). Note that both sodium and potassium analogs are completely isostructural. An interesting pattern with a change in symmetry depending on the size of the alkaline cation is observed in the structures piypite and its synthetic analogs (**Table 22**). $Rb_4Cu_4O_2(SO_4)_4{\cdot}(Cu^+_{0.83}Rb_{0.17}Cl)$ and $K_4Cu_4O_2(SO_4)_4{\cdot}(Na,Cu)Cl$ crystallize in *I*4 space group, while $Na_4Cu_4O_2(SO_4)_4{\cdot}(MCl)$ (*M* = Na, Cu, □) crystallizes in *P*4/*n*. It can be seen that filling of the channels with metal chloride (*Me*Cl) complexes shows significant variations. It should be noted that the structural features of piypite from the fumaroles of Tolbachik volcano have not been studied to date. Effenberger and Zemann (1984) explicitly state in their article that “the nature of the *Me* atoms is not completely clear”.

Table 21. Crystallographic parameters of known chlorothionite-type $A_2Cu(SO_4)X_2$ compounds.

Phase modification	α-phase				β-phase
Mineral/Synthetic	synthetic	chlorothionite	synthetic	synthetic	synthetic
Formula	$Na_2Cu(SO_4)Cl_2$	$K_2Cu(SO_4)Cl_2$	$K_2Cu(SO_4)Cl_2$	$K_2Cu(SO_4)Br_2$	$Rb_2Cu(SO_4)Cl_2$
Space group	*Pnma*	*Pnma*	*Pnma*	*Pnma*	*C2/c*
a, Å	7.0324(2)	7.7320(15)	7.73	7.73	7.4645(7)
b, Å	5.60540(10)	6.078(1)	6.08	6.30	16.0377(18)
c, Å	16.0344(4)	16.2920(30)	16.29	16.43	7.6580(8)
β,º					116.327(6)
V, Å^3	632.07(3)	765.64	765.60	800.12	821.68(15)
R_1	0.0244	0.032	-	-	0.019
Reference	Fujihala et al., 2020	Giacovazzo et al., 1974	Bo et al., 2020	Bo et al., 2020	this work

In the same series of syntheses, where $Rb_2Cu_2(SO_4)_3$ was obtained, "hydrolangbeinite" $Rb_2Cu_2(SO_4)_3(H_2O)$ was found, formed as a result of a minor hydration of the initial mixture of reagents. Hydrated langbeinites are currently unknown for any composition of minerals or synthetic compounds. The obtained new compound shows the probability of detecting such compounds (especially for copper-containing ones) in the zones of fumaroles exposed to intense atmospheric precipitation. Alkali copper sulfates are known to form multiple hydrated "offsprings" during exposure to moist air (Siidra et al., 2021).

In the determined new structural architectures, a number of features were revealed which were seldom observed before. The first is the bidentate coordination of the tetrahedral sulfate group via edge sharing to the Cu^{2+} coordination polyhedron. Until recently, such coordination was known only for the chlorothionite structure. The second is formation of "high-coordinated" CuO_7 polyhedra. We considered such coordination when describing crystal structure of saranchinaite (Siidra et al. 2018). The structures of the new compounds suggest that such coordination is not in fact so uncommon, at least among anhydrous alkali copper sulfates. All of the described features clearly indicate the importance of further systematic studies of anhydrous copper-sulfate systems. Their exploration, particularly of the new copper-oxide substructures with new coordination environments, is highly likely to lead to new potentially interesting magnetic properties due to unusual arrangements of magnetically active Cu^{2+} cations. The effect of the alkali cation size on the Cu^{2+} coordination has been demonstrated recently for the family of synthetic hydrogen selenites (Charkin et al. 2019); one can expect that it will also be pronounces in other families, including sulfates.

Tables 17-20, listing the crystallographic parameters, show that anhydrous sulfates are a fruitful playground for the synthesis of new anhydrous compounds known previously only as prototype-structures in minerals. Conversely, it is highly probable that compounds, obtained so far only as synthetics, may exist as minerals in high-temperature fumaroles with strongly oxidizing conditions and in sublimates of natural coal fires (Pautov et al., 2020).

Table 22. Crystallographic parameters of known piypite-type $Rb_4[Cu_4O_2(SO_4)_4]\cdot(M\mathrm{Cl})$ compounds.

Phase modification	α-phase	β-phase	
Mineral/Synthetic	synthetic	piypite	synthetic
Formula	$Na_4[Cu_4O_2(SO_4)_4]\cdot(M\mathrm{Cl})$ (M = Na, Cu, □)	$K_4[Cu_4O_2(SO_4)_4]\cdot(Me\mathrm{Cl})$	$Rb_4[Cu_4O_2(SO_4)_4]\cdot(Cu^{+}_{0.83}Rb_{0.17}Cl)$
Space group	*P*4/*n*	*I*4	*I*4
a, Å	18.451(1)	13.60(2)	14.171(14)
c, Å	4.9520(2)	4.98(1)	4.991(5)
V, Å^3	1685.86(15)	921.1	1002(2)
R_1	0.028	0.035	0.043
Reference	Kahlenberg et al. 2000	Effenberger and Zemann, 1984	this work

It is worth noting here that synthetic analogs of various minerals, including sulfates, have been obtained using various synthetic approaches, which do not necessarily mimic the natural processes (or, more exactly, the currently adopted formation mechanisms). By now, condensation from vapor phase or interaction of hot gases with basaltic scoria are considered to be the most likely formation mechanisms of fumarolic minerals. Yet, our studies clearly indicate that vapor transport in water-free systems can be neglected at least until 600°C wherein the only volatile species are copper chlorides. At least some of the species produces herein have most likely crystallized from melts. Several test experiments have shown that at least some Rb-containing compositions melt at as low temperatures as 400 – 450°C; moreover, good quality crystals and homogeneous samples were not produced even after long-time subsolidus heat treatments. Additional experiments are clearly necessary to elucidate the role of reaction kinetics in solid-state processes. The other synthetic approach, applied successfully to preparation of analogs of chlorothionite, is crystallization from hot aqueous solutions. However, one can expect competitive formation of less soluble double sulfates, *e.g.* Tutton salts, or hydrolysis products, *e.g.* analogs of hatrochalcite. Overall, the chemistry of hydrates with low water content remains in many respects a *terra incognita*. A possible solution lies in exploiting media with low chemical potential of water; our current example is the $Rb_2Cu_2(SO_4)_3\cdot H_2O$, formed under low pressure of water vapors (given the sealed tube had survived internal pressure upon annealing). A test experiment with the initially wet sulfate charge annealed in a temperature gradient between ambient and 650°C produced good quality single crystals of various known hydrates including $CuSO_4\cdot 5H_2O$ in the relatively cold part of the sealed silica tube. Therefore, this approach is promising in producing various hydrates hardly accessible in any other way. The use of moist non-aqueous solvents seems to be not straightforward as they either do not

dissolve most inorganic sulfates (alcohols) or coordinate competitively to copper (acetonitrile). The process involving water evidently take place also under natural conditions, *e.g.* upon hydration-dehydration cycles. Yet, our studies of such processes for selected copper sulfate minerals indicate that these are very complicated (Siidra et al., 2021), include numerous steps and are not always reversible even for single-phase specimens. It is however very likely that these studies, extended into more complex systems, will produce even more intricate and intriguing architectures, compositions, and possibly properties. Some of these studies are now in progress.

8.6 Conclusion

This chapter aims at a detailed description of the geochemical nature of mineral formation on volcanic fumarols (Siidra et al., 2021). The eight new rubidium sulfates were obtained and their crystal structures characterization discussed: $Rb_2Cu(SO_4)Cl_2$, $Rb_4Cu_4O_2(SO_4)_4{\cdot}(Cu_{0.83}Rb_{0.17}Cl)$, $Rb_2Cu(SO_4)_2$, $Rb_2Cu_5O(SO_4)_5$ and $Rb_2Cu_2(SO_4)_3(H_2O)$. Our study shows that mineralogical diversity involves with the intensive exchange with the host basaltic scoria in the fumaroles. Sulfate cations Na and K are major in the minerals of the Tolbachik volcano, while Rb and Cs are rare in fumarolic minerals. Since these cations are not common as minerals, it is very important to study crystal structures with these cations as synthetic phases. This chapter was devoted to the crystal chemistry of rubidium sulfates, and the next one will be about morphotropism in fumarolic minerals related anhydrous cesium sulfates.

9. Morphotropism in fumarolic minerals related anhydrous sulfates: crystal structures of $Cs_2Cu(SO_4)_2$ and $Cs_2Co_2(SO_4)_3$

9.1 Introduction

Until recently, anhydrous sulfates of alkali and transition metals were a "blind-spot" in the crystal chemistry of sulfates. This fact is explained by the weak stability of such compounds in humid air (Siidra et al., 2021). While hydrated species are represented by a fairly large number of synthetic compounds and minerals (Hawthorne et al., 2000). However, in the last decade, in high-temperature fumaroles with strongly oxidizing conditions, on Tolbachik volcano (Kamchatka, Russia) (Vergasova and Filatov, 2012), a large number of new mineral species have been discovered. Many of them are represented by new structure types (e.g. Siidra et al., 2018; Filatov et al., 2020; Zubkova et al., 2021), as well as having no analogues among known synthetic materials (Siidra et al., 2017). Among them are unusual anhydrous cesium and copper sulfates (Pekov et al., 2018). We have obtained recently a number of synthetic mineral counterparts (e.g. Nekrasova et al., 2021; Siidra et al., 2020). Magnetic (Nekrasova et al., 2020) and electrochemical (Kovrugin et al., 2019) properties have been studied on pure synthetic counterparts. Notably, that most of the known alkali-copper sulfate representatives are structurally based on copper-sulfate three-dimensional frameworks (Borisov et al., 2021).

While we have synthesized recently several examples of Rb-Cu sulfates (Siidra et al., 2021), no Cs anhydrous sulfates with copper and cobalt have been reported to date. In order to fill this gap and to look for possible alkali cation size influence on the structural architecture, we have undertaken this study.

Single crystals of $Cs_2Cu(SO_4)_2$ and $Cs_2Co_2(SO_4)_3$ were synthesized by the solid-state reactions in vacuum. The products consisted of dark blue crystals of $Cs_2Cu(SO_4)_2$, sky-blue crystals of $Cs_2Cu_3(SO_4)_4$ (**Figure 77**) and green crystals of $Cs_2Cu_{3.5}O_{1.5}(SO_4)_3$ and violet $Cs_2Co_2(SO_4)_3$ crystals.

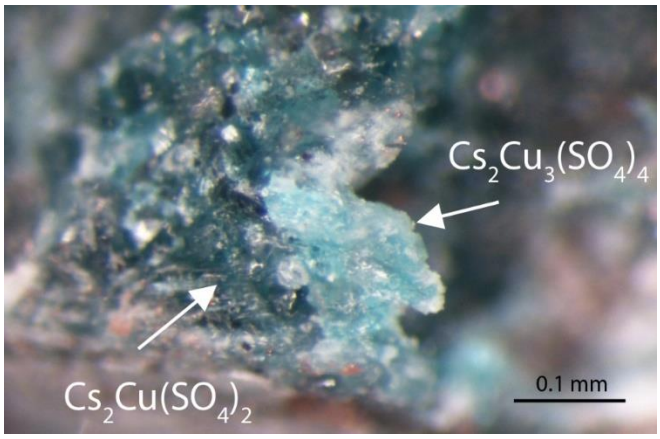

Figure 77. Crystalline aggregates of $Cs_2Cu(SO_4)_2$ and $Cs_2Cu_3(SO_4)_4$ under optical microscope.

9.2 Single-crystal X-ray studies

$Cs_2Cu(SO_4)_2$ is monoclinic, $P2_1/n$, a = 9.685(3) Å, b = 7.920(3) Å, c = 12.141(4) Å, β = 91.416(8)°, V = 931.0(5) Å^3, R_1 = 0.042 (**Table 23**). $Cs_2Co_2(SO_4)_3$ is orthorhombic, $P2_12_12_1$, a = 4.8810(7) Å, b = 14.920(2) Å, c = 17.164(3) Å, V = 1249.9(3) Å^3, R_1 = 0.049. In both structures, all atoms were refined anisotropically. Selected interatomic distances are given in **Table S24**. The bond-valence sums for the atoms in both structures were calculated using parameters given by Gagné and Hawthorne (2015) for Cu^{2+}-O, Co^{2+}-O, Cs^{+}-O and S^{6+}-O bonds. The results are summarized in **Table S25** and **S26**. The bond-valence sums for all atoms are in a good agreement with their expected formal valencies.

Table 23. Crystallographic data and refinement parameters for $Cs_2Cu(SO_4)_2$ and $Cs_2Co_2(SO_4)_3$. Experiments were carried out at 100 K with AgKα radiation on Bruker Smart DUO, CCD.

	$Cs_2Cu(SO_4)_2$	$Cs_2Co_2(SO_4)_3$
Space group	$P2_1/n$	$P2_12_12_1$
a(Å)	9.685(3)	4.8810(7)
b(Å)	7.920(3)	14.920(2)
c(Å)	12.141(4)	17.164(3)
β(°)	91.416(8)	
V(Å^3)	931.0(5)	1249.9(3)
D_x (g/cm^3)	3.721	3.570
Crystal size, mm^3	0.20×0.20×0.15	0.10×0.15×0.15
θ max (°)	26.344	25.198
h, k, l range	-15 – 12	-7 – 7
	-12 – 11	-14 – 22
	-19 – 19	-25 – 25
Total reflections collected	16754	13460
Unique reflections (R_{int})	3770(0.07)	4542(0.08)
Unique reflections F > 4σ(F)	2389	2909
R_1	0.042	0.049
wR_1	0.085	0.060
S	1.011	0.991
$\rho max, min$ /e·Å^{-3}	1.434/-1.768	1.501/-1.324
CCDC	2103648	2104096

9.3 Structure description of $Cs_2Cu(SO_4)_2$

There are two symmetrically independent Cs^+ cations in the structure of $Cs_2Cu(SO_4)_2$. All Cs-O bond lengths ≤ 3.80 Å were taken into consideration. Cs1 site is coordinated by eleven O atoms, whereas Cs2 – by ten O atoms. Individual Cs-O bond distances range from 2.985(4) to 3.721(5) Å.

Cu1 atom forms four very strong Cu-O_{eq} bonds (≤ 2 Å) resulting in a strongly CuO_4 configuration which is complemented by a fifth, longer Cu-O_{ap} bond of 2.195(4) Å, to form CuO_5 polyhedron (**Figure 78**). According to Burns and Hawthorne (1995), such coordination can be described as intermediate from square-pyramidal to triangular-bipyramidal. All Cu-O bonds ≤3.05 Å were taken into consideration. Note, the presence of very short Cu1-S1 distance of 2.5837(16) Å.

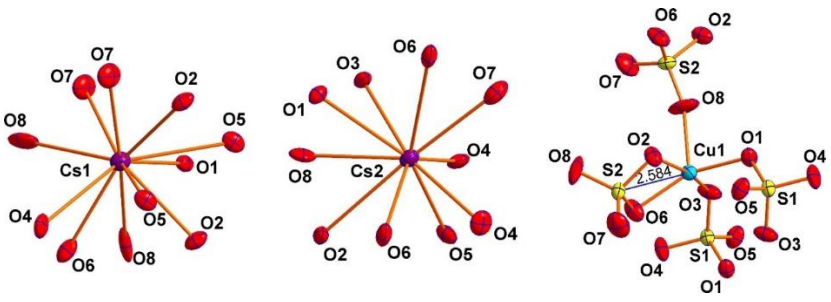

Figure 78. Coordination of atoms in the structure of $Cs_2Cu(SO_4)_2$. Thermal ellipsoids are drawn at the 50% probability level.

There are two symmetrically independent S^{6+} cations in the structure. These are tetrahedrally coordinated by four O atoms with the average <S-O> bond length of 1.47 Å. This coordination is typical for sulfates (Hawthorne et al. 2000).

The Cu-centered CuO_5 polyhedra and SO_4 tetrahedra form $[Cu(SO_4)_2]^{2-}$ layers with large voids depicted in **Figure 79**. Cs^+ cations are located in the interlayer space under and above the voids (**Figure 80** a,b). Unique structural feature of $Cs_2Cu(SO_4)_2$ is the edge-sharing of CuO_5 polyhedra and $S2O_4$ tetrahedra. This type of interpolyhedral connectivity, to the best of our knowledge, has not been described before. Edge-sharing between CuO_6 octahedra and SO_4 tetrahedra is rare and has been described in anhydrous sulfates only (Cu-S distances are given in brackets): chlorothionite, $K_2CuCl_2(SO_4)$ (Cu-S = 2.593 Å) (Giacovazzo *et al*., 1976), δ-$Rb_2Cu(SO_4)_2$ (Cu-S = 2.572 Å) and several other Rb-Cu sulfates (Siidra *et al*., 2021) and γ-$KNaCu(SO_4)_2$ (Cu-S = 2.810 Å) (Borisov *et al*., 2021). Edge sharing has also been recently observed in a complex Zn sulfate majzlanite, $K_2Na(ZnNa)Ca(SO_4)_4$ (Siidra *et al*., 2020), with the Zn-S distance of 2.870 Å.

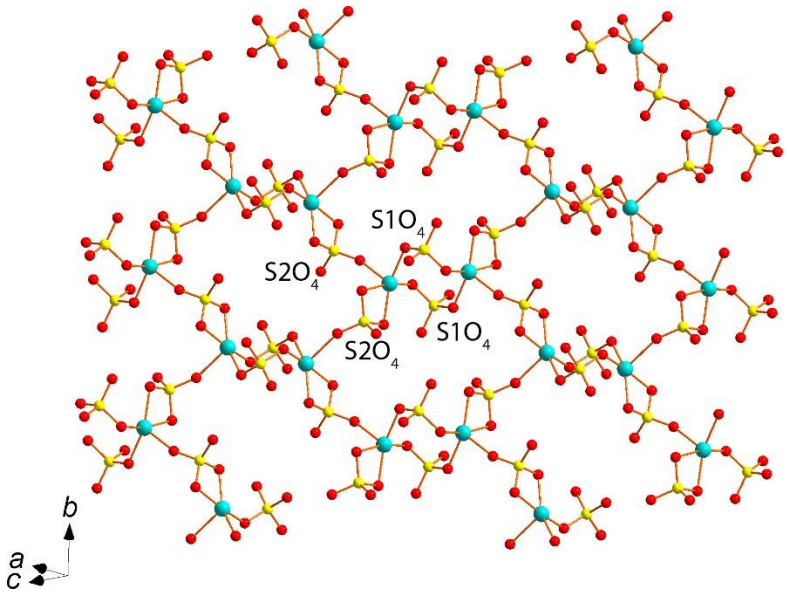

Figure 79. $[Cu(SO_4)_2]^{2-}$ layer in the structure of $Cs_2Cu(SO_4)_2$.

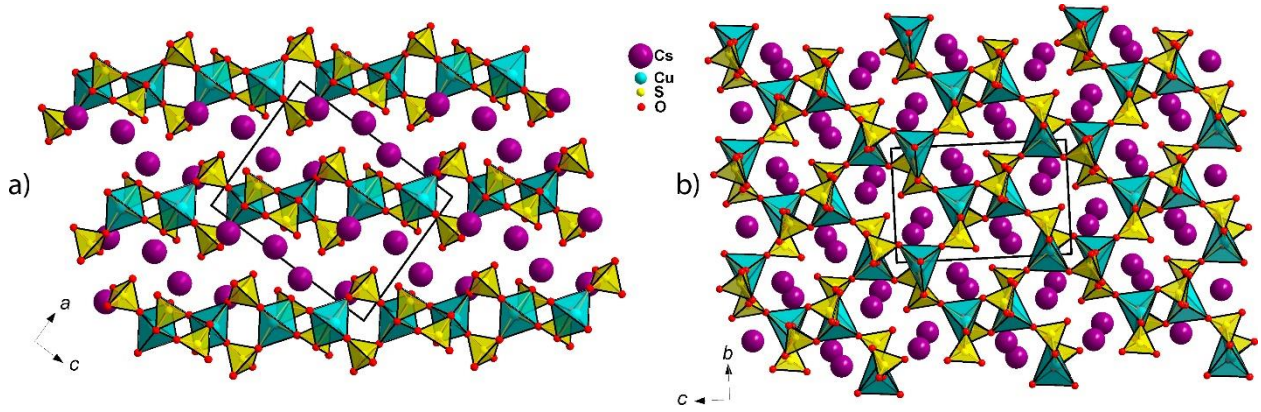

Figure 80. General projections of the crystal structure of $Cs_2Cu(SO_4)_2$ (a,b). Cs-O bonds are not shown for clarity.

9.4 Structure description of $Cs_2Co_2(SO_4)_3$

Each of the Cs1 and Cs2 atoms is surrounded by eleven oxygen atoms (**Figure 81**). In general, both Cs atoms have similar coordination environments to those described above in $Cs_2Cu(SO_4)_2$.

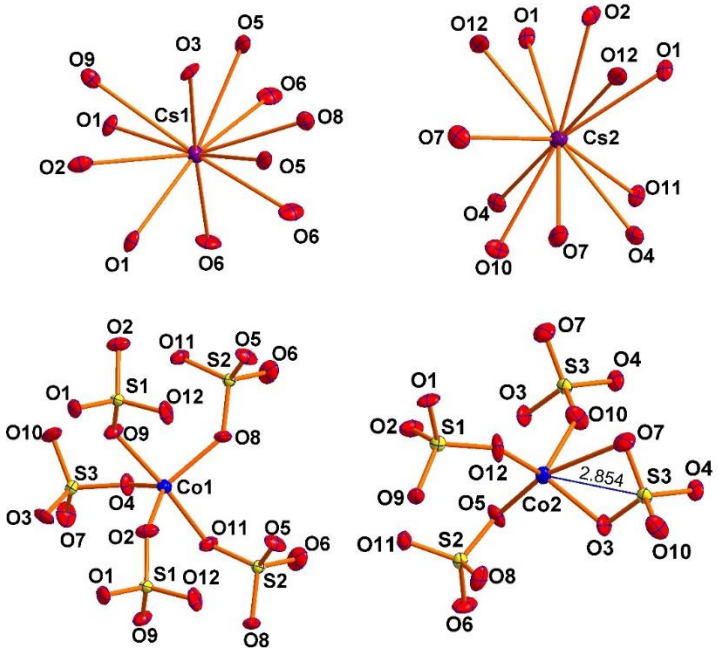

Figure 81. Coordination of atoms in the structure of $Cs_2Co_2(SO_4)_3$. Thermal ellipsoids are drawn at the 50% probability level.

Two Co sites have different coordination. Co1 has CoO_5 triangular-bipyramidal coordination. Co1-O8, Co1-O2 and Co1-O4 bonds, with bond length values close to 2.0 Å, are located almost in plane, whereas slightly elongated Co1-O11 and Co1-O9 bonds are sited on the axis. Co2 atom forms four short and strong bonds in the range 1.948(7)-1.992(7) Å thus forming CoO_4 tetrahedron. The latter is complemented by the formation of the fifth long Co-O bond of 2.689(7) Å. $Co2O_5$ [4+1] coordination can be described as transitional from tetrahedral to trigonal bipyramidal.

Sulfate groups are distorted only slightly in the structure of $Cs_2Co_2(SO_4)_3$. The average <S–O> bond length of each of the three sulfate groups is 1.47 Å, which is in a very good agreement with the grand average distance of 1.473 Å given for sulfate minerals by Hawthorne et al. (2000).

In general, the structural topology of the layer in $Cs_2Co_2(SO_4)_3$ is similar to that described above for $Cs_2Cu(SO_4)_2$. The interconnection of Co-centered polyhedra with sulfate tetrahedra occurs via common vertices as well as via common edges with the formation of $[Co_2(SO_4)_3]^{2-}$ corrugated layers with elliptical large cavities (**Figure 82**a). This layered structural topology is the result of the adaptation of cobalt-sulfate species to the large cesium cations in the interlayer (**Figure 82**b).

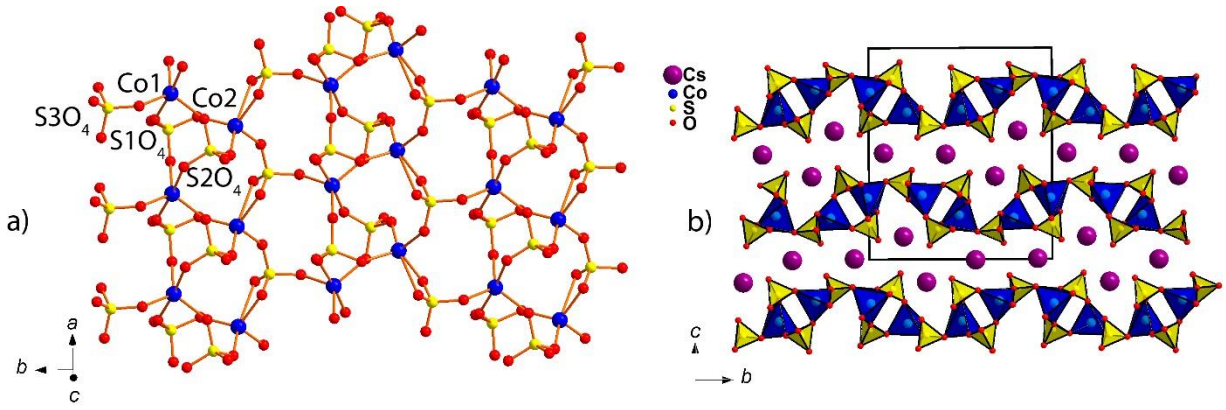

Figure 82. $[Co_2(SO_4)_3]^{2-}$ layer in the structure of $Cs_2Co_2(SO_4)_3$ (a). General projection of the crystal structure of $Cs_2Co_2(SO_4)_3$ (b). Cs-O bonds are not shown for clarity.

9.5 Conclusion

Both new compounds have no structural analogs and add to the family of anhydrous alkali transition metal sulfates. Only one but hydrated cesium-copper sulfate $Cs_2[Cu(H_2O)_6](SO_4)_2$ (Ballirano et al., 2007) was previously reported. Except of this Tutton salt, cesium copper sulfates are unknown to date. The same is true for alkali cobalt sulfates. Cesium copper sulfate Tutton salt (Kockelmann et al., 2001) and alum $CsCo(SO_4)_2(H_2O)_{12}$ (Beattie et al., 1981) are the only known hydrated representatives, whereas anhydrous species have not been reported.

The determination of the crystal structure of $Cs_2Cu(SO_4)_2$ is important, since it completes the series of $A_2Cu(SO_4)_2$ (A = Na, K, Rb, Cs) compounds listed in **Table S27** and **Figure 83.** The first representative of this family, with determined structure, was saranchinaite $Na_2Cu(SO_4)_2$ (Siidra *et al*., 2018a), discovered in 2015 (proposal IMA 2015-019). Before the discovery of saranchinaite, the structural features of the $A_2Cu(SO_4)_2$ compounds were unknown. Despite the fact that unsuccessful attempts to determine the structural features of the products of kröhnkite $Na_2Cu(SO_4)_2(H_2O)_2$ dehydration continued for many decades (see e.g. Testasicca *et al*. 2016). During the last three years it was found that $A_2Cu(SO_4)_2$ (A = Na, K, Rb, Cs) compounds represent a morphotropic series consisting of at least five different structural modifications (α-, β-, γ-, δ- and ε-phase) (**Table S27**). With an increase in the ionic radius of the alkali metal/metals, embedded in the $[Cu(SO_4)_2]^{2-}$ framework, symmetry-breaking transformations occur.

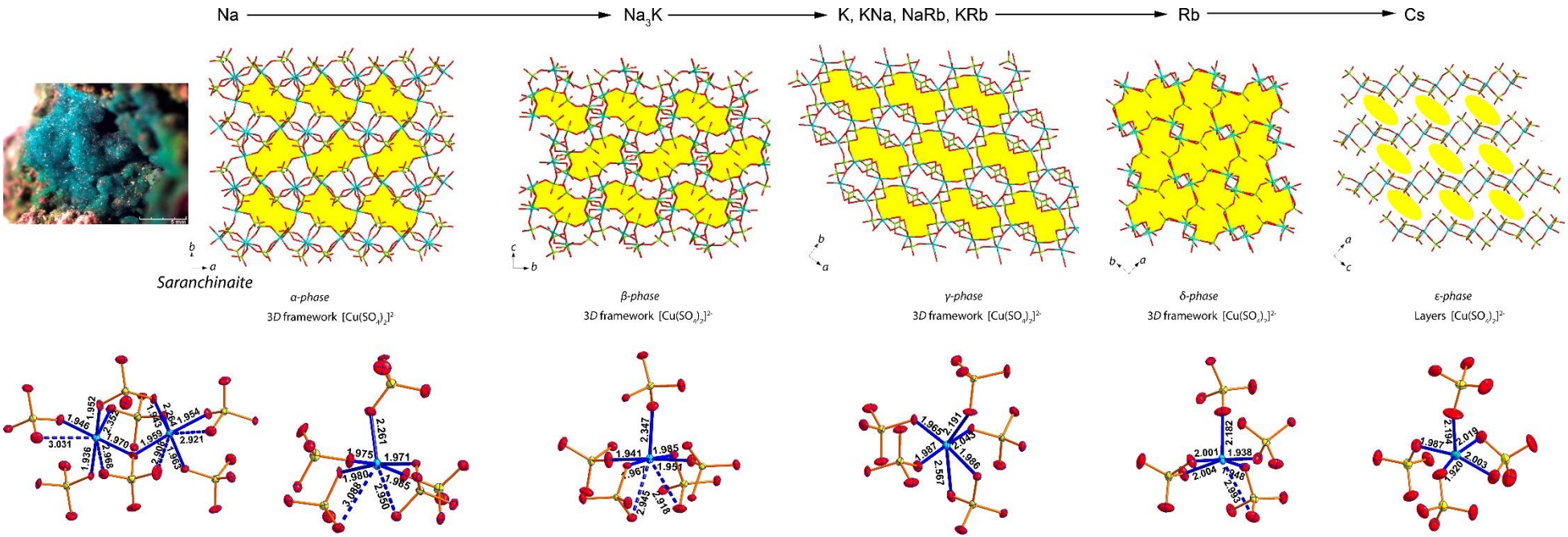

Figure 83. Evolution of $[Cu(SO_4)_2]^{2-}$ moieties in the structures of saranchinaite (on photo) morphotropic series $A_2Cu(SO_4)_2$ (A = Na, K, Rb, Cs) compounds. Elliptical channels are marked by yellow (above). Coordination of CuO_n polyhedra by SO_4 groups in each phase (below). Cu-O bonds >2.6 Å are shown by the blue dotted lines. See the text for details.

Cu^{2+} sites coordination environments demonstrate significant changes in the saranchinaite morphotropic series. There are four symmetrically independent Cu sites in saranchinaite $Na_2Cu(SO_4)_2$ (Siidra *et al*., 2018) and its synthetic analogue (Kovrugin et al., 2019). Coordination environments of Cu1 and Cu4 atoms are similar, thus coordination of Cu4 atom only is represented in **Figure 83**. Each of Cu atoms in saranchinaite forms four very strong Cu-O_{eq} bonds (≤ 2 Å) resulting in CuO_4 squares which are complemented by a fifth, longer Cu-O_{ap} bond of ~2.3 Å, to form CuO_5 distorted tetragonal pyramids. There are also two essentially longer Cu-O_{add} bonds in the 2.9-3.1 Å. Taking them into consideration, the overall coordination polyhedra of Cu^{2+} can be considered as "octahedra with one split vertex". Note, saranchinaite is the only representative, where Cu-centered (namely Cu2- and Cu3-centered) polyhedra share one with each other via common oxygen corner into dimeric unit (**Figure 83**). In addition to usual corner sharing, each CuO_7 polyhedron shares two of its edges with sulfate tetrahedra (Cu-S distance is ~3.0 Å). Alkali atoms are embedded in the several types of channels (large elliptical ones are marked by yellow in **Figure 83**). Refinement of the crystal structure of the mineral (Siidra *et al*., 2018) shows the presence of the minor potassium admixture ($Na_{0.7}K_{0.3}$) in one of eight symmetrically independent alkali sites.

Cu-centered dimers are disintegrated into isolated CuO_7 polyhedra in $K(Na,K)Na_2[Cu_2(SO_4)_4]$ (Siidra et al. 2021). Apart from this difference, no other significant changes in the coordination of the bivalent copper cation from the mineral described above are observed. There are two symmetrically independent copper sites in $K(Na,K)Na_2[Cu_2(SO_4)_4]$, both with very similar coordination environments ($Cu1O_7$ is represented in **Figure 83**). The overall structural topology of $[Cu(SO_4)_2]$ framework (**Figure 83**) is significantly different from that one in saranchinaite. Thus the increase of the Na:K ratio to ~3:1 results in a complete rearrangement of $[Cu(SO_4)_2]^{2-}$ framework.

Further increase of the Na:K ratio to ~1:1 in $KNaCu(SO_4)_2$ (Borisov et al., 2021) results in both significant changes in Cu^{2+} coordination environments and overall topology of the framework. Four Cu-O bonds with distances around 2 Å form a nearly square planar configuration, the bond with a fifth O atom is somewhat longer (~ 2.2 Å) and its orientation is almost perpendicular to the square plane. There is an additional Cu-O bond of 2.6 Å strongly bent away from the 180 degrees which would be expected for an ideal [4+1+1] octahedron. CuO_6 polyhedron shares one of its edges with SO_4 tetrahedron with Cu-S distance 2.8 Å in $KNaCu(SO_4)_2$ (Borisov et al., 2021). The same structure type is adopted by $K_2[Cu_2(SO_4)_2]$ (Zhou et al., 2020), $RbNa[Cu(SO_4)_2]$ and $RbK[Cu(SO_4)_2]$ (Siidra et al., 2021) showing this framework architecture to be flexible (**Table S27**).

Pure rubidium $Rb[Cu(SO_4)_2]$ (Siidra et al., 2021) crystallizes in *Pna*2_1 space group (**Table S27**). Only large elliptical channels remain in $[Cu(SO_4)_2]^{2-}$ open-framework (**Figure 83**). One symmetrically

independent Cu atom forms CuO_5 distorted tetragonal pyramid with Cu-O_{ap} bond of 2.182 Å. One additional long Cu-O bond of 2.994(4) Å results in [4+1+(1)] CuO_6 strongly distorted octahedron. Two of the O-O octahedron edges are bidentantly bridged with SO_4 tetrahedra (Cu-S distances are 2.6 and 3.0 Å).

Finally, $Cs[Cu(SO_4)_2]$ title compound, illustrated in detail in this thesis, has a layered character. All of the features of the Cu^{2+} coordination by sulfate groups to form CuO_5 polyhedra are described above.

Observed trend in a gradient decrease of Cu atom coordination number simultaneously with increase of the *A* metal ionic radii, which in turn define morphotropic boundaries, is an interesting example of the chemical tuning. The similar phenomenon has been recently described in the family of $(AX)[Cu(HSeO_3)_2]$ (*A* = Na, K, NH_4, Rb, Cs; *X* = Cl, Br) compounds (Charkin et al., 2019). Determination of the structural architectures of anhydrous sulfates in saranchinaite morphotropic series should be useful in phase identification and decomposition products of hydrated alkali transition metal sulfates $A^{+}_2M^{2+}(SO_4)_2{\cdot}nH_2O$ (e.g. Majzlan et al., 2021) with various possible and existing applications.

$Cs_2Co_2(SO_4)_3$ is a new representative of another morphotropic series - orthorhombic $A_2M^{2+}_2(SO_4)_3$ (**Table S28**). We have not succeeded yet to obtain $Cs_2Cu_2(SO_4)_3$ representative. Similar to previously described $K_2Cu_2(SO_4)_3$ (Lander at al., 2017) and $Rb_2Cu_2(SO_4)_3$ (Siidra et al., 2021), $Cs_2Co_2(SO_4)_3$ crystallizes also in $P2_12_12_1$. Unit-cell metrics are also similar with *a* parameter value almost the same in all three known to date representatives. However, $[Cu_2(SO_4)_3]^{2-}$ moieties are represented by one-dimensional bands in $K_2Cu_2(SO_4)_3$ and $Rb_2Cu_2(SO_4)_3$, whereas $[Co_2(SO_4)_3]^{2-}$ layers are formed in studied $Cs_2Co_2(SO_4)_3$. It is not clear yet, whether Cs^+ cation or Co^{2+} or both define this morphotropic boundary.

10. Conclusion

Obtaining synthetic analogues of known sulphate minerals can be useful for inorganic chemistry and materials science as well as mineralogy and geochemistry. In contrast, mineral crystals of sufficient size can help to establish the complex crystal structures of polycrystalline materials when it is almost impossible to synthesise crystals of enough size for single crystal X-ray diffraction analysis (e.g. zeolites (Cundy & Cox, 2005)). Also, the study of different methods of synthesis of mineral analogs and their behaviour at high temperatures helps to understand the crystallisation processes of minerals in nature (such as on volcanic fumarols, discussed in this work). Minerals and mineral-like synthetic compounds can serve as inspiration for the design of new materials in many areas of solid state chemistry, as shown in the present work.

This work is dedicated to investigation of structural features and properties of sulfate minerals and related materials. A wide range of synthesis and modification methods was used during the work. 19 new synthetic compounds (7 new structure types) were obtained and structurally characterized by single-crystal and powder X-ray diffraction. All new compounds were obtained in anhydrous A_2SO_4-$M^{2+}SO_4$-($M^{2+}O$) system by the solid-state synthesis and not gas-transport reactions. All of the obtained new compounds have fumarolic mineral analogues or structurally related mineral species.

The work summarises information on the new fumarolic mineral glikinite, $Zn_3O(SO_4)_2$, its chemical and physical properties. It is the fourth anhydrous zinc sulfate mineral known to date. Glikinite was found in Tolbachik volcano, Kamchatka, Russia. The crystal structure of glikinite is based on OZn_4 tetrahedra sharing common corners, thus forming $[Zn_3O]^{4+}$ chains. Sulfate groups interconnect $[Zn_3O]^{4+}$ chains into a 3*D* framework.

A single-phase polycrystalline saranchinaite analog $Na_2Cu(SO_4)_2$ can be obtained by the sol-gel method. $Na_2Cu(SO_4)_2$ is completely hydrated in air and transforms into $Na_2Cu(SO_4)_2{\cdot}2H_2O$ krohnkite. An unusual structural feature of $Na_2Cu(SO_4)_2$ is the presence of heptahedral CuO_7 coordination [4+1+2] with two additional long Cu–O bonds, which are interconnected through common O corners in polar chains. Electrochemical, magnetic, thermal and optical behavior of $Na_2Cu(SO_4)_2$ have also been determined. The magnetic behavior of $Na_2Cu(SO_4)_2$ reflects its crystal structure with one half of copper cations as mainly paramagnetic and the other half as strongly engaged in antiferromagnetic dimer interactions. Electrochemical tests showed a limited electrochemical performance and low mobility of Na ions in the structure.

The synthesis, crystal structure and properties of Zn and Mg analogs of itelmenite, $Na_2CuMg_2(SO_4)_4$ (Nazarchuk et al., 2018) and synthetic analog of glikinite, $Zn_3O(SO_4)_2$ (Nazarchuk et al., 2020) were reported. Synthetic analogues of both minerals were obtained during studies of phase formation in the Na_2SO_4-$CuSO_4$-$MgSO_4$-($ZnSO_4$) systems which lead to essentially different results. The mineral itelmenite, ideally $Na_2CuMg_2(SO_4)_4$, a new structure type, with novel stoichiometry for anhydrous sulfates with alkali and transition metals: $A^{+2}M_2^{+3}(SO_4)_4$ where (A = alkali metal, M = transition metal). $Na_2CuMg_2(SO_4)_4$ and $Na_2CuZn_2(SO_4)_4$ were evaluated for Na^+ ion diffusion. For the Zn compound, several by-products were observed which are synthetic analogs of puninite $Na_2Cu_3O(SO_4)_2$ (Siidra et al., 2017), as well as hermannjahnite $CuZn(SO_4)_2$ (Siidra et al., 2018). All of them were prepared via solid-state reactions in open systems. The $Na_2CuMg_2(SO_4)_4$, $Na_2CuZn_2(SO_4)_4$ and $(Zn,Cu)_3O(SO_4)_2$ were structurally characterized by the single-crystal XRD. In the Zn-bearing system, the admixture of Cu^{2+} likely controls the formation of itelmenite-type and glikinite-type phases.

The synthesis, crystal structure characterization and magnetic properties of synthetic analogs of puninite $Na_2Cu_3O(SO_4)_3$ (Siidra et al., 2017), euchlorine $NaKCu_3O(SO_4)_3$ (Scordari & Stasi, 1990), fedotovite $K_2Cu_3O(SO_4)_3$ (Starova et al., 1991) and the related $Rb_2Cu_{3.07}O_{0.07}(SO_4)_3$, $Cs_2Cu_{3.5}O_{1.5}(SO_4)_3$. For $A_2Cu_3O(SO_4)_3$ (A = Na, K) compounds showed the condensation of individual S= ½ Cu^{2+} ions into S = 1 Cu_6 hexamers interacting at lower temperature following debated models. For larger A = Rb, the lattice changes allow for the admission of non-stoichiometric amount of CuO (x = 0.07), but turns into well-ordered interstitial CuO for A = Cs with stoichiometric x = 0.5 and a double supercell. We showed the structural emergence of Cu^{2+}_{14} tetradecamers which originally act as S = 1 centers due to strong intra-magnetic exchanges. The low temperature square plane S = 1 clusters interactions are discussed on the basis of magnetic measurements along with their *ab-initio* (DFT) and quantum Monte carlo (QMC) calculations. Our comprehensive analysis of the experimental data and 1st principle results suggests that all compounds of the Na-to-Cs series are better described by a (S = 1) square-lattice interaction topology. This excludes the Haldane physics but highlights the importance of anisotropy of S = 1 macrospins.

A remarkable polymorphism in a family of $A_2M_3(SO_4)_4$ (A = Rb, Cs M = Co, Ni) was investigated. This series of compounds was synthesized by the inspiration of mineral itelmenite, $Na_2CuMg_2(SO_4)_4$. New compounds were obtained by solid-state syntheses and structurally characterized by single-crystal and powder X-ray diffraction. In order to establish the temperature of crystallization of synthetic phases differential thermal analysis combined with thermogravimetric analyses were directly performed on the mixtures of precursors. The synthesis conditions were investigated and the stability and complexity of the three polymorphs were discussed. $Rb_2Co_3(SO_4)_4$ and $Rb_2Ni_3(SO_4)_4$ show a 3D framework with 1D tunnels hosting Rb^+ cations. $Cs_2Co_3(SO_4)_4$ and $Cs_2Ni_3(SO_4)_4$ are different, the cobalt one is 3D whereas

the nickel one is 2D with parallel layers surrounded by isolated Cs^+ cations. The connectivity between the cobalt/nickel polyhedra is promising for further magnetic properties measurements but for the moment, the phase stability investigation led to the conclusion that the targeted phases cannot be obtained without impurities using solid state synthesis routes.

The result of the synthesis, crystal structure characterization of new five Rb copper sulfates: $Rb_2Cu(SO_4)Cl_2$, $Rb_4Cu_4O_2(SO_4)_4{\cdot}(Cu_{0.83}Rb_{0.17}Cl)$, $Rb_2Cu_2(SO_4)_3$, $Rb_2Cu_5O(SO_4)_5$ and $Rb_2Cu_2(SO_4)_3(H_2O)$ were reported. The geochemistry of rubidium in volcanic environments was discussed.

And at last two novel anhydrous sulfates $Cs_2Cu(SO_4)_2$ and $Cs_2Co_2(SO_4)_3$ were described. Both of the compounds were synthesized by the solid-state reactions in vacuum. Both new compounds have no structural analogs and add to the family of anhydrous alkali transition metal sulfates. The first representative of this family, with determined structure, was saranchinaite $Na_2Cu(SO_4)_2$. In the crystal structure of $Cs_2Cu(SO_4)_2$ Cu-centered CuO_5 polyhedra and SO_4 tetrahedra form $[Cu(SO_4)_2]^{2-}$ layers with large voids. Unique structural feature of $Cs_2Cu(SO_4)_2$ is the edge-sharing of CuO_5 polyhedra and SO_4 tetrahedra. This type of interpolyhedral connectivity has not been described before. In general, the structural topology of the $Cs_2Co_2(SO_4)_3$ is similar to $K_2Cu_2(SO_4)_3$. The interconnection of Co-centered polyhedra with sulfate tetrahedra occurs via common vertices as well as via common edges with the formation of $[Co_2(SO_4)_3]^{2-}$ corrugated layers with elliptical large cavities.

The chemistry of anhydrous sulfates provides rare and specific opportunities for stabilizing less common environments (e.g. CuO_7) for such magnetically active cations as Cu^{2+}, Co^{2+} and Ni^{2+}. It is also possible that in more complex systems mixed-cations as e.g. Co^{2+} and Cu^{2+} would order to provide new uncommon crystal structures and magnetic behavior. Investigation of pseudo-binary and more complex sulfate systems are expected to shed more light into the crystal chemistry and magnetochemistry of these families.

Bibliography

1. Adam M., Hovestreydt E., Ruf M., Kaercher J. Reaching a new highpoint with crystallography software - APEX3 // Acta Crystallographica. - 2015. - Vol.A 71. - P.s194-s194.
2. Albuquerque A. F., Alet F., Corboz P., Dayal P., Feiguin A., Fuchs S., Gamper L., Gull E., Gürtler S., Honecker A., Igarashi R., Körner M., Kozhevnikov A., Läuchli A., Manmana S. R., Matsumoto M., McCulloch I. P., Michel F., Noack R. M., Pawłowski G., Pollet L., Pruschke T., Schollwöck U., Todo S., Trebst S., Troyer M., Werner P. Wessel S. The ALPS project release 1.3: Open-source software for strongly correlated systems // Journal of Magnetism and Magnetic Materials. - 2007. - Vol. 310(2). - P. 1187-1193.
3. Alcover I. B. David R., Daviero-Minaud S., Filimonov D., Huvé M., Roussel P., Kabbour H., Mentré O. Reversible Exsolution of Nanometric Fe_2O_3 Particles in $BaFe_{2-x}(PO_4)_2$ ($0 \leq \times \leq 2/3$): The Logic of Vacancy Ordering in Novel Metal-Depleted Two-Dimensional Lattices // Crystal Growth and Design. - 2015. - Vol. 15(9). - P. 4237-4247.
4. Alpers C., Jambor J. L., Nordstrom D. Sulfate minerals: Crystallography, geochemistry, and environmental significance // Reviews in Mineralogy & Geochemistry. - 2000. - Vol. 40. -P. 1-608.
5. Amann P., Kataev V., Möller A. Synthesis and characterization of $Na_{11}[CuO_4][SO_4]_3$ // Journal of Solid State Chemistry. - 2004. - Vol. 177(8). - P. 2889-2895.
6. Amann P., Möller A. Reactivity, Syntheses, and Crystal Structures of $Na_5[MO_2][X]$ with M = Co^+, Ni^+, Cu^+; X = CO_3^{2-}, SO_4^{2-}, SO_3^{2-}, S^{2-}, and $Na_{25}[CuO_2]_5[SO_4]_4[S]$ // Zeitschrift für anorganische und allgemeine Chemie - 2003. - Vol. 629(10). - P. 1643-1650.
7. Åsbrink S. A, Norrby L. J. Refinement of the crystal structure of copper(II) oxide with a discussion of some exceptional e.s.d.'s // Acta Crystallographica. - 1970. - Vol. B26. - P. 8-15.
8. Back M. H., Miller N. Use of Ferrous Sulphate Solutions for X-Ray Dosimetry // Nature - 1957. - Vol. 179. - P. 321-322.
9. Blatov V. A., Shevchenko A. P., Proserpio D. M. Applied Topological Analysis of Crystal Structures with the Program Package ToposPro // Crystal Growth & Design. - 2014. - Vol. 14(7). - P. 3576-3586.
10. Bo X., Wang D., Wan B., and Wan X.G. Calculated magnetic exchange interactions in the quantum spin chain materials $K_2CuSO_4Cl_2$ and $K_2CuSO_4Br_2$. // Physical Reviews – 2020. – Vol. B101 - P. 024416.

11. Boghosian S., Fehrmann R., Nielsen K., Liptay G., Snoeck R., Balzarini J., Fransson B., Ragnarsson U., Francis G. Synthesis and Crystal Structure of $Na_3V(SO_4)_3$. Spectroscopic Characterization of $Na_3V(SO_4)_3$ and $NaV(SO_4)_2$ // Acta Chemica Scandinavica. - 1994. - Vol. 48 - P. 724-731.
12. Boivin E., Chotard J. N., Bamine T., Carlier D., Serras P., Palomares V., Rojo T., Iadecola A., Dupont L., Bourgeois L., Fauth F., Masquelier C., Croguennec L. Vanadyl-type defects in Tavorite-like $NaVPO_4F$: from the average long range structure to local environments // Journal of Materials Chemistry. - 2017. - Vol. A5(47) - P. 25044-25055.
13. Boivin E., Chotard J. N., Ménétrier M., Bourgeois L., Bamine T., Carlier D., Fauth F., Suard E., Masquelier C., Croguennec L. Structural and electrochemical studies of a new Tavorite composition: $LiVPO_4OH$ // Journal of Materials Chemistry. - 2016. - Vol. A4(28). - P. 11030-11045.
14. Boyanov B. DTA and TGA study of $MeSo_4$ (Me = Fe, Co, Ni) dissociation in the presence of coke // Journal of Mining and Metallurgy. - 2002. - Vol. B38(1-2). - P. 103-116.
15. Britvin S., Dolivo-Dobrovolsky D., Krzhizhanovskaya M. Software for processing the X-ray powder diffraction data obtained from the curved image plate detector of Rigaku RAXIS Rapid II diffractometer // Zapiski Rossiiskogo Mineralogicheskogo Obshchestva. - 2017. - Vol. 146 - P. 104-107.
16. Bubnova R. S., Firsova V. A., Filatov S. K. Software for determining the thermal expansion tensor and the graphic representation of its characteristic surface (theta to tensor-TTT) // Glass Physics and Chemistry. - 2013. - Vol. 39. - P. 347-350.
17. Burns P.C. and Hawthorne, F.C. Coordination geometry pathways in Cu^{2+} oxysalt minerals // Canadian Mineralogist. – 1995 - Vol. 33. - P.889-905.
18. Chaplygin I.V., Lavrushin V.Y., Dubinina E.O., Bychkova Y.V., Inguaggiato S. and Yudovskaya M.A. Geochemistry of volcanic gas at the 2012-13 New Tolbachik eruption, Kamchatka. // Journal of Volcanology and Geothermal Research. - 2016 - Vol. 323. - P. 186-193.
19. Chaplygin I.V., Taran Y.A., Dubinina E.O., Shapar V.N. and Timofeeva I.F. Chemical composition and metal capacity of magmatic gases of Gorelyi volcano, Kamchatka // Doklady Earth Sciences. – 2015 – Vol. 463. - P. 690-694.
20. Charkin D.O., Markovski M.R., Siidra O.I., Nekrasova D.O. and Grishaev V.Yu. (2019) Influence of the alkali cation size on the Cu^{2+} coordination environments in $(AX)[Cu(HSeO_3)_2]$ (A = Na, K, NH_4, Rb, Cs; X = Cl, Br) layered copper hydrogen selenite halides. // Zeitschrift für Kristallographie - Crystalline Materials. – 2019- Vol. 234. - P. 739-747.

21. Chen G., Zhang B., Zhao J., Chen H. Improved process for the production of cellulose sulfate using sulfuric acid/ethanol solution // Carbohydrate polymers. - 2013. - Vol. 95(1). - P. 332-337.
22. Churikova T., Dorendorf F. and Wörner G. Sources and fluids in the mantle wedge below Kamchatka, evidence from across-arc geochemical variation // Journal of Petrology.- 2001 - Vol. 42. – P. 1567-1593.
23. Churikova T.G., Gordeychik B.N., Edwards B.R., Ponomareva V.V. and Zelenin E.A. The Tolbachik volcanic massif: A review of the petrology, volcanology and eruption history prior to the 2012-2013 eruption // Journal of Volcanology and Geothermal Research – 2015a – Vol. 307. – P. 3-21.
24. Churikova T.G., Gordeychik B.N., Iwamori H., Nakamura H., Ishizuka O., Nishizawa T., Haraguchi S., Miyazaki T. and Vaglarov B.S. Petrological and geochemical evolution of the Tolbachik volcanic massif, Kamchatka, Russia // Journal of Volcanology and Geothermal Research. - 2015b - Vol. 307. - P. 156-181.
25. Cole D. E. C., Evrovski J. The Clinical Chemistry of Inorganic Sulfate // Critical Reviews in Clinical Laboratory Sciences. - 2000. - Vol. 37(4). - P. 299-344.
26. Cundy C., Cox P. The Hydrothermal Synthesis of Zeolites: Precursors, Intermediates and Reaction Mechanism // Microporous and Mesoporous Materials. - 2005. - Vol. 82(1-2). P. 1-78.
27. David R., Kabbour H., Filimonov D., Huvé M., Pautrat A., Mentré O. Reversible topochemical exsolution of iron in $BaFe^{2+}_2(PO_4)_2$ // Angewandte Chemie - International Edition. - 2014. - Vol. 53(49). - P. 13365-13370.
28. Donatello S., Fernández-Jiménez A., Palomo A. Very High Volume flyash Cements. Early age Hydration Study Using Na_2SO_4 as an Activator // Journal of the American Ceramic Society. - 2013. - Vol. 96(3). - P. 900-906.
29. Dwibedi D., Gond R., Dayamani A., Araujo R.B., Chakraborty S., Ahuja R., Barpanda P. $Na_{2.32}Co_{1.84}(SO_4)_3$ as a new member of the alluaudite family of high-voltage sodium battery cathodes // Dalton Transactions. - 2017. - Vol. 46(1). - P. 55-63.
30. Effenberger H. and Zemann J. The crystal structure of caratiite // Mineralogical Magazine. – 1984 – Vol. 48. – P. 541-546.
31. Effenberger H., Zemann J. The crystal structure of caratiite // Mineralogical Magazine. - 1984. - Vol. 48. - P. 541-546.
32. Fehrmann R., Boghosian S., Papatheodorou G., Nielsen K., Berg R., Bjerrum N., Underhill A. The crystal structure of $NaV(SO_4)_2$ // Acta Chemica Scandinavica - 1991. - Vol. 45. - P. 961-964.

33. Fehrmann R., Boghosian S., Papatheodorou G.N., Nielsen K., Berg R.W., Bjerrum N. Crystal Structure and Vibrational Spectra of $Na_2VO(SO_4)_2$ // Inorganic Chemistry - 1990. - Vol. 29(18). - P. 3294-3298.
34. Fujihala M., Mitsuda S., Mole R.A., Yu D.H., Watanabe I., Yano S., Kuwai T., Sagayama H., Kouchi T., Kamebuchi H. and Tadokoro M. Spin dynamics and magnetic ordering in the quasi-one-dimensional S=1/2 antiferromagnet $Na_2CuSO_4Cl_2$ // Physical Reviews. – 2020 – Vol. B101. – P. 024410.
35. Fujihala M., Sugimoto T., Tohyama T., Mitsuda S., Mole R. A., Yu D.H., Yano S., Inagaki Y., Morodomi H., Kawae T., Sagayama H., Kumai R., Murakami Y., Tomiyasu K., Matsuo A., Kindo K. Cluster-Based Haldane State in an Edge-Shared Tetrahedral Spin-Cluster Chain: Fedotovite $K_2Cu_3O(SO_4)_3$ // Physical Review Letters. - 2018. - Vol. 120(7). - P.77201.
36. Furrer A., Podlesnyak A., Pomjakushina E., Pomjakushin V. Spin triplet ground-state in the copper hexamer compounds $A_2Cu_3O(SO_4)_3$ (A = Na, K) // Physical Review B. - 2018. - Vol. 98(18). - P. 180410.
37. Gasteiger H. Krischer K., Scrosati B. Electrochemical Cells: Basics. In Lithium Batteries (eds B. Scrosati, K.M. Abraham, W. Van Schalkwijk and J. Hassoun). - 2013.
38. Gattow G. and Zemann J. Über Doppelsulfatsalze vom Typ $A^{+}{}_2B^{2+}{}_2(SO_4)_3$ // Zeitschrift für Anorganische und Allgemeine Chemie. – 1958 – Vol. 293. - P. 233-240.
39. Gavryushkin P., Thomas V., Bolotina N., V. B. V., Golovin A., Seryotkin Y., Fursenko D., Litasov K. Hydrothermal Synthesis and Structure Solution of $Na_2Ca(CO_3)_2$: “Synthetic Analogue” of Mineral Nyerereite // Crystal Growth & Design. - 2016. - Vol. 16(4). - P. 1983-190.
40. Giacovazzo C. Scandale E. and Scordari F. (1976) The crystal structure of chlorothionite $CuK_2Cl_2SO_4$ // Zeitschrift für Kristallographie - Crystalline Materials. – 1976 – Vol. 144. – P. 226-237.
41. Goñi A., Iturrondobeitia A., Gil de Muro I., Lezama L., Rojo T. $Na_{2.5}Fe_{1.75}(SO_4)_3$/Ketjen/rGO: An advanced cathode composite for sodium ion batteries // Journal of Power Sources. - 2017. - Vol. 369 - P. 95-102.
42. Hamelet S., Gibot P., Casas-Cabanas M., Bonnin D., Grey C. P., Cabana J., Leriche J. B., Rodriguez-Carvajal J., Courty M., Levasseur S., Carlach P., Thournout M. V., Tarascon J. M., Masquelier C. The effects of moderate thermal treatments under air on $LiFePO_4$ - based nano powders // Journal of Materials Chemistry. - 2009. - Vol. 19(23). - P. 3979-3991.

43. Hase M., Rule K. C., Hester J. R., Fernandez-Baca J. A., Masuda T., Matsuo Y. A possible magnetic structure of the cluster-based haldane compound fedotovite $K_2Cu_3O(SO_4)_3$ // Journal of the Physical Society of Japan. - 2019. - Vol. 88(9). - P. 1-5.
44. Hawthorne F.C., Krivovichev S.V. and Burns P.C. The crystal chemistry of sulfate minerals. In Sulfate Minerals – Crystallography, Geochemistry and Environmental Significance (C.N. Alpers, J.L. Jambor, D.K. Nordstrom, eds.). Mineralogical Society of America and Geochemical Society // Reviews in Mineralogy and Geochemistry. -2020 – Vol. 40. - P. 1-112.
45. Kahlenberg V., Piotrowski A. and Giester G. Crystal structure of $Na_4[Cu_4O_2(SO_4)_4]$·MeCl (Me: Na, Cu, vac) - the synthetic Na-analogue of piypite (caratiite) // *Mineralogical Magazine*. – 2000- Vol. **64**. - P. 1099-1108.
46. Kornyakov I.V., Vladimirova V.A., Siidra O.I. and Krivovichev S.V. Expanding the averievite family, $(MX)Cu_5O_2(T^{5+}O_4)_2$ (T^{5+} = P, V; M = K, Rb, Cs, Cu; X = Cl, Br): synthesis and single-crystal X-ray diffraction study // Molecules. - 2021 - Vol. 26. – P. 833.
47. Kovrugin V. M., David R., Chotard J. N., Recham N., Masquelier C. A High Voltage Cathode Material for Sodium Batteries: $Na_3V(PO_4)_2$ // Inorganic Chemistry. - 2018. - Vol. 57(15). - P. 8760-8768.
48. Kovrugin V. M., Nekrasova D. O., Siidra O. I., Mentré O., Masquelier C., Stefanovich S. Y., Colmont M. Mineral-Inspired Crystal Growth and Physical Properties of $Na_2Cu(SO_4)_2$ and Review of $Na_2M(SO_4)_2(H_2O)_x$ (x = 0-6) Compounds // Crystal Growth & Design. - 2019. - Vol. 19(2). - P. 1233-1244.
49. Krivovichev S. Topological complexity of crystal structures: Quantitative approach // Acta Crystallographica. - 2012. - Vol. A68. - P.393-398.
50. Krivovichev S. V, Mentre O., Siidra O. I., Colmont M., Filatov S. K. Anion-Centered Tetrahedra in Inorganic Compounds // Chemical Reviews. - 2013. - Vol. 113(8). - P. 6459-6535.
51. Lander L., Batuk D., Colin C. V, Alves D., Corte D., Tarascon J. Synthesis, Structure, and Electrochemical Properties of K - Based Sulfates $K_2M_2(SO_4)_3$ with M = Fe and Cu // Inorganic Chemistry. - 2017. - Vol. 56(4) - P. 2013-2021.
52. Lander L., Rousse G., Abakumov A., Sougrati M. T., Tendeloo G., Tarascon J. M. Structural, electrochemical and magnetic properties of a novel $KFeSO_4F$ polymorph // Journal of Materials Chemistry. - 2015. - Vol. A3. - P. 19754-19764.
53. Lim A. R., Kim S. H. Study on structural phase transitions and relaxation processes of $Cs_2Co(SO_4)_2·6H_2O$ and $Cs_2Zn(SO_4)_2·6H_2O$ crystals // Materials Chemistry and Physics. - 2009. - Vol. 117(2-3). - P. 557-561.

54. Long G. J. A Mössbauer Effect And Magnetic Study of $Fe_2(SO_4)_3$ and $Fe_2(MoO_4)_3$, Two L-Type Ferrimagnets BT // Chemical Mössbauer Spectroscopy. - 1984. -P. 95-111.
55. Marsh R.E. Some thoughts on choosing the correct space group // Acta Crystallographica. – 1995 - Vol. B51. – P. 897-907.
56. Masquelier C. and Croguennec L. Polyanionic (phosphates, silicates, sulfates) frameworks as electrode materials for rechargeable Li (or Na) Batteries // Chemical Reviews. – 2013 – Vol. 113. – P. 6552-6591.
57. Menyailov I.A. and Nikitina L.P. Chemistry and metal contents of magmatic gases: the new Tolbachik volcanoes case (Kamchatka) // *Bulletin Volcanologique.* – 1980 – Vol. **43**. – P. 195-205.
58. Mikhailov M. M., Yuryev S. A., Lapin A. N., Lovitskiy A. A. The effects of heating on $BaSO_4$ powders' diffuse reflectance spectra and radiation stability // Dyes and Pigments. - 2019. - Vol. 163. - P. 420-424.
59. Möller A., Sobotka B. M., Baier J., Freimuth A. Ein Natrium-Oxocobaltat(II)-Sulfat: $Na_8[CoO_3][SO_4]_2$ // Zeitschrift für anorganische und allgemeine Chemie. - 2002. - Vol. 628(12). - P. 2705-2708.
60. Nandi P., Deshpande D., Kher V. Dehydration steps in $CuSO_4 \cdot 5H_2O$ crystals // Proceedings of the Indian Academy of Sciences - Chemical Sciences. - 1979. - Vol. A8(1). - P. 113-124.
61. Nath R., Padmanabhan M., Baby S., Thirumurugan A., Ehlers D., Hemmida M., Nidda H.-A. V., Tsirlin A. A. Quasi-two-dimensional S = 1/2 magnetism of $Cu[C_6H_2(COO)_4][C_2H_5NH_3]_2$ // Physical Review B. - 2015. - Vol. 91(5). - P.54409.
62. Nath R., Tsirlin A. A., Khuntia P., Janson O., Förster T., Padmanabhan M., Li J., Skourski Y., Baenitz M., Rosner H., Rousochatzakis I. Magnetization and spin dynamics of the spin S = 1/2 hourglass nanomagnet $Cu_5(OH)_2(NIPA)_4 \cdot 10H_2O$ // Physical Review B. - 2013. - Vol. 87(21). - P. 214417.
63. Nazarchuk E. V., Siidra O. I., Nekrasova D. O., Shilovskikh V. V, Borisov A. S., Avdontseva E. Y. Glikinite, $Zn_3O(SO_4)_2$, a new anhydrous zinc oxysulfate mineral structurally based on OZn4 tetrahedra // Mineralogical Magazine. - 2020. - Vol. 84(4). - P. 563-567.
64. Nazarchuk E., Siidra O., Agakhanov A., Lukina E., Avdontseva E., Karpov G. Itelmenite, $Na_2CuMg_2(SO_4)_4$, a new anhydrous sulfate mineral from the Tolbachik Volcano // Mineralogical Magazine. - 2018. - Vol. 82(6). - P. 1-18.

65. Neagu D., Oh T. S., Miller D. N., Ménard H., Bukhari S. M., Gamble S. R., Gorte R. J., Vohs J. M., Irvine J. T. S. Nano-socketed nickel particles with enhanced coking resistance grown in situ by redox exsolution // Nature communications. - 2015. - Vol. 6. - P. 8120.

66. Nekrasova D. O., Siidra O. I., Zaitsev A. N., Ugolkov V. L., Colmont M., Charkin D. O., Mentré O., Chen R., Kovrugin V. M., Borisov A. S. A fumarole in a one-pot: synthesis, crystal structure and properties of Zn- and Mg-analogs of itelmenite and a synthetic analog of glikinite // Physics and Chemistry of Minerals. - 2021. - Vol. 48. - P. 6.

67. Nekrasova D. O., Tsirlin A. A., Colmont M., Siidra O., Vezin H., Mentré O. Magnetic hexamers interacting in layers in the $(Na,K)_2Cu_3O(SO_4)_3$ minerals // Physical Review B. - 2020. - Vol. 102(18). - P. 184405.

68. Nekrasova, D. O., Tsirlin, A. A., Colmont, M., Siidra, O. I., Arévalo-López, Á. M., Mentré, O. From (S = 1) Spin Hexamer to Spin Tetradecamer by CuO Interstitials in $A_2Cu_3O(CuO)_x(SO_4)_3$ (A = Alkali) // Inorganic Chemistry. – 2021. – Vol. 60(23). – P. 18185–18191.

69. Nielsen K., Boghosian S., Fehrmann R., Berg R. W. The Crystal Structure and Spectroscopic Characterization of a Green V^{IV} Compound, $Na_8(VO)_2(SO_4)_6$ // Acta Chemica Scandinavica. - 1999. - Vol. 53 - P. 15-23.

70. Oben B., Froyen G., Maclachlan K., Leongamornlert D., Abascal F., Zheng-Lin B., Yellapantula V., Derkach A., Geerdens E., Diamond B., Arijs I., Maes B., Vanhees K., Hultcrantz M., Manasanch E., Kazandjian D., Lesokhin A., Dogan A., Zhang Y., Maura F. Whole-genome sequencing reveals progressive versus stable myeloma precursor conditions as two distinct entities // Nature Communications. - 2021. - Vol. 12.(1). -P. 1861.

71. Opahle I., Koepernik K., Eschrig H. Full potential band structure calculation of iron pyrite // Computational Materials Science. - 2000. - Vol. 17(2-4). - P. 206-210.

72. Palacín M. R. Recent advances in rechargeable battery materials: a chemist's perspective // Chemical Society Reviews. - 2009. - Vol. 38(9). - P. 2565-2575.

73. Pautov L.A., Mirakov M.A., Siidra O.I., Faiziev A.R., Nazarchuk E.V., Karpenko V.Yu. and Makhmadsharif S. Falgarite, $K_4(VO)_3(SO_4)_5$, a new mineral from sublimates of a natural underground coal fire at the tract of Kukhi-Malik, Fan-Yagnob coal deposit, Tajikistan // Mineralogical Magazine. – 2020 – Vol. 84. – P. 455-462.

74. Pekov I. V, Zubkova N. V, Agakhanov A. A., Pushcharovsky D. Y., Yapaskurt V. O., Belakovskiy D. I., Vigasina M. F., Sidorov E. G., Britvin S. N. Cryptochalcite $K_2Cu_5O(SO_4)_5$ and cesiodymite $CsKCu_5O(SO_4)_5$ - two new isotypic minerals and the K-Cs isomorphism in this solid-solution series // European Journal of Mineralogy. - 2018. - Vol. 30(3) - P. 593-607.

75. Pekov I. V, Zubkova N. V, Pushcharovsky D.Y. Copper minerals from Volcanic exhalations - a unique family of natural compounds: crystal-chemical review // Acta Crystallographica. - 2018. - Vol. B74. - P. 502-518.
76. Pekov I.V., Zubkova N.V., Yapaskurt V.O., Belakovskiy D.I., Chukanov N.V., Lykova I.S., Savelyev D.P., Sidorov E.G. and Pushcharovsky D.Yu. Wulffite, $K_3NaCu_4O_2(SO_4)_4$, and parawulffite, $K_5Na_3Cu_8O_4(SO_4)_8$, two new minerals from fumarole sublimates of the Tolbachik volcano, Kamchatka, Russia // Canadian Mineralogist. – 2014 – Vol. 52. – P. 699-716.
77. Perdew J. P., Burke K., Ernzerhof M. Generalized gradient approximation made simple // Physical Review Letters. - 1996. - Vol. 77(18). - P. 3865.
78. Petrícek V., Dušek M., Palatinus L. Crystallographic computing system JANA2006: General features // Zeitschrift fur Kristallographie. - 2014. - Vol. 229(5). - P. 345-352.
79. Popolitov E.I. and Volynets O.N. Geochemistry of quaternary volcanic rocks from the Kurile-Kamchatka island arc // Journal of Volcanology and Geothermal Research. –1982 – Vol. 12. – P. 299-316.
80. Portnyagin M., Duggen S., Hauff F., Mironov N., Bindeman I., Thirlwall M. and Hoernle K. Geochemistry of the late Holocene rocks from the Tolbachik volcanic field, Kamchatka: Quantitative modelling of subduction-related open magmatic systems // Journal of Volcanology and Geothermal Research. – 2015 – Vol. 307. – P. 133-155.
81. Reynaud M., Rodriguez-Carvajal J., Chotard J.-N., Tarascon J.-M., Rousse G. Magnetic structure and properties of orthorhombic $Li_2Ni(SO_4)_2$: A possible magnetoelectric material // Physical Review B. - 2014. - Vol. 89. - P. 104419.
82. Reynaud M., Rousse G., Chotard J.-N., Rodriguez-Carvajal J., Tarascon J.-M. Marinite $Li_2M(SO_4)_2$ (M = Co, Fe, Mn) and $Li_1Fe(SO_4)_2$: Model compounds for super-super-exchange magnetic interactions // Inorganic chemistry. - 2013. - Vol. 52(18). - 10456-10466.
83. Rodríguez-Carvajal J. Recent advances in magnetic structure determination by neutron powder diffraction // Physica B: Condensed Matter. - 1993. - Vol. 192(1-2). - P. 55-69.
84. Rousse G. and Tarascon J.-M. Sulfate-based polyanionic compounds for Li-ion batteries: synthesis, crystal chemistry, and electrochemistry aspects // Chemistry of Materials. – 2014 – Vol. 26. – P. 394-406.
85. Schäffer S. J. C., Berg R. W. catena-Poly[tetra-sodium [[cis-dioxido-trans-bis-(sulfato-κO)molybdate(VI)]-μ-sulfato-κO:O']] // Acta Crystallographica. - 2008. - Vol. E64(11). - P. i73-i73.

86. Scordari F., Stasi F. The crystal structure of euchlorine, $NaKCu_3O(SO_4)_3$, Locality: Vesuvius, Italy // Neues Jahrbuch fur Mineralogie, Abhandlungen - 1990. - Vol. 161(3). - P. 241-253.

87. Sheldrick G. M. Crystal structure refinement with SHELXL // Acta Crystallographica. - 2015. - Vol. C71. - P. 3-8.

88. Sidis Y., Bourges P., Keimer B., Regnault L., Bossy J., Ivanov A., Hennion B., Gautier-Picard P., Collin G. Magnetic Resonance Peak and Nonmagnetic Impurities // Bonča J., Prelovšek P., Ramšak A., Sarkar S. (eds) Open Problems in Strongly Correlated Electron Systems. NATO Science Series (Series II: Mathematics, Physics and Chemistry), Springer, Dordrecht. - 2010. - Vol. 15.

89. Siidra O. I., Borisov A. S., Lukina E. A., Depmeier W., Platonova N. V, Colmont M., Nekrasova D. O. Reversible hydration/dehydration and thermal expansion of euchlorine, ideally $KNaCu_3O(SO_4)_3$ // Physics and Chemistry of Minerals. - 2019. - Vol. 46(4). - P. 403-416.

90. Siidra O. I., Nazarchuk E. V, Zaitsev A. N., Lukina E. A., Avdontseva E. Y., Vergasova L. P., Vlasenenko N. S., Filatov S. K., Turner R. W., Karpov G. A. Copper oxosulphates from fumaroles of Tolbachik Volcano: puninite, $Na_2Cu_3O(SO_4)_3$ a new mineral species and structure refinements of kamchatkite and alumoklyuchevskite // European Journal of Mineralogy. - 2017. - Vol. 29(3) - P. 499-510.

91. Siidra O.I., Borisov A.S., Charkin D.O., Depmeier W. and Platonova N.V. Evolution of fumarolic anhydrous copper sulfate minerals during successive hydration/dehydration // Mineralogical Magazine – 2021– Vol. – 85. – P. 262-277.

92. Siidra O.I., Kozin M.S., Depmeier W., Kayukov R.A. and Kovrugin V.M. Copper – lead selenite bromides: A new large family of compounds partly having Cu^{2+} substructures derivable from Kagome-nets // Acta Crystallographica. – 2018 – Vol. - B74 – P. 712-724.

93. Siidra O.I., Lukina E.A., Nazarchuk E.V., Depmeier W., Bubnova R.S., Agakhanov A.A., Avdontseva E.Yu., Filatov S.K. and Kovrugin V.M. Saranchinaite, $Na_2Cu(SO_4)_2$, a new exhalative mineral from Tolbachik Volcano, Kamchatka, Russia, and a product of the reversible dehydration of kröhnkite, $Na_2Cu(SO_4)_2(H_2O)_2$ // Mineralogical Magazine – 2018 – Vol. – 82 – P.257-274.

94. Siidra O.I., Nazarchuk E.V., Agakhanov A.A. and Polekhovsky Yu.S. (2019) Aleutite $[Cu_5O_2](AsO_4)(VO_4)\cdot(Cu_{0.5}\square_{0.5})Cl$, a new complex salt-inclusion mineral with Cu^{2+} substructure derived from Kagome-net // Mineralogical Magazine – 2019 – Vol. – 83. – P. 847-853.

95. Siidra O.I., Nazarchuk E.V., Lukina E.A., Zaitsev A.N. and Shilovskikh V.V. Belousovite, $KZn(SO_4)Cl$, a new sulphate mineral from the Tolbachik volcano with apophyllite sheet-topology // Mineralogical Magazine – 2018 – Vol. 82. – P. 1079-1088.

96. Siidra O.I., Nazarchuk E.V., Zaitsev A.N. and Shilovskikh V.V. Majzlanite, $K_2Na(ZnNa)Ca(SO_4)_4$, a new anhydrous sulphate mineral with complex cation substitutions from Tolbachik volcano // Mineralogical Magazine – 2020 –Vol. 84. – P. 153-158.
97. Siidra, O. I., Nekrasova, D. O., Charkin, D. O., Zaitsev, A. N., Borisov, A. S., Colmont, M., Mentré, O., Spiridonova, D. V. Anhydrous Alkali Copper Sulfates – a Promising Playground for New Cu^{2+} Oxide Complexes: New Rb-Analogues of Fumarolic Minerals // Mineralogical Magazine. -2021. –Vol. 85 (6). – P. 831–845.
98. Singh P., Shiva K., Celio H., Goodenough J. Eldfellite, $NaFe(SO_4)_2$: An Intercalation Cathode Host for Low-Cost Na-ion Batteries // Energy & Environmental Science. - 2015. - Vol. 8(10). - P. 3000-3005.
99. Soldatov T.A., Smirnov A.I., Povarov K.Yu., Hälg M., Lorenz W.E.A. and Zheludev A. Spin gap in the quasi-one-dimensional S=1/2 antiferromagnet $K_2CuSO_4Cl_2$ // Physical Reviews. – 2018 – Vol. B98. - P. 144440.
100. Spiridonova D. V., Krivovichev S. V., Britvin S. N., Yakovenchuk V. N. Crystal Chemistry of Ion-Exchanged Forms of Zorite, a Natural Analogue of the ETS-4 Titanosilicate Material. In: Krivovichev S. (eds) Minerals as Advanced Materials II. Springer, Berlin, Heidelberg. - 2011. - P. 199-204.
101. Subban C. V, Ati M., Rousse G., Abakumov A. M., Tendeloo G. V., Janot R., Tarascon J. M. Preparation, Structure, and Electrochemistry of Layered Polyanionic Hydroxysulfates: $LiMSO_4OH$ (M = Fe, Co, Mn) Electrodes for Li-Ion Batteries // Journal of the American Chemical Society. - 2013. - Vol. 135(9). - P. 3653-3661.
102. Sun M., Rousse G., Abakumov A. M., Saubanère M., Doublet M. L., Rodríguez-Carvajal J., Tendeloo G. V., Tarascon J. M. $Li_2Cu_2O(SO_4)_2$: a Possible Electrode for Sustainable Li-Based Batteries Showing a 4.7 V Redox Activity vs Li^+/Li^0 // Chemistry of Materials. - 2015. - Vol. 27(8). - P. 3077-3087.
103. Symonds R.B. and Reed M.H. Calculation of multicomponent chemical equilibria in gas-solid-liquid systems: calculation methods, thermochemical data, and applications to studies of high-temperature volcanic gases with examples from Mount St. Helens // American Journal of Science – 1993 – Vol. 293. – P. 758-864.
104. Taran Yu.A., Hedenquist J.W., Korzhinsky M.A., Tkachenko S.I. and Shmulovich K.I. Geochemistry of magmatic gases from Kudryavy volcano, Iturup, Kuril Islands // Geochimica et Cosmochimica Acta – 1995 – Vol. 59. – P. 1749-1761.

105. Tedesco D. and Toutain J.-P. Chemistry and emission rate of volatiles from White Island Volcano (New Zealand) // Geophysical Research Letters – 1991 – Vol. 18. – P. 113-116.
106. Todo S., Kato K. Cluster Algorithms for General- S Quantum Spin Systems // Physical Review Letters. - 2001. - Vol. 87(4). - P. 047203.
107. Vergasova L.P. and Filatov S.K. New mineral species in products of fumarole activity of the Great Tolbachik Fissure Eruption // Journal of Volcanology and Seismology – 2012 – Vol. 6. – P. 281-289.
108. Vergasova L.P., Filatov S.K., Serafimova E.K. and Stalova G.L. Piypite $K_2Cu_2O(SO_4)_2$ - a new mineral of volcanic sublimates // Doklady USSR Academy of Sciences, Earth Science Sections – 1984 – Vol. 275. – P. 714-717.
109. Vergasova L.P., Filatov S.K., Serafimova Y.K. and Starova G.L. Fedotovite $K_2Cu_3O(SO_4)_3$ - a new mineral from volcanic sublimates // Doklady Akademii Nauk SSSR – 1988 – Vol. 299. – P. 961-964.
110. Vergasova L.P., Starova G.L., Filatov S.K. and Anan'ev V.V. Averievite $Cu_5(VO_4)_2O_2 \cdot n\mathit{MX}$ - a new mineral of volcanic exhalations // Doklady Akademii Nauk –1998 – Vol. 359. – P. 804-807.
111. Volynets A.O., Edwards B.R., Melnikov D., Yakushev A. and Griboedova I. Monitoring of the volcanic rock compositions during the 2012-2013 fissure eruption at Tolbachik volcano, Kamchatka // Journal of Volcanology and Geothermal Research –2015 – Vol. 307. – P. 120-132.
112. Xiang H. J., Kan E. J., Wei S. H., Whangbo M. H., Gong X. G. Predicting the spin-lattice order of frustrated systems from first principles // Physical Review B. - 2011. - Vol. 84(22). - P. 224429.
113. Zelenski M., Kamenetsky V.S. and Hedenquist J. Gold recycling and enrichment beneath volcanoes: A case study of Tolbachik, Kamchatka // Earth and Planetary Science Letters – 2016 – Vol. 437. – P. 35-46.
114. Zelenski M., Malik N. and Taran Y. Emissions of trace elements during the 2012-2013 effusive eruption of Tolbachik volcano, Kamchatka: Enrichment factors, partition coefficients and aerosol contribution // Journal of Volcanology and Geothermal Research – 2014 – Vol. 285. – P. 136-149.
115. Zelenski M.E., Fischer T.P., de Moor J.M., Marty B., Zimmermann L., Ayalew D., Nekrasov A.N. and Karandashev V.K. Trace elements in the gas emissions from the Erta Ale volcano, Afar, Ethiopia // Chemical Geology. – 2013 – Vol. 357. – P. 95-116.
116. Zhou H. A., Liu Z., Ang S. S., Zhang J. J. Synthesis, structure, and electrochemical performances of a novel three-dimensional framework $K_2[Cu(SO_4)_2]$ // Solid State Sciences. - 2020. - Vol. 100. - P. 106104.

Supplementary information

Table S1. Powder X-ray diffraction data for glikinite.

h	k	l	d_{meas}	I_{meas}	d_{calc}	I_{calc}
0	0	-1	6.9684	56	6.9760	57
1	0	0	6.4673	14	6.4941	33
1	1	0	4.6255	20	4.6248	37
1	0	1	3.9421	52	3.9405	53
1	0	-2	3.9041	38	3.9037	50
2	0	-1	3.6476	20	3.6488	100
0	0	-2	3.4832	100	3.4880	83
0	2	0	3.2943	49	3.2939	83
2	0	-2	3.2129	12	3.2196	40
0	1	-2	3.0805	9	3.0826	6
0	2	-1	2.9795	24	2.9786	36
1	2	0	2.9364	43	2.9376	49
1	0	2	2.6159	27	2.6154	20
2	0	1	2.5335	63	2.5344	77
2	0	-3	2.5068	63	2.5084	71
2	2	-1	2.4449	33	2.4450	98
1	1	-3	2.4165	16	2.4164	18
0	2	-2	2.3945	86	2.3948	77
2	1	1	2.3653	2	2.3654	3
2	2	0	2.3121	2	2.3124	3
1	3	0	2.0800	22	2.0802	19
3	1	-3	2.0408	4	2.0408	6
1	3	1	1.9185	3	1.9182	1
4	0	-2	1.8252	15	1.8244	23
3	2	-3	1.8252	10	1.7983	18

Table S2. Coordinates and isotropic displacement parameters ($Å^2$) of atoms in glikinite.

Atom	x	y	z	U_{eq}
Zn1	½	½	0	0.0154(5)
Zn2	-0.1252(4)	¾	0.2536(3)	0.0164(7)
Zn3	0.6595(4)	¾	0.7708(3)	0.0172(7)
S1	0.3528(6)	¾	0.3051(7)	0.0114(12)
S2	0.0624(7)	¾	0.7181(7)	0.0114(12)
O1	0.6280(14)	¾	0.0096(19)	0.009(2)
O2	0.1964(14)	0.9312(19)	0.7636(12)	0.017(2)
O3	-0.079(2)	¾	0.5212(19)	0.026(4)
O4	0.388(2)	0.570(2)	0.2148(16)	0.032(3)
O5	-0.046(2)	¾	0.8312(19)	0.030(4)
O6	0.139(3)	¾	0.262(3)	0.077(8)
O7	0.479(3)	¾	0.497(2)	0.091(10)

Table S3. Anisotropic displacement parameters (Å^2) of atoms in glikinite.

Atom	U^{11}	U^{22}	U^{33}	U^{23}	U^{13}	U^{12}
Zn1	0.0194(13)	0.0102(14)	0.0180(9)	0.0004(9)	0.0097(12)	-0.0022(7)
Zn2	0.0181(11)	0.013(2)	0.0123(11)	0	0.0021(9)	0
Zn3	0.0243(14)	0.015(2)	0.0125(11)	0	0.0089(9)	0
S1	0.015(2)	0.006(4)	0.011(2)	0	0.0039(17)	0
S2	0.0151(19)	0.011(4)	0.0064(17)	0	0.0039(17)	0
O1	0.007(4)	0.001(6)	0.013(4)	0	0.001(4)	0
O2	0.011(4)	0.021(8)	0.013(4)	-0.003(4)	0.000(3)	0.001(4)
O3	0.041(8)	0.010(11)	0.012(6)	0	-0.001(6)	0
O4	0.070(9)	0.006(9)	0.042(6)	0.002(5)	0.044(7)	0.004(6)
O5	0.023(7)	0.050(12)	0.027(7)	0	0.021(6)	0
O6	0.042(10)	0.055(17)	0.17(2)	0	0.075(13)	0
O7	0.14(2)	0.050(19)	0.009(7)	0	-0.032(11)	0

Table S4. Selected interatomic distances (in Å) in glikinite.

	1.878(5) ×2	S1-O7	1.361(15)
Zn1-O1			
Zn1-O2	2.191(10) ×2	S1-O6	1.435(18)
Zn1-O4	2.230(10) ×2	S1-O4	1.465(13) ×2
		<S1-O>	1.432
Zn2-O6	1.902(17)		
Zn2-O1	1.939(12)	S2-O3	1.413(14)
Zn2-O3	1.967(14)	S2-O5	1.435(13)
Zn2-O2	2.153(13) ×2	S2-O2	1.480(12) ×2
		<S2-O>	1.451
Zn3-O7	1.938(15)		
Zn3-O5	1.977(14)	O1-Zn1	1.878(5) ×2
Zn3-O1	1.987(13)	O1-Zn2	1.939(12)
Zn3-O4	2.144(15) ×2	O1-Zn3	1.987(13)

Table S5. Selected interatomic distances (in Å) in itelmenite (Nazarchuk et al. 2018), $Na_2CuMg_2(SO_4)_4$ and $Na_2CuZn_2(SO_4)_4$.

Itelmenite				$Na_2CuMg_2(SO_4)_4$				$Na_2CuZn_2(SO_4)_4$			
*M*1-O14	1.961(3)	Na2-O4	2.385(3)	*M*1-O13	1.950(3)	Na2-O4	2.376(4)	*M*1-O13	1.962(5)	Na2-O4	2.380(6)
*M*1-O13	1.961(3)	Na2-O13	2.447(4)	*M*1-O14	1.956(3)	Na2-O13	2.448(4)	*M*1-O14	1.994(6)	Na2-O14	2.428(7)
*M*1-O16	1.976(3)	Na2-O3	2.456(3)	*M*1-O16	1.976(3)	Na2-O3	2.459(4)	*M*1-O16	2.024(6)	Na2-O13	2.444(7)
*M*1-O2	2.032(3)	Na2-O14	2.465(3)	*M*1-O2	2.023(3)	Na2-O14	2.462(4)	*M*1-O2	2.011(6)	Na2-O7	2.462(6)
*M*1-O3	2.153(3)	Na2-O1	2.520(3)	*M*1-O3	2.164(3)	Na2-O7	2.530(4)	*M*1-O3	2.116(6)	Na2-O3	2.492(7)
*M*1-O2	2.826(3)	Na2-O7	2.544(3)	*M*1-O2	2.804(3)	Na2-O1	2.533(4)	*M*1-O2	2.850(6)	Na2-O1	2.533(7)
<*M*1-O>	2.152	Na2-O10	2.828(4)	<*M*1-O>	2.146	Na2-O10	2.829(4)	<*M*1-O>	2.160	Na2-O15	2.812(7)
		Na2-O15	2.846(3)			Na2-O15	2.830(4)			Na2-O10	2.868(7)
*M*2-O11	1.980(3)	<Na2-O>	2.561	*M*2-O11	1.962(3)	<Na2-O>	2.558	*M*2-O11	1.981(6)	<Na2-O>	2.552
*M*2-O8	2.028(3)			*M*2-O8	2.005(3)			*M*2-O8	2.021(6)		
*M*2-O9	2.048(3)	S1-O15	1.445(3)	*M*2-O9	2.026(3)	S1-O15	1.444(3)	*M*2-O9	2.026(6)	S1-O15	1.443(6)
*M*2-O6	2.050(3)	S1-O8	1.457(3)	*M*2-O6	2.038(3)	S1-O8	1.455(3)	*M*2-O6	2.034(5)	S1-O8	1.454(6)
*M*2-O5	2.168(3)	S1-O12	1.475(3)	*M*2-O5	2.136(3)	S1-O12	1.465(3)	*M*2-O5	2.161(6)	S1-O12	1.465(6)
*M*2-O12	2.791(3)	S1-O13	1.501(3)	*M*2-O12	2.790(4)	S1-O13	1.500(3)	*M*2-O12	2.800(7)	S1-O13	1.509(6)
<*M*2-O>	2.178	<S1-O>	1.470	<*M*2-O>	2.160	<S1-O>	1.466	<*M*2-O>	2.171	<S1-O>	1.468
*M*3-O15	2.000(3)	S2-O11	1.453(3)	*M*3-O15	1.990(3)	S2-O11	1.456(3)	*M*3-O15	2.010(6)	S2-O11	1.452(6)
*M*3-O7	2.041(3)	S2-O10	1.465(3)	*M*3-O1	2.036(3)	S2-O10	1.463(3)	*M*3-O1	2.030(5)	S2-O10	1.465(6)
*M*3-O10	2.043(3)	S2-O2	1.484(3)	*M*3-O10	2.038(3)	S2-O3	1.474(3)	*M*3-O10	2.037(5)	S2-O2	1.475(6)
*M*3-O1	2.046(3)	S2-O3	1.484(3)	*M*3-O7	2.041(3)	S2-O2	1.482(3)	*M*3-O7	2.048(6)	S2-O3	1.481(5)
*M*3-O4	2.116(3)	<S2-O>	1.472	*M*3-O4	2.127(3)	<S2-O>	1.469	*M*3-O4	2.151(6)	<S2-O>	1.468
*M*3-O12	2.211(3)			*M*3-O12	2.222(4)			*M*3-O12	2.288(6)		
<*M*3-O>	2.076	S3-O7	1.465(3)	<*M*3-O>	2.076	S3-O4	1.454(3)	<*M*3-O>	2.094	S3-O4	1.469(5)
		S3-O4	1.469(3)			S3-O7	1.460(3)			S3-O7	1.469(6)
Na1-O3	2.393(3)	S3-O1	1.470(2)	Na1-O3	2.375(4)	S3-O1	1.467(3)	Na1-O3	2.405(6)	S3-O1	1.480(5)
Na1-O16	2.480(4)	S3-O14	1.487(3)	Na1-O16	2.488(4)	S3-O14	1.490(3)	Na1-O16	2.480(7)	S3-O14	1.486(6)
Na1-O5	2.493(3)	<S3-O>	1.473	Na1-O5	2.516(4)	<S3-O>	1.468	Na1-O5	2.485(7)	<S3-O>	1.476
Na1-O6	2.528(3)			Na1-O6	2.525(4)			Na1-O6	2.486(7)		
Na1-O13	2.725(4)	S4-O5	1.462(3)	Na1-O13	2.683(4)	S4-O5	1.451(3)	Na1-O13	2.686(7)	S4-O5	1.451(5)
Na1-O2	2.756(3)	S4-O9	1.468(3)	Na1-O2	2.728(4)	S4-O9	1.468(3)	Na1-O2	2.739(7)	S4-O9	1.466(6)
Na1-O8	2.876(4)	S4-O6	1.480(3)	Na1-O8	2.857(4)	S4-O16	1.475(3)	Na1-O8	2.743(7)	S4-O16	1.483(6)
Na1-O9	2.879(4)	S4-O16	1.483(3)	Na1-O9	2.883(4)	S4-O6	1.481(3)	Na1-O9	2.888(7)	S4-O6	1.486(6)
Na1-O16	3.134(4)	<S4-O>	1.473	Na1-O16	3.108(4)	<S4-O>	1.469	Na1-O16	3.142(7)	<S4-O>	1.472
Na1-O6	3.155(4)			Na1-O6	3.175(4)			Na1-O6	3.250(7)		
<Na1-O>	2.742			<Na1-O>	2.734			<Na1-O>	2.730		

Table S6. Selected interatomic distances (in Å) in glikinite (Nazarchuk et al. 2020) and $(Zn,Cu)_3O(SO_4)_2$.

Glikinite				$(Zn,Cu)_3O(SO_4)_2$			
*M*1-O1	1.878(5) ×2	S1-O7	1.361(15)	*M*1-O1	1.878(4) ×2	S1-O7	1.406(18)
*M*1-O2	2.191(10) ×2	S1-O6	1.435(18)	*M*1-O2	2.206(9) ×2	S1-O6	1.41(2)
*M*1-O4	2.230(10) ×2	S1-O4	1.465(13) ×2	*M*1-O4	2.233(10) ×2	S1-O4	1.473(10) ×2
< *M*1-O>	2.100	<S1-O>	1.432	< M1-O>	2.105	<S1-O>	1.441
*M*2-O6	1.902(17)	S2-O3	1.413(14)	*M*2-O6	1.91(2)	S2-O3	1.453(11)
*M*2-O1	1.939(12)	S2-O5	1.435(13)	*M*2-O1	1.956(12)	S2-O5	1.481(12)
*M*2-O3	1.967(14)	S2-O2	1.480(12) ×2	*M*2-O3	1.982(13)	S2-O2	1.465(10) ×2
*M*2-O2	2.153(13) ×2	<S2-O>	1.451	*M*2-O2	2.165(10) ×2	<S2-O>	1.466
< M2-O>	2.023			< M2-O>	2.036		
		O1-*M*1	1.878(5) ×2			O1-*M*1	1.878(4) ×2
*M*3-O7	1.938(15)	O1-*M*2	1.939(12)	*M*3-O7	1.906(19)	O1-*M*2	1.982(13)
*M*3-O5	1.977(14)	O1-*M*3	1.987(13)	*M*3-O5	1.966(13)	O1-*M*3	1.966(13)
*M*3-O1	1.987(13)	<O1-M>	1.921	*M*3-O1	1.966(12)	<O1-*M*>	1.926
*M*3-O4	2.144(15) ×2			*M*3-O4	2.149(11) ×2		
<*M*3-O>	2.038			<*M*3-O>	2.027		

Table S7. Cu–O bond lengths (in Å) and bond valence sums (in valence units = vu) in the structures of synthetic $Na_2Cu(SO_4)_2$ and its 'natural' analogue saranchinaite. Interatomic distances with bond valence values ≤ 0.03 vu are given in italics.

Atoms	$Na_2Cu(SO_4)_2$	saranchinaite	Atoms	$Na_2Cu(SO_4)_2$	saranchinaite
Cu1–O14	1.929(2) [0.51]	1.947(7) [0.49]	Cu3–O1	1.928(2) [0.51]	1.936(7) [0.50]
Cu1–O19	1.938(2) [0.50]	1.945(7) [0.49]	Cu3–O4	1.938(2) [0.50]	1.946(7) [0.49]
Cu1–O5	2.020(2) [0.40]	2.027(8) [0.39]	Cu3–O7	1.946(2) [0.49]	1.952(7) [0.48]
Cu1–O15	2.025(2) [0.39]	2.041(7) [0.38]	Cu3–O3	1.968(2) [0.46]	1.970(7) [0.46]
Cu1–O23	2.287(2) [0.19]	2.283(8) [0.20]	Cu3–O31	2.352(2) [0.16]	2.352(7) [0.16]
Cu1–O29	2.839(3) [0.04]	2.777(9) [0.05]	Cu3–O9	2.938(2) [0.03]	2.968(7) [0.03]
Cu1–O32	3.065(3) [0.02]	3.100(9) [0.02]	Cu3–O24	3.012(3) [0.03]	3.030(7) [0.03]
avg. [BVS]	2.173 [2.03]	2.170 [1.98]	avg. [BVS]	2.297 [2.17]	2.308 [2.14]
Cu2–O13	1.947(2) [0.48]	1.943(7) [0.49]	Cu4–O30	1.960(2) [0.47]	1.975(7) [0.45]
Cu2–O26	1.950(2) [0.48]	1.954(7) [0.48]	Cu4–O16	1.962(2) [0.47]	1.971(7) [0.46]
Cu2–O3	1.951(2) [0.48]	1.959(7) [0.47]	Cu4–O18	1.979(2) [0.45]	1.985(7) [0.44]
Cu2–O6	1.961(2) [0.47]	1.963(7) [0.47]	Cu4–O12	1.980(2) [0.44]	1.980(7) [0.44]
Cu2–O2	2.264(2) [0.21]	2.264(7) [0.21]	Cu4–O9	2.260(2) [0.21]	2.261(7) [0.21]
Cu2–O23	2.882(2) [0.04]	2.921(8) [0.04]	Cu4–O31	2.942(2) [0.03]	2.950(7) [0.03]
Cu2–O17	2.954(2) [0.03]	2.747(7) [0.04]	Cu4–O10	3.101(2) [0.02]	3.089(7) [0.02]
avg. [BVS]	2.273 [2.19]	2.250 [2.18]	avg. [BVS]	2.181 [2.06]	**4.13**.03]

Table S8. Fractional atomic coordinates and equivalent isotropic displacement parameters (Å^2) for $Na_2Cu(SO_4)_2$.

	Wyck.	***x***	***y***	***z***	U_{eq}
Cu1	2*a*	0.65609(5)	0.08192(2)	0.67816(4)	0.01217(8)
Cu2	2*a*	0.92876(4)	0.31679(2)	0.01401(4)	0.01093(7)
Cu3	2*a*	0.91081(4)	0.53094(2)	0.96563(4)	0.01197(7)
Cu4	2*a*	0.89707(4)	0.52912(3)	0.47885(4)	0.01186(7)
S1	2*a*	0.60565(9)	0.41610(5)	0.90180(8)	0.01128(14)
S2	2*a*	0.76450(9)	0.70714(5)	0.91773(8)	0.01073(14)
S3	2*a*	0.05254(9)	0.45514(4)	0.28300(8)	0.01026(13)
S4	2*a*	0.67229(9)	0.68374(5)	0.40606(8)	0.01126(14)
S5	2*a*	0.78049(9)	0.13367(5)	0.44059(8)	0.01191(14)
S6	2*a*	0.97359(9)	0.40412(5)	0.76051(8)	0.01197(14)
S7	2*a*	0.43129(9)	−0.05616(5)	0.65715(8)	0.01223(14)
S8	2*a*	0.79549(9)	0.14240(4)	0.99755(8)	0.01037(13)
Na1	2*a*	0.28374(17)	0.42257(9)	0.05243(18)	0.0250(3)
Na2	2*a*	0.28937(16)	0.41204(9)	0.61718(16)	0.0224(3)
Na3	2*a*	0.97519(17)	0.68519(9)	0.24565(15)	0.0216(3)
Na4	2*a*	0.61794(18)	0.54975(9)	0.66348(14)	0.0227(3)
Na5	2*a*	0.36251(19)	0.80324(10)	0.41809(18)	0.0329(4)
Na6	2*a*	0.60322(16)	0.58649(9)	0.08643(14)	0.0206(3)
Na7	2*a*	0.93999(18)	0.72662(9)	0.66951(14)	0.0219(3)
Na8	2*a*	0.62924(16)	0.26826(9)	0.15688(14)	0.0185(3)
O1	2*a*	0.8793(3)	0.05876(13)	0.0332(2)	0.0156(5)
O2	2*a*	0.0095(3)	0.36789(14)	0.2326(2)	0.0169(5)
O3	2*a*	0.9646(3)	0.41646(13)	0.9106(2)	0.0127(4)
O4	2*a*	0.8555(3)	0.64283(14)	0.0212(2)	0.0140(4)
O5	2*a*	0.5001(3)	0.67831(15)	0.3825(2)	0.0172(5)
O6	2*a*	0.8496(3)	0.79062(13)	0.9545(2)	0.0156(5)
O7	2*a*	0.6906(3)	0.50090(14)	0.9158(3)	0.0196(5)
O8	2*a*	0.6124(3)	0.71596(16)	0.9370(3)	0.0219(5)
O9	2*a*	0.8839(3)	0.47591(15)	0.6825(2)	0.0198(5)
O10	2*a*	0.7158(3)	0.67068(15)	0.2801(2)	0.0196(5)
O11	2*a*	0.7358(3)	0.21729(15)	0.3789(3)	0.0233(5)
O12	2*a*	0.7437(3)	0.61348(14)	0.5066(2)	0.0150(4)
O13	2*a*	0.7122(3)	0.34973(14)	0.9861(2)	0.0173(5)
O14	2*a*	0.5091(3)	0.01872(13)	0.7465(2)	0.0154(4)
O15	2*a*	0.2109(3)	0.47467(15)	0.2731(2)	0.0179(5)
O16	2*a*	0.0571(3)	0.45993(13)	0.4317(2)	0.0132(4)
O17	2*a*	0.9005(3)	0.32126(15)	0.7164(2)	0.0236(5)
O18	2*a*	0.9410(3)	0.11454(15)	0.4323(2)	0.0191(5)
O19	2*a*	0.7944(3)	0.14012(15)	0.5922(2)	0.0163(4)
O20	2*a*	0.5572(3)	0.39300(17)	0.7565(3)	0.0261(6)
O21	2*a*	0.1359(3)	0.40572(17)	0.7667(3)	0.0245(5)
O22	2*a*	0.6436(3)	0.13436(15)	0.0157(3)	0.0212(5)
O23	2*a*	0.7919(3)	0.16699(15)	0.8573(2)	0.0185(5)
O24	2*a*	0.7606(3)	0.67814(16)	0.7810(2)	0.0207(5)
O25	2*a*	0.4868(3)	−0.13493(14)	0.7314(3)	0.0224(5)
O26	2*a*	0.8861(3)	0.20960(13)	0.0959(2)	0.0132(4)
O27	2*a*	0.4778(3)	0.42807(18)	0.9578(3)	0.0292(6)
O28	2*a*	0.7261(3)	0.76692(14)	0.4690(3)	0.0197(5)
O29	2*a*	0.4664(3)	−0.05172(16)	0.5253(2)	0.0214(5)
O30	2*a*	0.2613(3)	−0.04830(15)	0.6356(3)	0.0209(5)
O31	2*a*	0.9422(3)	0.51881(14)	0.2035(2)	0.0176(5)
O32	2*a*	0.6699(3)	0.06576(15)	0.3808(3)	0.0206(5)

Table S9. Atomic displacement parameters [Å^2] for $Na_2Cu(SO_4)_2$.

	U_{11}	U_{22}	U_{33}	U_{12}	U_{13}	U_{23}
Cu1	0.01181(18)	0.01203(16)	0.01322(18)	−0.00062(14)	0.00455(15)	0.00115(13)
Cu2	0.01225(18)	0.00830(15)	0.01223(17)	0.00033(13)	0.00362(15)	0.00201(13)
Cu3	0.01182(17)	0.00771(14)	0.01596(17)	0.00000(14)	0.00349(15)	−0.00040(14)
Cu4	0.01106(17)	0.01199(16)	0.01282(17)	0.00125(14)	0.00399(15)	−0.00083(14)
S1	0.0096(3)	0.0114(3)	0.0125(3)	0.0001(3)	0.0028(3)	0.0012(3)
S2	0.0102(3)	0.0097(3)	0.0118(3)	−0.0009(3)	0.0024(3)	0.0013(2)
S3	0.0117(3)	0.0092(3)	0.0098(3)	0.0008(3)	0.0030(3)	−0.0004(2)
S4	0.0117(4)	0.0098(3)	0.0117(3)	−0.0003(3)	0.0026(3)	−0.0003(3)
S5	0.0117(4)	0.0124(3)	0.0115(3)	0.0010(3)	0.0031(3)	0.0019(3)
S6	0.0142(4)	0.0108(3)	0.0113(3)	0.0006(3)	0.0043(3)	0.0005(3)
S7	0.0118(3)	0.0106(3)	0.0137(4)	−0.0006(3)	0.0029(3)	0.0009(3)
S8	0.0100(3)	0.0089(3)	0.0120(3)	0.0001(3)	0.0028(3)	−0.0013(2)
Na1	0.0200(7)	0.0208(7)	0.0373(9)	−0.0038(6)	0.0133(7)	−0.0031(6)
Na2	0.0184(7)	0.0196(7)	0.0274(8)	0.0002(6)	0.0039(7)	0.0001(6)
Na3	0.0208(7)	0.0235(7)	0.0180(7)	−0.0026(6)	0.0021(6)	0.0004(6)
Na4	0.0229(8)	0.0278(8)	0.0166(7)	−0.0036(6)	0.0048(6)	−0.0007(5)
Na5	0.0305(9)	0.0211(8)	0.0460(10)	0.0050(6)	0.0099(8)	−0.0019(7)
Na6	0.0184(7)	0.0257(7)	0.0188(7)	−0.0008(6)	0.0071(6)	−0.0004(6)
Na7	0.0249(8)	0.0228(7)	0.0157(7)	−0.0008(6)	0.0023(6)	−0.0041(5)
Na8	0.0158(7)	0.0219(7)	0.0182(7)	0.0015(5)	0.0056(6)	0.0008(5)
O1	0.0162(12)	0.0079(9)	0.0238(12)	0.0018(8)	0.0077(10)	0.0022(8)
O2	0.0235(13)	0.0119(10)	0.0138(11)	−0.0025(9)	0.0032(10)	−0.0044(8)
O3	0.0210(11)	0.0090(9)	0.0099(10)	0.0008(8)	0.0073(10)	0.0017(7)
O4	0.0163(11)	0.0109(10)	0.0125(10)	0.0028(9)	0.0007(9)	0.0001(8)
O5	0.0110(11)	0.0150(10)	0.0241(12)	0.0006(9)	0.0027(10)	−0.0013(9)
O6	0.0125(11)	0.0085(9)	0.0261(12)	−0.0021(8)	0.0063(10)	−0.0024(8)
O7	0.0137(11)	0.0091(10)	0.0329(14)	−0.0026(8)	0.0019(11)	−0.0004(9)
O8	0.0116(11)	0.0230(12)	0.0325(14)	0.0013(9)	0.0086(11)	0.0077(10)
O9	0.0242(13)	0.0192(11)	0.0158(11)	0.0047(10)	0.0055(11)	0.0064(9)
O10	0.0235(13)	0.0229(12)	0.0137(11)	−0.0033(10)	0.0075(10)	−0.0018(9)
O11	0.0288(15)	0.0159(11)	0.0221(13)	0.0068(10)	0.0025(12)	0.0082(10)
O12	0.0165(12)	0.0153(10)	0.0130(10)	0.0068(8)	0.0041(9)	0.0018(8)
O13	0.0145(11)	0.0153(10)	0.0228(12)	0.0034(9)	0.0065(10)	0.0089(9)
O14	0.0181(11)	0.0112(10)	0.0189(11)	−0.0039(8)	0.0084(10)	−0.0033(8)
O15	0.0136(11)	0.0179(11)	0.0249(12)	−0.0005(9)	0.0100(10)	−0.0028(9)
O16	0.0158(11)	0.0142(10)	0.0095(10)	0.0016(8)	0.0035(9)	−0.0012(8)
O17	0.0308(14)	0.0134(11)	0.0248(13)	−0.0041(10)	0.0053(12)	−0.0070(10)
O18	0.0162(12)	0.0192(11)	0.0246(12)	0.0037(9)	0.0105(11)	0.0078(9)
O19	0.0177(12)	0.0200(11)	0.0118(10)	−0.0051(9)	0.0055(10)	−0.0023(9)
O20	0.0316(15)	0.0282(14)	0.0134(11)	0.0013(11)	−0.0014(11)	−0.0045(10)
O21	0.0180(12)	0.0346(14)	0.0240(13)	0.0043(11)	0.0111(11)	0.0028(11)
O22	0.0128(11)	0.0217(12)	0.0303(14)	−0.0028(9)	0.0083(11)	−0.0035(10)
O23	0.0236(13)	0.0199(11)	0.0100(10)	0.0013(10)	0.0020(10)	0.0003(8)
O24	0.0251(13)	0.0237(12)	0.0116(11)	−0.0061(10)	0.0031(11)	−0.0033(9)
O25	0.0211(13)	0.0127(11)	0.0322(14)	0.0031(9)	0.0060(12)	0.0069(10)
O26	0.0178(11)	0.0090(9)	0.0112(10)	−0.0040(8)	0.0018(9)	−0.0015(8)
O27	0.0214(13)	0.0324(14)	0.0413(17)	0.0054(11)	0.0211(14)	0.0076(12)
O28	0.0228(13)	0.0123(10)	0.0211(12)	−0.0050(9)	0.0020(11)	−0.0038(9)
O29	0.0231(13)	0.0304(13)	0.0117(11)	0.0004(10)	0.0070(10)	−0.0014(10)
O30	0.0121(11)	0.0225(12)	0.0276(14)	−0.0006(9)	0.0051(11)	0.0082(10)
O31	0.0185(11)	0.0174(11)	0.0163(11)	0.0058(9)	0.0043(10)	0.0064(9)
O32	0.0169(12)	0.0216(12)	0.0205(12)	−0.0030(10)	0.0013(11)	−0.0050(9)

Table S10. Na–O bond lengths (in Å) in the structures of synthetic $Na_2Cu(SO_4)_2$ and its 'natural' analogue saranchinaite. Percent difference equal or more than ±2% is given in italics.

Atoms	$Na_2Cu(SO_4)_2$	saranchinaite	Atoms	$Na_2Cu(SO_4)_2$	saranchinaite
Na1–O27	2.224(3)	2.219(9)	*Na5–O17	*2.368(3)*	*2.482(9)*
Na1–O6	2.366(3)	2.388(9)	*Na5–O5	*2.385(3)*	*2.475(8)*
Na1–O1	2.575(3)	2.600(8)	*Na5–O20	*2.521(3)*	*2.622(9)*
Na1–O15	2.637(3)	2.650(9)	*Na5–O29	*2.557(3)*	*2.622(9)*
Na1–O25	2.680(3)	2.727(9)	*Na5–O11	2.806(3)	2.799(9)
Na1–O14	2.759(3)	2.728(9)	*Na5–O19	2.887(3)	2.898(8)
Na1–O3	2.801(3)	2.785(9)	<*Na5–O>	*2.587*	*2.650*
Na1–O21	2.821(3)	2.799(10)			
<Na1–O>	2.608	2.612	Na6–O22	2.275(3)	2.288(8)
			Na6–O10	2.328(3)	2.350(9)
Na2–O21	2.331(3)	2.331(9)	Na6–O14	2.451(2)	2.447(8)
Na2–O28	2.409(3)	2.428(9)	Na6–O7	2.486(3)	2.502(9)
Na2–O32	2.417(3)	2.417(9)	Na6–O8	2.536(3)	2.539(9)
Na2–O20	2.420(3)	2.404(9)	Na6–O4	2.685(3)	2.706(9)
Na2–O16	2.475(3)	2.494(8)	Na6–O27	2.858(3)	2.831(10)
Na2–O29	3.012(3)	3.017(9)	<Na6–O>	2.517	2.523
<Na2–O>	2.511	2.515			
			Na7–O24	2.348(3)	2.340(9)
Na3–O4	2.308(3)	2.312(8)	Na7–O2	2.398(3)	2.414(9)
Na3–O19	2.338(3)	2.364(8)	Na7–O18	2.428(3)	2.445(9)
Na3–O17	2.369(3)	2.352(10)	Na7–O28	2.431(3)	2.459(9)
Na3–O10	2.463(3)	2.468(10)	Na7–O26	2.444(3)	2.458(8)
Na3–O23	2.613(3)	2.596(9)	Na7–O12	2.685(3)	2.683(9)
Na3–O31	2.625(3)	2.614(10)	<Na7–O>	2.456	2.467
<Na3–O>	2.453	2.451			
			Na8–O8	2.247(3)	2.258(9)
Na4–O12	2.418(3)	2.426(9)	*Na8–O25*	*2.309(3)*	*2.345(9)*
Na4–O29	2.423(3)	2.410(9)	Na8–O11	2.312(3)	2.330(9)
Na4–O24	2.479(3)	2.493(9)	Na8–O13	2.433(3)	2.449(9)
Na4–O32	2.500(3)	2.514(9)	Na8–O22	2.551(3)	2.558(9)
Na4–O7	2.562(3)	2.557(9)	Na8–O26	2.714(3)	2.747(9)
Na4–O9	2.603(3)	2.652(9)	<Na8–O>	2.428	2.448
Na4–O20	2.726(3)	2.726(9)			
<Na4–O>	2.530	2.540			

* – Na5 = $Na_{1.00}$ in synthetic $Na_2Cu(SO_4)_2$ and $Na_{0.71(2)}K_{0.29(2)}$ in saranchinaite

Table S11. IR spectra of $A_2Cu_3O(SO_4)_3$ (A = Na, K), $Rb_2Cu_{3.07}O_{0.07}(SO_4)_3$, $Cs_2Cu_{3.5}O_{1.5}(SO_4)_3$.

Vibrational mode	Compound				
	Na	K/Na	K	Rb	Cs
ν_1 (SO4)	957sh 980vs 996sh	985s (sh) 990s	983s 993sh	956vw 976w 988w	979s
ν_3 (SO4)	1023vs 1045sh	1038s 1058 s 1095 w	1032sh 1039vs 1057vs 1087sh, 1099sh	1033 vs 1062 s 1094w	1022vs 1063vs 1097vw 1112sh

	1074vs 1102w 1118vs 1130sh 1155 s 1169sh 1183w 1210 vs		1148 vs 1160 sh 1211sh 1220s 1230sh		1135vw 1147sh 1163vw 1186w 1214sh 1227s
		1148s 1160sh 1212 w 1224s 1241w		1145s 1158sh 1211sh 1219vs 1234sh	
	1250w 605 vs 623 s 635s 648w 666s 685vw		1255s 599s 609sh 624 w 638w 643sh 661 s 696s		
ν_4 (SO4)		599s 621 w 636 w 660 s 694s		602 vs 612 sh 631w 640sh 655 s 692 s	605vs 623w 652s 658sh 692w
					435vw
		455w	456vw 467vw	452vw 482vw	
ν (Cu–O)		485w 513w 545 vs	486w 514w 543s	491sh 510w 546vs	488vw 494vw 542vs 593w
	519s				

w = weak; vw= very weak; **s** = strong; vs = very strong; sh =shoulder.

Table S12. Cu–O bond lengths (in Å) in the structures of synthetic $(Na,K)_2CuO(SO_4)_3$ series

				$KNaCu_3O(SO_4)_3$				**$K_2Cu_3O(SO_4)_3$**			
Cu(1)-O(2)	1.938(3)	Na(1)-O(7)	2.378(4)	Cu(1)-O(7)	1.945(10)	K(1)-O(7)	2.678(10)	Cu(1)-O(6)	1.941(8)	K(1)-O(11)	2.767(9)
Cu(1)-O(6)	1.947(3)	Na(1)-O(11)	2.451(4)	Cu(1)-O(2)	1.954(9)	K(1)-O(11)	2.739(10)	Cu(1)-O(2)	1.953(7)	K(1)-O(8)	2.803(10)
Cu(1)-O(1)	1.956(3)	Na(1)-O(8)	2.485(4)	Cu(1)-O(6)	1.956(9)	K(1)-O(12)	2.827(11)	Cu(1)-O(7)	1.964(8)	K(1)-O(7)	2.802(8)
Cu(1)-O(7)	1.972(3)	Na(1)-O(6)	2.519(4)	Cu(1)-O(1)	1.961(9)	K(1)-O(8)	2.844(13)	Cu(1)-O(1)	1.978(8)	K(1)-O(12)	2.919(9)
		Na(1)-O(10)	2.551(4)			K(1)-O(6)	2.850(11)			K(1)-O(6)	3.022(9)
Cu(2)-O(1)	1.929(2)	Na(1)-O(12)	2.841(4)	Cu(2)-O(1)	1.914(8)	K(1)-O(10)	2.889(11)	Cu(2)-O(1)	1.909(7)	K(1)-O(10)	3.047(10)
Cu(2)-O(11)	1.977(3)	Na(1)-O(5)	2.877(4)	Cu(2)-O(11)	1.951(11)	K(1)-O(5)	3.124(13)	Cu(2)-O(11)	1.976(9)	K(1)-O(5)	3.193(10)
Cu(2)-O(3)	1.983(3)			Cu(2)-O(3)	1.978(11)			Cu(2)-O(3)	1.972(8)		
Cu(2)-O(5)	2.005(3)	Na(2)-O(4)	2.212(3)	Cu(2)-O(5)	2.016(10)	Na(1)-O(4)	2.256(11)	Cu(2)-O(5)	2.018(9)	K(2)-O(4)	2.517(9)
Cu(2)-O(13)	2.195(3)	Na(2)-O(8)	2.335(4)	Cu(2)-O(13)	2.225(11)	Na(1)-O(8)	2.385(13)	Cu(2)-O(13)	2.200(9)	K(2)-O(14)	2.675(9)
		Na(2)-O(13)	2.427(3)			Na(1)-O(14)	2.462(12)			K(2)-O(8)	2.691(9)
Cu(3)-O(2)	1.928(2)	Na(2)-O(3)	2.432(3)	Cu(3)-O(2)	1.913(8)	Na(1)-O(3)	2.504(11)	Cu(3)-O(2)	1.910(6)	K(2)-O(13)	2.694(9)
Cu(3)-O(14)	1.946(3)	Na(2)-O(14)	2.461(3)	Cu(3)-O(14)	1.948(11)	Na(1)-O(4)	2.574(15)	Cu(3)-O(14)	1.936(8)	K(2)-O(4)	2.795(10)
Cu(3)-O(10)	1.980(3)	Na(2)-O(4)	2.576(4)	Cu(3)-O(10)	1.993(10)	Na(1)-O(13)	2.646(14)	Cu(3)-O(10)	1.985(9)	K(2)-O(3)	2.869(9)
Cu(3)-O(9)	2.005(3)			Cu(3)-O(9)	2.018(11)	Na(1)-O(9)	2.866(14)	Cu(3)-O(9)	2.031(9)	K(2)-O(9)	3.155(10)
Cu(3)-O(12)	2.320(3)	S(3)-O(12)	1.465(3)	Cu(3)-O(12)	2.282(11)			Cu(3)-O(12)	2.342(9)		
		S(3)-O(13)	1.469(3)			S(3)-O(12)	1.457(11)			S(3)-O(12)	1.467(9)
S(1)-O(4)	1.439(3)	S(3)-O(11)	1.481(3)	S(1)-O(4)	1.468(10)	S(3)-O(14)	1.475(11)	S(1)-O(4)	1.447(8)	S(3)-O(13)	1.471(8)
S(1)-O(5)	1.479(3)	S(3)-O(14)	1.483(3)	S(1)-O(5)	1.479(12)	S(3)-O(11)	1.482(10)	S(1)-O(5)	1.476(10)	S(3)-O(11)	1.474(8)
S(1)-O(6)	1.485(3)			S(1)-O(6)	1.487(10)	S(3)-O(13)	1.495(10)	S(1)-O(6)	1.488(9)	S(3)-O(14)	1.490(8)
S(1)-O(3)	1.492(3)			S(1)-O(3)	1.503(13)			S(1)-O(3)	1.509(10)		
S(2)-O(8)	1.445(3)			S(2)-O(8)	1.445(10)			S(2)-O(8)	1.462(9)		
S(2)-O(9)	1.474(3)			S(2)-O(7)	1.474(9)			S(2)-O(9)	1.490(10)		
S(2)-O(7)	1.488(3)			S(2)-O(10)	1.490(11)			S(2)-O(7)	1.482(9)		
S(2)-O(10)	1.496(3)			S(2)-O(9)	1.495(13)			S(2)-O(10)	1.487(9)		

Table S14. Atomic coordinates (x 10^4) and equivalent isotropic and anisotropic displacement parameters (E^2x10^3) for $Na_2Cu_3O(SO_4)_3$.

	x	*y*	*z*	U_{eq}	U_{11}	U_{22}	U_{33}	U_{23}	U_{13}	U_{12}
Cu(1)	15875(1)	-2519(1)	2976(1)	12(1)	9(1)	8(1)	17(1)	-1(1)	3(1)	0(1)
Cu(2)	14767(1)	206(1)	3409(1)	12(1)	13(1)	11(1)	11(1)	-3(1)	4(1)	1(1)
Cu(3)	15144(1)	-5218(1)	3596(1)	12(1)	12(1)	12(1)	12(1)	4(1)	4(1)	1(1)
Na(1)	18028(1)	-2447(2)	3548(2)	37(1)	15(1)	41(1)	50(1)	20(1)	7(1)	-1(1)
Na(2)	16724(1)	2210(2)	5471(1)	22(1)	16(1)	22(1)	25(1)	-4(1)	6(1)	-6(1)
S(1)	16612(1)	336(1)	3685(1)	12(1)	11(1)	10(1)	13(1)	-2(1)	2(1)	-2(1)
S(2)	13371(1)	-5382(1)	2103(1)	12(1)	10(1)	10(1)	15(1)	0(1)	4(1)	-1(1)
S(3)	14909(1)	-7506(1)	5082(1)	10(1)	12(1)	9(1)	9(1)	0(1)	4(1)	0(1)
O(1)	15000	-1076(4)	2500	11(1)	13(2)	8(2)	9(2)	0	2(2)	0
O(2)	15000	-3934(4)	2500	9(1)	9(2)	8(2)	9(2)	0	1(2)	0
O(3)	15973(2)	564(3)	4135(2)	18(1)	16(2)	22(2)	16(2)	-8(1)	6(1)	-1(1)
O(4)	17363(2)	1051(3)	4302(2)	19(1)	18(2)	14(2)	19(2)	-4(1)	1(1)	-7(1)
O(5)	16302(2)	874(3)	2645(2)	19(1)	19(2)	21(2)	13(2)	3(1)	2(1)	-8(1)
O(6)	16779(2)	-1213(3)	3674(2)	17(1)	12(2)	10(2)	24(2)	-4(1)	3(1)	-2(1)
O(7)	16795(2)	-3838(3)	3105(2)	18(1)	12(2)	9(2)	32(2)	-5(1)	6(1)	2(1)
O(8)	12598(2)	-6115(3)	1946(2)	18(1)	12(2)	15(2)	26(2)	-1(1)	7(1)	-4(1)
O(9)	13780(2)	-5944(3)	1447(2)	20(1)	18(2)	22(2)	23(2)	-8(1)	13(1)	-9(1)
O(10)	13933(2)	-5560(3)	3176(2)	19(1)	15(2)	24(2)	18(2)	6(1)	6(1)	-1(1)
O(11)	14430(2)	-8477(3)	4260(2)	16(1)	16(2)	14(2)	16(2)	-7(1)	6(1)	-1(1)
O(12)	14311(2)	-6757(3)	5407(2)	16(1)	16(2)	17(2)	17(2)	-2(1)	9(1)	3(1)
O(13)	15527(2)	-8296(3)	5909(2)	14(1)	16(2)	14(2)	13(1)	4(1)	6(1)	-1(1)
O(14)	15401(2)	-6482(3)	4742(2)	15(1)	14(2)	15(2)	15(2)	4(1)	4(1)	-2(1)

Table S15. Atomic coordinates (x 10^4) and equivalent isotropic and anisotropic displacement parameters (E^2x10^3) for $K_2Cu_3O(SO_4)_3$.

	x	*y*	*z*	U_{eq}	U_{11}	U_{22}	U_{33}	U_{23}	U_{13}	U_{12}
Cu(1)	15786(1)	-2535(2)	2940(1)	19(1)	18(1)	12(1)	24(1)	-1(1)	3(1)	-1(1)
Cu(2)	14806(1)	179(2)	3425(1)	18(1)	21(1)	16(1)	18(1)	-3(1)	7(1)	-1(1)
Cu(3)	15138(1)	-5212(2)	3596(1)	18(1)	18(1)	19(1)	15(1)	6(1)	4(1)	2(1)
K(1)	18041(2)	-2646(4)	3753(3)	47(1)	26(2)	57(3)	51(2)	16(2)	6(2)	-5(2)
K(2)	16747(2)	2485(3)	5616(2)	31(1)	23(2)	31(2)	37(2)	-3(2)	8(2)	-6(1)
S(1)	16468(2)	253(3)	3644(3)	20(1)	19(2)	15(2)	24(2)	-1(2)	5(2)	-5(1)
S(2)	13519(2)	-5339(3)	2162(3)	20(1)	18(2)	19(2)	23(2)	0(2)	6(2)	-2(1)
S(3)	14930(2)	-7505(4)	5091(2)	14(1)	21(2)	14(2)	10(2)	2(1)	9(2)	-1(1)
O(1)	15000	-1078(11)	2500	15(3)	27(7)	7(6)	11(6)	0	7(5)	0
O(2)	15000	-3950(10)	2500	8(3)	10(4)	0(4)	11(4)	0	2(3)	0
O(3)	15884(4)	572(9)	4100(7)	27(2)	15(5)	31(6)	35(6)	-27(5)	11(4)	-7(4)
O(4)	17159(4)	938(9)	4230(7)	29(2)	21(5)	25(5)	38(6)	-6(5)	6(5)	-7(4)
O(5)	16206(5)	688(10)	2583(7)	34(3)	35(6)	45(6)	24(6)	4(5)	11(5)	-16(5)
O(6)	16594(4)	-1296(9)	3685(6)	24(2)	17(5)	20(5)	31(6)	-5(4)	6(4)	-7(4)
O(7)	16605(4)	-3801(9)	2966(7)	26(2)	13(4)	19(5)	43(6)	-12(5)	8(4)	-1(4)
O(8)	12806(4)	-6012(9)	2033(7)	25(2)	11(4)	29(6)	34(6)	7(5)	6(4)	-1(4)
O(9)	13848(4)	-5838(9)	1421(7)	25(2)	27(5)	32(6)	24(6)	-11(5)	17(4)	-6(4)
O(10)	14053(4)	-5588(10)	3198(6)	27(2)	20(5)	42(6)	15(5)	6(4)	0(4)	-2(4)
O(11)	14516(4)	-8480(8)	4280(6)	20(2)	22(5)	19(5)	17(5)	-7(4)	3(4)	1(4)
O(12)	14378(4)	-6774(9)	5417(6)	22(2)	25(5)	20(5)	25(5)	-2(4)	14(4)	4(4)
O(13)	15485(4)	-8273(9)	5914(6)	21(2)	20(5)	24(5)	19(5)	7(4)	8(4)	3(4)
O(14)	15364(4)	-6484(8)	4722(6)	22(2)	25(5)	15(5)	26(6)	13(4)	9(4)	-4(4)

Table S16. Atomic coordinates (x 10^4) and equivalent isotropic and anisotropic displacement parameters (E^2x10^3) for $KNaCu_3O(SO_4)_3$.

	x	*y*	*z*	U_{eq}	U_{11}	U_{22}	U_{33}	U_{23}	U_{13}	U_{12}
Cu(1)	15827(1)	-2550(2)	2947(2)	20(1)	11(1)	9(1)	32(1)	-2(1)	1(1)	-1(1)
Cu(2)	14834(1)	172(2)	3438(2)	21(1)	11(1)	14(1)	30(2)	-2(1)	2(1)	1(1)
Cu(3)	15165(1)	-5247(2)	3619(2)	21(1)	13(1)	16(1)	26(1)	5(1)	1(1)	1(1)
K(1)	18067(2)	-2610(4)	3726(4)	37(1)	15(2)	41(2)	48(3)	9(2)	5(2)	-3(2)
Na(1)	16764(4)	2364(6)	5471(6)	32(2)	21(4)	27(4)	40(5)	-5(3)	4(3)	-5(3)
S(1)	16549(2)	300(4)	3681(4)	21(1)	11(2)	16(2)	28(3)	-4(2)	0(2)	-1(2)
S(2)	13463(2)	-5442(4)	2067(4)	21(1)	10(2)	14(2)	33(3)	2(2)	4(2)	-1(2)
S(3)	15019(2)	-7513(4)	5154(3)	16(1)	10(2)	9(2)	24(2)	0(2)	2(2)	0(1)
O(1)	15000	-1094(12)	2500	22(4)	11(8)	0(7)	51(13)	0	8(8)	0
O(2)	15000	-3996(13)	2500	14(3)	10(5)	13(5)	19(6)	0	6(4)	0
O(3)	15972(6)	596(10)	4146(9)	25(3)	27(7)	22(6)	13(7)	-12(5)	-4(5)	-7(5)
O(4)	17290(5)	1009(11)	4320(11)	30(3)	0(5)	27(6)	50(10)	2(6)	-3(5)	-4(4)
O(5)	16222(6)	795(11)	2612(9)	28(3)	29(7)	29(6)	11(7)	6(5)	-7(5)	-13(5)
O(6)	16690(6)	-1263(10)	3718(9)	24(3)	15(6)	19(6)	25(8)	-4(5)	-4(5)	0(4)
O(7)	16665(6)	-3900(9)	3105(10)	27(3)	9(6)	4(5)	59(10)	-5(5)	6(6)	0(4)
O(8)	12714(6)	-6108(10)	1877(10)	27(3)	22(6)	14(6)	46(9)	8(5)	15(6)	-2(4)
O(9)	13813(6)	-6002(11)	1372(10)	28(3)	24(6)	33(7)	29(8)	-15(6)	13(6)	-12(5)
O(10)	14021(6)	-5673(10)	3147(8)	19(3)	16(6)	20(6)	19(7)	10(5)	5(5)	-3(4)
O(11)	14587(5)	-8536(10)	4329(9)	20(3)	9(5)	20(6)	16(7)	1(5)	-9(5)	-6(4)
O(12)	14439(6)	-6762(10)	5415(9)	23(3)	9(5)	18(6)	39(9)	-1(5)	5(5)	4(4)
O(13)	15618(6)	-8270(9)	6047(9)	22(3)	24(6)	6(5)	26(8)	5(5)	0(5)	7(4)
O(14)	15457(6)	-6499(10)	4796(10)	27(3)	25(7)	20(6)	34(8)	11(6)	9(6)	-3(5)

Table S17. Bond lengths (in Å) for $A_2M_3(SO_4)_4$(*A* = Rb, Cs *M* = Co, Ni)

(1) Cs2Ni3(SO4)4		**(2) Cs2Co3(SO4)4**				**(3) Rb2Ni3(SO4)4**		**(4) Rb2Co3(SO4)4**	
Cs(1)-O(1)	3.043(5) x2	Cs(1)-O(3)	3.027(4)	Co(2)-O(6)	1.995(3)	Rb(1)-O(1)	2.7751(18)	Rb(1)-O(4)	2.8072(13)
Cs(1)-O(3)	3.058(5)	Cs(1)-O(4)	3.036(4)	Co(2)-O(16)	2.003(4)	Rb(1)-O(2)	2.8889(19)	Rb(1)-O(2)	2.9297(13)
Cs(1)-O(2)	3.128(6)	Cs(1)-O(7)	3.137(4)	Co(2)-O(12)	2.021(4)	Rb(1)-O(3)	2.9201(19)	Rb(1)-O(5)	2.9304(14)
Cs(1)-O(3)	3.212(5)	Cs(1)-O(2)	3.227(3)	Co(2)-O(2)	2.060(3)	Rb(1)-O(5)	2.9672(18)	Rb(1)-O(6)	2.9973(14)
Cs(1)-O(2)	3.424(6)	Cs(1)-O(1)	3.279(3)	Co(2)-O(10)	2.109(3)	Rb(1)-O(8)	2.9811(18)	Rb(1)-O(1)	3.0003(14)
Cs(1)-O(3)	3.437(6)	Cs(1)-O(9)	3.284(3)			Rb(1)-O(4)	3.0073(19)	Rb(1)-O(3)	3.0194(15)
Cs(1)-O(5)	3.449(5)	Cs(1)-O(13)	3.354(4)	Co(3)-O(11)	1.999(4)	Rb(1)-O(7)	3.0871(18)	Rb(1)-O(7)	3.1278(14)
		Cs(1)-O(14)	3.366(5)	Co(3)-O(7)	2.038(4)	Rb(1)-O(7)	3.1300(18)	Rb(1)-O(7)	3.1426(14)
Ni(1)-O(8)	2.006(5)	Cs(1)-O(15)	3.434(6)	Co(3)-O(14)	2.061(4)				
Ni(1)-O(8)	2.006(5)	Cs(1)-O(16)	3.482(5)	Co(3)-O(1)	2.090(4)	Ni(1)-O(2)	1.9856(17)	Co(1)-O(5)	2.0112(13)
Ni(1)-O(4)	2.077(5)x2			Co(3)-O(3)	2.209(3)	Ni(1)-O(2)	1.9856(17)	Co(1)-O(5)	2.0112(13)
Ni(1)-O(5)	2.165(5)x2	Cs(2)-O(5)	3.058(4)	Co(3)-O(10)	2.240(3)	Ni(1)-O(7)	2.1097(17)	Co(1)-O(7)	2.1438(13)
		Cs(2)-O(8)	3.080(3)			Ni(1)-O(7)	2.1097(17)	Co(1)-O(7)	2.1438(13)
Ni(2)-O(1)	2.009(5)	Cs(2)-O(16)	3.201(4)	S(1)-O(12)	1.447(4)	Ni(1)-O(6)	2.1481(17)	Co(1)-O(8)	2.1874(13)
Ni(2)-O(6)	2.056(5)	Cs(2)-O(2)	3.207(4)	S(1)-O(11)	1.453(4)	Ni(1)-O(6)	2.1481(17)	Co(1)-O(8)	2.1874(13)
Ni(2)-O(7)	2.061(5)	Cs(2)-O(13)	3.241(4)	S(1)-O(13)	1.456(4)				
Ni(2)-O(6)	2.077(5)	Cs(2)-O(12)	3.243(4)	S(1)-O(5)	1.472(3)	Ni(2)-O(1)	1.9759(17)	Co(2)-O(4)	1.9990(13)
Ni(2)-O(4)	2.118(5)	Cs(2)-O(7)	3.270(4)			Ni(2)-O(3)	2.0332(18)	Co(2)-O(2)	2.0439(13)
Ni(2)-O(5)	2.155(5)	Cs(2)-O(6)	3.338(4)	S(2)-O(9)	1.459(4)	Ni(2)-O(8)	2.0457(18)	Co(2)-O(6)	2.0885(14)
		Cs(2)-O(15)	3.411(6)	S(2)-O(4)	1.461(3)	Ni(2)-O(5)	2.0537(17)	Co(2)-O(1)	2.0922(13)
S(1)-O(3)	1.438(5)	Cs(2)-O(11)	3.416(4)	S(2)-O(3)	1.470(4)	Ni(2)-O(4)	2.0880(17)	Co(2)-O(3)	2.1265(13)
S(1)-O(7)	1.445(5)			S(2)-O(10)	1.511(3)	Ni(2)-O(6)	2.3770(17)	Co(2)-O(8)	2.3938(13)
S(1)-O(4)	1.509(5)	Co(1)-O(15)	2.044(4)						
S(1)-O(5)	1.521(5)	Co(1)-O(8)	2.077(4)	S(3)-O(8)	1.463(4)	S(1)-O(3)	1.4639(18)	S(1)-O(1)	1.4658(13)
		Co(1)-O(5)	2.085(3)	S(3)-O(1)	1.469(3)	S(1)-O(5)	1.4649(18)	S(1)-O(5)	1.4663(13)

S(2)-O(2)	1.446(5)	Co(1)-O(4)	2.093(3)	S(3)-O(6)	1.477(4)	S(1)-O(2)	1.4688(18)	S(1)-O(2)	1.4678(13)
S(2)-O(8)	1.469(5)	Co(1)-O(9)	2.150(4)	S(3)-O(2)	1.482(3)	S(1)-O(6)	1.4967(17)	S(1)-O(8)	1.4896(14)
S(2)-O(1)	1.488(5)	Co(1)-O(13)	2.200(4)						
S(2)-O(6)	1.517(5)			S(4)-O(15)	1.431(4)	S(2)-O(4)	1.4634(18)	S(2)-O(3)	1.4614(13)
				S(4)-O(14)	1.442(4)	S(2)-O(8)	1.4654(18)	S(2)-O(6)	1.4651(14)
				S(4)-O(16)	1.467(4)	S(2)-O(1)	1.4734(18)	S(2)-O(4)	1.4728(13)
				S(4)-O(7)	1.468(4)	S(2)-O(7)	1.4784(18)	S(2)-O(7)	1.4766(13)

Table S18. Bond Valence Sums for (1) $Cs_2Ni_3(SO_4)_4$, (2) $Cs_2Co_3(SO_4)_4$, (3) $Rb_2Ni_3(SO_4)_4$ and (4) $Rb_2Co_3(SO_4)_4$.

(1) $Cs2Ni_3(SO_4)_4$		(2) $Cs_2Co_3(SO_4)_4$				(3) $Rb_2Ni_3(SO_4)_4$		(4) $Rb_2Co_3(SO_4)_4$	
atoms	BVS	atoms	BVS	atoms	BVS	atoms	BVS	atoms	BVS
Cs1	1.050(6)	Cs1	1.204(4)	O5	2.034(14)	Rb1	1.291(3)	Rb1	1.1517(18)
Ni1	1.915(12)	Cs2	1.212(4)	O6	2.052(18)	Ni1	1.926(4)	Co1	1.957(3)
Ni2	1.915(12)	Co1	1.973(9)	O7	2.166(16)	Ni2	1.915(4)	Co2	1.964(3)
S1	5.97(4)	Co2	1.984(10)	O8	2.071(16)	S1	6.014(16)	S1	6.031(12)
S2	5.92(5)	Co3	2.007(9)	O9	1.946(16)	S2	6.062(16)	S2	6.083(13)
O1	2.01(3)	S1	6.29(3)	O10	1.959(13)	O1	2.202(9)	O1	2.010(8)
O2	2.02(3)	S2	6.02(3)	O11	2.13(2)	O2	2.113(8)	O2	2.077(5)
O3	2.01(3)	S3	6.04(3)	O12	2.13(2)	O3	2.071(8)	O3	1.990(6)
O4	1.97(2)	S4	6.34(4)	O13	2.013(15)	O4	2.014(8)	O4	2.170(7)
O5	1.89(2)	O1	1.967(15)	O14	2.14(2)	O5	2.027(10)	O5	2.119(6)
O6	2.01(2)	O2	2.090(14)	O15	2.18(2)	O6	1.816(8)	O6	2.016(8)
O7	1.98(2)	O3	1.967(14)	O16	2.14(2)	O7	1.978(7)	O7	1.976(5)
O8	1.91(2)	O4	2.091(18)			O8	2.024(9)	O8	1.850(6)

Table S19. Atomic coordinates and equivalent isotropic and anisotropic displacement parameters for (1) $Cs_2Ni_3(SO_4)_4$

	x	*y*	*z*	U_{eq}	U_{11}	U_{22}	U_{33}	U_{23}	U_{13}	U_{12}
Cs(1)	0.20139(13)	0.78636(3)	0.35957(8)	0.0362(2)	0.0498(4)	0.0302(3)	0.0374(4)	-0.0015(3)	0.0275(3)	-0.0061(2)
Ni(1)	0	1	0	0.0137(4)	0.0124(7)	0.0197(7)	0.0086(7)	0.0001(5)	0.0018(5)	-0.0002(5)
Ni(2)	-0.10736(18)	0.51544(5)	0.17902(12)	0.0124(3)	0.0111(5)	0.0178(5)	0.0078(5)	0.0002(4)	0.0012(4)	0.0001(3)
S(1)	0.0386(4)	0.59580(9)	0.5735(2)	0.0129(6)	0.0127(10)	0.0155(9)	0.0101(9)	-0.0002(7)	0.0024(7)	0.0002(6)
S(2)	-0.1194(4)	0.90037(9)	0.6318(2)	0.0122(6)	0.0113(10)	0.0145(9)	0.0097(9)	-0.0005(7)	0.0005(7)	-0.0010(6)
O(1)	0.0914(10)	0.9239(3)	0.5506(7)	0.0153(18)	0.012(3)	0.022(3)	0.011(3)	0.000(2)	0.001(2)	0.000(2)
O(2)	-0.1827(11)	0.8245(3)	0.5931(7)	0.024(2)	0.042(4)	0.010(3)	0.022(3)	0.000(2)	0.012(3)	-0.001(2)
O(3)	0.0819(11)	0.6691(3)	0.6413(7)	0.0190(18)	0.024(3)	0.017(3)	0.016(3)	-0.001(2)	0.005(2)	-0.005(2)
O(4)	0.2715(9)	0.5492(3)	0.6487(7)	0.0149(18)	0.005(3)	0.027(3)	0.011(3)	0.004(2)	-0.001(2)	0.004(2)
O(5)	0.3381(10)	0.9426(3)	0.1493(6)	0.0148(17)	0.016(3)	0.020(3)	0.008(2)	-0.001(2)	0.002(2)	-0.0014(19)
O(6)	-0.3525(9)	0.9454(3)	0.5413(7)	0.0141(18)	0.010(3)	0.021(3)	0.010(3)	0.004(2)	0.000(2)	0.0035(19)
O(7)	-0.0300(10)	0.5950(3)	0.3770(6)	0.0171(18)	0.023(3)	0.021(3)	0.007(3)	-0.004(2)	0.003(2)	-0.001(2)
O(8)	-0.0546(10)	0.9151(3)	0.8281(7)	0.0181(18)	0.014(3)	0.026(3)	0.012(3)	0.001(2)	-0.001(2)	-0.001(2)

Table S20. Atomic coordinates and equivalent isotropic and anisotropic displacement parameters for (2) $Cs_2Co_3(SO_4)_4$

	x	*y*	*z*	U_{eq}	U_{11}	U_{22}	U_{33}	U_{23}	U_{13}	U_{12}
Cs(1)	-0.14105(4)	0.47657(3)	0.42298(2)	0.02193(9)	0.01622(14)	0.01649(13)	0.03309(18)	-0.00032(12)	0.00034(14)	0.00060(13)
Cs(2)	0.25018(4)	0.71357(3)	0.81336(2)	0.02164(9)	0.02081(15)	0.01476(13)	0.02934(17)	0.00212(13)	0.00029(15)	-0.00107(12)
Co(1)	0.95950(7)	0.84028(6)	0.63115(4)	0.01143(17)	0.0108(3)	0.0110(3)	0.0125(3)	0.0015(2)	0.0013(2)	0.0008(2)
Co(2)	0.54592(7)	0.56834(6)	0.64524(4)	0.01240(17)	0.0120(3)	0.0118(3)	0.0134(3)	-0.0027(2)	-0.0018(2)	-0.0007(2)
Co(3)	0.19322(7)	0.40301(6)	0.59038(4)	0.01227(17)	0.0117(3)	0.0111(3)	0.0140(3)	-0.0016(2)	0.0005(2)	-0.0022(2)
S(1)	-0.08849(12)	0.53524(11)	0.70152(7)	0.0100(3)	0.0080(4)	0.0093(4)	0.0127(5)	0.0002(4)	0.0009(4)	-0.0002(4)
S(2)	0.24371(14)	0.66934(10)	0.53825(7)	0.0104(3)	0.0087(5)	0.0087(4)	0.0138(5)	0.0008(4)	0.0008(4)	-0.0003(4)
S(3)	0.63757(13)	0.85710(10)	0.73474(7)	0.0098(3)	0.0100(5)	0.0085(4)	0.0108(5)	0.0004(4)	0.0006(4)	-0.0014(3)
S(4)	0.49385(13)	0.37045(11)	0.48940(7)	0.0103(3)	0.0094(5)	0.0090(4)	0.0124(5)	0.0018(4)	0.0005(4)	-0.0019(4)
O(1)	0.6918(4)	0.8012(4)	0.8145(2)	0.0189(10)	0.0276(19)	0.0168(16)	0.0124(15)	0.0044(14)	-0.0035(15)	0.0025(13)
O(2)	0.5391(4)	0.9740(3)	0.7497(2)	0.0163(9)	0.0182(17)	0.0146(14)	0.0161(15)	0.0066(14)	0.0004(14)	-0.0027(13)
O(3)	0.1492(4)	0.5668(3)	0.4992(2)	0.0174(9)	0.0160(17)	0.0165(15)	0.0198(16)	-0.0057(14)	-0.0038(14)	0.0011(13)
O(4)	0.1595(4)	0.7774(4)	0.5779(3)	0.0241(10)	0.0151(17)	0.0171(16)	0.040(2)	0.0053(14)	0.0099(17)	-0.0053(17)
O(5)	-0.0327(4)	0.6737(3)	0.7111(2)	0.0208(10)	0.027(2)	0.0103(14)	0.0252(18)	-0.0050(14)	-0.0056(16)	0.0023(13)
O(6)	0.5463(4)	0.7559(4)	0.6907(3)	0.0222(10)	0.0195(18)	0.0162(16)	0.031(2)	-0.0020(14)	-0.0069(17)	-0.0077(15)
O(7)	0.3459(4)	0.3214(4)	0.5110(2)	0.0229(11)	0.0197(19)	0.0246(18)	0.0244(19)	-0.0073(16)	0.0100(16)	-0.0057(15)
O(8)	0.7593(4)	0.9032(3)	0.6816(2)	0.0195(9)	0.0154(16)	0.0204(16)	0.0228(17)	0.0037(15)	0.0075(16)	0.0055(13)
O(9)	0.3473(4)	0.7316(4)	0.4795(2)	0.0212(10)	0.0221(19)	0.0187(17)	0.0229(18)	-0.0085(15)	0.0104(16)	-0.0037(14)
O(10)	0.3250(4)	0.5928(3)	0.6061(2)	0.0183(10)	0.0170(18)	0.0167(16)	0.0212(17)	-0.0003(13)	-0.0073(14)	0.0042(13)
O(11)	0.0021(5)	0.4601(4)	0.6425(3)	0.0390(16)	0.039(3)	0.029(2)	0.049(3)	0.007(2)	0.028(2)	-0.007(2)
O(12)	-0.2370(5)	0.5393(4)	0.6678(3)	0.0387(14)	0.017(2)	0.030(2)	0.069(3)	-0.0045(19)	-0.019(2)	0.005(2)
O(13)	-0.0914(5)	0.4637(4)	0.7817(2)	0.0290(13)	0.048(3)	0.0201(18)	0.0190(18)	0.0013(18)	-0.0017(18)	0.0061(15)
O(14)	0.5748(5)	0.2623(4)	0.4496(3)	0.0387(14)	0.021(2)	0.031(2)	0.064(3)	0.0133(18)	-0.005(2)	-0.031(2)
O(15)	0.4799(6)	0.4820(5)	0.4322(3)	0.0473(17)	0.052(3)	0.039(3)	0.051(3)	-0.002(2)	0.009(3)	0.033(2)
O(16)	0.5736(5)	0.4153(5)	0.5649(3)	0.0353(14)	0.023(2)	0.050(3)	0.033(2)	0.011(2)	-0.0116(18)	-0.027(2)

Table S21. Atomic coordinates and equivalent isotropic and anisotropic displacement parameters for (3) $Rb_2Ni_3(SO_4)_4$

	x	*y*	*z*	U_{eq}	U_{11}	U_{22}	U_{33}	U_{23}	U_{13}	U_{12}
Rb(1)	0.16190(3)	0.83602(3)	0.10182(4)	0.02202(11)	0.01613(13)	0.02297(15)	0.03236(16)	-0.00033(11)	0.01601(12)	-0.00377(12)
Ni(1)	0.5	1	0	0.00840(16)	0.0092(2)	0.0079(2)	0.0089(2)	0.00033(16)	0.00503(16)	0.00090(15)
Ni(2)	-0.25109(4)	0.62716(4)	0.01507(4)	0.00943(11)	0.00919(14)	0.01071(15)	0.00957(15)	-0.00217(11)	0.00548(12)	-0.00246(11)
S(1)	0.51722(7)	0.66243(7)	0.18910(7)	0.00719(18)	0.0078(2)	0.0078(3)	0.0069(2)	-0.0008(2)	0.0043(2)	-0.00008(19)
S(2)	-0.11674(7)	0.93268(7)	0.24675(7)	0.0077(2)	0.0072(2)	0.0081(3)	0.0083(3)	-0.00051(19)	0.0042(2)	-0.00063(19)
O(1)	-0.1245(2)	0.8167(2)	0.1261(2)	0.0129(6)	0.0131(8)	0.0130(9)	0.0138(8)	-0.0030(7)	0.0075(7)	-0.0063(7)
O(2)	0.4884(2)	0.8260(2)	0.1352(2)	0.0126(7)	0.0169(9)	0.0089(8)	0.0141(8)	-0.0001(7)	0.0092(7)	0.0036(7)
O(3)	0.3630(2)	0.5754(2)	0.0980(2)	0.0142(7)	0.0115(8)	0.0150(9)	0.0158(9)	-0.0041(7)	0.0063(7)	-0.0056(7)
O(4)	0.0446(2)	1.0073(2)	0.3085(2)	0.0172(7)	0.0106(8)	0.0227(10)	0.0179(9)	-0.0081(8)	0.0065(7)	-0.0079(8)
O(5)	0.3501(2)	1.0920(2)	0.3318(2)	0.0133(7)	0.0127(8)	0.0151(9)	0.0169(9)	-0.0017(7)	0.0109(7)	-0.0002(7)
O(6)	0.5648(2)	0.8337(2)	-0.1322(2)	0.0114(6)	0.0133(8)	0.0141(8)	0.0064(8)	0.0009(7)	0.0045(7)	-0.0013(6)
O(7)	0.2491(2)	0.9508(2)	-0.1617(2)	0.0118(6)	0.0106(8)	0.0117(8)	0.0122(8)	0.0034(7)	0.0048(7)	0.0028(7)
O(8)	0.1314(2)	0.3552(2)	0.1202(2)	0.0145(7)	0.0171(9)	0.0181(10)	0.0125(9)	-0.0053(7)	0.0104(7)	-0.0067(7)

Table S22. Atomic coordinates and equivalent isotropic and anisotropic displacement parameters for (4) $Rb_2Co_3(SO_4)_4$

	x	*y*	*z*	U_{eq}	U_{11}	U_{22}	U_{33}	U_{23}	U_{13}	U_{12}
Rb(1)	1.16213(2)	1.16676(2)	0.10348(3)	0.02433(8)	0.01793(8)	0.02490(10)	0.03623(13)	0.00042(7)	0.01794(8)	0.00442(8)
Co(1)	0.5	1	0	0.00917(10)	0.01051(12)	0.00837(12)	0.00960(14)	-0.00064(10)	0.00566(10)	-0.00144(11)
Co(2)	0.74777(3)	1.37387(3)	0.01363(3)	0.01015(7)	0.00994(8)	0.01073(9)	0.01090(10)	0.00204(7)	0.00595(7)	0.00275(8)
S(1)	0.48255(5)	0.83820(4)	0.31066(5)	0.00783(11)	0.00831(13)	0.00830(14)	0.00773(16)	-0.00050(11)	0.00457(12)	-0.00006(13)
S(2)	0.88458(4)	1.06796(5)	0.24608(5)	0.00828(11)	0.00774(13)	0.00926(14)	0.00801(16)	0.00040(11)	0.00396(12)	0.00087(13)
O(1)	0.35219(16)	0.90911(15)	0.33221(17)	0.0152(4)	0.0153(5)	0.0167(6)	0.0192(6)	0.0023(4)	0.0129(5)	0.0003(5)
O(2)	0.36382(15)	0.42461(15)	0.10045(17)	0.0153(4)	0.0125(5)	0.0153(5)	0.0181(6)	0.0054(4)	0.0075(5)	0.0064(5)
O(3)	0.95590(16)	1.49412(17)	0.19357(18)	0.0192(5)	0.0120(5)	0.0240(6)	0.0205(7)	-0.0080(5)	0.0070(5)	-0.0085(6)
O(4)	0.87512(16)	1.18443(15)	0.12703(17)	0.0149(4)	0.0162(5)	0.0145(5)	0.0167(6)	0.0043(4)	0.0102(5)	0.0080(5)
O(5)	0.51180(16)	0.67705(14)	0.36682(17)	0.0149(4)	0.0188(5)	0.0101(5)	0.0174(6)	0.0013(4)	0.0100(5)	0.0051(5)
O(6)	0.87062(17)	1.14308(16)	0.37886(17)	0.0172(5)	0.0204(6)	0.0201(6)	0.0159(6)	-0.0070(5)	0.0127(5)	-0.0078(5)
O(7)	0.75352(15)	0.95266(15)	0.16169(16)	0.0136(4)	0.0123(5)	0.0124(5)	0.0149(6)	-0.0031(4)	0.0058(4)	-0.0025(5)
O(8)	0.43494(15)	0.83290(15)	0.13422(15)	0.0138(4)	0.0160(5)	0.0176(6)	0.0081(5)	-0.0024(4)	0.0062(4)	0.0000(5)

Table S23. Summary of the different syntheses attempted to prepare the title compounds and obtained phases.

Formula	Preparation method T(°C)	Heating time (h)	Duration (h)	Cooling time (h)	XRDP analysis
$Cs_2Ni_3(SO_4)_4$	c) 700	7	10	96 to 500°C and 5 to 25°C	c) $Cs_2Ni_3(SO_4)_4$, Cs_2SO_4.
	d) 600	7	2	10 to 100°C	d) $Cs_2Ni_3(SO_4)_4$, Cs_2SO_4, $NiSO_4$
$Cs_2Co_3(SO_4)_4$	d) 600 °C	7	3	12 to 100°C	d) $Cs_2Co_3(SO_4)_4$, $Cs_2Co_2(SO_4)_3$, $CoSO_4$
	e) 560	7	3	Quenched	e) $Cs_2Co_3(SO_4)_4$, $Cs_2Co_2(SO_4)_3$
	f) 530	7	2	60 to 100°C	f) $Cs_2Co_3(SO_4)_4$, $Cs_2Co_2(SO_4)_3$
$Rb_2Ni_3(SO_4)_4$	f) 750 °C	7	18	96 to 500°C	f) $Rb_2Ni_3(SO_4)_4$, Rb_2SO_4.

	g) 600	7	1.5	10 to 100°C	g) $Rb_2Ni_3(SO_4)_4$, $Rb_2Ni_2(SO_4)_3$
	h) 600°C	7	24	10 to 100°C	h) $Rb_2Ni_2(SO_4)_3$, $NiSO_4$
	i) 600	7	24	70 to 500°C and 10 to 25°C	i) $Rb_2Ni_3(SO_4)_4$, $Rb_2Ni_2(SO_4)_3$, $NiSO_4$
	j) 600	7	6	Furnace off	j) $Rb_2Ni_3(SO_4)_4$, $Rb_2Ni_2(SO_4)_3$, $NiSO_4$
$Rb_2Co_3(SO_4)_4$	d) 750	7	34	40 to 200°C	d) $Rb_2Co_3(SO_4)_4$ $Rb_2Co_2(SO_4)_3$
	e) 600	7	1.5	10 to 100°C	e) $Rb_2Co_3(SO_4)_4$, $Rb_2Co_2(SO_4)_3$, $CoSO_4$
	f) 600	7	24	10 to 100°C	f) $Rb_2Co_3(SO_4)_4$, $Rb_2Co_2(SO_4)_3$, $CoSO_4$

Table S24. Selected interatomic distances (Å) in the structure of $Cs_2Cu(SO_4)_2$ and $Cs_2Co_2(SO_4)_3$.

$Cs_2Cu(SO_4)_2$				$Cs_2Co_2(SO_4)_3$			
Cs1-O5	2.985(4)	Cu1-O3	1.919(4)	Cs1-O6	2.991(7)	Co1-O8	1.994(7)
Cs1-O7	3.096(6)	Cu1-O1	1.986(4)	Cs1-O3	3.095(8)	Co1-O2	2.002(7)
Cs1-O7	3.170(5)	Cu1-O6	2.003(4)	Cs1-O1	3.114(7)	Co1-O4	2.017(6)
Cs1-O1	3.194(4)	Cu1-O2	2.019(4)	Cs1-O5	3.127(7)	Co1-O11	2.095(7)
Cs1-O6	3.250(5)	Cu1-O8	2.195(4)	Cs1-O6	3.241(8)	Co1-O9	2.120(7)
Cs1-O2	3.263(4)	Cu1-S1	2.5837(16)	Cs1-O8	3.295(8)		
Cs1-O4	3.469(5)			Cs1-O1	3.304(7)	Co2-O10	1.948(7)
Cs1-O5	3.504(4)	S1-O4	1.441(4)	Cs1-O9	3.331(8)	Co2-O12	1.956(7)
Cs1-O2	3.532(5)	S1-O5	1.448(4)	Cs1-O6	3.368(8)	Co2-O5	1.973(7)
Cs1-O8	3.679(7)	S1-O3	1.492(4)	Cs1-O2	3.431(8)	Co2-O3	1.992(7)
Cs1-O8	3.691(7)	S1-O1	1.504(4)	Cs1-O5	3.772(7)	Co2-O7	2.689(7)
		<S1-O>	1.471				
Cs2-O4	3.008(4)			Cs2-O7	3.121(8)	S1-O1	1.448(6)
Cs2-O3	3.029(4)	S2-O8	1.434(4)	Cs2-O11	3.141(8)	S1-O9	1.463(7)
Cs2-O5	3.187(4)	S2-O7	1.446(5)	Cs2-O7	3.188(8)	S1-O2	1.480(7)
Cs2-O6	3.286(4)	S2-O2	1.495(4)	Cs2-O12	3.203(7)	S1-O12	1.484(7)
Cs2-O8	3.310(6)	S2-O6	1.495(5)	Cs2-O4	3.236(7)	<S1-O>	1.469
Cs2-O7	3.323(5)	<S2-O>	1.468	Cs2-O10	3.316(8)		
Cs2-O1	3.383(4)			Cs2-O1	3.431(7)	S2-O6	1.444(7)
Cs2-O4	3.411(5)			Cs2-O4	3.462(7)	S2-O11	1.464(7)
Cs2-O2	3.584(4)			Cs2-O1	3.514(7)	S2-O8	1.488(6)
Cs2-O6	3.721(5)			Cs2-O2	3.550(8)	S2-O5	1.493(7)
				Cs2-O12	3.781(8)	<S2-O>	1.472
						S3-O7	1.447(8)
						S3-O10	1.464(6)
						S3-O4	1.474(6)
						S3-O3	1.486(8)
						<S3-O>	1.468

Table S25. Bond-valence values (expressed in valence units) for $Cs_2Cu(SO_4)_2$.

	O1	O2	O3	O4	O5	O6	O7	O8	$\Sigma_v a$
Cs1	0.11	0.10 0.05		0.06	0.19 0.05	0.10	0.14 0.12		0.91
Cs2	0.07	0.04	0.17	0.18 0.07	0.11	0.09 0.03	0.08	0.08	0.93
Cu1	0.43	0.39	0.52			0.41		0.24	1.99
S1	1.39		1.43	1.62	1.59				6.03
S2		1.42				1.42	1.60	1.65	6.09
$\Sigma_v c$	2.00	2.00	2.12	1.93	1.94	2.05	1.94	1.97	

Table S26. Bond-valence values (expressed in valence units) for $Cs_2Co_2(SO_4)_3$.

	O1	O2	O3	O4	O5	O6	O7	O8	O9	O10	O11	O12	$\Sigma_v a$
Cs1	0.14 0.09		0.14		0.13	0.18 0.10 0.07		0.09	0.08				1.03
Cs2	0.06 0.05	0.05		0.10 0.06			0.13 0.11	0.08			0.13	0.11 0.03	0.92
Co1		0.45		0.43				0.46	0.33		0.35		2.00
Co2			0.46		0.48		0.07			0.51		0.50	2.03
S1	1.59	1.47							1.54			1.46	6.06
S2					1.42	1.61		1.44			1.53		6.01
S3			1.45	1.49			1.60			1.53			6.07
$\Sigma_v c$	1.93	1.97	2.05	2.08	2.03	1.96	1.91	2.07	1.95	2.04	2.01	2.1	

Table S27. Crystallographic parameters of known saranchinaite morphotropic series $A_2[Cu(SO_4)_2]$ compounds.

Phase modification	α-phase		β-phase	γ-phase				δ-phase	ε-phase
Mineral/Synthetic	saranchinaite	synthetic	synthetic	synthetic	synthetic	synthetic	synthetic	synthetic	synthetic
Formula	$Na_2[Cu(SO_4)_2]$	$Na_2[Cu(SO_4)_2]$	$K(Na,K)Na_2[Cu_2(SO_4)_4]$	$KNa[Cu(SO_4)_2]$	$K_2[Cu_2(SO_4)_2]$	$RbNa[Cu(SO_4)_2]$	$RbK[Cu(SO_4)_2]$	$Rb_2[Cu(SO_4)_2]$	$Cs_2[Cu(SO_4)_2]$
Space group	$P2_1$	$P2_1$	$P2_1/c$	$C2/c$	$C2/c$	$C2/c$	$C2/c$	$Pna2_1$	$P2_1/n$
a, Å	9.0109(5)	8.9711(3)	12.5085(9)	15.9721(10)	16.0433(11)	16.034(3)	16.1865(14)	9.2521(4)	9.685(3)
b, Å	15.6355(8)	15.5482(5)	9.3166(7)	9.4576(6)	9.7819(7)	9.560(2)	10.0026(9)	10.9671(5)	7.920(3)
c, Å	10.1507(5)	10.1421(3)	12.7894(10)	9.0679(6)	9.2341(7)	9.170(2)	9.3923(8	8.9612(4)	12.141(4)
β,°	107.079(2)	107.155(1)	107.775(2)	93.6350(10)	93.2680(10)	92.792(6)	92.149(2)		91.416(8)
V, Å^3	1367.06(12)	1351.73(7)	1419.28(19)	1367.02(15)	1446.79(18)	1403.9(5)	1519.6(2)	909.28(7)	931.0(5)
R_1	0.030	0.020	0.030	0.029	0.017	0.030	0.025	0.019	0.044
Reference	Siidra et al., 2018	Kovrugin et al., 2019	Siidra et al., 2021	Borisov et al., 2021	Zhou et al., 2020	Siidra et al., 2021	Siidra et al., 2021	Siidra et al., 2021	this work

Table S28. Crystallographic parameters of orthorhombic $A_2M^{2+}{}_2(SO_4)_3$ compounds.

Formula	$K_2Cu_2(SO_4)_3$	$Rb_2Cu_2(SO_4)_3$	$Cs_2Co_2(SO_4)_3$
Space group	$P2_12_12_1$	$P2_12_12_1$	$P2_12_12_1$
a, Å	4.81065(1)	4.8359(19)	4.8810(7)
b, Å	11.91795(3)	12.294(4)	14.920(2)
c, Å	18.67516(4)	19.036(7)	17.164(3)
V, Å^3	1070.704(4)	1131.7(7)	1249.9(3)
R_1	0.048	0.052	0.049
Reference	Lander et al., 2017	Siidra et al., 2021	this work